

GEOLOGICA ULTRAIECTINA

Mededelingen van de
Faculteit Geowetenschappen
Universiteit Utrecht

No. 236

**Evolving dynamical regimes during
secular cooling of terrestrial planets:**

insights and inferences from numerical models

Peter van Thienen

The research described in this thesis was carried out at:
Faculty of Geosciences
Vening Meinesz Research School of Geodynamics
Utrecht University
Budapestlaan 4
3584 CD Utrecht
The Netherlands

http://www.geo.uu.nl/Research/Theoretical_Geophysics/

ISBN: 90-5744-095-4

Evolving dynamical regimes during secular cooling of terrestrial planets:

insights and inferences from numerical models

Evoluerende dynamische regimes tijdens seculiere afkoeling van terrestrische planeten:

inzichten en conclusies uit numerieke modellen

(met een samenvatting in het Nederlands)

PROEFSCHRIFT

TER VERKRIJGING VAN DE GRAAD VAN DOCTOR
AAN DE UNIVERSITEIT UTRECHT
OP GEZAG VAN DE RECTOR MAGNIFICUS, PROF. DR. W.H. GISPEN,
INGEVOLGE HET BESLUIT VAN HET COLLEGE VOOR PROMOTIES
IN HET OPENBAAR TE VERDEDIGEN
OP MAANDAG 24 NOVEMBER 2003 DES MIDDAGS TE 2:30 UUR

DOOR

Peter van Thienen

Geboren op 10 oktober 1975, te Rotterdam

Promotores: Prof. Dr. R.D. van der Hilst^{*,†}
Prof. Dr. N.J. Vlaar^{*}
Co-promotor: Dr. A.P. van den Berg^{*}

^{*}Faculty of Geosciences
Utrecht University

[†]Cecile and Ida Green Professor of Earth and Planetary Sciences
Department of Earth, Atmospheric and Planetary Sciences
Massachusetts Institute of Technology, Cambridge MA, USA

... que tu no sabes que cosa seã coluros, lineas, paralelos, zodiacos, cliticac, polos, solsticios, equinocios, planetas, signos, puntos, medidas, de que se compone la esfera celeste, y terrestre, que si todas estas cosas supieras; o parte dellas, vieras claramente, que de paralelos hemos cortado, que de signos visto, y que de imagines hemos dexado atras, y vamos dexando agora.

“...for thou knowest nothing about colures, lines, parallels, zodiacs, ecliptics, poles, solstices, equinoxes, planets, signs, bearings, the measures of which the celestial and terrestrial spheres are composed; if thou wert acquainted with all these things, or any portion of them, thou wouldst see clearly how many parallels we have cut, what signs we have seen, and what constellations we have left behind and are now leaving behind.”

“...jij hebt geen weet van de coluren, lijnen, parallellen, zodiacken, ecliptica's, polen, solstitia, equinoxen, planeten, tekenen, punten en maten waaruit de hemelbol en aardbol bestaan; als je al deze dingen of een deel ervan kende, zou je zonder meer inzien hoeveel parallellen wij hebben doorsneden, hoeveel sterrenbeelden wij hebben gezien, en hoeveel constellaties wij achter ons hebben gelaten en nog achter ons laten.”

(zegt Don Quichot tegen Sancho Panza in het hoofdstuk “Over het beroemde avontuur met de betoverde boot” van “De vernuftige edelman Don Quichot van La Mancha” deel 2, door Miguel de Cervantes Saavedra. English translation by John Ormsby; Nederlandse vertaling door Barber van de Pol; oorspronkelijke tekst uit de eerste druk van “Segunda parte del ingenioso cauallero Don Quixote de la Mancha”, Madrid, 1615)

Members of the dissertation committee:

Prof. Dr. B.H.W.S. de Jong
Faculty of Geosciences
Utrecht University

Prof. Dr. Y. Ricard
Laboratoire de Sciences de la Terre
Ecole Normale Supérieure de Lyon

Prof. Dr. H.A. van der Vorst
Department of Mathematics
Utrecht University

Prof. Dr. M.J.R. Wortel
Faculty of Geosciences
Utrecht University

Prof. Dr. D.A. Yuen
Department of Geology and Geophysics & Minnesota Supercomputing Institute
University of Minnesota

Contents

1	Introduction.	11
2	Model description	17
2.1	Conservation equations	17
2.2	Equation of state	20
2.3	Rheological model	20
2.4	Solid state phase transitions	21
2.4.1	Basalt to eclogite phase transition	21
2.4.2	Mantle phase transitions	22
2.5	Partial melting of peridotite and basalt	23
2.6	Fractionation of trace elements	24
2.7	Crustal growth	26
3	Numerical methods	27
3.1	Discretization of the energy equation	27
3.2	Discretization of the Stokes equation	28
3.3	Time integration	28
3.4	Particle tracers	29
3.5	Crustal growth	30
4	Plate tectonics on the terrestrial planets	31
4.1	Introduction	31
4.2	Description of the numerical models	34
4.2.1	Equations and procedure	34
4.2.2	Model parameters	37
4.3	Results	39
4.4	Discussion	43
4.4.1	Plate tectonics on Earth	43
4.4.2	Plate tectonics on Venus	44
4.4.3	Plate tectonics on Mars	45
4.5	Conclusions	45

5	Assessment of the cooling capacity of plate tectonics and flood volcanism in the evolution of Earth, Mars and Venus	47
5.1	Introduction	48
5.2	Numerical model	50
5.2.1	Plate tectonics	53
5.2.2	Extrusion mechanism	55
5.2.3	Input parameters	57
5.2.4	Solving the equation	61
5.3	Results	61
5.3.1	Mantle cooling rates	61
5.3.2	Plate tectonics on Earth	64
5.3.3	Sensitivity of plate tectonics results to the model parameters	66
5.3.4	Plate tectonics on Mars and Venus	67
5.3.5	Effects of planetary parameters on heat transfer by plate tectonics	70
5.3.6	Extrusion mechanism on Earth	70
5.3.7	Sensitivity of the extrusion mechanism heat transfer	71
5.3.8	Extrusion mechanism on Mars and Venus	71
5.3.9	Effects of planetary parameters on the extrusion mechanism heat transfer	71
5.4	Discussion	74
5.4.1	Plate tectonics on the early Earth	74
5.4.2	Extrusion mechanism on the early Earth	74
5.4.3	Cooling mechanisms of Mars and Venus	77
5.5	Conclusions	79
6	Production and recycling of oceanic crust in the early Earth	81
6.1	Introduction	81
6.2	Numerical model setup	84
6.2.1	Description of the numerical model	84
6.2.2	Rheology	88
6.2.3	Fractionation of trace elements	90
6.2.4	Model geometry and boundary conditions	90
6.3	Results	90
6.3.1	Sensitivity to initial conditions	91
6.3.2	Dynamics of crustal growth and recycling	92
6.3.3	Long-term thermal and chemical development	94
6.3.4	Lower mantle size	98
6.4	Discussion	101
6.4.1	Large Archean mantle plumes	101
6.4.2	Rapid resurfacing	102
6.4.3	Thermal evolution of the mantle	103
6.4.4	Geochemical evolution of the mantle	103
6.5	Conclusions	105

7	On the formation of continental silicic melts in thermo-chemical mantle convection models: implications for early Earth and Venus	107
7.1	Introduction	108
7.2	Model description	110
7.2.1	Governing equations	110
7.2.2	Computational methods	113
7.2.3	Solid state phase transitions	113
7.2.4	Partial melting	114
7.2.5	Crustal growth	115
7.2.6	Metamorphic phase stability fields	116
7.2.7	Initial conditions	118
7.3	Results	119
7.3.1	Geodynamical settings	119
7.3.2	Conditions of partial melting	121
7.3.3	Production rates of continental material	121
7.3.4	Distribution of felsic material in the crust	122
7.4	Discussion	122
7.5	Conclusions	124
8	Interaction between small-scale mantle diapirs and a continental root	125
8.1	Introduction	126
8.2	Numerical model setup	129
8.2.1	Description of the numerical model	129
8.2.2	Model geometry and initial and boundary conditions	135
8.2.3	Model parameters	135
8.3	Results of numerical modelling	136
8.3.1	General characteristics	137
8.3.2	Linear rheology results	137
8.3.3	Composite rheology results: grain size variation	139
8.3.4	Viscosity component ratios	141
8.3.5	Deformation maps	144
8.3.6	Dehydration and viscosity	145
8.3.7	Ascent velocities	148
8.3.8	P,T paths	152
8.3.9	Stress and strainrate histories	154
8.4	Discussion and conclusions	154
9	Summary and Conclusions	159
9.1	Summary	159
9.2	Conclusions	162
9.2.1	Earth	162
9.2.2	Venus	163
9.2.3	Mars	163

Bibliography	165
A Error magnitude in the conservation of energy in the approximate melt segregation scheme	179
A.1 Conservation of energy	179
A.2 Thermal energy content	180
A.3 Error magnitude	181
B Discretization and benchmarking of the energy equation	185
B.1 The energy equation	185
B.2 Discretization	186
B.3 Benchmarks of latent heat consumption	188
Samenvatting en conclusies (Summary and conclusions in Dutch)	191
Dankwoord (Acknowledgments)	197
Curriculum vitae	199

Chapter 1

Introduction.

The large-scale geodynamics of the present-day Earth is to a large extent connected to plate tectonics. The formation of oceanic lithosphere at the spreading centers of mid-ocean ridges and the subduction of this lithosphere at subduction zones are the major expressions of this mechanism. It is ultimately driven by a temperature difference between the surface of the Earth and its interior, and efficiently transports heat to the surface, where it is transferred to the hydrosphere and atmosphere and finally radiated into space. This effectively cools the Earth's interior.

At mid-ocean ridges, new basaltic crust is formed by solidification of melt which is produced by pressure release partial melting in the hot upwelling mantle below the ridge. Much heat is released at this point through conduction and hydrothermal circulation (Stein, 1995), and the newly formed crust continues to cool as it moves away from the ridge to make place for new basaltic crust. This makes the plates an important factor in the cooling of the planet, facilitating about 70 % of the global surface heat flux (Pollack et al., 1993). The main force which drives this mechanism is *slab pull*, i.e. the force exerted by a negatively buoyant slab that is subducting (Stacey, 1992). When oceanic crust is created at mid ocean ridges, its intrinsic lower density (of both basalt and harzburgite relative to fertile peridotite) and relatively high temperature cause it to be positively buoyant. As it cools on its way from the ridge to a subduction zone, density increases, and at some point, the buoyancy becomes negative. This negative buoyancy is in fact the cause of the slab pull. A secondary driving force is ridge push, which is an order of magnitude weaker than slab pull (Turcotte and Schubert, 2002).

At subduction zones, the oceanic lithosphere sinks into the mantle below another lithosphere. As it moves downward, it heats up and fluids are released from the crust, which was hydrated by hydrothermal circulation of ocean water. This facilitates partial melting in the overlying mantle wedge, leading to the formation of a volcanic arc parallel to the subduction zone. This process itself at a continental margin or the accretion of these arcs in an oceanic case to existing continental masses is seen as an important mechanism for continental growth in the present-day Earth, together with the accretion of oceanic plateaux and intraplate volcanism (Rudnick, 1995).

Early in the planet's 4.57 billion year history, its internal temperature was higher by some hundreds of degrees Celsius than at present. This heat originated mainly from three sources. The first is the release of potential (gravitational) energy during accretion of the Earth. This took place over a period of 50 to 100 million years (Allègre et al., 1995; Halliday and Lee, 1999), providing enough energy to completely melt the planet (Horedt, 1980). The second heat source is the release of gravitational energy by core differentiation. The mean age of core differentiation was determined by Pb-Pb isotope geochemistry at 4.45 Ga (Allègre et al., 1995). The amount of heat released was sufficient to raise the core temperature by some thousands of degrees (Horedt, 1980). The decay of radioactive elements forms the third heat source, which is the most important for long-term development (Stevenson, 2003). Short-lived isotopes, specifically ^{244}Pu , ^{236}U and ^{26}Al with half lives of 76 Myr, 24 Myr and 0.72 Myr, respectively, and longer-lived isotopes such as ^{40}K , ^{235}U , ^{238}U , and ^{232}Th added large amounts of heat. ^{26}Al by itself produced enough energy to raise the core temperature by 10000 K (Ruff and Anderson, 1980). The decay of radioactive isotopes continues to provide heat at an ever decreasing rate. This elevated internal temperature had a major impact on the process of the formation of lithosphere from upwelling mantle flows as it occurs today at mid-ocean ridges. At a higher mantle temperature, upwelling material crosses the solidus at greater depth and therefore has a longer melting path, producing a thicker basaltic crust and underlying Harzburgite layer (Vlaar, 1986; Vlaar and Van den Berg, 1991). Clearly, a thicker crust can only be produced when upwelling and melting can take place over the complete depth range between solidus and surface, as is approximately the case at mid ocean ridges presently. In situations where upwelling material cannot rise to shallow levels, the production of greater crustal thicknesses is mitigated.

Since both basalt and harzburgite have a lower density than the undepleted peridotite mantle source rock, the layering that is created at mid-ocean ridges is gravitationally intrinsically stable. Cooling of this package, however, increases its density up to a point where the lithosphere is no longer positively buoyant, after which active subduction can take place. For the present-day Earth, this is at about 20 to 40 million years (Oxburgh and Parmentier, 1977; Vlaar and Van den Berg, 1991; Davies, 1992) after formation. For a thicker pile which is produced in a hotter mantle (Sleep and Windley, 1982; Vlaar, 1986; Vlaar and Van den Berg, 1991), this neutral buoyancy age is increased up to several hundreds of million years or more (Vlaar and Van den Berg, 1991). This hinders plate tectonics as we observe it in the present-day Earth. Numerical models of a subduction system by Van Hunen (2001) show that the present-day subduction style is feasible in a mantle that is up to 150 Kelvin hotter than it is today. At still higher mantle temperatures, these models show that the slab breaks off at very shallow levels, due to a combined effect of weaker rheology and increased buoyancy of a thicker partly eclogitic crust, removing slab pull and causing a rebound.

Our closest neighbours in the solar system, Mars and Venus are comparable in size and composition to Earth, and may be or have been subject to the same processes. Although both planets do not have plate tectonics today (Zuber, 2001; Nimmo and McKenzie, 1996), it may have been active during their earlier histories. Sleep (1994) interprets the current geology of Mars in a framework of early plate tectonics on this planet. Satel-

potential temperature ($^{\circ}\text{C}$)	viscosity	scale factor
1350	1.000	1.000
1450	0.258	0.713
1550	0.077	0.523
1650	0.026	0.402
1750	0.010	0.316

Table 1.1: The scaling of the magnitude and length scale of temperature variations in the mantle as a function of potential mantle temperature relative to the present temperature of about 1350°C , using the scaling relations of McKenzie and Bickle (1988). The viscosity is computed assuming diffusion creep only and using an activation energy of 300 kJmol^{-1} and an activation volume of $6 \cdot 10^{-6} \text{ m}^3\text{mol}^{-1}$ (Karato and Wu, 1993) at a depth of 300 km.

lite measurements of crustal magnetization on the southern hemisphere of Mars show a pattern more or less similar to magnetic striping found on the Earth's ocean floor. Although both the width and signal magnitude are much larger than on Earth, a similar plate tectonic origin has been suggested (Acuña et al., 1999; Connerney et al., 1999). Crater counts indicate that Venus has undergone a global resurfacing between 300 and 600 Myr before present (Schaber et al., 1992; Nimmo and McKenzie, 1998). We therefore do not have evidence for processes prior to the resurfacing, but episodic plate tectonics has been suggested for this planet (Turcotte, 1993).

Because viscosity is strongly temperature dependent, a higher mantle temperature in the early Earth (or other planets) also has consequences for the dynamics of mantle convection. A reduced viscosity results in faster flow and reduces the buildup of large temperature contrasts. McKenzie and Bickle (1988) use the boundary layer analysis of Turcotte and Oxburgh (1967) to estimate that the magnitude and length scale of temperature variations scale with the viscosity to the power $\frac{1}{4}$. From this we find that for a mantle that is 100 K hotter than it is today, both the scale and the magnitude of the variations would be reduced to about 70 percent of the present values. For still higher mantle temperatures, this reduces further down to about 30 percent for a 400 K hotter mantle, see Table 1.1 (a similar argument with an even larger decrease in viscosity and therefore variations is given in Nisbet et al., 1993). In other words, this line of reasoning predicts that in a hotter mantle circulation patterns have a smaller scale than the $x \cdot 10^3$ km of ridge to subduction zone which is the surface expression of present-day mantle convection. Furthermore, hypothetical mantle plumes, associated with hotspots like Hawaii and Iceland, with excess temperatures of up to 200 to 250°C (Herzberg and O'Hara, 1998), would have both a smaller size and a reduced excess temperature in a hotter mantle. Direct evidence for hotter conditions in the early Earth comes from Archean geology (e.g. Nisbet et al., 1993).

In several parts of the world, rocks which have been formed during the Archean (3.8-2.5 Gyr) outcrop at the surface. An overview of these locations is shown in Figure 1.1.



Figure 1.1: Overview of Archean cratons on the Earth. Black indicates outcropping Archean rocks. After Condie (1981).

Evident differences in the geology of these cratons compared to continental areas of more recent age indicate different conditions of formation. Goodwin (1991) gives an overview of the characteristics of (preserved) Archean crust, which will be summarized here. The cratons are typically subcircular to oblong and have unexposed extensions. They generally consist of about 60% granitoid gneiss-migmatites, including substantial granulites. The presence of high grade metamorphic xenoliths originating from upper crustal material in these rocks indicates still older crust. Geochemistry of the gneisses points to a close mantle-derived petrogenesis (low Sr and Nd initial ratios), and a relatively deep melt origin of more than 40 km (high La/Yb ratios), except for the latest Archean igneous rocks, which are formed by melting in the crust itself (Eu depletion). 30% of the cratons is made up by massive granitoid plutons. The older plutonic rocks generally classify as tonalite-trondhjemite-granodiorite (TTG) suite, and the younger are characteristically potassic granites. Also, small but significant amounts of layered mafic to ultramafic intrusives are found. Greenstone belts form about 10% of the exposed Archean rocks. These generally consist of tholeiitic to komatiitic lava flow sequences on top of which are felsic pyroclastic rocks (the former and the latter in varying proportions) and sediments. Most greenstone belts have been formed either around 3.5 Ga or around 2.7 Ga.

The style of tectonic deformation during the Archean shows a large horizontal component, with later vertical motions. Also, the intrusion of diapirs forming dome structures is important. An example of the resulting structures can be seen in Figure 1.2, which shows

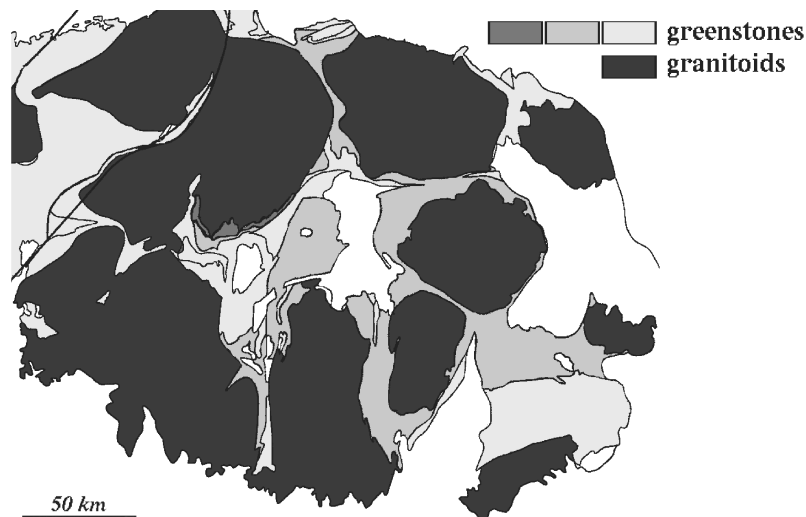


Figure 1.2: Overview map of the eastern Pilbara terrane, showing a typical structure of granites surrounded by greenstone belts (modified from Zegers and Van Keken, 2001).

a simplified geologic map of the Archean eastern Pilbara region in Australia, consisting largely of granite bodies of 50 to 100 km diameter, surrounded by greenstones. Seismological determination of upper mantle structure tells us that Archean cratons are usually underlain by thick roots down to about 250 km depth or deeper (Grand, 1994; Trampert and Woodhouse, 1996; Fischer and Van der Hilst, 1999), characterized by high seismic velocities. They are thought to consist of relatively cold and depleted mantle peridotite, and are often invoked to explain the long-term stability of these cratons (Forte and Perry, 2000; De Smet et al., 2000a). Numerical modelling experiments have shown that mantle diapirs could be important agents in the growth of continental roots during the Archean and Proterozoic (De Smet et al., 1998; Van Thienen et al., 2003a, chapter 8). These mantle diapirs are generally on a scale of 50 to 100 km and penetrate an existing root while producing melt, and a complementary depleted low density residue, thus adding depleted material to the continental root.

These results from numerical models are confirmed by geological data. Samples of cratonic lithosphere are found as xenoliths in kimberlite intrusions (Nixon and Boyd, 1973) and as larger bodies in some orogenic belts (Brueckner and Medaris, 1998; Van Roermund and Drury, 1998). It is proposed that many of these mantle rocks are emplaced into the lithosphere by diapirs from the convecting sublithospheric mantle (Nicolas, 1986) in a variety of geodynamic environments (Green and Gueguen, 1983; Nicolas et al., 1987; Fabriès et al., 1991). The PT paths derived from some cratonic peridotites from the Norwegian Western Gneiss Region (Van Roermund and Drury, 1998; Drury et al., 2001) imply that these rocks were part of diapirs that intruded cratonic lithosphere of Archean to

early Proterozoic age (the cooling age of these rocks is 1.7-1.8 Ga, but the Sm-Nd model age indicates a depletion age of 2.5-3.0 Ga). Drury et al. (2001) have shown that the PT path of these peridotites is consistent with PT paths of diapiric upwellings calculated from the thermo-chemical convection models of De Smet et al. (2000a).

It is the aim of this thesis to investigate the types of geodynamics that may have been important under the strongly different thermal conditions of the early Earth, both in the cooling of the planet's interior and in the formation and recycling of oceanic crust and of the continents, and also in the evolution of Mars and Venus. Furthermore, the demise of these processes as the planets cool towards the present temperature are investigated.

The tools which are used in the research are numerical models. These include both relatively simple models based on parametric descriptions of processes and 2-D thermo-chemical mantle convection models including compositional differentiation by partial melting.

An overview of the contents of this thesis will be given below.

Following this introduction, the main physical concepts and model equations which describe the physics are presented in chapter 2. The numerical techniques that are used to solve the model equations of chapter 2 are described in chapter 3. In following chapters, the numerical models presented in chapters 2 and 3 are applied to the problem area of this thesis. These chapters more or less show a progression in time and a zooming from large scale to smaller scale. First, the conditions under which different geodynamic regimes operate and the global thermal characteristics of these regimes are mapped out using simple models based on parameterizations of the relevant processes. In chapter 4, the effect of mantle temperature and gravitational acceleration on the time scales of the development of negative buoyancy of oceanic lithosphere is investigated in a plate tectonic setting for the terrestrial planets Earth, Venus and Mars. This gives an indication of the conditions that allow Earth-like plate tectonics to take place on the terrestrial planets. Next, in chapter 5, the cooling capacity and time characteristics of both plate tectonics and stagnant-lid basalt extrusion mechanism are assessed and compared, using a parametric approach. The following chapters consider in more detail the dynamics of crustal growth and recycling in a hot mantle. Numerical thermochemical mantle convection models on a scale of hundreds to 1500 km are used to investigate the local processes rather than the global effects. Chapter 6 deals with the formation of a basaltic oceanic crust from a convecting mantle and the recycling of the crust back into the mantle. Numerical thermochemical convection models are used in this chapter, and the focus is both on the dynamics of the processes and on the implications for mantle chemistry. In chapter 7, modelling results of self-consistent continental growth in a dynamical mantle convection model are presented. The dynamics and time and spatial scales of the process are investigated, and results are linked to the petrology and geochemistry of Archean continental material as found in the cratons. Chapter 8 deals with the effect of different rheological models on the development of small scale mantle diapirs impinging on a growing continental root. These plumes add relatively light material to the root of a continent as produced in chapter 7 and have a stabilizing effect on it. In the concluding chapter 9, a summary and general conclusions of this thesis will be given, from the interpretation of the combined results of the different chapters.

Chapter 2

Model description

In this thesis, both simple parameterized models of mantle dynamical processes and more complex thermo-chemical mantle convection models are used. The models of the former type will be described in detail in chapters 4 and 5. The models of the latter type will be described below. First, the governing equations and the rheological model will be treated. This will be followed by a description of the implementation of solid state phase transitions of crustal and mantle material included in the models. Finally, the implementation of partial melting of crustal and mantle material and associated fractionation of trace elements and production of crustal material will be described.

2.1 Conservation equations

The model is described by the following transport equations derived from conservation of energy, mass and momentum, respectively, applying the extended Boussinesq approximation (Steinbach et al., 1989; De Smet et al., 1998). The first is the energy equation:

$$\rho c_p \left(\frac{\partial T}{\partial t} + u_j \partial_j T \right) - \alpha T \frac{dp}{dt} = \tau_{ij} \partial_j u_i + \partial_j (k \partial_j T) + \rho_0 H + \frac{\Delta S}{c_p} \frac{dF}{dt} T + \sum_k \frac{\gamma_k \delta \rho_k T}{\rho_0^2 c_p} \frac{d\Gamma_k}{dt} \quad (2.1)$$

In this expression, T is the temperature, p pressure, F the degree of depletion, and H the internal heat productivity (see Table 2.1 for other symbols and section 2.5 for the definition of the degree of depletion).

Conservation of mass and momentum under the incompressibility condition implies

$$\partial_j u_j = 0 \quad (2.2)$$

From conservation of momentum and the assumption of an infinite Prandtl number we get the Stokes equation, describing viscous flow:

$$\partial_j \tau_{ij} = \partial_i \Delta p - \Delta \rho g_i \quad (2.3)$$

where $\Delta \rho$ is the density perturbation with respect to a uniform background density ρ_0 (see equation (2.8)) and Δp is the dynamic pressure perturbation with respect to a hydrostatic pressure $p_0 = \rho_0 g z$. Equations (2.1)-(2.3) are non-dimensionalized using the following expressions:

$$T = \Delta T \cdot T', x_i = h \cdot x'_i, t = \frac{h^2}{\kappa} \cdot t', u_i = \frac{\kappa}{h} \cdot u'_i, p = \frac{\eta_0 \kappa}{h^2} \cdot p', \tau = \frac{\eta_0 \kappa}{h^2} \tau'$$

with ΔT the temperature scale, h the depth scale, κ the thermal diffusivity, ρ_0 the density scale, g the gravitational acceleration, τ the differential stress, and η_0 the viscosity scale. A uniform thermal conductivity is assumed in the models. Potentially important effects of specifically the temperature dependence of thermal conductivity (Hofmeister, 1999), including delayed cooling of the mantle and focussing of magmatism (Schott et al., 2001; Van den Berg and Yuen, 2002; Van den Berg et al., 2003), are thus not included.

symbol	property	definition	value/unit
c_p	heat capacity at constant pressure		1250 Jkg ⁻¹ K ⁻¹
Di	dissipation number	$\frac{\alpha g h}{c_p}$	
F	degree of depletion		
g	gravitational acceleration		9.8 ms ⁻²
H	radiogenic heat productivity		Wkg ⁻¹
h	length scale		
k	thermal conductivity	$\kappa \rho_0 c_p 0$	Wm ⁻¹ K ⁻¹
R	internal heating number	$\frac{H_0 h^2}{c_p \kappa \Delta T}$	
Ra	thermal Rayleigh number	$\frac{\rho_0 \alpha \Delta T g h^3}{\kappa \eta_0}$	
Rb	compositional Rayleigh number	$\frac{\delta \rho g h^3}{\kappa \eta_0}$	
Rc	phase Rayleigh number	$\frac{\delta \rho g h^3}{\kappa \eta_0}$	
S	melt productivity function		s ⁻¹
ΔS	entropy change upon full differentiation		300 Jkg ⁻¹ K ⁻¹
t	time		s
T	temperature		°C
T_0	non-dimensional surface temperature		$\frac{273}{\Delta T}$
ΔT	temperature scale		°C
w	vertical velocity		ms ⁻¹
z	depth		m
$z_0(T)$	temperature dependent depth of phase transition		m
α	thermal expansion coefficient		$3 \cdot 10^{-5}$ K ⁻¹
Γ	phase function	$\frac{1}{2} \left(1 + \sin\left(\pi \frac{z - z_0(T)}{\delta z}\right) \right)$	
δz	depth range of phase transition		m

Table 2.1: Symbols of the energy and momentum equations (2.4)-(2.6), the rheology equations (2.9)-(2.12), the depletion equation (2.7) and the fractionation equations (2.13) and (2.14).

symbol	property	definition	value/unit
κ	thermal diffusivity		$10^{-6} \text{ m}^2 \text{ s}^{-1}$
ρ_0	reference density		3416 kgm^{-3}
$\delta\rho$	density difference upon full depletion	$\frac{\partial\rho}{\partial F}$	-226 kgm^{-3}
$\delta\rho_k$	density increase of phase transition k	$\frac{\partial\rho}{\partial T}$	kgm^{-3}
Φ	viscous dissipation	ηe^2	$\text{Jm}^{-3} \text{ s}^{-1}$
B_1	diffusion creep prefactor		Pas
B_2	dislocation creep prefactor		$\text{Pa}^{\text{n}2} \text{ s}$
C_0	cohesion factor		0 Pa
E_1	diffusion creep activation energy		$270 \cdot 10^3 \text{ Jmol}^{-1}$
E_2	dislocation creep activation energy		$485 \cdot 10^3 \text{ Jmol}^{-1}$
e_{ij}	strain rate tensor	$\partial_j u_i + \partial_i u_j$	s^{-1}
e	second invariant of the strain rate tensor	$[\frac{1}{2} e_{ij} e_{ij}]^{\frac{1}{2}}$	s^{-1}
$f(F)$	composition dependent viscosity prefactor		
n_1	diffusion creep stress exponent		1
n_2	dislocation creep stress exponent		3.25
n_y	yield exponent		10
R	gas constant		$8.341 \text{ Jmol}^{-1} \text{ K}^{-1}$
V_1	diffusion creep activation volume		$6 \cdot 10^{-6} \text{ m}^3 \text{ mol}^{-1}$
V_2	dislocation creep activation volume		$17.5 \cdot 10^{-6} \text{ m}^3 \text{ mol}^{-1}$
$\dot{\epsilon}$	strainrate		s^{-1}
$\dot{\epsilon}_y$	yield strainrate		10^{-15} s^{-1}
η	viscosity		Pas
η_0	reference viscosity		10^{20} Pas
η_y	yield viscosity		Pas
σ_n	normal stress		Pa
τ_{ij}	deviatoric stress tensor	ηe_{ij}	Pa
τ	second invariant of the deviatoric stress tensor	$[\frac{1}{2} \tau_{ij} \tau_{ij}]^{\frac{1}{2}}$	Pa
τ_y	yield stress		Pa
c_m^0	initial concentration of trace element m		
c_m^l	concentration of trace element m in melt		
c_m^s	concentration of trace element m in residue		
K	partition coefficient		10^{-2}

Table 2.1: Symbol definitions (continued)

This results in the following non-dimensional equations:

$$\frac{\partial T}{\partial t} + u_j \partial_j T - Di(T + T_0)w =$$

$$\partial_j \partial_j T + \frac{Di}{Ra} \Phi - \frac{\Delta S}{c_p} \frac{dF}{dt} (T + T_0) + \sum_k \gamma_k \frac{Rc_k}{Ra} Di (T + T_0) \frac{d\Gamma_k}{dt} + RH \quad (2.4)$$

$$\partial_j u_j = 0 \quad (2.5)$$

$$\partial_j \tau_{ij} - \partial_i \Delta p - (RaT - RbF - \sum_k Rc_k \Gamma_k) = 0 \quad (2.6)$$

The conservation of composition is described by

$$\frac{DF}{Dt} = S(P, T, F) \quad (2.7)$$

where D/Dt denotes the substantial derivative and S is a source function, see section 2.5.

2.2 Equation of state

Convection is driven by density perturbations of different nature. These are described by the equation of state:

$$\rho = \rho_0 \left\{ 1 - \alpha(T - T_{ref}) + \sum_k \Gamma_k \frac{\delta \rho_k}{\rho_0} + \frac{\delta \rho}{\rho_0} F \right\} = \rho_0 + \Delta \rho \quad (2.8)$$

The last three bracketed terms represent the effects of thermal expansion, phase transitions and depletion. The latter two will be discussed in sections 2.4 and 2.5.

2.3 Rheological model

The deformation of material is accounted for by three separate deformation mechanisms, which are: diffusion creep, dislocation creep, and brittle failure. The former two are described by the following equation:

$$\eta_i = f(F) B_i \exp \left[\frac{E_i + PV_i}{RT} \right] \sigma^{1-n_i} \quad (2.9)$$

which is the standard Arrhenius formulation (Karato and Wu, 1993; Van den Berg and Yuen, 1998) with the addition of a composition dependent prefactor $f(F)$. The index i indicates the flow mechanism, either 1 for diffusion creep or 2 for dislocation creep. The other symbols are explained in Table 2.1. The activation energies E_i and volume V_i are based on Karato and Wu (1993), as is the prefactor B_i , in which an assumed constant and uniform grainsize of 1 mm is incorporated. The composition dependent prefactor $f(F)$ has a value of 1 for fertile peridotite and basalt (which have the same viscosity parameters in our models). For depleted peridotite (harzburgite) we apply a prefactor value of 10 for a degree of depletion over 0.05, and a linearly increasing value between $F = 0.005$ and

$F = 0.05$ from 1 to 10. This is intended to mimic the effect of dehydration during partial melting on the viscosity (Karato, 1986; Hirth and Kohlstedt, 1996; Mei and Kohlstedt, 2000a,b).

For eclogite, the composition dependent viscosity prefactor $f(F)$ has a value of 0.1. Although Jin et al. (2001) find that for an eclogite with equal amounts of the two main constituents garnet and omphacite, the strength is comparable to harzburgite (which is hydrous in their experiments), Piepenbreier and Stöckhert (2001) find evidence in eclogite microstructures for a much lower flow strength than predicted from omphacite experimental flow laws. We translate this result to our latter viscosity prefactor value of 0.1.

The third deformation mechanism in the composite rheology model, brittle failure, is approximated by a yield mechanism which is included to approximate the effects of fracturing-like behaviour when the shear stress exceeds a certain yield stress τ_y . We use a formulation of Van Hunen et al. (2002):

$$\eta_y = \tau_y \dot{\epsilon}_y^{-1/n_y} \dot{\epsilon}^{(1/n_y)-1} \quad (2.10)$$

The symbols are explained in Table 2.1. We prescribe the yield stress τ_y , the yield strain rate $\dot{\epsilon}_y$ and the yield exponent n_y . The latter describes the brittleness of the behaviour (Van Hunen et al., 2002). We apply a value of 10, which gives a reasonable approximation of pure brittle behaviour. The yield strength τ_y is determined as a function of depth using Byerlee's law (e.g. Lockner, 1995):

$$\tau_y = C_0 + \mu \sigma_n \quad (2.11)$$

in which we approximate the normal stress with the lithostatic pressure (e.g. Moresi and Solomatov, 1998):

$$\tau_y = C_0 + \mu \rho g z \quad (2.12)$$

We use a low value of 0.03 for the friction coefficient μ , consistent with results of (Moresi and Solomatov, 1998) for the mobilization of the Earth's lithosphere, and assume the cohesion term C_0 to be of minor importance and set it to 0.

The diffusion and dislocation creep viscosities are inversely added to define an effective ductile creep viscosity (Van den Berg et al., 1993) and the minimum of this value and the local yield viscosity is used for the local effective viscosity.

2.4 Solid state phase transitions

2.4.1 Basalt to eclogite phase transition

The main reason for the stability of crustal material at the surface of the Earth is its inherent reduced density compared to mantle material, which allows the crust to 'float' on top of the mantle. Under specific conditions of temperature and pressure, however, basaltic crust may undergo a series of phase transitions to develop a different mineralogy that significantly increases the density of the assemblage resulting in the high pressure

form eclogite. The transition from light to dense means a transition from buoyant to gravitationally unstable, which results in a tendency of the transformed crust to sink into the mantle. In a plate tectonic setting, the dense eclogite contributes to the slab pull that is the main driving force of subduction. In a non-plate tectonic setting, it may cause delamination of the lower crust (Vlaar et al., 1994). This latter process is an important factor in several models in this thesis.

In the models, basalt is transformed into heavier eclogite upon reaching depths in excess of 30 km in our model. The kinetics of this transition are approximated assuming a constant relaxation time for the transition of 1.25 Myr. The depth of 30 km (0.9 GPa) we use is somewhat less than the depth of about 40 km (1.2 GPa) which Hacker (1996) states as the minimum pressure of basalt to eclogite transformation. However, as we are dealing with melt products in a mantle that is hotter than the present, their composition is more MgO-rich (more towards komatiitic composition) than present day mid ocean ridge basalt (Nisbet, 1982). Experiments of Green and Ringwood (1967) have shown that the transition may occur at lower pressures and higher temperatures in MgO-rich rocks. Furthermore, lower pressure phase assemblages (above 0.7-0.8 GPa) may also contain garnet (Green and Ringwood, 1967; Ito and Kennedy, 1971; Hacker, 1996), thus raising the bulk density above that of the original basaltic phase assemblage. Phase boundary topography due to temperature effects is not taken into account, since this is expected to be dominated by kinetic effects because of the relatively low Clapeyron slope of about 1 MPa/K (Philpotts, 1990).

2.4.2 Mantle phase transitions

The phase transitions around 400 and 670 km depth are also taken into account separately for peridotite and eclogite, though without kinetics, assuming an equilibrium condition, which is a good approximation, particularly in a hotter Earth (Schmeling et al., 1999). The relevant parameters for these phase transitions are specified in Table 2.2. The phase transition is assumed to take place over a depth range, specified in Table 2.2. The phase function Γ_k for phase transition k is parameterized as a harmonic function over this depth range between 0 and 1, see Table 2.1. The latent heat consumption associated with the phase transitions is taken into account in the last term of equation (2.1), following Christensen and Yuen (1985). The phase transition of eclogite into perovskite lithology in the shallow lower mantle (e.g. Ringwood and Irifune, 1988; Irifune and Ringwood, 1993; Hirose et al., 1999) is not taken into account.

Dynamic effects have been predicted of the density inversion between eclogite and postspinel peridotite in the uppermost lower mantle (Irifune and Ringwood, 1993) caused by the deeper position of the phase transition of eclogite relative to the postspinel transition of peridotite. As recent work has indicated that the transition takes place around 720 km depth (Hirose et al., 1999) rather than around 800 km (e.g. Irifune and Ringwood, 1993), and has a positive Clapeyron slope which would lift the phase transition to even shallower levels in a cool sinking eclogite body, Hirose et al. (1999) predict that a body of basaltic crust with perovskite lithology would remain negatively buoyant and sink into the deeper mantle'. Earlier numerical experiments of Christensen (1988) show that an

transition	material	P_0 (GPa)	T_0 (K)	γ (Pa/K)	δz (km)	$\frac{\delta \rho}{\rho_0}$
400	peridotite	13.4	1756	$3 \cdot 10^6$	50	0.05
400	basalt	12.5	1747	$3 \cdot 10^6$	150	0.10
670	peridotite	22.4	1854	$-2.5 \cdot 10^6$	50	0.05

Table 2.2: Parameters of the phase transitions used in the models, based on Ringwood and Irifune (1988) and Irifune and Ringwood (1993). The first column indicates the approximate depth of the transition. P_0 and T_0 are the reference temperature and pressure for the phase transition, defining it in combination with the constant Clapeyron slope γ . The column marked δz indicates the depth range over which the transition is smeared out in the model and the last column gives the relative density contrast of the phase transition.

eclogite layer trapped in this density inversion zone in the uppermost lower mantle would probably not survive in a convecting mantle. Recent experiments by Kubo et al. (2002), however, indicate that slow kinetics of the lower mantle phase transition of basaltic material may delay the transition on the order of 10 million years, which may increase the residence time and depth extent of the shallow lower mantle density inversion zone. The density effects of the varying phase transitions are accounted for in a phase contribution term in the equation of state (2.8), scaled by the phase Rayleigh number Rc , in the momentum equation (2.6).

2.5 Partial melting of peridotite and basalt

Because of the presence of different phases in mantle peridotite, it does not have a single melting temperature, but melting takes place over a range of temperatures for a fixed pressure (see Figure 2.1). As a consequence, melting in the mantle is generally only partial because temperatures sufficient for complete melting are not reached. Another consequence is that the composition of the residual rock is a function of the degree of partial melting. The resulting melts for low degrees of partial melting are of basaltic composition (Jaques and Green, 1980; Herzberg and Zhang, 1996), changing to komatiitic compositions for higher degrees of melting (Walter, 1998).

Partial melting is modelled as an (irreversible) increase in the *degree of depletion* F , which is defined here as the mass fraction of melt produced from an initially unmelted material control volume of mantle peridotite. The extraction of melt from the source rock is described by two-phase flow models, for which different mathematical descriptions have been developed and applied in numerical models (McKenzie, 1984; Spiegelman, 1993a,b; Ogawa, 1997; Bercovici et al., 2001; Ricard et al., 2001). In this work, this is approximated by assuming all melt to be instantaneously segregated to the surface, similar to the approach of Ogawa (1988), see section 2.7. Compaction of the matrix due to the removal of melt is not taken into account. This results in an overestimate of the volume of depleted residual material (De Smet, 1999).

Evolution of the degree of depletion is described by equation (2.7). The source function S in (2.7) describes the distribution of the rate of partial melting. It applies a simple parameterization of the melting phase diagram of mantle peridotite (De Smet et al., 1998) in computing the local equilibrium degree of depletion and irreversibly updating actual local degree of depletion values accordingly. The corresponding latent heat effect results in extra terms in the energy equation, see appendix B. We use third order polynomial parameterizations of the solidus and the liquidus of mantle peridotite, based on Herzberg and Zhang (1996), down to a depth of 400 km (see Figure 2.1), assuming that melt produced below this depth is not segregated. Our isobaric melting curve, which is based on data presented by Jaques and Green (1980), is linear (see De Smet et al., 1998).

Many of the felsic rocks found in the Archean are plutonic or metamorphosed rocks that belong to the Tonalite-Trondhjemite-Granodiorite or TTG suite (Goodwin, 1991). These are thought to be formed by partial melting of metabasalts (Rapp et al., 1991). On the basis of trace element partitioning, Foley et al. (2002) and Foley et al. (2003) found that most TTG's have been formed by partial melting of metabasalts or metagabbros in the amphibolite facies, leaving behind an eclogitic residue.

Therefore, the partial melting of material of a basaltic composition, formed in the model by partial melting of mantle peridotite, is also included. A simplified phase diagram similar to that of peridotite in our model is used, assuming the melt residue is increasingly depleted in 'felsic material' which makes up the melt. We use a fifth order polynomial parameterization of the solidus and liquidus of Green (1982) for hydrated tholeiite (5 wt.% water), see Figure 2.1.

The density of mantle material is related to the degree of depletion F (Jordan, 1979). In the buoyancy term of the Stokes equation (2.6), we use a linearized parameterization of the composition dependent density (Vlaar and Van den Berg, 1991), and the coefficient $\partial\rho/\partial F$ enters the compositional Rayleigh number Rb , in the momentum equation (2.6) (see also De Smet et al., 1998, 2000b). We assume all melt to be removed instantaneously to shallower or surface levels. Because of this assumption, we neglect the buoyancy effect of melt retention, which leads to an underestimate of the buoyancy term (e.g. Scott and Stevenson, 1989; Buck and Su, 1989; Jha et al., 1994). This partly cancels the overestimation of the volume of depleted residue mentioned above.

2.6 Fractionation of trace elements

The behaviour of a single incompatible trace element is monitored in the models using Lagrangian particle tracers. Upon partial melting, the concentration of the trace element is adjusted in each tracer using an equilibrium melting formulation (see e.g. Philpotts, 1990) for each integration time step (which implies that we assume equilibration between the melt and the residue during an integration time step, and consider a new batch of melt in the following time step):

$$c_m^l = \frac{c_m^o}{F + K_m(1 - F)} \quad (2.13)$$

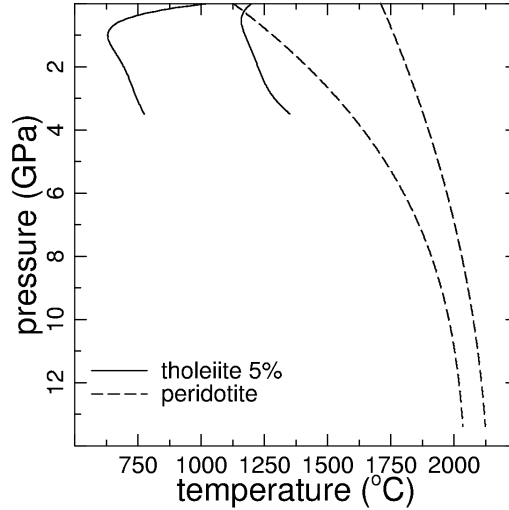


Figure 2.1: Solidus and liquidus for peridotite and basalt (tholeiite, assumed to be hydrated) used in the model calculations. The peridotite curves are based on Herzberg and Zhang (1996), the basalt curves on Green (1982), representing a tholeiite with 5 wt.% water.

$$c_m^s = K_m c_m^l \quad (2.14)$$

with c_m^s and c_m^l the mass concentrations of trace element m in solid (residue) and liquid (melt), c_m^o the initial concentration before fractionation, F the melt fraction and K_m the distribution coefficient.

The result of the above is that an enriched crust (generally by a factor 5-20) and a depleted residual mantle are formed. The internal heating rate is a function of the trace element concentration in the models. The most important heat producing species in the Archean mantle are U, Th and K. The former two have bulk partition coefficients of $1.1 \cdot 10^{-4}$ and $1.7 \cdot 10^{-4}$, respectively, for spinel peridotites in equilibrium with a basaltic melt (Beattie, 1993), though temperature, composition, oxygen fugacity and the presence of volatiles may influence these values. The partition coefficients for K between olivine and basalt, orthopyroxene and basalt and clinopyroxene and basalt are 0.007, 0.01-0.02 and 0.03, respectively (Henderson, 1982). We prescribe a distribution coefficient of 10^{-2} for the single incompatible heat producing element in our model which represents U, Th and K. This value of the partition coefficient is consistent with values for K, but somewhat larger than the values mentioned above for spinel peridotites for U and Th. It is however small enough to allow significant fractionation and thus redistribution of heat productivity, but not so small that different degrees of melting result in the same residue concentrations of virtually zero. This allows the evaluation of the development of our trace element in a

more general sense rather than limited to U, Th and K.

2.7 Crustal growth

The melt that is produced is extracted instantaneously and deposited at the top boundary, where the melt flux is transformed into an inflow boundary condition, thus producing a basaltic crust in the case of melting of peridotite, and a felsic crust in the case of melting of basalt or eclogite. This approximate melt segregation scheme is represented in Figure 2.2.

Isotope mass concentrations for the two types of melt are calculated separately in the melting column and resulting averaged (weighed using the melt mass fractions) concentrations are assigned to the respective inflowing crustal materials.

In the current approximation, the compaction of the residual mantle due to the melt removal is neglected. An estimate of the magnitude of the error in the energy balance which is thus introduced is calculated in Appendix A.

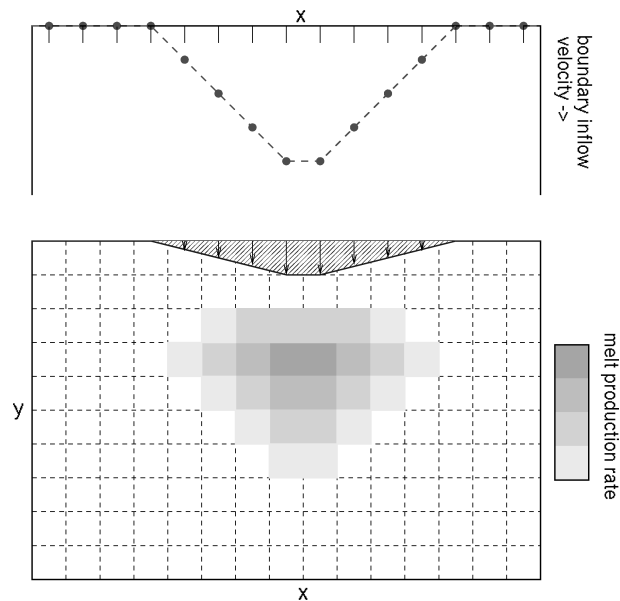


Figure 2.2: Graphical representation of the approximate melt segregation scheme employed in the numerical models. The degree of partial melting, indicated in grey tones, is integrated column-wise and transformed into an inflow velocity for the top boundary. Basaltic and/or felsic material enters the computational domain here, depending on the (relative amounts of) material that is melting below the regions of inflow.

Chapter 3

Numerical methods

The equations which describe the processes to be modelled (see chapter 2) can only be solved analytically in very simplified cases, and therefore discretization of the equations is required to solve them numerically on computers. Two different methods are used to evaluate the evolution of the different quantities. For the evolution of the temperature and velocity fields, a finite element method (Cuvelier et al., 1986) is applied, based on the SEPRAN package (Segal and Praagman, 2002). The discretization of the finite element equations will be described in more detail in sections 3.1 and 3.2. For the evolution of composition and trace element concentrations, a particle tracer method is used (Hockney and Eastwood, 1988), which will be described in section 3.4.

3.1 Discretization of the energy equation

Discretization of the energy equation (2.4), described in appendix B, results in the following system of equations:

$$M\dot{\vec{T}} + A\vec{T} = \vec{R} \quad (3.1)$$

In this expression, \vec{T} is a vector containing the temperature values at the nodal points of the finite element mesh. M is the mass matrix, in which the heat capacity and part of the effect of adiabatic compression and latent heat consumption and release is included. A is the stiffness matrix, combining the effects of advection, diffusion, adiabatic compression and latent heat. The right hand side vector \vec{R} includes internal heating and heating by viscous dissipation, as well as terms from latent heat effects and adiabatic compression. This set of equations is constructed for a mesh of triangular elements, which are in fact sub-elements of the quadratic triangular elements used for the Stokes equation (see section 3.2) using linear base functions (Van den Berg et al., 1993). In order to stabilize the solution of the discrete heat equation (3.1) in regions where advection dominates diffusion, the classical Streamline Upwind Petrov Galerkin method (see Segal, 1993) is applied.

3.2 Discretization of the Stokes equation

The discretization of the Stokes equation (2.6) results in a system of linear equations:

$$S\vec{U} + L^T\vec{p} = \vec{F} \quad (3.2)$$

where \vec{U} and \vec{p} are vectors of the velocity components in the nodal points and the dynamical pressure in the barycenters of the elements, respectively. This equation is solved using the penalty function method (Cuvelier et al., 1986), using a small but finite perturbation to the continuity equation, which in discretized form becomes (Cuvelier et al., 1986):

$$D\vec{p} = \frac{1}{\varepsilon}L\vec{U} \quad (3.3)$$

with D the pressure mass matrix and ε the penalty function parameter (10^{-6}).

Equation (3.3) is used to eliminate the pressure from (3.2). The resulting discretized Stokes equation is solved on a mesh consisting of triangular quadratic Crouzeix-Raviart elements (Segal and Praagman, 2002).

3.3 Time integration

The combination of energy and Stokes equations is integrated in time using a predictor-corrector time stepping scheme (Van den Berg et al., 1993). In the predictor step, the energy equation is integrated using an Euler implicit scheme:

$$M[\vec{U}^{(n)}]\Delta t^{-1}[\vec{T}^{*(n+1)} - \vec{T}^{(n)}] + A[\vec{U}^{(n)}]\vec{T}^{*(n+1)} = \vec{R}^{(n+1)} \quad (3.4)$$

Using the predicted temperature vector $\vec{T}^{*(n+1)}$, a solution for the Stokes equation for the predictor step $\vec{U}^{*(n+1)}$ is computed:

$$S\vec{U}^{*(n+1)} = \vec{F}[\vec{T}^{*(n+1)}] \quad (3.5)$$

In the corrector step, both the old solution for t^n and the predicted solution for $t^{(n+1)}$ are used in a Crank-Nicolson integration step:

$$\begin{aligned} M[\vec{U}^{*(n+1)}]\Delta t^{-1}[\vec{T}^{(n+1)} - \vec{T}^{(n)}] + \frac{1}{2}A[\vec{U}^{*(n+1)}]\vec{T}^{(n+1)} + \frac{1}{2}A[\vec{U}^{(n)}]\vec{T}^{(n)} = \\ \frac{1}{2}[\vec{R}^{(n+1)} + \vec{R}^{(n)}] \end{aligned} \quad (3.6)$$

followed by a corrector step for the Stokes equation:

$$S\vec{U}^{(n+1)} = \vec{F}[\vec{T}^{(n+1)}] \quad (3.7)$$

The non-linearity in the Stokes equation, introduced by the strain rate dependence of the dislocation creep and yield components of the viscosity (see section 2.3), resulting in

the stiffness matrix being dependent on the velocity solution, is solved by Picard iteration until the difference between successive solutions drops below a prescribed threshold of 10^{-2} in a suitable norm (Van den Berg et al., 1993).

The time step Δt is determined by taking the minimum of time steps prescribed by two criteria. The first is the Courant-Friedrichs-Levy criterion (see Van den Berg et al., 1993):

$$\Delta t_{cfl} = \min \left[\frac{h_x}{u_x}, \frac{h_y}{u_y} \right] \quad (3.8)$$

The time step Δt_{cfl} resulting from this criterion is multiplied by a factor f_{cfl} , which has a value of 0.01-0.5. The second criterion for the integration time step is that the normalized difference between the supremum norms of the old and the predicted temperature vector must not exceed a prescribed factor ϵ_T , which has a value of 0.02.

3.4 Particle tracers

The evolution of quantities like composition and trace element concentration is evaluated in a Lagrangian framework, to prevent numerical problems associated with non-physical oscillations and artificial diffusion of these quantities which is inherent to using an advection-diffusion equation in an Eulerian framework (Vreugdenhil, 1993; Segal, 1993). A particle tracer method is applied (Hockney and Eastwood, 1988). A set of particle tracers (generally 300,000-400,000) is homogeneously but randomly distributed over the computational domain. Associated with each tracer, values are defined for different fields like composition and trace element concentration, but also for other quantities used in the computations (effective thermal expansivity α and specific heat c_p , buoyancy, internal heating rate).

All these quantities are in some way a function of quantities which are defined on the particle tracers. The latent heat effect of partial melting, evaluated on the particle tracers, is included in the effective thermal expansivity and effective specific heat (see appendix B). The compositional part of the buoyancy depends on the tracer defined composition, and the basalt to eclogite phase transition, also defined on the tracers, has a buoyancy effect as well. The internal heating rate depends on the trace element concentration, which is also defined and evolved on the particle tracers. The quantities which are a function of the tracer fields are computed on the tracers as well, so that interpolation of the resulting fields from the tracers to the finite elements is postponed to the latest. This results in a higher accuracy being maintained because of the higher spatial resolution of the particle tracer field relative to the finite elements compared to the case where these quantities are computed on the finite elements after interpolation of the required quantities from the tracers to the mesh. This is specifically important for resolving the buoyancy effect of thin strands of material well below the scale of the finite elements, and for accurately accounting for the consumption of latent heat in the vicinity of the solidus.

The values of these quantities are adjusted each time step according to the appropriate equations, see chapter 2, due to partial melting.

The advective part of the change in the Eulerian fields is dealt with by advection of the particle tracers with the convective flow field. A fourth order Runge-Kutta scheme is applied. Interpolation of tracer particle field values to the finite element mesh is done using the Particle-in-Cell (PIC) method (Hockney and Eastwood, 1988). Tracer values are first interpolated to the nodal points of a regular grid, called the helpcell mesh. Helpcell nodal point values are then interpolated to the finite element Gauss point on which the field value is required using a bilinear interpolation from the grid points of the helpcell containing the evaluation point.

3.5 Crustal growth

The helpcell mesh is also used in the computation of melt segregation and production of crust through an inflow boundary condition, see section 2.7. The degree of depletion increment is integrated over columns centered on the helpcell mesh nodal points. For each column, the amount of melt produced is calculated (separately for melting peridotite, which forms basalt, and melting basalt/eclogite, which may form a felsic melt) and, using the time step Δt , transformed into an inflow velocity which is prescribed on the top helpcell nodal point on which the column is centered, see Figure 2.2. In the same manner, the concentration of trace elements in the inflowing crust is calculated, separately for basaltic and felsic material. The inflow velocity on the top boundary which is calculated in this way on the helpcell nodal points is interpolated to the finite element mesh nodal points on the top boundary using quadratic interpolation. When inflow of both felsic and basaltic material is prescribed, inflowing tracers are randomly assigned either a felsic or a basaltic composition, such that the ratio of the two types of inflowing tracers represents the ratio of inflow velocities for the two species.

Chapter 4

Plate tectonics on the terrestrial planets

Abstract

Plate tectonics is largely controlled by the buoyancy distribution in oceanic lithosphere, which correlates well with the lithospheric age. Buoyancy also depends on compositional layering resulting from pressure release partial melting under mid-ocean ridges, and this process is sensitive to pressure and temperature conditions which vary strongly between the terrestrial planets and also during the secular cooling histories of the planets. In our modelling experiments we have applied a range of values for the gravitational acceleration (representing different terrestrial planets), potential temperatures (representing different times in the history of the planets), and surface temperatures in order to investigate under which conditions plate tectonics is a viable mechanism for the cooling of the terrestrial planets. In our models we include the effects of mantle temperature on the composition and density of melt products and the thickness of the lithosphere. Our results show that the onset time of negative buoyancy for oceanic lithosphere is reasonable (less than a few hundred million years) for potential temperatures below $\sim 1500^{\circ}\text{C}$ for the Earth and $\sim 1450^{\circ}\text{C}$ for Venus. In the reduced gravity field of Mars a much thicker stratification is produced and our model indicates that plate tectonics could only operate on reasonable time scales at a potential mantle temperature below about $1300 - 1400^{\circ}\text{C}$.

4.1 Introduction

Plate tectonics is characterized by mid-ocean ridges, where oceanic crust and underlying depleted mantle is created by partial melting of upwelling mantle material, and subduction zones, where oceanic lithosphere including the basaltic crust moves underneath another

This chapter has been submitted by P. van Thienen, N.J. Vlaar and A.P. van den Berg for publication in *Physics of the Earth and Planetary Interiors*.

oceanic or a continental lithosphere into the underlying mantle. The two main driving forces for the plate tectonic process are ridge push and slab pull, of which the latter is generally an order of magnitude larger than the former (Turcotte and Schubert, 2002). Slab pull is caused by negative buoyancy of the cold descending lithosphere which may include the effect of the uplift of the olivine-spinel phase boundary in the cold slab. Resistive forces originate from friction and, in case the slab reaches this depth, a downward deflection of the spinel-postspinel phase boundary around 670 km depth. In order to make plate tectonics work, the plates must have sufficient negative buoyancy. Furthermore, the plates must conform to specific mechanical properties. They must act as stress guides and be strong enough to withstand the high tensional stresses associated with slab pull, which are on the order of 1 GPa (Turcotte and Schubert, 2002), while being able to bend at the subduction zone (e.g. Conrad and Hager, 2001).

Geologists interpret rocks from Archean and Proterozoic cratons as evidence for the beginning of modern style plate tectonics sometime between 4.0 Ga (De Wit, 1998) and 2.0 Ga (Hamilton, 1998), with the difference between these ages mainly stemming from the interpretation of rocks as either an equivalent of modern arc setting material or something with significantly different characteristics. But whatever the timing, at some point in the Earth's thermal evolution the force balance and mechanical properties of an oceanic type lithosphere became favorable for plate tectonics.

A suitable diagnostic for the buoyancy and gravitational stability of the oceanic lithosphere is the density defect thickness *d.d.t.* (Oxburgh and Parmentier, 1977):

$$d.d.t. = \int \left(\frac{\rho_m - \rho}{\rho_m} \right) dz \quad (4.1)$$

In this expression, ρ_m is the density of the underlying mantle, ρ the local temperature and composition dependent density, and z the depth coordinate. The integral is taken over the thickness of the lithosphere. This parameter indicates whether a column of oceanic lithosphere experiences a net buoyancy force in upward or downward direction. Whether a net force results in actual vertical movement also depends on resistive forces and the mechanical properties of the lithosphere (e.g. Conrad and Hager, 2001). We also note that the criteria for starting and maintaining plate tectonics are not necessarily the same (see McKenzie, 1977; Sleep, 2000; Stevenson, 2003). Since in a hotter Earth, a thicker low density crust and thicker subcrustal layer of light depleted melt residue would be produced from upwelling material, the resulting lithosphere is more buoyant and therefore more difficult to subduct (Sleep and Windley, 1982; Vlaar, 1985). Vlaar and Van den Berg (1991) present modelling results of the development of the density defect thickness for oceanic lithosphere produced in a hotter Earth, showing that it takes a significantly longer cooling period (on the order of hundreds of millions of years) for oceanic lithosphere to become negatively buoyant, whereas for present-day Earth-like conditions, gravitational instability sets in at an age of ~ 30 million years. However, we also see younger crust subducting, indicating that lithospheric buoyancy does not completely determine the dynamics.

Numerical mantle convection models of subduction zones (using a composite rheology model including diffusion creep, dislocation creep and a stress limiter) for higher than present-day mantle temperatures show that for potential temperatures of 1525°C and higher, subduction is eventually stopped by the reduced (temperature dependent) strength of the lithosphere (Van Hunen, 2001; Van Hunen et al., 2003); this results in frequent break-off of the subducting slab, which, in turn, prevents the buildup of sufficient slab pull.

An important consequence of one of the main distinguishing features between the terrestrial planets, the gravitational acceleration, is that on smaller planets a much thicker stratification could be developed as a result of partial melting in hot upwelling mantle, because under reduced gravity and pressure conditions the solidus and liquidus pressures correspond to greater depths. This effect is demonstrated in the work of Schott et al. (2001) on mantle convection models including compositional differentiation by pressure release partial melting of the Martian mantle. Such a thicker stratification is more buoyant, and therefore we can already predict that plate tectonics will be more difficult on Mars than on Earth.

It is clear from space observation that both Mars and Venus do not have plate tectonics nowadays (e.g. Zuber, 2001; Nimmo and McKenzie, 1996). We do not know, however, if in the earlier history of these planets plate tectonics has been active (Turcotte et al., 1999; Sleep, 1994, 2000). Satellite measurements of crustal magnetization on the southern hemisphere of Mars show a pattern more or less similar to magnetic striping found on the Earth's ocean floor, though both the width and signal magnitude are much larger than on Earth (Acuña et al., 1999; Connerney et al., 1999). Venus is thought to have undergone a global resurfacing event between 300 and 600 Myr ago (Schaber et al., 1992; Nimmo and McKenzie, 1998). Therefore we do not observe earlier material from which information can be obtained. No evidence is found for plate tectonics after the resurfacing.

In this work we will investigate under which thermal conditions plate tectonics may take place on terrestrial planets on the basis of buoyancy considerations. The dependency of the density defect thickness and specifically the time required for an oceanic lithosphere to obtain neutral buoyancy will be determined as a function of gravitational acceleration, representative of different planets, and potential temperature, representing different times in the thermal evolution of the planets subject to secular cooling. We model the lithospheric column as it would be produced at a mid-ocean ridge using a melting model for peridotite. A range of lithosphere thicknesses, corresponding to estimates for the present and early Earth, Mars and Venus is used in combination with a 1D numerical conductive cooling model to determine the cooling history of the lithosphere, and from this, the density defect thickness time series.

4.2 Description of the numerical models

4.2.1 Equations and procedure

The modeling approach presented here is an extension of that of Vlaar and Van den Berg (1991), using a 1-D melting model of McKenzie (1984). The main differences between their work and the present approach are (1) our inclusion of the effect of melting temperature on the composition and density of oceanic crust and (2) our use of different lithosphere thicknesses representative of the different terrestrial planets. The effect of the first point is that the increased buoyancy expected for a thicker crust, that is produced in a hotter mantle, is balanced by its higher density. The second modification mainly causes a steeper geotherm and, therefore, higher temperatures in the lower crust compared to the case with a (greater) constant lithosphere thickness. The sensitivity of the model to lithosphere thickness will be investigated below. The model is based on a 1-D evaluation of an adiabatically rising column beneath a mid-ocean ridge. In the region between solidus and liquidus in p, T -space, the pressure derivative of the melt fraction by weight F can be derived (see Vlaar and Van den Berg, 1991):

$$\frac{dF}{dp} = \frac{-\frac{c_p}{T} \left(\frac{\partial T}{\partial p} \right)_F + \frac{\alpha}{\rho}}{\Delta S + \frac{c_p}{T} \left(\frac{\partial T}{\partial F} \right)_p} \quad (4.2)$$

For an explanation of the symbols, see Table 4.1. The ordinary differential equation (ODE) (4.2) is integrated numerically in p using a fourth order Runge-Kutta scheme, starting from a surface value of the degree of melting, corresponding to a given extrusion temperature (see Figure 4.1). For any integration step, the temperature, occurring in the right hand side of the ODE (4.2) is computed from the parameterization of the phase diagram for mantle peridotite. The parameterization is based on polynomial approximations of the liquidus $T_L(P)$ and solidus $T_S(P)$, based on data from Herzberg and Zhang (1996), and the isobaric variation between 0 and 1 of F between liquidus and solidus, based on McKenzie and Bickle (1988). Integration of equation (4.2) is stopped when the solidus is reached, marking the deepest melting in the column. The corresponding temperature profile is calculated simultaneously from the solidus, liquidus and melting curve parameterizations for local pressure and corresponding F values.

The inclusion of the overburden pressure of the crust thus produced refines the solution in a number of iterative steps, and reduces the amount of basaltic crust produced (see Vlaar and Van den Berg, 1991). In order to do this, we need to account for the density of the basaltic crust. As we are considering the complete crust, we account for the average composition and corresponding average density, disregarding any differentiation processes in the crust that result in denser cumulates at the bottom and shallow lighter residual phases. We parameterize the crustal density as a function of T_{ex} (the temperature at which magma erupts at the surface). A relation between T_{ex} and MgO content of primitive magmatic rocks has been described by Nisbet (1982). The MgO content affects the mineralogy of these rocks and, thus, also the density. Generally, primitive rocks

symbol	property	value/unit
c	basalt solidification contraction	0.90
c_p	specific heat mantle	1250 Jkg ⁻¹ K ⁻¹
c_p	specific heat crust	1000 Jkg ⁻¹ K ⁻¹
F	mass fraction of melt	-
p	pressure	Pa
T	temperature	°C
α	thermal expansion coefficient	$3 \cdot 10^{-5}$ K ⁻¹
$\delta\rho$	density decrease upon full depletion	-226 kgm ⁻³
ΔS	entropy change upon full melting	300 Jkg ⁻¹ K ⁻¹
κ	thermal diffusivity	10^{-6} m ² s ⁻¹
ρ	mantle density	3416 kgm ⁻³
ϕ	residual melt fraction	0.01

Table 4.1: Relevant parameters used in the melting and cooling models.

with higher MgO contents have a higher density. For 58 published analyses of basalts, komatiitic basalts and komatiites, and a picrite (see Figure 4.2) we computed the CIPW normative composition in terms of mineral phases (e.g. Philpotts, 1990), and we calculated bulk rock densities using individual mineral densities (including the effect of iron content on the densities of olivine and the pyroxenes). A least squares best fit of the resulting densities as a function of T_{ex} (i.e., MgO content) was constructed:

$$\rho = 1500 + 1.925 \cdot T_{ex} - 5.153 \cdot 10^{-4} T_{ex}^2 \quad (4.3)$$

where ρ is the density of the solidified melt product (kgm⁻³). The parameterized density (4.3) is shown as the dashed curve in Figure 4.2. Although the mantle composition of Venus and Mars may be slightly different from the Earth's mantle, we assume expression (4.3) to be valid for these planets as well.

Resulting crustal thicknesses for Earth and Mars are shown in Figure 4.3, together with earlier results from McKenzie and Bickle (1988), and based on those by Sleep (1994), and by Vlaar and Van den Berg (1991). Vlaar and Van den Berg (1991) show that it is important to include the effect of crustal overburden. This results in significantly smaller crustal thicknesses than those found by McKenzie and Bickle (1988) and Sleep (1994). Our results are consistent with those of Vlaar and Van den Berg (1991), the slightly smaller thicknesses in our Earth case resulting from the inclusion of the effect on melt product density of the potential temperature and the use of different parameterizations of solidus, liquidus and melting curve.

Using a specified surface temperature and the potential temperature extrapolated to the depth of the base of the lithosphere as boundary conditions, the evolution of the temperature profile is computed for the lithosphere by solving the time dependent 1-D heat equation for the cooling of a column of oceanic lithosphere with a second order finite difference scheme and Crank-Nicolson time integration. For each experiment, a constant

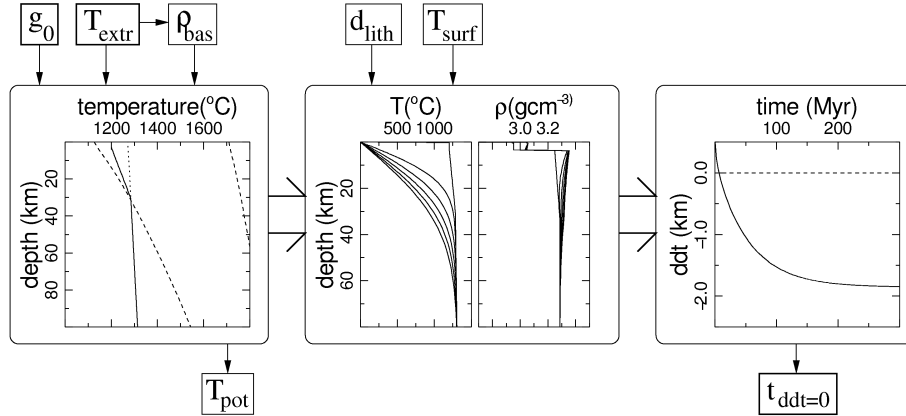


Figure 4.1: Experimental setup. From a prescribed magma extrusion temperature (which also gives the crustal density through equation (4.3)) and gravitational acceleration, a geotherm, material stratification (crust+depleted root) and corresponding density profile are calculated. Using a prescribed lithosphere thickness as the domain extent for finite difference calculations and using a prescribed surface temperature as the top boundary condition, the development of the geotherm is integrated in time and corresponding density profiles are again computed. The development of the density defect thickness, calculated using expression (4.1), is thus evaluated as a function of time and the zero buoyancy age is found.

domain size is used, spanning the depth of the lithosphere in thermal equilibrium (far from the ridge).

The use of a finite plate thickness in the same spirit as the analytical plate models of McKenzie (1967), Crough (1975), Doin and Fleitout (1996), and Dumoulin et al. (2001) allows for a balance to set in between the bottom heat flux into the lithosphere and the top boundary heat flux; this results in a steady state situation, whereas a halfspace model shows a continuously declining surface heat flux and a geotherm that changes accordingly.

Density profiles corresponding to the conductively evolving geotherm and computed composition profiles (i.e., degree of depletion and basaltic crust) are computed, and from these the density defect thickness is determined as a function of time (see Figure 4.1). From this we obtain the zero density defect thickness time, which is the time required for the oceanic lithosphere to become neutrally buoyant.

The extrusion temperature, which occurs as a boundary condition in the solution of (4.2) and which is directly linked to the potential temperature (see Figure 4.1), is used as a control parameter, to select for different stages in the thermal evolution of a planet. The gravitational acceleration is implicitly present in the pressure dependent depth of solidus and liquidus, and can thus be used as a control parameter to select for different planets. The computation of the thermal evolution of an oceanic lithospheric column depends

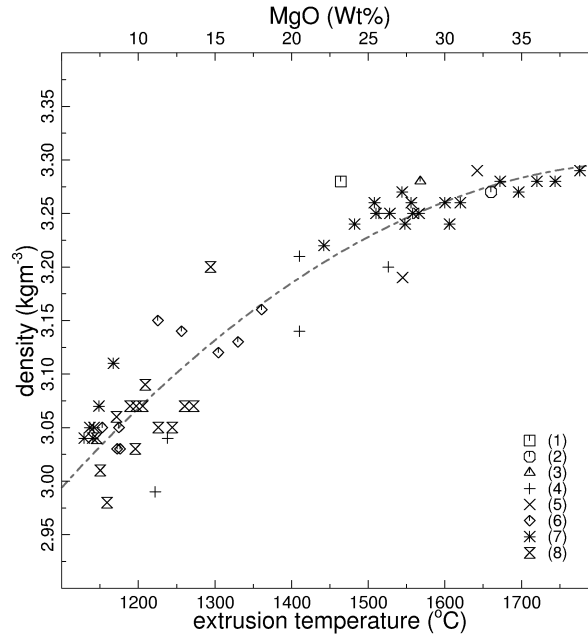


Figure 4.2: Primitive magmatic rock densities as a function of MgO content or extrusion temperature, of 58 basalts, komatiitic basalts, komatiites and a picrite. The quadratic best fit for the entire set (see equation (4.3)) is shown by the dashed curve. References for the data are: (1) Parman et al. (1997), (2) Green et al. (1975), (3) Smith et al. (1980), (4) Ludden and Gelinas (1982), (5) Nishihara and Takahashi (2001), (6) Kerr et al. (1996), (7) Puchtel et al. (1998) and (8) Arndt and Nesbitt (1982).

on the surface temperature, T_{surf} , which is specified. This makes up the third control parameter. The potential mantle temperature, gravitational acceleration and the surface temperature span the parameter space which we will investigate for different lithosphere thicknesses.

4.2.2 Model parameters

Relevant input parameters for the melting and cooling models are listed in Table 4.1.

The surface temperature, T_{surf} , of the planet we are dealing with defines the thermal upper boundary condition of the 1-D cooling model for a mantle column. For the Earth, T_{surf} has been buffered for most of its history by the presence of liquid water on the surface. Oxygen isotope studies suggest the presence of liquid water and possibly even oceans as far back as 4.4 Ga (Wilde et al., 2001; Peck et al., 2001). For Venus we only know the present thermal conditions, which show an average T_{surf} of $467^{\circ}C$. On Mars

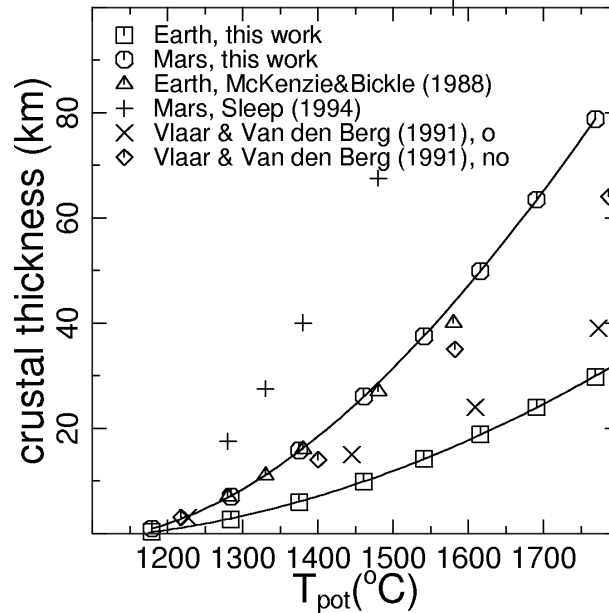


Figure 4.3: Thickness of the crust as produced at mid-ocean ridges, for Earth and Mars. The results of McKenzie and Bickle (1988) do not include the effect of the overburden pressure of the crust, and therefore give an overestimate of the thickness. The results for Mars by Sleep are those of McKenzie and Bickle (1988) divided by a factor of 0.4 to correct for different gravity and a somewhat more iron-rich composition of the basalts (Sleep, 1994). The results of Vlaar and Van den Berg (1991), with (o) and without (no) including the effect of the crustal overburden, clearly show that the crustal overburden is an important effect that should not be neglected.

the average T_{surf} is significantly lower, $\sim -55^{\circ}C$. However, morphological features strongly reminiscent of flow channels suggest that liquid water may have been present on the surface in the early history of the planet (e.g. Jakosky and Phillips, 2001), which implies that more present day Earth-like surface conditions may have prevailed during the planet's earlier evolution (Baker, 2001). Based on this information, we find neutral buoyancy ages as a function of potential temperature and gravitational acceleration for two different values of T_{surf} . The first is $0^{\circ}C$, which is representative of Earth and perhaps Mars during most of its history. The second value applied is $467^{\circ}C$, which is representative of present time Venus, and possibly for an unknown part of its history.

We also consider the effect of varying T_{surf} for a fixed value for the gravitational acceleration ($9.8m.s^{-2}$) for a range of potential temperatures.

We do the experiments using a number of values for the lithosphere thickness, spanning the range of values expected for the terrestrial planets during their evolution.

The present oceanic lithosphere thickness on Earth is estimated to be about 100-125 km (Parsons and Sclater, 1977; Stein and Stein, 1992). Convection scaling analysis (e.g. Parsons and McKenzie, 1978) indicates that this value will be smaller for higher mantle temperatures. Additionally, the strong temperature dependence of viscosity (e.g. Karato and Wu, 1993) will also decrease the lithosphere thickness for higher mantle temperatures.

For Venus and Mars, the lithosphere thickness is not well constrained for the present stagnant lid situations, and are more uncertain for hypothetical plate tectonics scenarios. Smrekar and Parmentier (1996) constructed numerical convection models for the interaction of mantle plumes with boundary layers applied to Venus and found that models with a lithosphere of 100-150 km thickness resulted in the best fit with data for large volcanic rises on Venus. Independently, Nimmo and McKenzie (1996) found that a conductive lid of less than 150 km thickness results in the best fit of their gravity models to observations. These results indicate that the present lithospheric thickness of Venus is probably less than 150 km, and may be relatively close to that of the Earth. However, we need to stress that these are lithosphere thickness values for the present stagnant-lid situation. In a plate tectonics setting, the thickness may be different but is probably less because of the more efficient transport of heat to shallow levels in a plate tectonics setting relative to a stagnant lid regime.

Spherical convective numerical models of the thermal evolution of Mars by McKenzie et al. (2002) show lithosphere thicknesses of around 200 km for the present and less than 100 km for the early history of the planet, again in a stagnant lid regime. Earlier work by Solomon and Head (1990), based on estimates of the elastic thickness of the Martian lithosphere, resulted in mechanical lithosphere thicknesses of less than 20 up to 140 km. They used the conversion chart of McNutt (1984), which defines the mechanical lithosphere thickness as the depth of the $600^{\circ}C$ isotherm. Extrapolation to mantle temperatures results in estimates for the thermal lithosphere that are approximately twice these values.

These constraints allow us to pick the lithosphere thickness for the different models. We use a thickness of 100 km for a model with surface temperature $0^{\circ}C$, representing the Earth and Mars. For Mars, we also run a model with a 200 km lithosphere. For Venus, with a surface temperature of $467^{\circ}C$, we use a lithosphere thickness of 150 km. Obviously, smaller thickness values are required for the earlier, hotter histories. We will investigate the sensitivity to lithosphere thickness to determine the magnitude this effect.

4.3 Results

First we illustrate the development of the density defect thickness $d.d.t.$ as a function of time for the model Earth and Mars in Figure 4.4. In each case the lithospheric column has a positive $d.d.t.$ at $t=0$ (the time of formation), which means that it is positively buoyant. For the present-day Earth ($T_{pot} = 1353^{\circ}C$ in Figure 4.4a) we see that the column becomes negatively buoyant (crosses the $d.d.t. = 0$ line) after about 25 Myr, which is close to earlier results (30 Myr) of Vlaar and Van den Berg (1991). At lower potential temperatures, negative buoyancy is reached in a shorter time. Higher potential

temperatures result in greater neutral buoyancy ages, and we observe in this figure that the *d.d.t.*-curve corresponding to a potential temperature of 1625°C shows a constant positive buoyancy that is no longer decreasing with age after about 150 Myr. In Figure 4.4b, model Mars shows similar curves, which, as a result of the lower gravitational acceleration, have been shifted upwards by about 1 km on the *d.d.t.* axis. As a consequence, longer neutral buoyancy ages are observed for low mantle temperatures, and neutral buoyancy is no longer reached for potential temperatures representative of Earth.

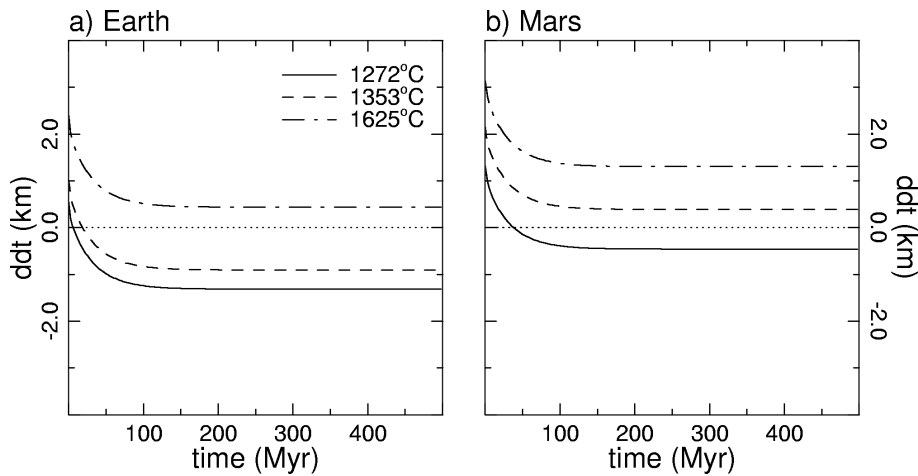


Figure 4.4: Density defect thickness time series for the Earth (a) and Mars (b) for potential mantle temperatures of 1272°C (solid curves), 1353°C (dashed curves) and 1625°C (dash-dotted curves). For positive values of the *d.d.t.* the oceanic lithosphere is buoyant.

Resulting neutral buoyancy times (density defect thickness *d.d.t.* = 0) as a function of potential temperature and gravitational acceleration are presented in Figure 4.5a for $T_{surf} = 0^{\circ}\text{C}$ and a lithosphere thickness of 100 km. The horizontal axis represents the potential mantle temperature, and the vertical axis shows the gravitational acceleration, which enables the comparison of the different terrestrial planets. The contours are lines of equal neutral buoyancy times. Note that the solidus temperature at the surface is 1125°C , which implies that no differentiation takes place below this temperature. This means that compositional buoyancy due to compositional differentiation is lost and that any negative deviation from the adiabat results in a negative buoyancy. As a consequence 'lithosphere' in a mid-ocean ridge setting would immediately become negatively buoyant due to cooling. The planet specific gravitational accelerations are indicated in the figure as horizontal lines and labeled for Earth, Venus, and Mars. The maximum contour that is included is that of 500 Myr. Here the neutral buoyancy age is increasing asymptotically to infinity for increasing potential temperature, indicating that for higher values of the potential temperature the lithosphere does not become negatively buoyant at all. The dash-dotted

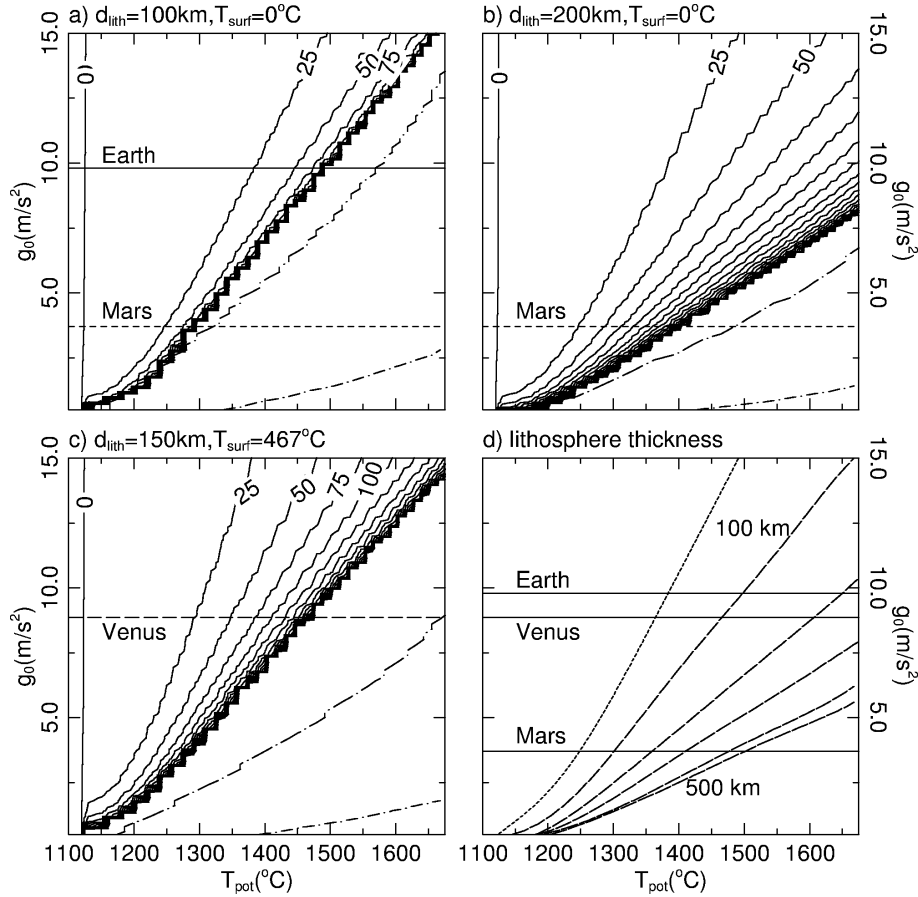


Figure 4.5: Frames a-c show contours of the neutral buoyancy (density defect thickness = 0) times. a) Surface temperature is 0°C and lithosphere thickness is 100 km, potentially applicable to both Earth and Mars. The gravitational accelerations for these terrestrial planets are included as horizontal lines (solid: Earth, dashed: Mars). b) Surface temperature is 0°C and lithosphere thickness is 200 km, potentially applicable to Mars, including the gravitational acceleration of Mars (dashed line). c) Surface temperature is 467°C and lithosphere thickness is 150 km, potentially applicable to Venus, including the gravitational acceleration of Venus (long-dashed line). d) Variation of neutral buoyancy times as a function of lithosphere thickness for a surface temperature of 0°C . Gravitational acceleration values for Earth, Venus and Mars are indicated by solid lines. The 25 Myr isoline is indicated by the dotted curve. Dashed curves indicate the position of the 500 Myr isoline for lithosphere thicknesses of 100 km, 150 km, 200 km, 300 km and 500 km.

curves in Figure 4.5a indicate where the fixed lithospheric thickness, of in this case 100 km, is equal to the thickness of the compositional stratification (basaltic crust and harzburgitic root) produced at mid-ocean ridges (long dashes) and where the lithospheric thickness is equal to the crustal thickness (short dashes). Lithospheric thickness is greater to the left of these curves. Results to the right of the latter curve are ignored since the expected internal convection in the crust is not included in the current model. For the present-day Earth, with a potential temperature of $1300 - 1350^\circ\text{C}$, we obtain a neutral buoyancy age for oceanic lithosphere of about 20-25 million years, which is consistent with earlier estimates of 40-50 Myr (Oxburgh and Parmentier, 1977), 30 Myr (Vlaar and Van den Berg, 1991), and 20 Myr (Davies, 1992). For a hotter Earth the neutral buoyancy age increases to about 100 million years near $T_{pot} \sim 1500^\circ\text{C}$ and much longer times are obtained for only slightly higher temperatures. For Mars (dashed line), neutral buoyancy times already rise to hundreds of million years for a moderate potential temperature below 1300°C , in line with much stronger compositional differentiation under low-gravity conditions on Mars (Schott et al., 2001). The Martian lithosphere may however be thicker than 100 km. When assuming a thicker lithosphere of 200 km for Mars, as shown in Figure 4.5b, neutral buoyancy ages are less than 150 Myr below potential temperatures of 1350°C , and rise to 500 Myr around 1400°C .

When applying a surface temperature of 467°C , consistent with present-day Venus, cooling of the lithosphere becomes slower and therefore neutral buoyancy ages become longer (Figure 4.5c, where a lithosphere thickness of 150 km is applied). For a Venusian gravitational acceleration neutral buoyancy ages of about 500 million years can be observed for a potential temperature of 1480°C .

The effect of lithosphere thickness on the neutral buoyancy age is illustrated in Figure 4.5d for a surface temperature of 0°C . Solid lines indicate the position of the terrestrial planets. The dotted curve indicates the 25 Myr isoline of the neutral buoyancy age. The position of this curve is relatively insensitive to lithosphere thicknesses, since initial cooling of the oceanic lithosphere takes place at shallow levels. The dashed curves indicate 500 Myr isolines of the neutral buoyancy age for lithosphere thicknesses of 100 km, 150 km, 200 km, 300 km and 500 km. It is evident that a greater lithosphere thickness allows cooling of the lithosphere to deeper levels and lower temperatures, decreasing its buoyancy. Thus a thick lithosphere may significantly prolong neutral buoyancy ages.

The effect of surface temperature on the neutral buoyancy age is more clearly illustrated in Figure 4.6. In this figure, the neutral buoyancy age is contoured as a function of potential temperature on the horizontal axis and T_{surf} on the vertical axis for a constant Earth-like gravity of 9.8 m s^{-2} and a lithosphere thickness of 150 km. It is evident that the effect of T_{surf} is greatest for high mantle potential temperatures near the asymptotic increase of the neutral buoyancy age. For the present-day Earth's potential temperature of about 1350°C , an increase in T_{surf} of about 500°C is required to double the neutral buoyancy age from 20 to 40 Myr. In general, the higher T_{surf} of Venus causes a shift in the neutral buoyancy age contours of up to 125°C along the the potential temperature axis. It is clear from this figure that the difference in surface temperature between Earth and Mars is not an important factor in explaining the different types of dynamics.

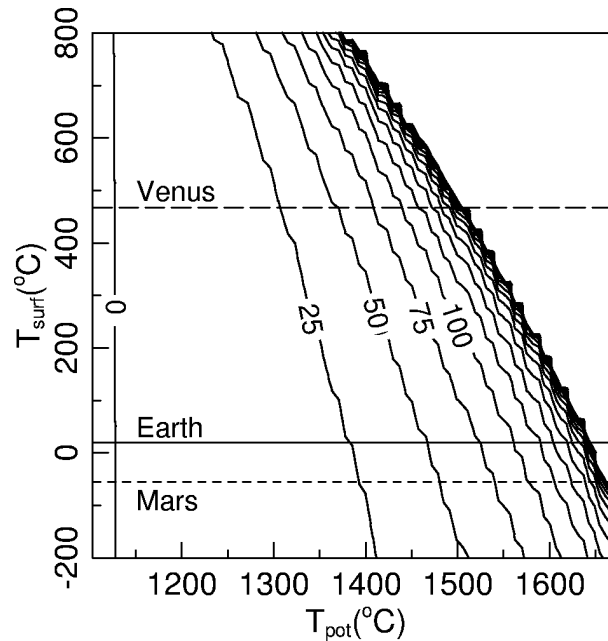


Figure 4.6: Neutral buoyancy (density defect thickness = 0) times for a constant gravitational acceleration of 9.8 m s^{-2} and lithosphere thickness of 150 km as a function of potential temperature and surface temperature. The horizontal lines indicate the position of Venus (long-dashed), Earth (solid) and Mars (dashed).

4.4 Discussion

4.4.1 Plate tectonics on Earth

The accretion of the Earth, the differentiation of the core (Horedt, 1980), and the decay of short-lived isotopes (Ruff and Anderson, 1980) each supplied enough heat to melt at least a significant part of the Earth. Furthermore, geochemical evidence (Murthy, 1992a) and modeling efforts (e.g. Abe, 1993a,b, 1997) indicate that the early Earth had a magma ocean for some time. This means that the potential temperature of the mantle has dropped from a very high value outside the scale of the horizontal axis of Figure 4.5a to a present-day value of about $1300 - 1350^{\circ}\text{C}$, and that the Earth passed through stages covered by most of the Earth ($g_0 = 9.81 \text{ m s}^{-2}$) line in Figure 4.5a. We do not know, however, the exact timing of the cooling. The high magnesium contents of Archean komatiites indicate extrusion temperatures of $1520 - 1580^{\circ}\text{C}$, corresponding to potential temperature of $1600 - 1900^{\circ}\text{C}$ (Nisbet et al., 1993). This is based on the assumption of dry melting, which was validated by Arndt et al. (1998). Others, however, propose that the generation of komatiites took place under hydrous conditions at mantle temperatures only 100°C

higher than the present (e.g. Stone et al., 1997; Parman et al., 1997), suggesting potential mantle temperatures during the Archean that are only moderately higher than present-day.

The difficulty of maintaining plate tectonics at higher mantle temperatures in the Earth has already been addressed by different authors (Sleep and Windley, 1982; Vlaar, 1985; Vlaar and Van den Berg, 1991; Davies, 1992). The opposing effect of a more komatiitic composition of the crust was discussed by Arndt (1983) and Nisbet and Fowler (1983). They suggest that a thin (comparable to the present) oceanic crust rich in komatiites may allow plate tectonics to operate, and that the reduced resistive forces as a consequence of the higher mantle temperature and temperature dependent rheology could make it more efficient. Upwelling in a mid-ocean ridge system in a hotter mantle, however, produces a thick crust, as the supersolidus path of the ascending material is longer. Our results take into account the temperature dependent composition of the basaltic crust and show that this thicker crust, although denser due to its composition being closer to komatiitic, is not dense enough to facilitate subduction at potential temperatures above about 1500°C for the Earth on reasonable time scales, confirming the results of Vlaar and Van den Berg (1991) which did not include the effect of higher temperatures on melt product composition and density. We note, however, that the buoyancy approach is only one of many to investigate the conditions under which plate tectonics may operate. Other factors include stresses required to initiate subduction (e.g. McKenzie, 1977), bending of the lithosphere (e.g. Conrad and Hager, 2001), and temperature dependent rheology with strong impact on the mechanical coherency of subducting lithosphere (Van Hunen, 2001; Van Hunen et al., 2003), which may be important but are beyond the scope of this paper.

4.4.2 Plate tectonics on Venus

Nimmo and McKenzie (1998) estimate the potential mantle temperature of Venus to be about $1300 - 1500^{\circ}\text{C}$. Because of the history of Venus (e.g., accretion, core differentiation) and the composition (e.g., radiogenic heating) being similar to Earth, one may expect that Venus has experienced a hot early history as well, perhaps including a magma ocean period. Calculations indicate that the surface heat flux of the planet is about half of the radiogenically produced heat, which means that the planet must be heating up (Nimmo and McKenzie, 1998). From crater count studies, Venus appears to have undergone global resurfacing about 300-600 Myr ago (Schaber et al., 1992; Nimmo and McKenzie, 1998). No evidence of plate tectonics has been found. So if Venus has had plate tectonics, it must have been before the (last?) global resurfacing. Episodic plate tectonics has been suggested for Venus (Turcotte, 1993), and also on the basis of our results there is no reason to disqualify Venus for plate tectonics. Assuming a more or less constant surface temperature during (part of) the history of the planet, Figure 4.5c shows that reasonable neutral buoyancy ages are possible for potential temperatures below about 1450°C , or even below about 1650°C when assuming a more Earth-like surface temperature (see Figures 4.5d and 4.6). But although buoyancy considerations allow plate tectonics on present-day Venus, it does not take place. The atmosphere of Venus is dry, and if this can be extended to the mantle, this increases the mantle strength, fault friction and melting temperature relative to the Earth (Nimmo and McKenzie, 1998). Because dry rocks are significantly

stronger than hydrous rocks (Chopra and Paterson, 1984; Karato, 1986), plate tectonics could be hindered by this effect. Indeed, the present-day difference in tectonic style between Earth and Venus has been ascribed to the presence of water in the mantle of the former and the absence in the latter planet (Mackwell et al., 1998). Alternatively, the accumulation of compositionally buoyant mantle material, residue from partial melting, in the shallow upper mantle may have a stabilizing effect on the lithosphere (Parmentier and Hess, 1992).

4.4.3 Plate tectonics on Mars

Although different in scale and intensity, linear patterns of rock magnetization on the southern hemisphere have been linked with magnetic striping found on the Earth's ocean floors, and a similar plate tectonic origin has been suggested (Acuña et al., 1999; Connerney et al., 1999). Sleep (1994) interprets surface features of Mars in a plate tectonic framework. Nimmo and Stevenson (2000) investigate the link between surface heat flow and the planetary magnetic field and suggest that the presence of a Martian magnetic field during the first 500 Myr may have been related to a process causing a high surface heat flux such as plate tectonics. Spohn et al. (2001) show cooling histories for Mars based on parameterized models for different modes of heat transfer, including a similar scenario with early plate tectonics followed by a stagnant lid regime. However, the rapid formation of a thick (several hundred kilometer) gravitationally stable and geochemically depleted layer in the Martian mantle in models of Schott et al. (2001) would argue against an early plate tectonic history for Mars. So far, no robust evidence for plate tectonics on Mars has been found, and Mars presently appears to be in the stagnant lid regime (Reese et al., 1998). Our results show that buoyancy considerations allow plate tectonics only for a relatively small range of potential temperatures, below approximately $1300\text{--}1400^\circ\text{C}$ (Figure 4.5a,b). Since Mars has a higher surface to volume ratio than Earth, one would expect the planet to cool faster. However, the opposing effect of the early formation of a several hundred kilometer thick buoyant layer of melt residue will strongly reduce the efficiency of convective cooling of the planet (Schott et al., 2002). As a consequence, Mars possibly never cooled down sufficiently to reach the operational temperature window for Earth-like plate tectonics, and might well have a potential temperature above $1300\text{--}1400^\circ\text{C}$. The presence of such a thick depleted root might have obstructed large-scale melt extraction from the mantle required for massive volcanism which was absent during the past 1-2 Gyr of Mars' history, despite the possibly elevated internal temperature. Recently, indications of less widespread recent volcanism (< 100 Myr) have been found (Hartmann et al., 1999), providing arguments for an elevated internal temperature.

4.5 Conclusions

Based on buoyancy arguments, we find the following maximum potential mantle temperatures for which neutral buoyancy is reached on reasonable time scales (within 500 Myr): 1500°C for Earth, 1450°C for Venus (or 1650°C when assuming cooler surface condi-

tions in the earlier history of the planet), and $1300 - 1400^{\circ}\text{C}$ for Mars. Whether plate tectonics will actually take place also depends on other factors, like water content of the mantle, however. Geological evidence indicates that plate tectonics has been active on Earth since the Proterozoic (Hamilton, 1998), and possibly much earlier (De Wit, 1998). The potential temperature at which oceanic lithosphere may become negatively buoyant within 500 Myr, 1500°C , might be representative of the late Archean, a time which also appears to mark a change in the geology (Richter, 1988). We speculate that at this time the geodynamic regime changed from a different mechanism to modern style plate tectonics dominated by dipping slabs sinking into the mantle. On the basis of buoyancy arguments, we propose that it is possible that Venus had a period of plate tectonics during its history, although this may have been hindered by a high planetary surface temperature. It appears unlikely that Mars had plate tectonics during its early, presumably hotter, history, because of its relatively low operational temperature window below $1300 - 1400^{\circ}\text{C}$ above which negative buoyancy is not reached on reasonable time scales.

Chapter 5

Assessment of the cooling capacity of plate tectonics and flood volcanism in the evolution of Earth, Mars and Venus

Abstract

Geophysical arguments against plate tectonics in a hotter Earth, based on buoyancy considerations, require an alternative means of cooling the planet from its original hot state to the present situation. Such an alternative could be extensive flood volcanism in a more stagnant-lid like setting. Starting from the notion that all heat output of the Earth is through its surface, we have constructed two parametric models to evaluate the cooling characteristics of these two mechanisms: plate tectonics and basalt extrusion / flood volcanism. Our model results show that for a steadily (exponentially) cooling Earth, plate tectonics is capable of removing all the required heat at a rate of operation comparable to or even lower than its current rate of operation, contrary to earlier speculations. The extrusion mechanism may have been an important cooling agent in the early Earth, but requires global eruption rates two orders of magnitude greater than those of known Phanerozoic flood basalt provinces. This may not be a problem, since geological observations indicate that flood volcanism was both stronger and more ubiquitous in the early Earth. Because of its smaller size, Mars is capable of cooling conductively through its lithosphere at significant rates, and as a result may have cooled without an additional cooling mechanism. Venus, on the other hand, has required the operation of an additional cooling agent for probably every cooling phase of its possibly episodic history, with rates of activity comparable to those of the Earth.

This chapter has been submitted by P. van Thienen, N.J. Vlaar and A.P. van den Berg for publication in *Journal of Geophysical Research*.

5.1 Introduction

The literature of the past decades contains several examples of parameterized convection models for the secular cooling of the Earth during its history (e.g. Sharpe and Peltier, 1978; Davies, 1980; Turcotte, 1980; Spohn and Schubert, 1982; Christensen, 1985; Honda and Iwase, 1996; Yukutake, 2000). Depending on the parameters which are chosen, these models show varying rates of cooling for the Earth. Similar models have been produced for Mars (e.g. Stevenson et al., 1983; Schubert and Spohn, 1990; Nimmo and Stevenson, 2000) and Venus (e.g. Solomatov and Zharkov, 1990; Parmentier and Hess, 1992). These are generally based on a power-law relation between the vigour of convection, represented by the thermal Rayleigh number, and the surface heat flow, represented by the Nusselt number. This latter corresponds to the transport of heat through the boundary between the solid and liquid/gaseous planetary spheres. In the modern Earth, this transport is part of the plate tectonic process, which in fact forms a quite efficient convective cooling mechanism (see Figure 5.1a).

The early Earth, however, is thought to have been hotter by up to several hundreds of

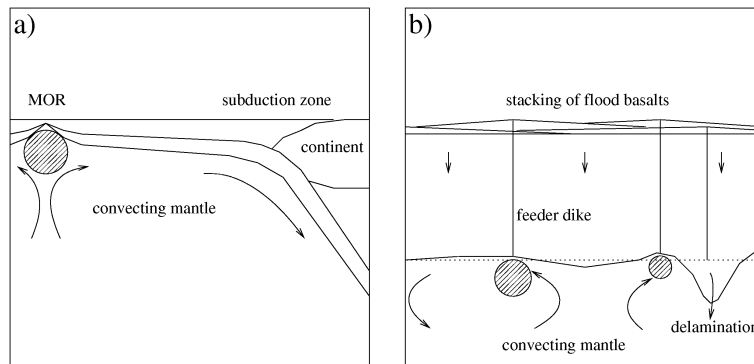


Figure 5.1: Visualization of the plate tectonics and extrusion mechanisms. a) Plate tectonics. A lithospheric column is produced at the mid-ocean ridge by partial melting of upwelling material (hatched area). As it moves towards the subduction zone, it cools down and the lithosphere thickens. At some point, the heat flow through the surface may match the mantle heat flow into the base of the lithosphere, and a steady state situation is reached. b) Extrusion mechanism. Partial melting in the hot convecting mantle underneath the lithosphere (hatched areas) generates basaltic melts that migrate up to the surface, where they form flood basalts. As layer after layer of flood basalts is stacked onto the rest, lower crustal material may delaminate. Essentially the crust itself convects, upwards in the melt phase and downwards in the solid phase. Cooling takes place both by the advection of heat by the basalt and by conduction from the mantle through the lithosphere. The downward convection of the crust will decrease the conductive heat flux out of the mantle.

Kelvin (e.g. Nisbet et al., 1993). In a hotter Earth plate tectonics is counteracted by a thicker layering of oceanic crust and depleted crustal root produced in the melting process, remaining positively buoyant over very long times (Sleep and Windley, 1982), thus preventing subduction to take place (Vlaar, 1986; Vlaar and Van den Berg, 1991; Van Thienen et al., 2003c, chapter 4). Venus and Mars presently do not have plate tectonics (Nimmo and McKenzie, 1996; Zuber, 2001).

The timing of the initiation of modern style plate tectonics is still under debate. Whereas some authors interpret all observations on Archean cratons in a plate-tectonic framework (De Wit, 1998; Kusky, 1998), others find the differences between the Archean granite-greenstone terrains and Phanerozoic tectonically active areas sufficiently large to discount plate tectonics as the mechanism of formation (Hamilton, 1998). The resulting range in estimates for the initiation of plate tectonics is 4.2-2.0 Ga. Ophiolites are considered to be obducted oceanic crust, and are therefore often used as a proxy for plate tectonics (e.g. Kusky et al., 2001). The oldest undisputed ophiolite sequences are about 2 Gyr old. The discovery of a 2.5 Ga ophiolite sequence in China (Kusky et al., 2001) has been disputed by others (Zhai et al., 2002).

An alternative mechanism to plate tectonics for the recycling of oceanic crust into the mantle may be the formation of eclogite in the deep lower parts of a thickened basaltic crust, which subsequently delaminates due to its intrinsic higher density. This process was modeled by Vlaar et al. (1994). The upward transport of melts to produce a basaltic crust and the downward movement of earlier layers of basalt below this, together with delaminating eclogite, in fact form a small scale convection cycle in the lithosphere itself (see Figure 5.1b). The delamination of eclogite allows the upward flow of fertile material that can then melt and add more basalt to the crust. This in theory is a very efficient way of removing heat from the Earth. Furthermore, it is consistent with geological evidence, which indicates that flood volcanism was quite common during the Archean (Arndt, 1999).

In this work we will evaluate the potential effect of both cooling mechanisms on the cooling history of the Earth, Mars and Venus. Reese et al. (1998) have also investigated the cooling efficiency of plate tectonics and stagnant lid regimes on Earth, Mars and Venus, using both boundary layer analysis and numerical models. However, here we apply a different approach to both modelling the cooling behaviour and examining the parameter space in which all plausible cooling histories of the terrestrial planets are defined.

In our models, the amount of activity required to obtain a certain cooling rate is determined as a function of potential temperature. More specifically, in the case of plate tectonics, we determine how fast it must operate to generate a certain planetary mantle cooling rate. We express this rate of operation with a parameter called the turnover time τ , which indicates the average lifetime of oceanic lithosphere from creation at a mid-ocean ridge to its removal from the planetary surface and return into the mantle at a subduction zone. In the case of flood volcanism, we ascertain the average volumetric rate of basalt production, expressed as an equivalent layer thickness added to the global surface area (or an active fraction of this) per unit time: the extrusion rate δ .

As the exact cooling history of the terrestrial planets remains unknown, we construct several model cooling histories that are then evaluated in the framework of the two cooling mechanisms described above. This allows us to estimate the rates of activity of the mech-

anisms in the early planetary histories, which for the Earth can be linked to geological observations.

5.2 Numerical model

For the two different geodynamical regimes described above we apply two different numerical models. The first, concerning the plate tectonics regime, is presented in section 5.2.1. The second, which concerns the basalt extrusion mechanism, will be treated in section 5.2.2.

The basic heat balance equation is applied:

$$C \frac{d}{dt} \langle T \rangle = H_T - Q \quad (5.1)$$

with

$$C = \int_V \rho c_p dV \quad (5.2)$$

$$H_T = \int_V H dV \quad (5.3)$$

$$Q = \int_{\delta V} \vec{q} \cdot \vec{n} dA = Q_{surf} - Q_{core} \quad (5.4)$$

The symbols are explained in Table 5.1. The heat fluxes through the top and bottom boundaries of the model are combined in the term Q of equation (5.4). The Q_{surf} -term is different for the two mechanisms that are studied. The definition of this term for each mechanism will be given below. The total heat flux out of the mantle is treated separately in the following sections. The core heat flux into the mantle is used as an input parameter, and the choice of its value will be discussed below in section 5.2.3. The internal heating due to the decay of radioactive elements is represented by H_T in equation (5.3).

symbol	parameter	definition	value/unit
A	surface area		m^2
C	mantle heat capacity		JK^{-1}
c_p	specific heat		$\text{Jkg}^{-1}\text{K}^{-1}$
d_{lith}	lithosphere thickness		m
f	active fraction of surface area		-
k	thermal conductivity	$\kappa\rho c_p$	$\text{Wm}^{-1}\text{K}^{-1}$
H	radiogenic heating rate		Wm^{-3}
H_T	mantle radiogenic heating rate		W
N	number of oceanic ridges		-
\vec{n}	normal vector		-
n	order of plate model series		-
Q	heat flux		W
Q_{core}	core heat flux		W
Q_{surf}	surface heat flux		W
\vec{q}	heat flow	$-k\nabla T$	Wm^{-2}
q_0	surface heat flow	$-k\frac{dT}{dz}$	Wm^{-2}
R	planetary radius		km
R_{core}	core radius		km
T	temperature		$^{\circ}\text{C}$
T_{pot}	potential temperature		$^{\circ}\text{C}$
T_{surf}	surface temperature		$^{\circ}\text{C}$
t	time/age		s
u	half spreading rate		ms^{-1}
\vec{u}	velocity		ms^{-1}
V	volume		m^3
w	vertical velocity		ms^{-1}
y_{L0}	plate thickness		m
δ	extrusion rate		ms^{-1}
θ	latitude		radians
κ	thermal diffusivity		m^2s^{-1}
ρ	density		kgm^{-3}
τ	turnover time		s
ϕ	angle / longitude		radians

Table 5.1: Symbol definitions

Although equation (5.1) describes the rate of change of the volume averaged temperature of the mantle, we want to express the results in terms of potential mantle temperature. Therefore we have obtained a simple relation between the rates of change of the volume averaged and potential temperatures. This relation was determined by volume integration in a spherical shell of several synthetic geotherms (adiabatic profile at depth and

linear profile in top 100 km). The resulting expression, showing excellent correlation ($R > 0.999$), is:

$$\frac{d}{dt} \langle T \rangle = f_{T_{avg}} \frac{d}{dt} T_{pot} \quad (5.5)$$

The scaling factor $f_{T_{avg}}$ is different for the different planets because of size effects. The values are listed in Table 5.2.

property	Earth	Mars	Venus
R (km)	6371	3397	6052
R_{core} (km)	3480	1700 ^{(1),(2),(3)}	3400 ⁽⁴⁾
c_{pm} (Jkg ⁻¹ K ⁻¹)	1250 ⁽⁵⁾	1250 ⁽⁵⁾	1250 ⁽⁵⁾
g_0 (ms ⁻²)	9.81 ⁽⁶⁾	3.7 ⁽⁶⁾	8.9 ⁽⁶⁾
T_{surf} (°C)	15 ⁽⁶⁾	-55 ⁽⁶⁾	457 ⁽⁶⁾
M (kg)		6.42 · 10 ²³ ⁽⁶⁾	
M_{sm}/M		0.75 ⁽²⁾	
$\langle \rho_m \rangle$ (kgm ⁻³)	4462 ⁽⁶⁾	3350	4234 ⁽⁴⁾
Q_{core} (TW)	3.5 – 10 ^{(7),(8)}	0.4 ⁽⁹⁾	0
$f_{T_{avg}}$	1.30	0.997	1.23

Table 5.2: Values for the planetary radius R , core radius R_{core} , average mantle specific heat c_{pm} , gravitational acceleration g_0 , surface temperature T_{surf} , planetary mass M , relative silicate mantle mass M_{sm}/M , average mantle density $\langle \rho_m \rangle$, core heat flux Q_{core} and temperature scaling term $f_{T_{avg}}$ (see text) used in the calculations for Earth, Mars and Venus. The average mantle density for Mars is calculated using planetary mass, silicate mantle mass fraction, and planetary and core size. References are: (1) Folkner et al. (1997), (2) Sanloup et al. (1999), (3) Yoder et al. (2003), (4) Zhang and Zhang (1995), (5) based on data from Saxena (1996) and Stixrude and Cohen (1993), (6) Turcotte and Schubert (2002), (7) Sleep (1990), (8) Anderson (2002), (9) heat flow from Nimmo and Stevenson (2000) for a 1700 km core.

To simplify the formulation of the problem, we assume that all heat transport from the mantle to the surface takes place in oceanic environments for plate tectonics. This is justified for the Earth by computing the magnitude of the continental mantle heat flow: Eighty-six percent of the present continental heat flux is accounted for by radiogenic heating, 58 percent of which is generated in the continental crust itself (Vacquier, 1998). Since about 30 percent of the global heat flux is through continental areas (Sclater et al., 1980; Pollack et al., 1993), this means that 15 percent of the current global heat flux is mantle heat (both radiogenic heat from the mantle and heat from mantle cooling) flowing through continental areas. We expect this fraction to be significantly smaller for the earlier Earth, because of the higher radiogenic heat production (causing a stronger blanketing effect) accompanied by a smaller amount of continental area relative to the oceanic domain. Furthermore, thicker roots of Archean cratons compared to post-Archean continental roots may divert mantle heat from the cratons (Davies, 1979; Ballard and Pollack, 1987, 1988).

For the extrusion models, we assume activity over the entire surface of the planets, since extensive volcanism on Earth also occurs in both continental (flood volcanism) and oceanic (plateaus) environments. Because both Venus and Mars do not have clearly distinguishable oceanic and continental areas, no continents will be taken into account for these planets.

5.2.1 Plate tectonics

In order to obtain an expression for the global surface heat flux Q_{surf} for the plate tectonics model, we use a plate model approximation (Carslaw and Jaeger, 1959; McKenzie, 1967; Turcotte and Schubert, 2002). The surface heat flow for this plate model is given by the following equation:

$$q_0(t) = \frac{k(T_1 - T_0)}{y_{L0}} \left[1 + 2 \sum_{n=1}^{\infty} \exp\left(-\frac{\kappa n^2 \pi^2 t}{y_{L0}^2}\right) \right] \quad (5.6)$$

In this equation, q_0 is the surface heat flow, k the thermal conductivity, T_0 and T_1 the surface and basal plate temperatures, y_{L0} the plate thickness, κ the thermal diffusivity and $t = x/u_0$ the age of the lithosphere, see Table 5.1, where x is the distance to the spreading ridge and u_0 the constant half spreading velocity.

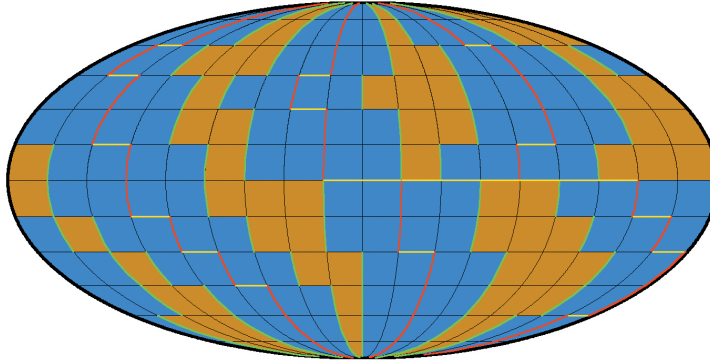


Figure 5.2: Conceptual visualization of the parameterization of plate tectonics as described in section 5.2.1 in a Mollweide projection, for a situation in which three oceans ($N = 3$) cover two thirds of the Earth's surface area. All oceans (blue) have the same uniform longitudinal extent ϕ , are bounded by subduction zones (green) at active continental (brown) margins, and have mid-ocean ridges (red) in the middle. Transform faults (yellow) may offset the ridge and consequently also the margin of the oceans. Note that only the transform faults connecting parts of ridge axes have been drawn.

In order to obtain the global surface heat flux, we need to integrate this equation over the entire planet's oceanic surface, and to do this we make some assumptions on the geometry of the system.

We consider a spherical planet that is divided in pole to pole segments. These are separated by subduction zones and continents and each has a central spreading ridge. The boundaries and ridges may be offset by transform faults, which will not influence the argumentation (see Figure 5.2). If such a segment has a longitudinal extent ϕ , its surface area A_s equals

$$A_s = 2\phi R^2 \quad (5.7)$$

We define the average time required to renew all oceanic crust as the turnover time τ . If we assume a fraction f of the entire planet's surface to be oceanic, i.e. involved in the plate tectonics system, divided in N segments of equal size, we can compute the turnover time τ by dividing the active surface area by the time derivative of the segment surface area:

$$\tau = \frac{4\pi R^2 f}{\frac{dA_s}{dt}} = \frac{4\pi R^2 f}{2NR^2 \frac{d\phi}{dt}} = \frac{2\pi f}{N \frac{d\phi}{dt}} \quad (5.8)$$

which gives us

$$\frac{d\phi}{dt} = \frac{2\pi f}{N\tau} \quad (5.9)$$

In this framework, the lithospheric age t in equation (5.6) can be rewritten:

$$t = \frac{x}{u} = \frac{\phi R \cos\theta}{\frac{1}{2} \frac{d\phi}{dt} R \cos\theta} = \frac{\phi}{\frac{1}{2} \frac{d\phi}{dt}} \quad (5.10)$$

with x the distance from the ridge, ϕ the corresponding longitudinal extent, θ the latitude and u the half spreading rate (hence the factor $\frac{1}{2}$ in the denominator of this expression).

We now compute the global oceanic heat flux by integrating equation (5.6) over the entire oceanic surface. This is done by considering $2N$ sections of oceanic crust from ridge to subduction zone, that have a longitudinal extent of

$$\phi_n = \frac{1}{2} \cdot \frac{2\pi f}{N} \quad (5.11)$$

The global oceanic heat flux now becomes

$$Q_{surf} = 2N \int_{\phi=0}^{\frac{\pi f}{N}} \int_{\theta=0}^{\pi} \frac{k\Delta T}{y_{L0}} \left[1 + 2 \sum_{n=1}^{\infty} \exp\left(-\frac{\kappa n^2 \pi^2}{y_{L0}^2} \cdot \frac{\phi}{\frac{1}{2} \frac{d\phi}{dt}}\right) \right] R^2 \sin\theta d\theta d\phi \quad (5.12)$$

Inserting equation (5.9) and integrating over θ gives

$$\begin{aligned} Q_{surf} &= 2N \int_{\phi=0}^{\frac{\pi f}{N}} \frac{2k\Delta TR^2}{y_{L0}} \left[1 + 2 \sum_{n=1}^{\infty} \exp\left(-\frac{n^2\pi\kappa N\tau\phi}{y_{L0}^2 f}\right) \right] d\phi \\ &= \frac{4k\Delta TR^2\pi f}{y_{L0}} \left\{ 1 + 2 \sum_{n=1}^{\infty} \frac{y_{L0}^2}{\pi^2 n^2 \tau \kappa} \left[1 - \exp\left(-\frac{n^2\kappa\tau\pi^2}{y_{L0}^2}\right) \right] \right\} \end{aligned} \quad (5.13)$$

Note that the number of ridges N has disappeared from the equation, although Q_{surf} depends on the number of segments N implicitly through τ . As equation (5.8) shows, τ can be constant when simultaneously changing both N and $\frac{d\phi}{dt}$ keeping $N\frac{d\phi}{dt}$ constant. In other words, a smaller number of ridges requires a higher spreading rate to obtain the same turnover time. Although the applied geometry only allows for integer values of N , we will allow it to have non-integer values as well, allowing a continuous range of possible global ridge lengths.

5.2.2 Extrusion mechanism

In the extrusion mechanism, we assume that, on long-term average, material is erupted and spreads out over the entire planetary surface. We define the rate at which this takes place as the extrusion rate δ , which indicates the time derivative of the extruded volume divided by the planetary surface area, or in other words the production of an equivalent thickness of crust per unit time. As all material that is extruded is stacked on top of existing crust in our model, pre-existing crustal material moves downward relative to the surface at the same rate as material is extruded, comparable to the permeable boundary approach of Monnereau and Dubuffet (2002) applied to Io. When (crustal) material reaches the depth of the lithosphere thickness, defined below in section 5.2.3, we assume it to delaminate (see Figure 5.1b). For the extrusion mechanism, a different formulation is used for the surface heat flux term of equation (5.1) than for the plate tectonics model. The surface heat flux Q_{surf} consists of two parts. The first is the heat advected by magma that is extruded onto the surface. We assume the magma to lose all its internal excess heat to the hydrosphere/atmosphere, taking on the surface temperature. The heat flux from this component is described by:

$$Q_{extru} = 4\pi R^2 f \delta \rho c_p \delta T \quad (5.14)$$

In this expression, f is the fraction of the planetary surface on which the mechanism is active, δ is the extrusion rate, and ρ is the density of the solidified magma (see Tables 5.1 and 5.2). δT is the temperature drop of the magma from the potential temperature to the surface temperature. This means that both latent heat consumption upon partial melting and release of latent heat during solidification, which are expected to cancel out, are not included explicitly. The second component of the surface heat flux is the conductive heat flux out of the mantle. Because in this scenario, there is continuous stacking of successive extrusive units, crustal material is continuously pushed downwards. As we assume a

constant lithosphere thickness (for a fixed potential temperature) and a fixed temperature at the lower boundary of the lithosphere consistent with the potential temperature, this causes an increase in the geothermal gradient in the deep lithosphere and a decrease at shallow levels (see Figure 5.3). In order to quantify this, we use a 1-D finite difference model of the thermal state of the lithosphere. We consider the heat equation:

$$\rho c_p \left(\frac{\partial T}{\partial t} + \vec{u} \cdot \nabla T \right) = \partial_j (k \partial_j T) + H \quad (5.15)$$

Steady state geotherms are assumed, and we simplify the equation to one dimension:

$$\rho c_p w \frac{\partial T}{\partial z} = \frac{\partial}{\partial z} \left(k \frac{\partial T}{\partial z} \right) + H \quad (5.16)$$

In this equation the extrusion of basalt is represented by the vertical velocity w , which we define to be equal in magnitude to the extrusion rate δ . We solve this equation numerically for the lithosphere, defined below in section 5.2.3, with the surface temperature and the potential temperature extrapolated to the base of the lithosphere as boundary conditions. A finite difference scheme (using 400 nodes for the lithosphere) is used to obtain geotherm and from this the conductive heat flux at the top of the lithosphere Q_{bl} , out of the mantle (see Figure 5.3).

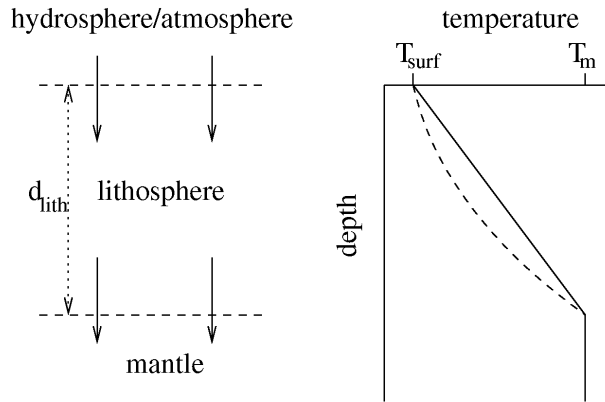


Figure 5.3: ‘Lithospheric convection’ in which, at the top boundary, material is added by magma extrusion and at the bottom boundary material is lost due to delamination, resulting in a constant lithosphere thickness. Geotherms are computed for this setting using expression (5.16) in a finite difference scheme, see text. For a situation without radiogenic heating, the trivial case of $w = \delta = 0$ (no extrusion and delamination) results in a linear geotherm (solid curve). For a finite downward velocity, the geotherm is deflected (dashed curve), resulting in a decreased conductive heat flux through the lithosphere.

Together the two components form the total surface heat flux:

$$Q_{surf} = Q_{extru} + Q_{bl} \quad (5.17)$$

5.2.3 Input parameters

The main input parameters for the different planets are listed in Table 5.2. The least constrained parameter in the models is the heat flux from the core into the mantle. Recent estimates for the present-day Earth range from 2.0 TW to 12 TW (Sleep, 1990; Anderson, 2002; Buffett, 2003). The former estimate is based on hotspot fluxes interpreted as associated with mantle plumes originating at the core mantle boundary (CMB) and, as Labrosse (2002) argues, is probably a lower limit because not all plumes that start at the CMB would make it to the surface. The latter is based on an evaluation of mantle heat transfer mechanisms near the CMB (Anderson, 2002; Buffett, 2003). Estimates for the core heat flux during the (early) history of the Earth are even more difficult to make. Thermal evolution calculations by Yukutake (2000) show the core heat flux decreasing from 12 TW at 4.4 Ga to a present value of 7.5 TW. A decreasing value is also found in the models of Labrosse et al. (1997). Buffett (2003) calculated that in the early Earth, before the formation of an inner core (the timing of which is uncertain, but in the range of 1.9-3.2 Ga, Yukutake, 2000), a core heat flux of about 15 TW would be required to drive the geodynamo. However, an increase of the core heat flux during the history of the Earth also seems plausible. Large temperature contrasts over the D'' layer (δT about 1200 K, Anderson, 2002) have been inferred suggesting slow heat transfer from the core. Recent results of numerical mantle convection modelling including temperature and pressure dependent thermal conductivity show a core heat flux fluctuating around a slightly increasing value and a temperature contrast across the bottom boundary layer increasing with time, showing the mantle to cool faster than the core, in line with planetary cooling from the top down (Van den Berg et al., 2003).

It is even more difficult to estimate the core heat fluxes for Mars and Venus. Nimmo and Stevenson (2000) reasoned that, as a superadiabatic temperature gradient is required to drive convection, the maximum obtainable conductive heat flow would be realised along an adiabatic thermal gradient. They estimated this number for the Martian core to be $5 - 19 \text{ mWm}^{-2}$. The absence of a magnetic field suggests that the martian core does not convect and therefore this number may be an upper limit for the current martian core heat flow. Using a value of 10 mWm^{-2} and a core radius of 1700 km (see Table 5.2), this results in a core heat flux of 0.4 TW. For Venus, the adiabatic conductive heat flow would be $11 - 30 \text{ mWm}^{-2}$ (Nimmo, 2002). However, the calculations of Turcotte (1995) and Nimmo (2002) indicate that the mantle of Venus may be heating up and the core heat flux would therefore be declining. We will therefore not consider a core heat flux for Venus in our calculations.

Other input parameters that are not well constrained are the thickness of the cooling plate (in the plate model, used in the plate tectonics formulation, see section 5.2.1) and the lithosphere (used in the extrusion model, see section 5.2.2) as a function of potential temperature. The plate thickness does not directly correspond to a physical thickness of

crust or lithosphere, but is obtained by matching the plate model heat flow with oceanic heat flow measurements. The (thermal) lithospheric thickness is defined by the 1327°C (1600 K) isotherm (Turcotte and Schubert, 2002). Since the rheology of mantle material is strongly temperature dependent (e.g. Karato and Wu, 1993), the thickness of the (rheological) lithosphere is a function of the potential mantle temperature. We have obtained a parameterization for both the plate thickness in the plate tectonics model and the lithospheric thickness in the extrusion model using 2-D numerical convection models. A finite element mantle convection code (see Van den Berg et al., 1993) was used in these experiments. The experimental setup for the plate tectonics model is indicated in Figure 5.4a. Upwelling is prescribed in the left hand side limb of the model domain. A nonzero velocity corresponding to the plate velocity is prescribed on (most of) the top boundary. A relatively low half spreading rate of about 4 mm/yr is used to limit the length of lithosphere required to reach thermal equilibrium. Material leaves the domain through the right hand side boundary with the prescribed plate velocity. The lower boundary of the long horizontal limb of the domain is open and kept at a temperature consistent with the potential temperature of the model, allowing relatively warm material to rise into the domain and cold material to sink out of the domain. The viscosity is temperature and pressure dependent, using parameters from Karato and Wu (1993) halfway between their wet and dry parameters. We determined the surface heat flow for the steady state part of the lithosphere (far from the ridge, see Figure 5.4b). Through trial-and-error, we searched for an effective plate thickness y_{L0} in equation (5.6) to match the heat flow at the potential temperature of each model characterized by the value of the potential temperature T_{pot} . Because the models are kinematically driven, buoyancy is of minor importance and the results are insensitive to gravitational acceleration and therefore applicable to Mars and Venus as well. Second-order motion in the form of small-scale sublithospheric convection (see Parsons and Sclater, 1977; Sleep, 2002) may be different on the different planets due to possible differences in gravitational acceleration and mantle viscosity. As a consequence of the different gravity, the Rayleigh number describing this process will be a factor 2.5 smaller for Mars than for Earth (since $g_0^{Mars} \approx 0.4 \cdot g_0^{Earth}$), the effect of which is relatively minor. The Rayleigh number scales inversely with mantle viscosity, which may therefore be of greater importance. However, the mantle viscosities of Mars and Venus are not well constrained, but may be higher due to a possibly lower water content, which would cause a greater effective plate thickness. We assume the effective plate thickness parameterization obtained for Earth-like parameters to be valid for Mars and Venus as well, keeping this caveat in mind. The resulting expression for the effective plate thickness y_{L0} is

$$y_{L0} = 147.4 - 0.1453T_{pot} + 2.077 \cdot 10^{-4}T_{pot}^2 - 8.333 \cdot 10^{-8}T_{pot}^3 \quad (5.18)$$

with y_{L0} in km and T_{pot} in degrees Celsius. This expression gives an effective plate thickness of just under 125 km for the present day potential temperature of 1350°C . This is consistent with results of Parsons and Sclater (1977), but somewhat thicker than the 100 km found by Stein and Stein (1992).

An effective lithospheric thickness for the extrusion models was found using numerical convection simulations in a different, stagnant-lid convection mode. Heating is only

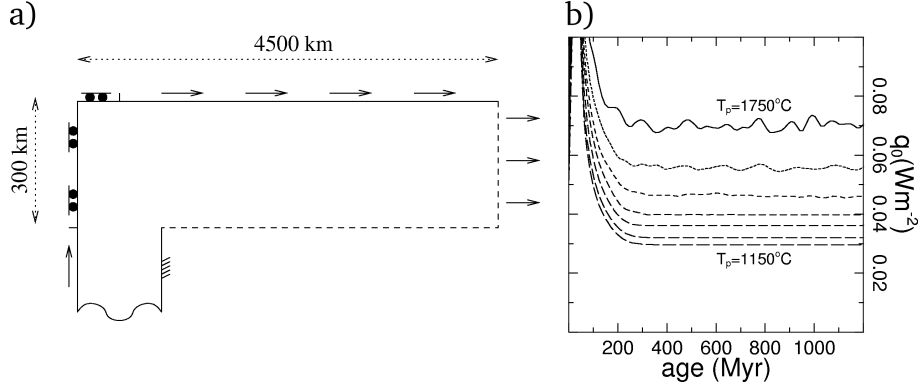


Figure 5.4: a) Numerical model setup. Adiabatic upwelling is prescribed in the left hand side limb of the model domain. A nonzero velocity is prescribed on (most of) the top boundary, corresponding to the plate velocity. Material leaves the domain through the right hand side boundary. The lower boundary of the long horizontal limb of the domain is open and kept at a temperature consistent with the potential temperature of the model. The viscosity is temperature and pressure dependent, using parameters from Karato and Wu (1993). b) Resulting surface heat flows for potential temperature of 1150°C (long-dashed curve) up to 1750°C (solid curve) in steps of 100°C . For these surface heat flows and potential temperatures, a plate thickness was sought that reproduces the surface heat flow in thermal equilibrium (far from the spreading ridge).

internal (zero bottom heat flux), and a zero temperature is prescribed on the top boundary. Side boundaries are periodic. The domain has a depth of 670 km, an aspect ratio of 1.5, a no-slip top boundary and a free slip bottom boundary. A series of models with different internal heating rates was started to generate a range of statistical steady state potential temperatures and lithospheric thicknesses. For each model, the lithospheric thickness, represented by the depth of the 1327°C isotherm is plotted against the potential temperature and a fit is computed for the entire set (see Figure 5.5):

$$d_{lith} = 6684 - 9.7352 \cdot T_{pot} + 4.7675 \cdot 10^{-3} \cdot T_{pot}^2 - 7.8049 \cdot 10^{-7} \cdot T_{pot}^3 \quad (5.19)$$

with d_{lith} in km and the potential temperature T_{pot} in degrees Celsius. Since these models are not kinematically driven but are convecting actively, we have done the experiments for different values for the gravitational acceleration, representing the different planets (see Table 5.2). As can be seen in Figure 5.5, the results of the experiments described above applied to Mars and Venus (in which the gravitational acceleration is the control parameter) nearly coincide with the best fit curve for Earth, so this curve is used for all planets (the possibly higher mantle viscosities for Venus and Mars, which would cause an increase in the lithosphere thickness, are kept in mind). We have tested the sensitivity of this result to the depth of the domain, rerunning several experiments with a doubled

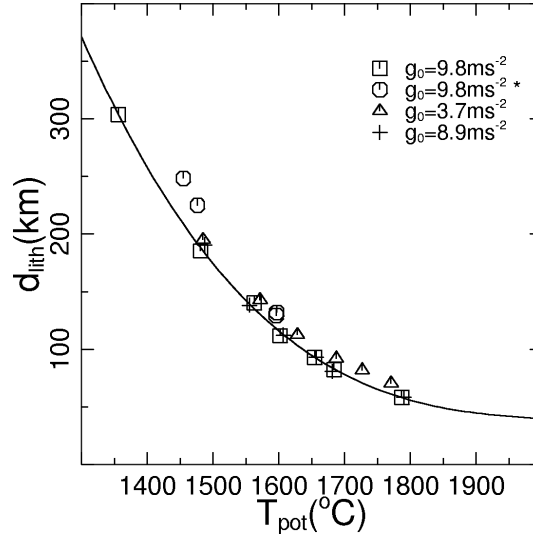


Figure 5.5: Lithosphere thickness as a function of mantle potential temperature in a stagnant lid setting, obtained from numerical convection experiments (see text). Symbols represent experiments for Earth (squares), Earth with a larger model domain (circles, see text), Mars (triangles) and Venus (crosses) values of gravity. The cubic best fit of the Earth data, used in the extrusion models (equation (5.19)), is indicated by the solid curve.

width and depth. Resulting lithosphere thicknesses are slightly greater but of comparable magnitude (see Figure 5.5).

We investigate the sensitivity of the results to the plate and lithosphere thickness, the core heat flux, the internal heating rate and the oceanic surface fraction in sections 5.3.3 and 5.3.7. In a more general planetary context we also investigate the effect of gravitational acceleration, planet size and surface temperature in sections 5.3.5 and 5.3.9.

The average mantle densities for Earth and Mars are calculated by dividing mantle mass over volume. In the case of Venus, we use the average of the results of two four-zone hydrostatic models by Zhang and Zhang (1995). The average heat capacities of the planetary mantles are approximated. Using data from Fei et al. (1991), one can calculate that the Earth's upper mantle heat capacity (for peridotite) is about $1250 \text{ J kg}^{-1} \text{ K}^{-1}$. For the lower, mantle, assuming a two phase assemblage of perovskite and magnesiowüstite, the heat capacity of the assemblage, using data from either Stixrude and Cohen (1993) or Saxena (1996), falls in the range of $1200\text{--}1300 \text{ J kg}^{-1} \text{ K}^{-1}$. We therefore apply a uniform value of $1250 \text{ J kg}^{-1} \text{ K}^{-1}$ for the entire Earth's mantle. Because of similar composition and temperatures and a smaller pressure interval in Mars and Venus, the same value is assumed for these planets.

5.2.4 Solving the equation

In the plate tectonics scenario, we solve equation (5.1) for the turnover time τ using equation (5.13) for the surface heat flux. This means we obtain the turnover time that is required to facilitate a specified cooling rate at a specified potential temperature.

In the extrusion mechanism case, we solve equation (5.1) for the extrusion rate δ , using equations (5.14) and (5.17) to obtain the corresponding surface heat flux, which gives us the required extrusion rate to obtain the specified cooling rate at the specified potential temperature.

In both cases, the parameter we want to solve for is not easily isolated from the equations. We therefore apply a bisection algorithm to compute the desired solutions numerically (see Table 5.3).

step	action
0	prescribe potential temperature and cooling rate for this experiment prescribe lower and upper boundary for ξ ($\xi_{lb}^{(0)}$ and $\xi_{ub}^{(0)}$) spanning the range in which the value of ξ is expected start loop with iteration counter $n=1$
1	compute $\xi_{bis}^{(n)} = (\xi_{lb}^{(n-1)} + \xi_{ub}^{(n-1)})/2$
2	compute $dT_{pot}/dt _{bis} = dT_{pot}/dt(\xi_{bis}^{(n)})$
3	compare $dT_{pot}/dt _{bis}$ to prescribed dT_{pot}/dt if relative mismatch $< \varepsilon_{bis}$, $\xi = \xi_{bis}^{(n)}$ and loop ends
4	- if $dT_{pot}/dt _{bis} < dT_{pot}/dt$, ξ must be greater than $\xi_{bis}^{(n)}$ → increase lower boundary of search domain: $\xi_{lb}^{(n+1)} = \xi_{bis}^{(n)}$ - if $dT_{pot}/dt _{bis} > dT_{pot}/dt$, ξ must be less than $\xi_{bis}^{(n)}$ → decrease upper boundary of search domain: $\xi_{ub}^{(n+1)} = \xi_{bis}^{(n)}$
5	$n = n + 1$ and return to step 1

Table 5.3: Numerical scheme which is used for solving the volume averaged heat equation (5.1), either for the plate tectonics model, in which case ξ indicates the turnover time τ , or for the flood volcanism case, where ξ indicates the extrusion rate δ .

5.3 Results

5.3.1 Mantle cooling rates

Results obtained from the models described in the previous sections are presented below. These results quantify the characteristics of the two cooling mechanisms, plate tectonics and flood volcanism, for specific cooling histories. Since the applied models represent quasi steady states, they do not tell us anything about the cooling histories of the Earth, Mars and Venus themselves. In this section we first explore the range of plausible cooling

histories in T_{pot} , dT_{pot}/dt -space, using simple approximations of two types of expected cooling behaviour. These scenarios will then be included in (the discussion of) the figures presenting the results of the model calculations as described in the previous sections, and aid the discussion of the results that may be relevant for the cooling histories of the terrestrial planets. Long-term decaying secular cooling will be approximated by an exponential cooling curve. Short-term cooling pulses will be viewed separately. Figure 5.6 shows five cooling histories in which a simple exponential cooling is assumed from a starting temperature of $1500 - 1900^\circ C$ at 4.0 Ga to the Earth's present estimated potential temperature of $1350^\circ C$. They were constructed by fitting the start and end points to the expression

$$T = T_0 \exp(at) \quad (5.20)$$

for which the corresponding cooling rate is

$$\frac{dT}{dt} = aT_0 \exp(at) \quad (5.21)$$

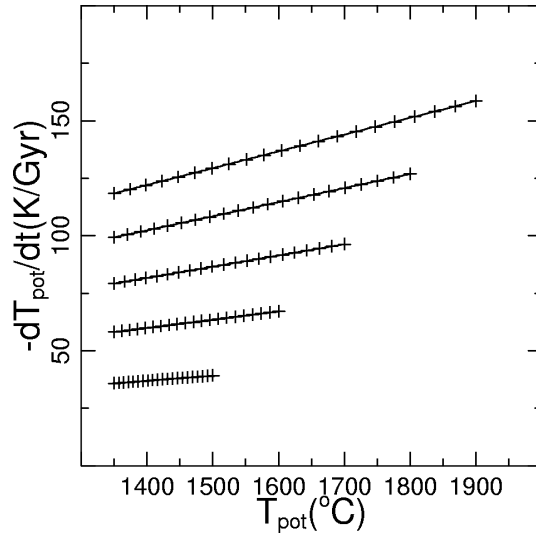


Figure 5.6: Exponential cooling curves in T_{pot} , dT_{pot}/dt -space, for starting temperatures of $1500, 1600, 1700, 1800$ and $1900^\circ C$. Markers are 200 Myr apart.

Markers are included at 200 Myr intervals to indicate the flow of time. These model cooling histories through T_{pot} , dT/dt -space will be used below in the discussion of the results as reference models. The initial temperatures shown seem to cover the range of temperatures inferred for the early Archean Earth mantle, and thus the area spanned by these curves contains plausible cooling histories for a steadily cooling Earth with an

exponential decay of both the potential temperature and the cooling rate. Because of the assumed similar formation histories and sizes of Mars and Venus compared to the Earth, we assume the same mantle temperature window to be valid for these two planets.

However, if the cooling of the planets is not an exponentially decaying process, or if the system diverges from this behaviour from time to time as in an episodic scenario, cooling rates may be significantly higher than those shown in Figure 5.6. This is illustrated by numerical models of secular cooling of the Earth by Van den Berg and Yuen (2002), which show fluctuating cooling rates with peak values of 300 to 500 K/Gyr during the early histories of their experiments. In Figure 5.7, we show maximum cooling rates that are obtained for a Gaussian shaped pulse in the cooling rate (Figure 5.7a,b). Figure 5.7c shows the temperature drop of the mantle caused by this cooling pulse on the horizontal axis. On the vertical axis, the duration of the cooling pulse ($\pm 2\sigma$) is indicated. Obviously high cooling rates are expected for short pulses with a large temperature drop, and lower cooling rates for longer pulses with smaller temperature drops. Nearly everywhere in this figure, the cooling rates are significantly higher than in the steady exponential cooling of Figure 5.6.

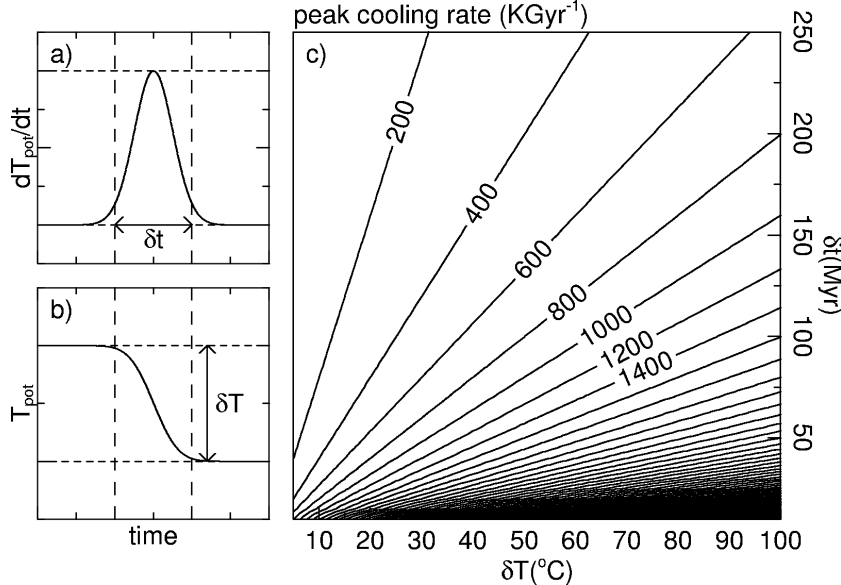


Figure 5.7: Peak cooling rates for mantle cooling pulses with Gaussian shape using arbitrary units (left hand side frames). The corresponding temperature drop is indicated on the horizontal axis, and the vertical axis signifies the duration ($\pm 2\sigma$) of the cooling pulse.

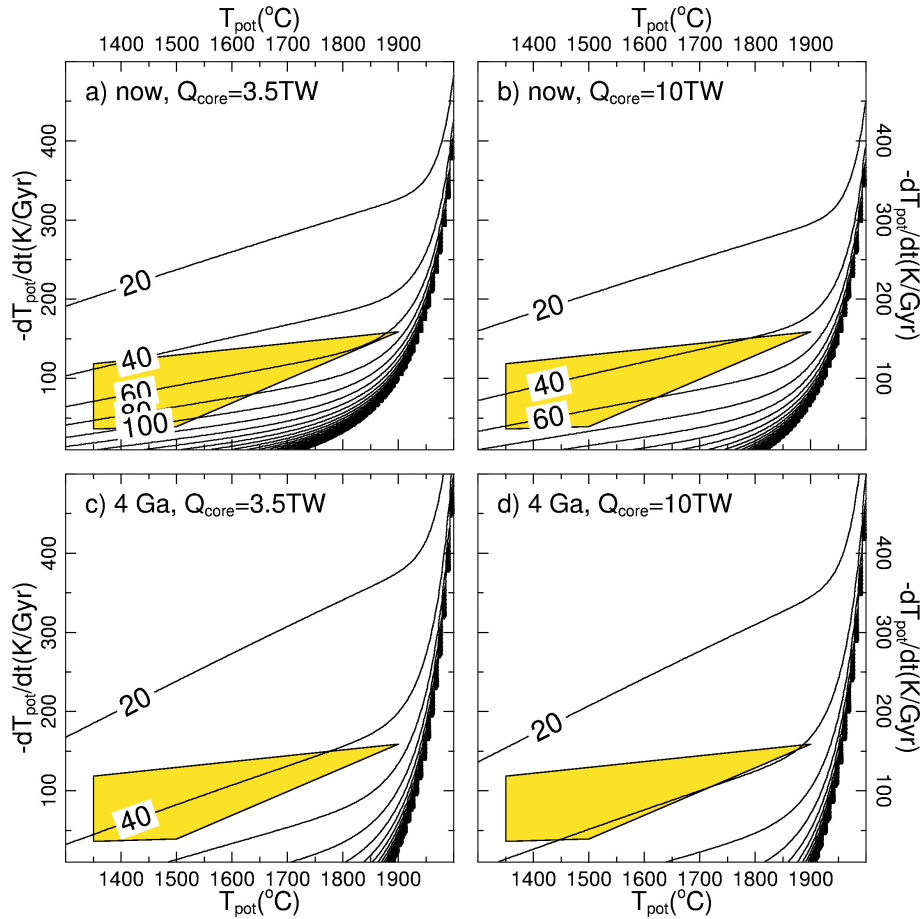


Figure 5.8: Results of the plate tectonics model for a core heat fluxes of 3.5 and 10 TW for the present and early Earth (in terms of radiogenic heat production rate and extent of the continents). Contours indicate the turnover time τ (in Myr) as a function of potential temperature (horizontal axis) and cooling rate (vertical axis). The shaded zone corresponds to the region spanned by the exponential cooling curves of Figure 5.6, and are thus representative of steady state secular cooling. Higher values on the vertical axis may be caused by cooling pulses, see Figure 5.7.

5.3.2 Plate tectonics on Earth

The computed results for the plate tectonics model described in section 5.2.1 applied to the Earth are presented in Figure 5.8a-d, showing contour levels of the turnover time τ ,

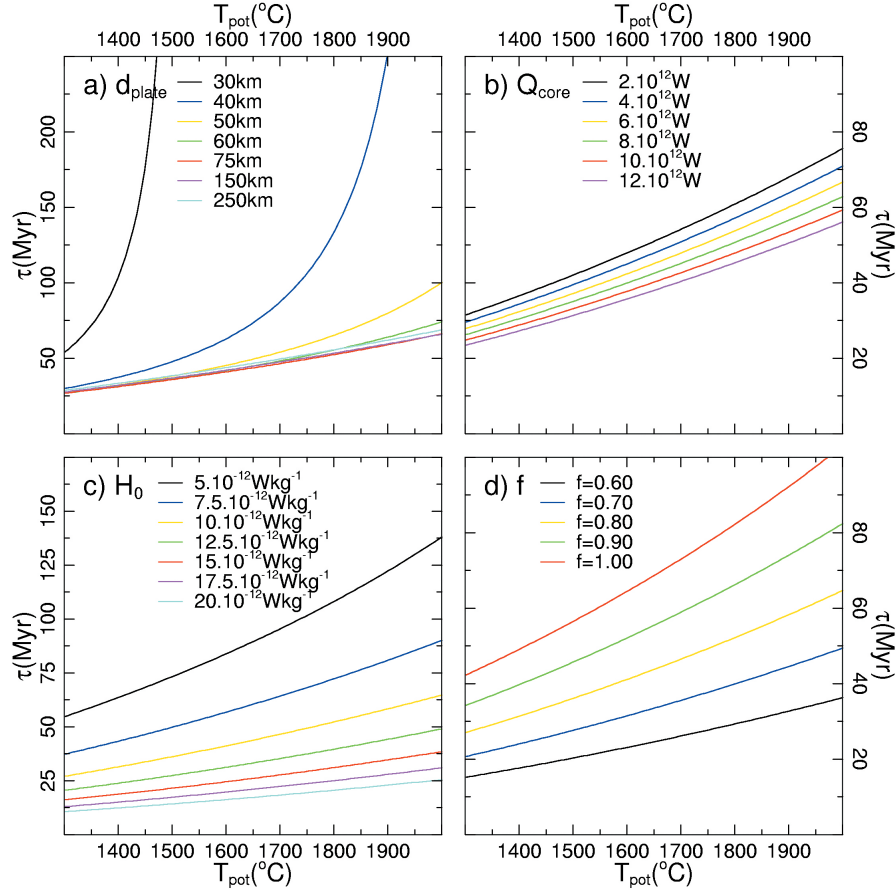


Figure 5.9: Sensitivity tests of the plate tectonics model to single parameters. Fixed values of the non-varying parameters are: Core heat flux $Q_{core} = 7\text{TW}$, plate thickness $d_{plate} = 100\text{km}$, internal heat productivity $H_0 = 10 \cdot 10^{-12}\text{Wkg}^{-1}$, oceanic surface fraction $f = 0.80$, mantle cooling rate $-\frac{dT_{pot}}{dt} = 100\text{Kgyr}^{-1}$. The curves show the turnover time τ as a function of a) plate thickness d_{plate} ; b) core heat flux Q_{core} ; c) internal heat productivity H_0 ; d) extent of the active area f .

for the present situation and for a case representing the early Earth (4 Ga) and for two different values for the core heat flux, 3.5 TW and 10 TW. The timings are based on the rate of internal heating ($4.8 \cdot 10^{-12}\text{Wkg}^{-1}$ for the present and $14.4 \cdot 10^{-12}\text{Wkg}^{-1}$ for the early Earth) and the (estimated) extent of the continents ($f = 0.63$ for the present and $f = 0.97$ for the early Earth, McCulloch and Bennett, 1994). All four frames show the

potential temperature of the mantle on the horizontal axis, and the mantle cooling rate on the vertical axis (in K/Gyr). The contours indicate the turnover time τ that is required to maintain a cooling rate at a potential temperature corresponding to the position in the diagram. The shaded area indicates the region occupied by the exponential cooling histories shown in Figure 5.6, with the present-day Earth plotting near the left hand vertical boundary of this region. Note that Figure 5.8a,b and c,d are two sets of sections through two 3-D boxes, in which the internal heating rate is plotted on the third axis. In such a 3-D representation, it is possible to track any cooling history independent of the internal heating rate, whereas in 2-D sections such as those of Figure 5.8a,b and c,d (and also other figures below), any cooling history tracked in an individual frame is for a fixed internal heating rate. Because such a 3-D representation is difficult to bring across in 2-D figures, we use the 2-D sections and keep this caveat in mind. The core heat fluxes represent the range of values found in the literature as discussed in section 5.2.3.

From these diagrams we observe that for a fixed cooling rate, a longer turnover time is required at higher mantle potential temperatures. This is a result of the decreased plate thickness at higher potential temperatures, which causes an increase in the conductive surface heat flow and therefore reduces the convective heat flow that is required to maintain the specified cooling rate. For a constant mantle potential temperature, obviously, higher cooling rates require a shorter turnover time. Each figure shows a region in the lower right hand side corner where required turnover times are more than 500 million years (which is the maximum contour plotted). In these regions heat conduction through a static lithosphere is essentially sufficient to generate the required rate of cooling. This is a combined effect of the low cooling rates that characterize this regime which is effectively a stagnant lid situation (Solomatov and Moresi, 1996) and a thin lithosphere which is the result of a high mantle potential temperature.

The range of turnover times allowed by our model results for the present-day Earth, assuming an exponential cooling model, is indicated in Figure 5.8a-b by the left hand vertical boundary of the shaded area that envelopes the exponential cooling curves of Figure 5.6. Turnover times of about 30 to about 90 million years are permissible, consistent with the average age of subducting lithosphere on the present-day Earth of about 70 million years (Juteau and Maury, 1999, Table 11.1). For the early Earth, results consistent with exponential cooling indicate turnover times of about 40-50 million years (right hand side boundary of shaded area in Figure 5.8c-d). The effect of an increased core heat flux is that the surface heat flux must also increase in order to obtain the same specified cooling rate.

5.3.3 Sensitivity of plate tectonics results to the model parameters

Figure 5.9 shows the sensitivity of the results of the previous section to changes in plate thickness, core heat flux, internal heating rate and extent of the oceanic domain. In the experiments which produced these curves, all parameters were fixed (including the plate thickness, which in the previous experiments was a function of potential temperature following equation (5.18), see figure caption for values), except for the single parameter under investigation. In descending order of sensitivity, plate thickness, internal heating

rate, oceanic surface fractional area and core heat flux influence the turnover time τ . There appears to be a threshold value for the importance of plate thickness. As Figure 5.9a shows, for thicknesses of more than 60 km, the effect of changing the thickness is minimal in the potential temperature range investigated. Below 60 km thickness, however, the turnover time increases strongly at higher temperatures. This effect is stronger for a thinner plate. It is caused by thermal conduction through the lithosphere taking over from conductive cooling of the lithosphere itself as the most important cooling factor. Note that the threshold thickness will be different for different cooling rates. The other parameters, core heat flux, internal heating rate and extent of the oceanic domain, have a more straightforward and linear effect, essentially scaling the turnover time more or less independent of the potential temperature (see Figures 5.9b,c,d).

5.3.4 Plate tectonics on Mars and Venus

The plate tectonics model of section 5.2.1 was also applied to Mars and Venus. The parameters that were adjusted to modify the model for these planets are the core and planetary radius (resulting in a different mantle heat capacity and surface to volume ratio), the surface temperature (controlling the surface heat flow), the average mantle density (controlling the mantle heat capacity), the core heat flux and the conversion factor between potential and volume averaged temperatures (resulting from different planetary radius and gravitational acceleration, which cause different adiabatic temperature profiles), using values listed in Table 5.2. Continents are assumed to be absent, so the oceanic surface fraction f is set to 1. The results of these experiments are shown in Figure 5.10. Two different values for the internal heating rate were used, which we assume to represent the present ($H_0 = 4.80 \cdot 10^{-12} \text{Wkg}^{-1}$) and early ($H_0 = 14.40 \cdot 10^{-12} \text{Wkg}^{-1}$) states of the planets. Again, the range of reasonable exponential cooling curves of Figure 5.6 is included as the shaded area. For present Mars, shown in Figure 5.10a, the results indicate that only extremely high cooling rates of more than 250 Kelvin per billion years requires the operation of plate tectonics. For lower, more likely cooling rates, turnover times are well over 500 million years, which essentially means that conductive cooling is sufficient. This is a result of the fact that, compared to the Earth, surface to volume ratio ($\sim R^2/R^3$) is relatively large. This results in conductive cooling through a comparatively greater surface area (scaling with R^2 , see equation (5.13)) of a comparatively smaller heat reservoir (equation (5.2), scaling with R^3), which is more efficient. The same goes for early Mars (characterized in our model by an increased internal heating rate $H_0 = 14.40 \cdot 10^{-12} \text{Wkg}^{-1}$), shown in Figure 5.10b, where the position of the planet may be expected in the right hand side half of the frame due to a higher mantle temperature. Venus, shown in Figure 5.10c-d (present and early), shows more Earth-like characteristics (see Table 5.2). At a probable present potential temperature similar to that of the Earth of 1300°C with an upper limit of 1500°C (Nimmo and McKenzie, 1998), turnover times for hypothetical plate tectonics would be on the order of tens to some hundreds of million years if we assume an exponential cooling scenario. A more likely scenario in which short episodes of rapid cooling (see Figure 5.7) and longer episodes of stagnation alternate would require turnover times of only some tens of million years or less (upper left of

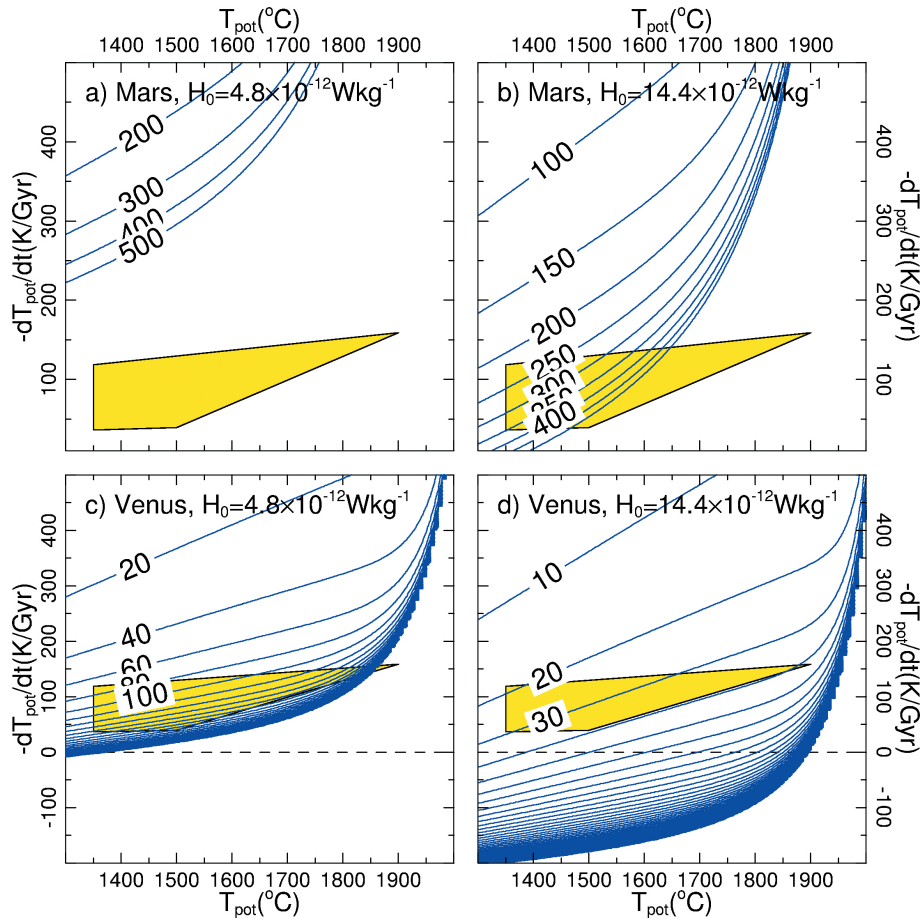


Figure 5.10: Turnover time τ for Mars and Venus for models with internal heating rates of 4.80Wkg^{-1} and 14.40Wkg^{-1} . For other model parameters, see Table 5.2. For an explanation of the figure see caption of Figure 5.8.

Figure 5.10c) in the cooling episodes and (many) hundreds of million years (lower left of this frame) during the stagnation periods. For early Venus, some cooling mechanism other than conduction definitely seems required (see Figure 5.10d). If plate tectonics were this mechanism, turnover times on the order of some tens of million years are required, comparable to the results for the early Earth (Figure 5.8c-d). Note that we have included negative values for the cooling rate, since Venus may be heating up at the moment (Nimmo, 2002) and may have had more heating episodes (Turcotte, 1995).

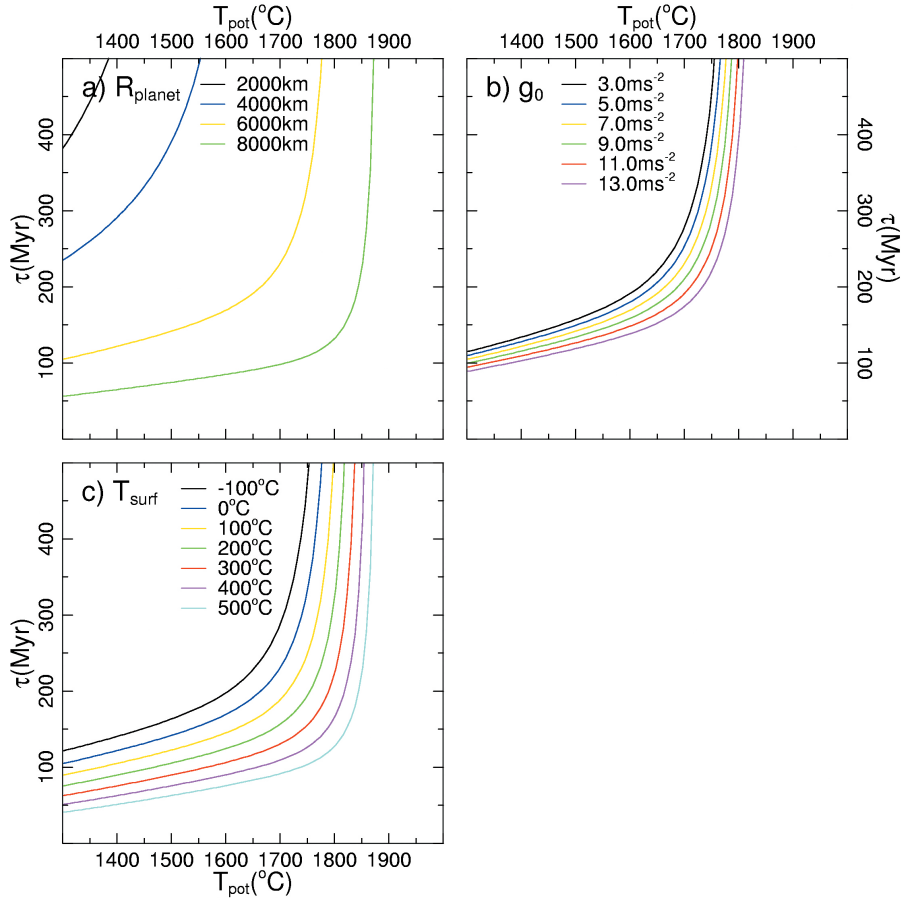


Figure 5.11: Variation of the turnover time τ as a function of (a) planet size R_{planet} , (b) gravitational acceleration g_0 and (c) surface temperature T_0 . Values of non-varying parameters are $Q_{core} = 1\text{TW}$, $d_{lith} = 100\text{km}$, $H_0 = 4.8 \cdot 10^{-12}\text{Wkg}^{-1}$, $f = 0.80$, $-dT_{pot}/dt = 100\text{Kgyr}^{-1}$, $g_0 = 7.0\text{ms}^{-2}$, $R = 6000\text{km}$. The core radius is half of the planetary radius in all cases. The potential to average temperature scaling factor $f_{T_{avg}}$ in equation (5.5) is recomputed for all different combinations of planet size and gravitational acceleration used.

5.3.5 Effects of planetary parameters on heat transfer by plate tectonics

In order to evaluate the effect of the different distinguishing parameters of the terrestrial planets separately, we have calculated the turnover time while varying one parameter (planetary radius, gravity or surface temperature) and keeping the others fixed. The results are shown in Figure 5.11a-c for these three parameters, respectively, for a fixed cooling rate of 100 K Gyr^{-1} (other parameters see figure caption). It is clear from this figure that the planet's size, through the surface area to volume ratio ($\sim R^2/R^3$), dominates the cooling behaviour of a planet, to such an extent that small planets can cool conductively at considerable rates, whereas larger planets need a more efficient cooling agent like plate tectonics to get a moderate cooling rate less than 100 K Gyr^{-1} . The gravitational acceleration affects the adiabatic gradient ($\alpha g T / c_p$), but this effect is relatively minor. An elevated surface temperature tends to reduce the conductive heat flow, and therefore faster plate tectonics, if present, is required to maintain a certain rate of cooling.

5.3.6 Extrusion mechanism on Earth

Figure 5.12 shows the results of the extrusion models. It is similar to Figure 5.8 but it shows different quantities, the extrusion rate δ (black contours) in mMyr^{-1} and the global volumetric extrusion rate (red contours) in $\text{km}^3 \text{yr}^{-1}$. The extrusion rate δ represents the global ($f = 1.0$) average thickness of basaltic crust produced in one million years. We consider this mechanism to operate globally (in contrast with plate tectonics), since continental flood volcanism is not uncommon. The extrusion rate δ and the global volumetric extrusion rate only differ by a factor of (surface area / 1 Myr). Again, four cases are investigated, using internal heating and continent extent values for the present ($H_0 = 4.80 \cdot 10^{-12} \text{ W kg}^{-1}$) and early (4 Ga, $H_0 = 14.40 \cdot 10^{-12} \text{ W kg}^{-1}$) Earth and two values for the core heat flux of 3.5 and 10 TW. The general trends are (1) a higher potential temperature reduces the lithosphere thickness and increases the temperature contrast over the lithosphere, thus increasing the conductive heat flux and decreasing the extrusion rate, (2) a higher cooling rate requires a greater extrusion rate, and (3) an increase in the internal heating rate (either radiogenic or from the core) requires an increase in the extrusion rate. For comparison, a rough estimate for the 'extrusion rate' of the present-day Earth is $\sim 70 \text{ km}^3 \text{ yr}^{-1}$ (100,000 km of ridges spreading at an average 2x5 cm/yr producing a crust of 7 km), which is somewhat less but of comparable magnitude to the numbers presented in Figure 5.12a,b (the left hand side boundary of the shaded area), although the mechanism is different. It is clear from Figure 5.12c and d that in the early Earth, conductive cooling through the lithosphere was sufficiently efficient above potential temperatures of approximately 1800°C in the exponential cooling cases, indicated by the shaded area, to generate cooling without requiring magmatic processes, since the required extrusion rate δ is below 0 here. For lower potential temperatures, global volumetric extrusion rates are up to an order of magnitude higher than for the present-day Earth, less than $500 \text{ km}^3 \text{ yr}^{-1}$.

5.3.7 Sensitivity of the extrusion mechanism heat transfer

The sensitivity of the extrusion rate δ to the lithosphere thickness (a), core heat flux (b), internal heating rate (c) and extent of the 'oceanic' domain (d) is shown in Figure 5.13. Strong effects can be seen for the lithosphere thickness, where sufficiently low values may result in completely conductive cooling (no extrusion required), and the internal heating rate. The effect of surface area (assuming that the extrusion mechanism is active on only a part of the planet's surface) is smaller, and that of the core heat flux is quite limited in the parameter range that was investigated.

5.3.8 Extrusion mechanism on Mars and Venus

Figure 5.14 shows the results of the extrusion model for Mars and Venus, for internal heating values assumed to represent the recent and early history, respectively, of these planets. The results for present day Mars (Figure 5.14a) at the estimated present location of Mars in $T_{pot}, dT/dt$ -space in the lower left hand side corner of the diagram indicate that only very limited volumetric extrusion rates are required for the cooling of Mars. Compared to Earth, the global volumetric extrusion rates are an order of magnitude smaller. In terms of extrusion rate δ , the difference is not as large due to the smaller surface area of Mars. Early Mars (Figure 5.14b) also requires only a small global volumetric extrusion rate, even for very high cooling rates, due to a combination of thinner lithosphere compared to present-day Mars and large surface area to volume ratio compared to larger planets. Things are quite different for Venus (Figure 5.14c,d). When assuming an exponential time dependence of planetary cooling as indicated by the shaded area, which may not be correct for Venus, we see volumetric extrusion rates on the order of 200-350 $km^3 yr^{-1}$, up to 5 times greater than the present-day Earth's plate tectonics crustal production rate, and comparable to the rate that would be required for the present-day Earth if the extrusion mechanism were the main cooling agent (see Figure 5.12a,b). Early Venus also shows model results similar to those of the early Earth (see Figure 5.12c,d consistent with the similarity of the model parameters for both planets). Note that we have again included negative values for the cooling rate to show the effect of possible periods of heating in the planet's history.

5.3.9 Effects of planetary parameters on the extrusion mechanism heat transfer

For the extrusion mechanism, the sensitivity for planetary parameters is also investigated. The presentation of the results is similar to that of the plate tectonics sensitivity tests of Figure 5.15, and the parameter values are the same. The results show that both the planetary size (using a fixed value for g_0 , which is rather artificial but the alternative would be to assume a relation between radius and gravitational acceleration, which is also artificial because of the dependence on composition) and the surface temperature may strongly affect the extrusion rate required for a prescribed cooling rate. The former

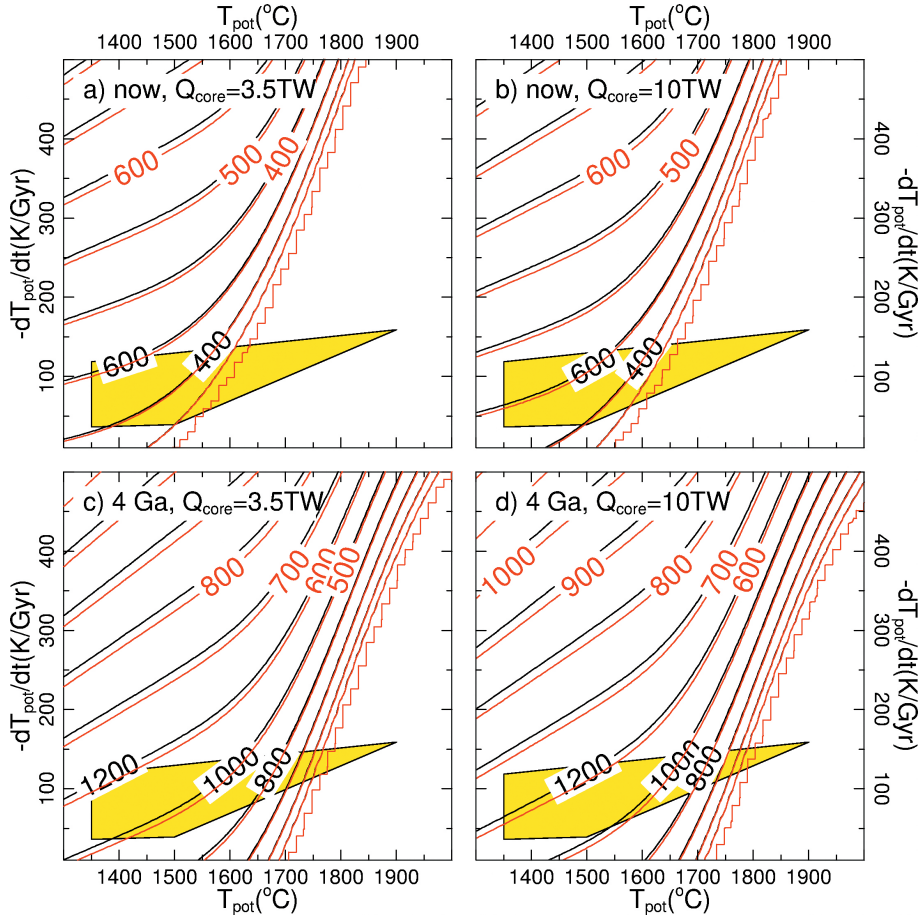


Figure 5.12: Results of the extrusion model for a core heat fluxes of 3.5 and 10 TW for the present and early Earth (in terms of radiogenic heat production rate and extent of the continents). Black contours indicate the extrusion rate δ in mMyr^{-1} , representing the average thickness of basaltic crust produced per million years for the entire planetary surface. Red contours indicate the global volumetric basalt production rate, in $\text{km}^3\text{yr}^{-1}$.

affects the planetary cooling efficiency through the surface area to volume ratio, and the latter is a factor in the temperature gradient over the lithosphere, determining the conductive heat transport. The gravitational acceleration, affecting the adiabatic gradient, has a limited effect, but obviously R_{planet} and g_0 are coupled quantities.

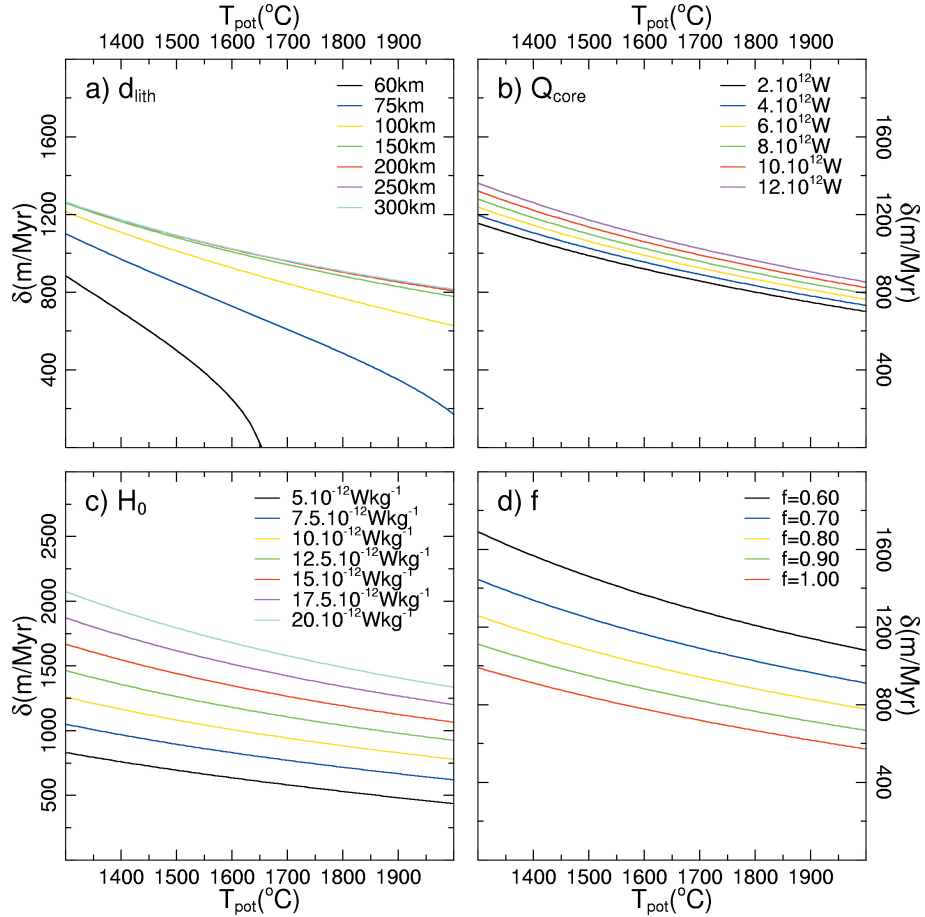


Figure 5.13: Sensitivity tests of the extrusion model to single parameters. Fixed values of the non-varying parameters are: Core heat flux $Q_{core} = 7\text{TW}$, lithosphere thickness $d_{lith} = 150\text{km}$, internal heat productivity $H_0 = 10 \cdot 10^{-12}\text{Wkg}^{-1}$, oceanic surface fraction $f = 0.80$, mantle cooling rate $-\frac{dT_{pot}}{dt} = 100\text{Kgyr}^{-1}$. The curves show the extrusion rate δ as a function of a) lithosphere thickness d_{lith} ; b) core heat flux Q_{core} ; c) internal heat productivity H_0 ; d) extent of the active area f .

5.4 Discussion

5.4.1 Plate tectonics on the early Earth

Many speculations about the nature of plate tectonics in a hotter Earth have been presented. They often involve faster spreading than in the present situation (e.g. Bickle, 1978, 1986) or a longer mid-ocean ridge system (e.g. Hargraves, 1986), to transport a greater heat flux from the mantle. Our results, however, show that the hotter mantle itself generates the most important means of removing the increased heat flux from the mantle by thinning the lithosphere relative to a cooler mantle and thus significantly increasing the conductive heat flow through the lithosphere. This effect has also been noticed by Bickle (1978). If we compare the slope of the exponential model cooling curves of Figure 5.6 in $T_{pot}, \frac{dT_{pot}}{dt}$ -space (indicated in Figure 5.8a-d by the shaded area) to the slope of the contours of equal turnover times, we observe that in all four models (Figure 5.8a-d) the turnover time required for a certain cooling rate increases faster with potential temperature than the actual cooling rate predicted by the exponential cooling model for higher mantle temperatures. In other words, the exponential cooling curves predict a *slower* rate of operation for plate tectonics rather than a faster at higher mantle temperatures. This is consistent with the argument of Hargraves (1986), who predicts slower plate tectonics on the basis of reduced slab pull and ridge push forces in a hotter mantle. Only when cooling pulses at much higher cooling rate (see Figure 5.7) than the exponential curve of Figure 5.6 are considered will the turnover time τ be reduced to lower values at higher mantle temperatures during these periods of increased cooling. However, in between these pulses, the turnover time will be significantly larger than in the exponential cooling case. As we only have a rough idea of the cooling history of the Earth, it is difficult to place the different geological eras in the diagrams produced in this work. Several authors have shown that plate tectonics becomes increasingly more difficult in a hotter Earth (Sleep and Windley, 1982; Vlaar, 1986; Vlaar and Van den Berg, 1991; Davies, 1992; Van Thienen et al., 2003c, chapter 4) on the basis of lithospheric buoyancy, which may limit the applicability of our plate tectonics results on the high end of the T_{pot} spectrum.

5.4.2 Extrusion mechanism on the early Earth

The volumetric extrusion rates found in our models can be compared to extrusion rates representative of processes similar to the extrusion mechanism in the more recent Earth, like hotspots and flood volcanism. Hotspots typically have basalt production rates of 0.02 to 0.04 $km^3 yr^{-1}$. Phanerozoic flood volcanism may have eruption rates two orders of magnitude higher, about 0.75 to more than 1.5 $km^3 yr^{-1}$ (Richards et al., 1989), with peak rates possibly up to 10 $km^3 yr^{-1}$ (White and McKenzie, 1995). These numbers are still significantly smaller than the volumetric production rates up to $x \cdot 100 km^3 yr^{-1}$ found in Figure 5.12.

This means that if the mechanism played an important role in the cooling of the early Earth, much more extensive hotspot and flood volcanism activity may have been required to have sufficient cooling capacity. Much evidence is found for Archean and Proterozoic

duration (Myr)	area (km ²)	eruption rate (km ³ yr ⁻¹)		
		d = 1 km	d = 3 km	d = 5 km
2409-2413	$7.42 \cdot 10^7$	18.6	55.7	92.8
2433-2451	$1.51 \cdot 10^8$	8.39	25.2	41.9
2582-2610	$7.37 \cdot 10^7$	2.63	7.90	13.2
2899-2903	$3.71 \cdot 10^7$	9.26	27.8	46.3

Table 5.4: Estimates of eruption rates for three different assumed flood basalt thicknesses d , based on areal extent estimates of superplume events by (Abbott and Isley, 2002, Table 8). The average of the minimum and maximum areal extent reported by Abbott and Isley (2002) has been listed and used in calculating the eruption rates. The lowest two estimates for the average flood basalt thickness (1 and 3 km) are consistent with estimates of surface area and volume of several Phanerozoic flood basalts, listed in Table 1 of White and McKenzie (1995). We speculate that the higher value (5 km) may be more representative of larger scale events in the Archean.

flood volcanism. Arndt (1999) discusses many occurrences all over the world. Abbott and Isley (2002) have identified a total of 62 superplume events and eras from the mid Archean to the present on the basis of flood basalts, dike swarms, high Mg rocks and layered intrusions, though especially for the Archean this is probably a lower limit because of preservation issues and lack of data. Using maximum dike widths and flood basalt surface area, they estimate the original extent of the flood basalts generated by the separate events. They find that both the magnitude and the frequency of these events was significantly higher during the late Archean and has declined since then. Abbott and Isley (2002) also identify six major events of which the estimated eruption volume of each was sufficient to cover at least 14-18% of the Earth's surface. When making an assumption about the average thickness of a flood basalt province, volumes can be computed and using estimated eruption times, volumetric eruption rates. In Table 5.4, estimates of eruption rates for four selected late Archean to early Proterozoic superplume events from Abbott and Isley (2002) have been calculated, using estimates for the average flood basalt thickness from Phanerozoic flood basalts (1-3 km, see Table 1 of White and McKenzie, 1995). The resulting numbers are of the same magnitude to up to one order of magnitude smaller than the eruption rates dictated by Figure 5.12c-d (lower middle to right corner for moderate cooling rates at Archean mantle temperatures). However, if we extrapolate further back to the early/middle Archean, we may expect volumetric extrusion rates to be even higher for these events, and the number of up to about $550 \text{ km}^3 \text{ yr}^{-1}$ required by Figure 5.12c-d for significant cooling rates is feasible with only a small number of active flood basalt provinces (last column of Table 5.4) for an early Earth that is only 150 Kelvin hotter than the present-day Earth (lower right corner of the shaded area in Figure 5.12c,d).

For higher temperatures during the early history of the Earth, the required extrusion rate is smaller and therefore the required amount and activity of flood volcanism is smaller

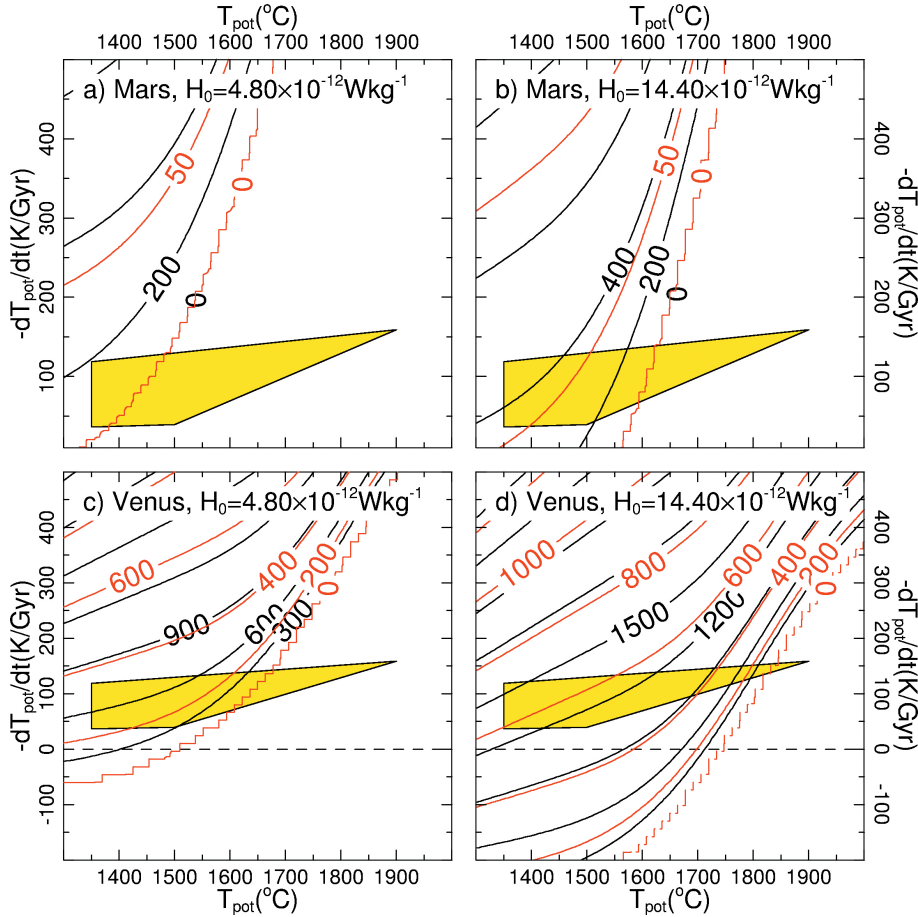


Figure 5.14: Results of the extrusion model for Mars and Venus, using two different values for the internal heating rate representing the recent and early histories of the planets. Black contours indicate the extrusion rate δ in mMyr^{-1} , representing the average thickness of basaltic crust produced per million years for the entire planetary surface area. Red contours indicate the global volumetric basalt production rate, in $\text{km}^3\text{yr}^{-1}$.

as well. For a hotter early Earth, say above 1750°C , the numbers of Table 5.4 are similar to those in Figure 5.12 and a single flood volcanism province may be sufficient, combined with global conductive cooling, to attain significant mantle cooling rates.

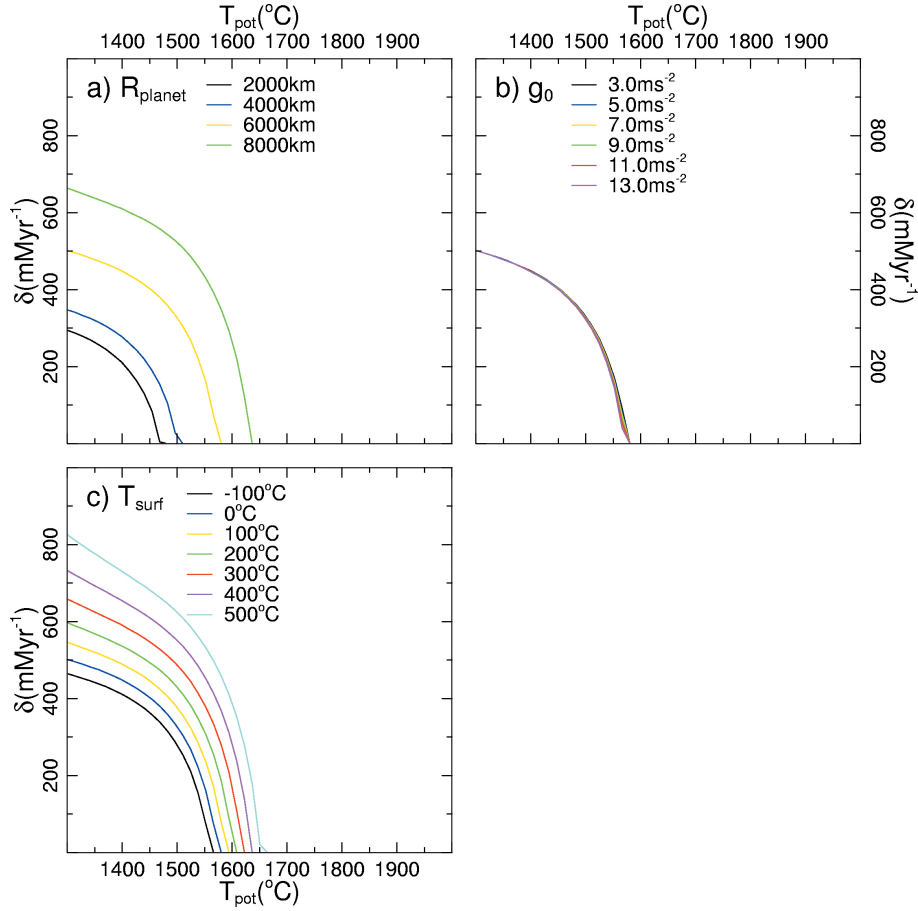


Figure 5.15: Variation of the extrusion rate δ as a function of (a) planet size R_{planet} , (b) gravitational acceleration g_0 and (c) surface temperature T_0 . Values of non-varying parameters are $Q_{core} = 1\text{TW}$, $d_{lith} = 100\text{km}$, $H_0 = 4.8 \cdot 10^{-12}\text{Wkg}^{-1}$, $f = 0.80$, $-dT_{pot}/dt = 100\text{Kgyr}^{-1}$, $g_0 = 7.0\text{ms}^{-2}$, $R = 6000\text{km}$. The core radius is half of the planetary radius in all cases. The potential to average temperature scaling factor $f_{T_{avg}}$ in equation (5.5) is recomputed for all different combinations of planet size and gravitational acceleration used.

5.4.3 Cooling mechanisms of Mars and Venus

The results, shown in Figure 5.10, clearly indicate that neither present nor early Mars requires plate tectonics to obtain considerable cooling rates on the order of 100 K/Gyr or more, and that the relatively small planet can cool conductively at considerable rates.

Nimmo and Stevenson (2000) suggest that plate tectonics or some other efficient cooling agent was active during the first 500 Myr of the history of Mars, in order to allow the core heat flow to rise above the conductive level and initiate core convection, which would produce a magnetic field of which the result is seen nowadays in the magnetisation of some ancient Martian crustal rocks (Acuña et al., 1999). During this initial phase, the model results of Nimmo and Stevenson (2000) show an average cooling rate of about 400 Kelvin per billion years, combined with a core heat flux of about 1.3 TW (using their 1450 km core size). Although our Mars models use a core heat flux of 0.4 TW, Figure 5.9 shows a low sensitivity of the results to variations in the core heat flux for Earth. For Mars, we expect the effect to be similarly small. Therefore, from the results of our model shown in Figures 5.10b and 5.14b (early Mars) at a cooling rate of 400K Gy^{-1} , we conclude that plate tectonics or basalt extrusion is not required to obtain this cooling rate at potential temperatures above $1700 - 1800^\circ\text{C}$, since conductive cooling through the lithosphere is able to sustain this cooling rate by itself. In other words, a significant contribution to the cooling of Mars by either plate tectonics or basalt extrusion is only to be expected when high cooling rates ($> 200\text{K Gy}^{-1}$) take place in a relatively cool early Mars ($T_{pot} < 1700 - 1800^\circ\text{C}$). This appears to be in contradiction with earlier work of Reese et al. (1998). Earlier work based on buoyancy considerations of oceanic lithosphere already showed that plate tectonics is only possible on Mars when it has a low potential temperature below $1350 - 1400^\circ\text{C}$ (Van Thienen et al., 2003c, chapter 4). Our new results add evidence to the unlikelyness of plate tectonics on Mars during its history. Our models, however, do not take into account that in the reduced gravity of Mars, partial melting would generate a thick stratification of depleted, and therefore inherently less dense, mantle peridotite (Schott et al., 2001, 2002). This effect would possibly extend the thickness of the effective lithosphere, which we assume to coincide with our thermally defined lithosphere, to greater depths. This thickening of the lithosphere would decrease the required turnover time in the plate tectonics models, and increase the required volumetric eruption rate the extrusion models. Another effect that is not included in the calculations is that the use of a temperature and pressure dependent thermal conductivity rather than a constant value may significantly reduce the efficiency of conductive cooling through the lithosphere (Van den Berg and Yuen, 2002). There is plenty of evidence for an active volcanic history of Mars, the most important of which is the Tharsis region with its immense volcanoes. It is magmatic/volcanic of origin, and measures about $3 \cdot 10^8\text{km}^3$ of material (Zuber, 2001). Most volcanic and magmatic activity took place during the Noachian and Hesperian (Dohm and Tanaka, 1999), spanning a period from 4.57 Ga to an estimated 2.9 Ga (Hartmann and Neukum, 2001). The minimum volumetric eruption rate is obtained from the ratio of the volume and maximum formation time, which is less than $0.2\text{km}^3\text{yr}^{-1}$. Since the system was possibly active for a shorter time, average eruption rates may have been higher, but the values probably remain low compared to for example the present day eruption rate at mid-ocean ridges of about $70\text{km}^3\text{yr}^{-1}$ (see above). Therefore, the magmatic activity involved in the formation of the Tharsis region probably did not have a strong effect on the cooling of Mars.

For Venus, the story is entirely different. The results for present Venus for both mechanisms (Figures 5.10c and 5.14c) show for the present estimated potential temperature

of about $1300 - 1500^{\circ}\text{C}$ (Nimmo and McKenzie, 1998) that some activity is required from either plate tectonics or basalt extrusion even if *no cooling at all* takes place. This is consistent with earlier results of Reese et al. (1998). The apparent lack of volcanic and plate tectonic activity on the present Venus therefore indicates the position of the planet in the diagrams is below the horizontal axis, or that the planet is heating up. This has also been suggested by Nimmo (2002).

Space observation of Venus indicates that the planet underwent global resurfacing between 300 and 600 million years before present (Schaber et al., 1992). During this episode of increased activity of crustal formation, Venus can be expected to have been cooling. Such a successive cooling and heating of Venus may be cyclical. Turcotte (1993, 1995) suggested that Venus has a history of periodic plate tectonics. From our results, plate tectonics and flood volcanism appear equally valid mechanisms of crustal production and heat loss in the cooling part of these hypothetical cycles.

5.5 Conclusions

Our model results show that for a steadily (exponentially) cooling Earth, plate tectonics is capable of removing all the required heat at a plate tectonic rate comparable to or even lower than the current rate of operation. This is contrary to the notion that faster spreading would be required in a hotter Earth to be able to remove the extra heat (e.g. Bickle, 1978). However, whether or not plate tectonics could work under these conditions is another question, which is addressed elsewhere (Sleep and Windley, 1982; Vlaar, 1985; Vlaar and Van den Berg, 1991; Van Thienen et al., 2003c, chapter 4). In the early Earth, the extrusion mechanism was probably more important, as indicated by ubiquitous flood basalts in the Archean (Arndt, 1999). For this mechanism to be able to contribute a significant part to the cooling of the Earth at rates comparable to the present rate of cooling, eruption rates up to one to two orders of magnitude higher than for Phanerozoic flood basalts are required. However, this is consistent with the increase in both frequency and magnitude of flood volcanism towards the Archean (Abbott and Isley, 2002). Mars seems to be capable of cooling conductively through its lithosphere without either plate tectonics or flood volcanism at significant cooling rates, due to its small size and, as a consequence, large surface to volume ratio. Only in hypothetical episodes of rapid cooling ($> 200\text{K}\text{Gyr}^{-1}$) during the early history of Mars, some additional mechanism may have been active, which can be either plate tectonics or flood volcanism. We confirm the inference of Nimmo (2002) that the mantle of Venus is heating up. This suggests a cyclicity of heating and cooling, as suggested earlier by Turcotte (1993, 1995). Throughout its history, this planet has required a mechanism additional to conduction for the cooling of its interior (assuming that the presently elevated surface temperature is representative of the planetary history), operating at rates comparable to those of the Earth.

Chapter 6

Production and recycling of oceanic crust in the early Earth

Abstract

Because of the strongly different conditions in the mantle of the early Earth regarding temperature and viscosity, present-day geodynamics cannot simply be extrapolated back to the early history of the Earth. We use numerical thermochemical convection models including partial melting and a simple mechanism for melt segregation and oceanic crust production to investigate an alternative suite of dynamics which may have been in operation in the early Earth. Our modelling results show three processes that may have played an important role in the production and recycling of oceanic crust: (1) Small scale ($x \cdot 100km$) convection involving the lower crust and shallow upper mantle. Partial melting and thus crustal production takes place in the upwelling limb and delamination of the eclogitic lower crust in the downwelling limb. (2) Large scale resurfacing events in which (nearly) the complete crust sinks into the (eventually lower) mantle, thereby forming a stable reservoir enriched in incompatible elements in the deep mantle. New crust is simultaneously formed at the surface from segregating melt. (3) Intrusion of lower mantle diapirs with a high excess temperature (about 250 K) into the upper mantle, causing massive melting and crustal growth. This allows for plumes in the Archean upper mantle with a much higher excess temperature than previously expected from theoretical considerations.

6.1 Introduction

As no oceanic crust on Earth is older than about 200 million years, we have no direct evidence on the nature of oceanic crust in the early Earth. Obducted oceanic sequences in

This chapter has been submitted by P. van Thienen, A.P. van den Berg and N.J. Vlaar for publication in *Tectonophysics*.

the form of ophiolites, in a strict definition, go back to about 800-900 million years before present, or back to about 2000 Ma when a broader definition is applied (Helmstaedt and Scott, 1992). The Archean, however, lacks ophiolites (Hamilton, 1998). A recent find of a 2.505 Ga ophiolite sequence in North China (Kusky et al., 2001) has been disputed by others (Zhai et al., 2002).

From theoretical considerations, several characteristics can be inferred about oceanic lithosphere in the early Earth. As a consequence of the higher mantle temperature, partial melting in shallow convective upwellings produced a layering of basaltic crust and underlying depleted (lherzolitic-harzburgitic) mantle peridotite much thicker than expected under modern day mid-oceanic ridges. As the extent of the continents is thought to have progressively grown through the Earth's history (McCulloch and Bennett, 1994), the extent of the complementary part that is the oceanic domain must have been larger than it is today. The more extensive differentiation of mantle peridotite generates more positive chemical buoyancy which takes a much longer time to be balanced by negative buoyancy due to cooling, and which would therefore be much more difficult to subduct on reasonable time scales (Sleep and Windley, 1982; Vlaar, 1985, 1986; Vlaar and Van den Berg, 1991). The dynamics of an oceanic lithosphere in the early Earth must therefore have been different from those in the present-day Earth. Crustal recycling must however have taken place because of the present relative paucity of Archean crustal material. Furthermore, isotopic evidence indicates crustal recycling during the Archean (Nielsen et al., 2002).

An alternative mechanism of recycling of oceanic crust into the mantle was proposed by Vlaar et al. (1994). When a basaltic crustal layer becomes sufficiently thick, a phase transition to eclogite may occur in the deeper parts (e.g. Hacker, 1996). In the presence of a sufficiently weak rheology, delamination of this dense crustal layer may take place and thus recycling of dense eclogite into the upper mantle. The space vacated by the delaminating eclogite can be filled up by inflowing mantle material, which may be fertile and undergo decompression melting, thus adding new material to the crust. This recycling mechanism may have contributed significantly to the early cooling of the Earth during the Archean (Vlaar et al., 1994). However, as the fertile mantle material replacing delaminated eclogite only undergoes partial melting, it produces a smaller volume of crust compared to the crust involved in the delamination. Therefore, the mechanism cannot be self-sustaining, since there is no complete recovery of the crust. An additional source of crustal material in the form of an active upwelling of fertile mantle rock (for example in mantle diapirs) is required to keep this process going. Related models concerning the delamination of eclogite have been presented by Parmentier and Hess (1992) in a general and abstract sense for terrestrial planets and by Zegers and Van Keken (2001) for the more specific subject of generation of continental material.

Geochemistry may give insight into the chemical state of the early Earth. Differentiation may be expected both in a solidifying magma ocean and during partial melting of an already solidified mantle.

The chemistry of the earliest material found on the present-day Earth's surface, 4.0-4.4 Ga detrital zircons (Wilde et al., 2001; Peck et al., 2001), indicates growth in a granitic magma, which means that production of continental crustal material and thus differentiation was already taking place.

The earliest continental rocks found on Earth (less than 4 Ga) show evidence in the form of isotope ratios ($^{143}\text{Nd}/^{144}\text{Nd}$, $^{176}\text{Hf}/^{177}\text{Hf}$) that these rocks have been derived from a mantle source that was already depleted in incompatible elements (Hamilton et al., 1983; Patchett, 1983; Vervoort et al., 1996; Blichert-Toft et al., 1999). Amelin et al. (2000) give a minimum age estimate of the derivation of the depleted mantle from a uniform chondritic reservoir of 4.08 Ga, based on $^{176}\text{Lu}/^{177}\text{Hf}$ data. They also note an increasing trend with decreasing age in the degree of depletion of the mantle from which the crustal rocks they have investigated are indirectly derived (higher ϵ_{Hf} for the 3.45 Ga Barberton and Pilbara rocks than for the 3.68-3.73 Ga Amitsoq gneisses).

Differentiation of the proto-mantle in a partially molten regime may be expected, but the result is only a change in the relative proportions of compatible and incompatible elements, retaining more or less chondritic relative abundances for the major elements (Abe, 1993b). Computations by Abe (1997) show that differentiation in a terrestrial magma ocean spanning at least the upper mantle probably took place and may be related to the Nd and Hf isotopic evidence for early mantle depletion.

On the basis of calculations of fractionation upon solidification of a terrestrial magma ocean of lithophile element ratios (Al/Ti, Ca/Ti, Ca/Al, Mg/Si, Si/Al) and comparison to primitive mantle ratios, McFarlane et al. (1994) conclude that "there is no surviving evidence of mineral fractionation" (p. 5161), which in their opinion means that: (1) no significant magma ocean was ever present in the Earth, (2) vigorous convection suppressed segregation of minerals from the magma or (3) that mantle convection wiped out the evidence for fractionation afterwards. Presnall et al. (1998), however, consider this to be too poorly constrained by element partitioning data.

These combined results from geochemistry suggest that chemical differentiation in the early mantle was an important process, as seen from isotope ratios, but that large scale inhomogeneities may have been rapidly remixed, as suggested by lithophile element ratios. This makes it difficult to come up with a viable starting scenario for numerical models of the mantle in the early Earth.

Numerical mantle convection models starting from a pristine mantle show the development of chemical heterogeneity in the mantle. Depending on the rate of internal heating due to the decay of radioactive isotopes, stratification of depleted and undepleted mantle material or mixing of these may occur on whole mantle scale (Ogawa, 1988; Kameyama et al., 1996; Ogawa, 2000). Walzer and Hendel (1997) modeled a simplified chemical segregation in the mantle, generating continents. In a more complex setup, they modeled the development of distinct pristine lower mantle and depleted upper and uppermost lower mantle reservoirs (Walzer and Hendel, 1999). The development of chemical stratification in the upper mantle underneath continents was demonstrated in thermochemical convection models (De Smet et al., 1998; De Smet, 1999; De Smet et al., 2000a). In these models, a continental root of depleted peridotite of about 200 kilometers develops, underneath which the remaining part of the upper mantle remains relatively fertile. Similar models by Schott et al. (2001) applied to Mars produce a thick (500 km) buoyant layer of melt residue, inhibiting recycling of crustal material.

Here we present results of numerical modelling experiments of mantle convection including pressure release partial melting. The model includes a simple approximate melt

segregation mechanism and basalt to eclogite phase transition, to account for the dynamic accumulation and recycling of the crust in an upper mantle subject to secular cooling. The focus of our investigations is on the dynamics of the production of oceanic crust and its recycling through the eclogite phase into the mantle. We investigate the conditions that favor such a mechanism, and discuss its consequences for the cooling history of the Earth. We also investigate the development and sustainability of the chemical differentiation that is caused by the process, both concerning the major elements and incompatible trace elements.

6.2 Numerical model setup

6.2.1 Description of the numerical model

We have used a 2-D Cartesian thermo-chemical convection code including partial melting. An extended Boussinesq approach was used, assuming infinite Prandtl number, including viscous dissipation, adiabatic compression, and latent heat of melting. Partial melting is modeled as an (irreversible) increase in the *degree of depletion* F , which has been defined here as the mass fraction of melt that is extracted from an initially unmelted material control volume of mantle material. The melt that is produced is extracted instantaneously and deposited at the top boundary. Here the melt flux is transformed into an inflow boundary condition, thus producing a basaltic crust. In the current approximation, the compaction of the residual mantle due to this melt removal is neglected. Time dependent internal heating due to the decay of radioactive elements was included and coupled to the concentration of a single incompatible element, which has an initial concentration of 1 and fractionates upon partial melting with a distribution coefficient of 0.01 (see section 6.2.3). Undepleted mantle material is characterized by a time dependent heat productivity with an initial value of $15 \cdot 10^{-12} \text{W kg}^{-1}$ and a half life value of radioactive decay of 2.5 Ga. For the compositionally evolving mantle material this time dependent value is multiplied with the local trace element concentration. The extraction of heat producing elements during partial melting results in a concentration of the heat productivity in the basalt produced by the partial melting.

The model is described by the following non-dimensional equations (De Smet et al., 1998). The energy equation (see Table 6.1 for explanation of the symbols used):

$$\begin{aligned} \frac{dT}{dt} - Di(T + T_0)w = \nabla^2 T - \frac{\Delta S}{c_p} \frac{dF}{dt} (T + T_0) + \sum_k \gamma_k \frac{Rc_k}{Ra} Di(T + T_0) \frac{d\Gamma_k}{dt} \\ + \frac{Di}{Ra} \Phi + R_H H \end{aligned} \quad (6.1)$$

The heating due to viscous dissipation is set to zero in the calculations to avoid extreme heating rates in the upper crust, where laterally varying amounts of crustal material is forced into the system at considerable rates, see below. We have verified that this has a minor effect on the resulting dynamics and thermal development of the subcrustal domain.

symbol	property	definition	value/unit
B_1	diffusion creep prefactor		Pas
B_2	dislocation creep prefactor		$\text{Pa}^{\text{m}^2}\text{s}$
C_0	cohesion factor		0 Pa
c_p	heat capacity at constant pressure		$1250 \text{ Jkg}^{-1}\text{K}^{-1}$
E_1	diffusion creep activation energy		$270 \cdot 10^3 \text{ Jmol}^{-1}$
E_2	dislocation creep activation energy		$485 \cdot 10^3 \text{ Jmol}^{-1}$
e_{ij}	strainrate tensor	$\partial_j u_i + \partial_i u_j$	s^{-1}
e	second invariant of the strainrate tensor	$[\frac{1}{2}e_{ij}e_{ij}]^{\frac{1}{2}}$	s^{-1}
$f(F)$	composition dependent viscosity prefactor		
F	degree of depletion		
g	gravitational acceleration		9.8 ms^{-2}
h	length scale		$1005 \cdot 10^3 \text{ m}$
H	radiogenic heat production		Wm^{-3}
n_1	diffusion creep stress exponent		1
n_2	dislocation creep stress exponent		3.25
n_y	yield exponent		10
P	pressure		Pa
R	Gas constant		$8.341 \text{ Jmol}^{-1}\text{K}^{-1}$
Ra	thermal Rayleigh number	$\frac{\rho_0 \alpha \Delta T g h^3}{\kappa \eta_0}$	
Rb	compositional Rayleigh number	$\frac{\delta \rho g h^3}{\kappa \eta_0}$	
Rc	phase Rayleigh number	$\frac{\delta \rho g h^3}{\kappa \eta_0}$	
S	melt productivity function		s^{-1}
ΔS	entropy change upon full differentiation		$300 \text{ Jkg}^{-1}\text{K}^{-1}$
t	time		s
T	temperature		$^{\circ}\text{C}$
T_0	non-dimensional surface temperature		$\frac{273}{\Delta T}$
ΔT	temperature scale		$2450 \text{ }^{\circ}\text{C}$
V_1	diffusion creep activation volume		$6 \cdot 10^{-6} \text{ m}^3 \text{ mol}^{-1}$
V_2	dislocation creep activation volume		$17.5 \cdot 10^{-6} \text{ m}^3 \text{ mol}^{-1}$
w	vertical velocity		ms^{-1}
z	depth		m
\hat{z}	unit vector in vertical (downward) direction		
$z_0(T)$	temperature dependent depth of phase transition		m
α	thermal expansion coefficient		$3 \cdot 10^{-5} \text{ K}^{-1}$
Γ	phase function	$\frac{1}{2} \left(1 + \sin \left(\pi \frac{z - z_0(T)}{\delta z} \right) \right)$	
$\delta \rho$	density difference (chemical or phase)		kgm^{-3}
$\dot{\epsilon}$	strainrate		s^{-1}
$\dot{\epsilon}_y$	yield strainrate		10^{-15} s^{-1}
η	viscosity		Pas
η_y	yield viscosity		Pas
κ	thermal diffusivity		$10^{-6} \text{ m}^2 \text{ s}^{-1}$
μ	friction coefficient		0.03
ρ_0	reference density		3416 kgm^{-3}
σ_n	normal stress		Pa
τ_y	yield stress		Pa

Table 6.1: Symbols of the energy and momentum equations (equations (6.1), (6.2), (6.3)) and the depletion evolution equation (6.4).

We use the Stokes equation in combination with a continuity equation for an infinite Prandtl number incompressible fluid:

$$\nabla[\eta(\nabla\vec{u} + \nabla\vec{u}^T)] - \nabla\Delta p = (RaT + RbF - \sum_k Rc_k\Gamma_k)\hat{z} \quad (6.2)$$

$$\nabla \cdot \vec{u} = 0 \quad (6.3)$$

Evolution of the degree of depletion is described by the following equation:

$$\frac{dF}{dt} = S(p, T, F) \quad (6.4)$$

The source function S in (6.4) describes the distribution of partial melting, applying a simple parameterization of the melting phase diagram of mantle peridotite (De Smet et al., 1998). We use a third order polynomial parameterizations of the solidus and the liquidus, based on Herzberg and Zhang (1996), down to a depth of 400 km, assuming that melt produced below this depth is not segregated. Our isobaric melting curve, which is based on data presented by Jaques and Green (1980), is linear (see De Smet et al., 1998).

The set of equations (6.1)-(6.4) was solved using finite element methods and a Predictor-Corrector time integration scheme, described in Van den Berg et al. (1993). The different finite element meshes used contain approximately 2200 and approximately 5100 triangular elements respectively (see Table 6.2), with a nodal point spacing of approximately 10-15 km. Tests have shown this to be sufficient to resolve the dynamics, since at lower resolution some characteristics of the dynamics are lost whereas a higher resolution results in the same behavior. The field description of the degree of depletion field F was transported using a Lagrangian particle tracer method (300 000 to 400 000 tracers). Fourth order Runge-Kutta time integration is used to advect the particle tracers with the mantle flow velocity. The transformation of particle tracer field values (the degree of depletion) to finite element Gauss points uses a Particle in Cell algorithm (Hockney and Eastwood, 1988).

The density of mantle material is related to the degree of depletion F (Jordan, 1979; Vlaar and Van den Berg, 1991). Also, basalt has its own density and is transformed into heavier eclogite upon reaching depths in excess of 30 km in our model. The kinetics of this transition are approximated assuming a constant relaxation time for the transition of 1.25 Myr. The depth of 30 km (0.9 GPa) we use is somewhat less than the depth of about 40 km (1.2 GPa) that Hacker (1996) states as the minimum pressure of basalt to eclogite transformation. However, as we are dealing with melt products in a mantle that is hotter than the present, their composition is more MgO-rich than present day mid ocean ridge basalt (Nisbet, 1982). Experiments of Green and Ringwood (1967) have shown that the transition may occur at lower pressures and higher temperatures in MgO-rich rocks. Furthermore, lower pressure phase assemblages (above 0.7-0.8 GPa) may also contain garnet (Green and Ringwood, 1967; Ito and Kennedy, 1971; Hacker, 1996), thus raising the bulk density above that of the original basaltic phase assemblage. We do not consider phase boundary topography due to temperature effects, since we expect this to

model	initial conditions		domain		
	$T_{\text{pot}}^{\text{start}}$ (C)	$d_{\text{crust}}^{\text{start}}$ (km)	# elements	# boundary points	width & depth (km)
M0	1464	0.0	2245	67	1005
M0b	1464	0.0	2245	67	1200
M1	1896	20.1	2245	67	1005
M2	1948	25.6	2245	67	1005
M3	1976	30.0	2245	67	1005
M4	2000	35.4	2245	67	1005
M5	2017	39.8	2245	67	1005
M6	2051	50.5	2245	67	1005
Mr	1976	30.0	5101	100	1005
Ms	1976	29.7	5101	100	1200

Table 6.2: Characteristics of the different model experiments. Models M0 and M0b are startup runs with increased radiogenic heating (see text). $T_{\text{pot}}^{\text{start}}$ is the potential temperature and $d_{\text{crust}}^{\text{start}}$ is the average crustal thickness, both at the start of the experiment. The number of boundary points indicates the number of model points of the triangular elements used in the discretization of the domain on a single domain boundary and is included as a measure of 1-D resolution.

be dominated by kinetic effects because of the relatively low Clapeyron slope of about 1 MPa/K (Philpotts, 1990).

The phase transitions around 400 and 670 km depth are also taken into account separately for peridotite and eclogite, though without kinetics (i.e., it is assumed to occur instantaneous). The relevant parameters for these phase transitions are given in Table 6.3. The phase transition of eclogite into perovskitite lithology in the shallow lower mantle (e.g. Ringwood and Irifune, 1988; Irifune and Ringwood, 1993; Hirose et al., 1999) is not taken into account. Dynamic effects have been predicted of the density inversion between eclogite and postspinel peridotite in the uppermost lower mantle (Irifune and Ringwood, 1993) caused by the deeper position of the transition of eclogite relative to the postspinel transition of peridotite. As recent work has indicated that the transition takes place around 720 km depth (Hirose et al., 1999) rather than around 800 km (e.g. Irifune and Ringwood, 1993), and has a positive Clapeyron slope that would lift the phase transition to even shallower levels in a cool sinking eclogite body, Hirose et al. (1999) predict that 'basaltic crust with perovskitite lithology would gravitationally sink into the deeper mantle' (their p.53). Earlier numerical experiments of Christensen (1988) show that an eclogite layer trapped in this density inversion zone in the uppermost lower mantle would probably not survive in a convecting mantle. Recent experiments by Kubo et al. (2002), however, indicate that slow kinetics of the lower mantle phase transition of basaltic material may delay the transition on the order of 10 million years, which may increase the residence time and depth extent of the shallow lower mantle density inversion zone. We have validated our assumption of the minor importance of the shallow lower mantle eclogite density inversion by performing an experiment in which it is included (eclogite 430kgm^{-3} lighter

transition	material	P_0 (GPa)	T_0 (K)	γ (Pa/K)	δz (km)	$\frac{\delta\rho}{\rho_0}$
400	peridotite	13.4	1756	$3 \cdot 10^6$	50	0.05
400	basalt	12.5	1747	$3 \cdot 10^6$	150	0.10
670	peridotite	22.4	1854	$-2.5 \cdot 10^6$	50	0.05

Table 6.3: Parameters of the phase transitions used in the models. The first column indicates the approximate depth of the transition, the column marked δz indicates the depth range over which the transition is smeared out and the last column gives the relative density contrast of the phase transition.

than peridotite between 670 and 720 km depth), which showed no significant stagnation of basaltic material in this density inversion zone. The density effects of the varying composition and phase transitions are accounted for in buoyancy contribution terms, scaled by the Rayleigh numbers Rb and Rc_k , in the momentum equation (6.2) (see also De Smet et al., 1998, 2000a).

6.2.2 Rheology

The deformation of material is accounted for by three separate deformation mechanisms, which are diffusion creep, dislocation creep, and brittle failure. The former two are described by the following equation:

$$\eta_i = f(F)B_i \exp\left[\frac{E_i + PV_i}{RT}\right] \sigma^{1-n_i} \quad (6.5)$$

which is the standard Arrhenius formulation (Karato and Wu, 1993; Van den Berg and Yuen, 1998) with the addition of a composition dependent prefactor $f(F)$. The index i indicates the mechanism, either 1 for diffusion creep or 2 for dislocation creep. The other symbols are explained in Table 6.1. The activation energies E_i and volume V_i are based on Karato and Wu (1993), as is the prefactor, in which an assumed constant and uniform grain size of 1 mm is incorporated. The composition dependent prefactor $f(F)$ has a value of 1 for fertile peridotite and basalt (which have the same viscosity parameters in our models). For depleted peridotite (harzburgite) we apply a prefactor value of 10 for a degree of depletion over 0.05, and a linearly increasing value between $F = 0.005$ and $F = 0.05$ from 1 to 10 (Van Thienen et al., 2003a, chapter 8). This is intended to mimic the effect of dehydration during partial melting on the viscosity (Karato, 1986; Hirth and Kohlstedt, 1996; Mei and Kohlstedt, 2000a,b).

For eclogite, the viscosity prefactor $f(F)$ has a value of 0.1. Although Jin et al. (2001) find that for an eclogite with equal amounts of the two main constituents garnet and omphacite, the strength is comparable to harzburgite (which is hydrous in their experiments), Piepenbreier and Stöckhert (2001) find evidence in eclogite microstructures for a much lower flow strength than predicted from omphacite experimental flow laws. We translate this result to our latter viscosity prefactor value of 0.1.

The third deformation mechanism, brittle failure, is approximated by a yield mechanism which is included to reproduce fracturing-like behavior when the stress supersedes a certain yield stress τ_y . We use the formulation of Van Hunen et al. (2002):

$$\eta_y = \tau_y \dot{\epsilon}_y^{-1/n_y} \dot{\epsilon}^{(1/n_y)-1} \quad (6.6)$$

The symbols are explained in Table 6.1. We prescribe the yield stress τ_y , the yield strain rate $\dot{\epsilon}_y$ and the yield exponent n_y . The latter describes the brittleness of the behavior (Van Hunen et al., 2002). We apply a value of 10, which gives a reasonable approximation of pure brittle behavior. The yield strength τ_y is determined as a function of depth using Byerlee's law (e.g. Lockner, 1995):

$$\tau_y = C_0 + \mu \sigma_n \quad (6.7)$$

in which we approximate the normal stress with the lithostatic pressure (e.g. Moresi and Solomatov, 1998):

$$\tau_y = C_0 + \mu \rho g z \quad (6.8)$$

We use a low value of 0.03 for the friction coefficient μ , consistent with results of Moresi and Solomatov (1998) for the mobilization of the Earth's lithosphere, and assume the cohesion term C_0 to be of minor importance and set it to 0.

The diffusion and dislocation creep viscosities are inversely added to define an effective ductile creep viscosity (Van den Berg et al., 1993) and the minimum of this value and the local yield viscosity is used for the local effective viscosity.

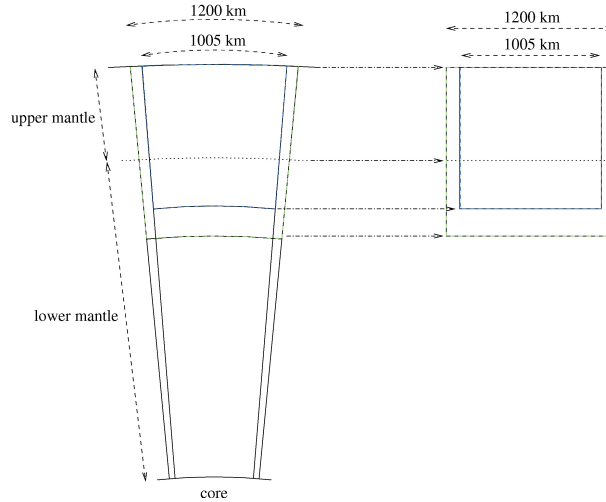


Figure 6.1: Setup of the 2-D square model domain measuring 1005 x 1005 km and 1200 x 1200 km in respective models listed in Table 6.2, representing the upper mantle and part of the lower mantle.

6.2.3 Fractionation of trace elements

The behavior of a single incompatible trace element is monitored in the models using the particle tracers. Upon partial melting, the concentration of the trace element is adjusted in each tracer using an equilibrium melting formulation (see e.g. Philpotts, 1990) for each integration time step (which essentially means that we assume equilibration between the melt and the residue during an integration time step, and consider a new batch of melt in the following time step). As mentioned above, the internal heating rate is a function of trace element concentration in the models. The result is that an enriched crust (generally by a factor 5-20) and a depleted residual mantle are formed.

The most important heat producing species in the Archean mantle are U and Th. These have bulk partition coefficients of $1.1 \cdot 10^{-4}$ and $1.7 \cdot 10^{-4}$, respectively, for spinel peridotites in equilibrium with a basaltic melt (Beattie, 1993), though temperature, composition, oxygen fugacity and the presence of volatiles may influence these values. We prescribe a distribution coefficient of 10^{-2} for the single incompatible heat producing element in our model which represents both U and Th. The value of the partition coefficient is somewhat larger than the values mentioned above for spinel peridotites. It is however small enough to allow significant fractionation and thus redistribution of heat productivity, but not so small that different degrees of melting result in the same residue concentrations of virtually zero. This allows us to regard the development of our trace element in a more general sense rather than limited to U and Th.

6.2.4 Model geometry and boundary conditions

For most models, we use a square computational domain of 1005 by 1005 km (see Figure 6.1), resulting in an upper mantle aspect ratio of 1.5. One extended model has dimensions of 1200x1200 km, resulting in an upper mantle aspect ratio of 1.8 (see section 6.3.4). We use a prescribed velocity on the upper boundary (controlled by basalt generation), periodical side boundaries and free slip conditions on the lower boundary. On the upper boundary we prescribe a temperature of $0^\circ C$. Although we are dealing with the early Earth, the presence of liquid water on the surface, as indicated by oxygen isotope ratios in zircons of up to 4.4 Gyr old (Wilde et al., 2001; Peck et al., 2001), validates this assumption. On the lower boundary we prescribe a zero heat flux boundary condition to approximate conditions of transient secular cooling of the model by excluding heat input from below.

6.3 Results

As the initial condition for the models (i.e. the state of the Earth after solidification of the magma ocean) is difficult to reconstruct, we start from a model configuration including an initial basaltic crust and underlying depleted zone. We first test the sensitivity of the long-term development of the models to the initial situation (temperature and initial thickness of crust and depleted zone). The results will be presented in section 6.3.1. After this,

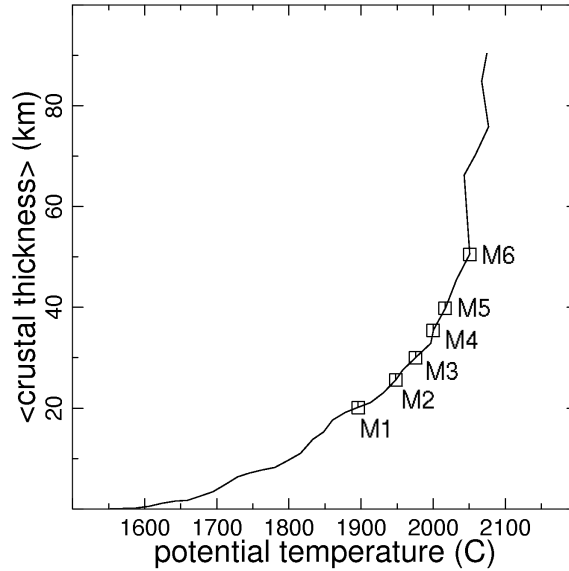


Figure 6.2: Development of the potential temperature and average crustal thickness of the initial model M0. Time progresses from the lower left to the upper right part of the curve. Symbols indicate the snapshots that are used as starting points for different cooling models (see Table 6.2).

the dynamics of crustal growth and recycling will be shown from the results of the model calculations (section 6.3.2). Next, we will present the long-term development of a number of models in section 6.3.3, and finally, the effect of the size of the model lower mantle is considered in section 6.3.4.

6.3.1 Sensitivity to initial conditions

We generate initial situations including a basaltic crust by starting model M0 (and M0b for a model with a larger domain width, see Table 6.2) with a uniform fertile composition, a geotherm that is below the solidus in the entire domain and a strongly increased internal heating of $250 \cdot 10^{-12}$ W/kg. The model rapidly heats up and starts melting, thus producing a crust. Different snapshots from the development of model M0 are used as starting points for a number of cooling and recycling models (M1-M6 in Table 6.2). Figure 6.2 shows the development of the potential temperature and accumulated crustal thickness for the startup model M0. The symbols in Figure 6.2 indicate the snapshots from which the cooling and recycling models are started. These are listed, together with their characteristics, in Table 6.2. In the cooling and recycling models M1-M6, the clock is initially reset to $t=0$, the internal heating is reset to $15 \cdot 10^{-12}$ W/kg (fertile mantle material value

representative of the early Earth), and natural decay with a half life of 2.5 Gyr is included.

In the two models with the thickest crust and highest initial temperature (M5 and M6, see Table 6.2), the entire crust sinks into the mantle within the first few million years of the model evolution. This is a result of the fact that a large part of the crust is transformed into the dense eclogite phase. The upwelling hot mantle material that replaces it locally completely melts, bringing the system back into a magma ocean regime. As our model assumptions are only valid for modest degrees of melting, we do not continue the calculations at complete melting, which is observed here. The results do show that a very thick basaltic crust of 40 km or more thickness is not sustainable on top of a hot, weak mantle in the early Earth.

The four somewhat cooler models M1-M4 (see Table 6.2) show higher rates of activity (vigor of convection and melt productivity) for higher initial temperature and greater crustal thickness. As a result of the higher crustal production rate, a higher cooling rate is observed for the hotter models, so that their volume averaged temperatures and surface heat fluxes converge after some hundreds of millions of years.

6.3.2 Dynamics of crustal growth and recycling

Three distinctive types of dynamics can be discerned in the process of crustal growth and recycling. The first is a small scale circulation near the bottom of the crust that transports eclogite down into the mantle and which produces new crust by partial melting of the upwelling part of the circulation. Figure 6.3 shows the development of such a coupled system in a zoom-in of model Mr. The left-hand frames show the composition field (individual particle tracers are plotted for basalt (black) and eclogite (red)), and the right-hand frames the temperature field (colors) and circular to oblong melt production zones (blue contours). In Figure 6.3a, no eclogite delamination is taking place but partial melting occurs in the upwelling flow near the right hand side thickened crustal region as indicated by the melting contours in the temperature frame. The melt that is produced is instantaneously transported vertically to the surface where it adds new material to the locally thickened crust. In the next frame (Figure 6.3b), eclogite starts to move downwards. At the same time, we see a similar but mirrored circulation arising below the left hand side thickened crustal region. About 4 million years later (Figure 6.3c), active delamination can be observed in both circulation systems, with high velocities in the common downwelling limb of the shallow circulations. Partial melting continues in the upwelling parts as indicated by the blue contours in the corresponding temperature snapshot. The recycling of eclogite into the mantle continues for tens of millions of years (see Figure 6.3d, 29 million years later).

Larger scale upwellings may add significantly more material to the crust. Figure 6.4 illustrates the development of a diapir originating from a lower mantle upwelling. As in Figure 6.3, the left-hand frames show the composition field and the right-hand frames the temperature field and the melting zone, which is quite large in this case. Because of its lower mantle origin, the material is both hot and fertile, indicated by the deep blue color, and starts melting at 400 km depth (which is the imposed maximum depth of melting in the model) in Figure 6.4a. Melting continues up to about 150 km depth, where the

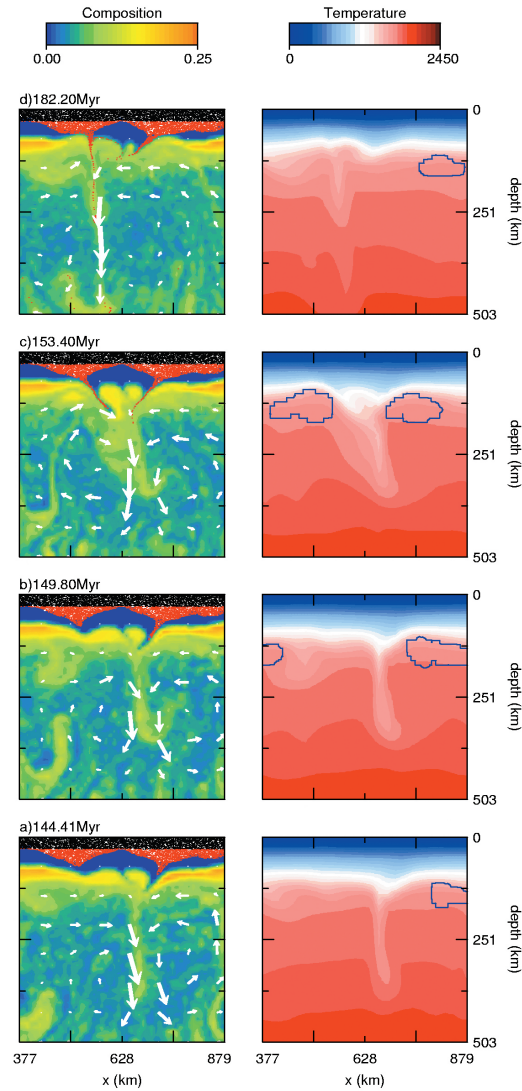


Figure 6.3: Four snapshots of composition and temperature from model Mr show how small scale circulations near the base of the crust allow recycling of eclogite into the mantle and production of new crust by partial melting of upwelling mantle peridotite. In the left hand side panels, the color scale from blue to orange indicates the degree of depletion F . Black and red tracers represent basalt and eclogite, respectively. The right hand side panels show the temperature field (color scale in degrees Celsius) and areas where partial melting is taking place (inside the contours).

diapiric ascent is stopped by the rapid increase of the temperature dependent viscosity (Figure 6.4b, note that the identical times of snapshots a and b indicate extremely fast upwelling in less than 10 kyr). The diapir head spreads out and the left-hand side rises further (Figure 6.4c) and melts up to a degree of nearly 0.30. The original diapir spreads out over nearly the entire domain of 1005 km. The large volume of melt produced locally thickens the crust by over 40 km (Figure 6.4d). The timescale on which this event takes place is extremely short. Although inflow of lower mantle material and partial melting continue for some millions of years, the rise of the diapir head through the upper mantle takes place in less than 20 kyr. This is the effect of the non-linear component of the rheology, as has been shown in the literature (Weinberg and Podladchikov, 1994; Larsen et al., 1997; Larsen and Yuen, 1997; Van Keken, 1997; Van Thienen et al., 2003a, chapter 8).

At least as catastrophic is the third type of dynamics, which is characterized by large scale delamination of a thickened crust into the mantle. Figure 6.5 shows the entire domain, starting just after the diapir event shown in Figure 6.4. The deeper part of the crust that is significantly thickened turns into eclogite in about 2 million years (Figure 6.5a) and sinks into the mantle. The right-hand side frame of Figure 6.5a shows that partial melting is taking place in the zone where material is sucked into the zone of upwelling created by the sinking crustal block. As the crustal block is quite cold and strong, it pulls down with it all the existing crustal material, which is mostly in the basalt phase and positively buoyant, see Figure 6.5b. Melting continues in the upper mantle, creating a new basaltic crust (Figure 6.5c). Note that this crust is significantly thinner (about 30 km) than the crust shown in Figure 6.5b. After the downgoing crust is sufficiently thinned it breaks off and further 'subduction' is halted. The basalt that was pulled down into the mantle has completely transformed into eclogite by now and the entire 'crustal lobe' sinks into the deeper mantle (Figure 6.5d). The complete replacement of the old crust by a new crust is illustrated by Figure 6.6, showing the variations of the formation age of crustal material. The figure, corresponding to the snapshot shown in Figure 6.5d, shows the old crust (blue) as it is sinking into the mantle, and the freshly produced crust (green, yellow, orange, purple) forming the new top of the domain. Note that the old crust has pulled down a significant amount of young crust (purple). In the upper part of the lower mantle, the subducted crust slowly heats up and becomes weaker. It breaks up allowing lower mantle peridotite to break into the upper mantle, while sinking crust replaces this material in the lower mantle (Figure 6.5d). Note the very short timescale of the whole process, where the replacement of the entire shallow crust takes place in less than 2 million years. The settling of the crust into the lower mantle to the bottom of the model domain takes much longer, on the order of 300 million years as both the density contrast between the sinking crust and the mantle decrease and the viscosity increases with depth (and decreasing strain rate).

6.3.3 Long-term thermal and chemical development

The thermal evolution of model Mr is illustrated in the lower panel of Figure 6.7 by the blue curve, showing the volume averaged temperature as a function of time. Three stages

can be discerned. During the first stage, lasting about 230 Myr, small scale delamination and crustal growth (see Figure 6.3) generate significant cooling of at a rate of about 300 K/Gyr (and crustal growth, as shown in the upper panel of Figure 6.7). The second, quite short, stage is characterized by rapid crustal growth and associated cooling, caused by lower mantle diapir ascent and complete resurfacing as shown in Figures 6.4 and 6.5. A drop in the volume averaged temperature of about 200°C can be observed, and an average (over the entire domain width) of over 40 km of crust is produced. The third stage shows an absence of crustal growth, and because of this and the fact that the lower mantle temperature results in a thicker lithosphere, the cooling rate is reduced relative to the first two stages. No absolute numbers for cooling rates are given here since the small model domain (1005 km depth) does not allow comparison to the Earth, as will be discussed below (see section 6.3.4, where the larger model domain width and depth model Ms will be discussed).

The evolution of the incompatible trace element distribution of model Mr is illustrated in Figure 6.8, which shows the incompatible trace element concentration at different times during its evolution. The initial concentration of the trace element is 1, and the distribution coefficient is 10^{-2} . The ten frames in this figure show the concentration field at 10 subsequent times during the evolution of the model. Initially, the lower mantle is pristine. The upper mantle shows an increasing trace element depletion for shallower depths, where the mantle peridotite is subject to melting. This shallow partial melting also produces the enriched basaltic layer at the top boundary. After some 15 million years, slightly depleted upper mantle material is entrained into the lower mantle flow. As the recycling of eclogite into the mantle progresses, we see an increasing amount of grey colored enriched eclogite 'blobs' in the upper mantle (frames at 154.6 Myr and 228.9 Myr). The progressive cooling and the accumulation of eclogite blobs in the deepest upper mantle forces a breakdown of completely separate lower mantle and upper mantle convection (frames at 230.4-241.91 Myr), as predicted by Christensen and Yuen (1985). This brings more highly depleted material and enriched eclogite blobs into the lower mantle. Over the following 300 million years, the enriched crust sinks deeper into the lower mantle and settles at the bottom boundary. The upper and lower mantle continue to mix and form a more or less uniform reservoir of moderately depleted peridotite in which blobs of eclogite are dispersed. The high content of heat producing elements of the settled crust in the lower mantle makes it a heat source for convection in the mantle above, which may entrain some material from this layer. But essentially it remains stable for the remaining 500 million years of the model run.

The development of the bulk and incompatible trace element chemistry of this model (Mr) is presented in Figure 6.9. Time series of the averaged degree of depletion of the peridotite present are shown in Figure 6.9a for the entire domain, and for the lithosphere (0-150 km depth), the upper mantle (150-670 km depth) and the lower mantle (670-1005 km depth) separately. During the first 230 million years, we see a steady increase in the average degree of depletion of the entire domain of model Mr (Figure 6.9a). The lower mantle stays nearly pristine during this entire period. The upper mantle doubles its average degree of depletion over this period of time. However, as the interaction between the upper and lower mantle increases due to the cooling of the model and the

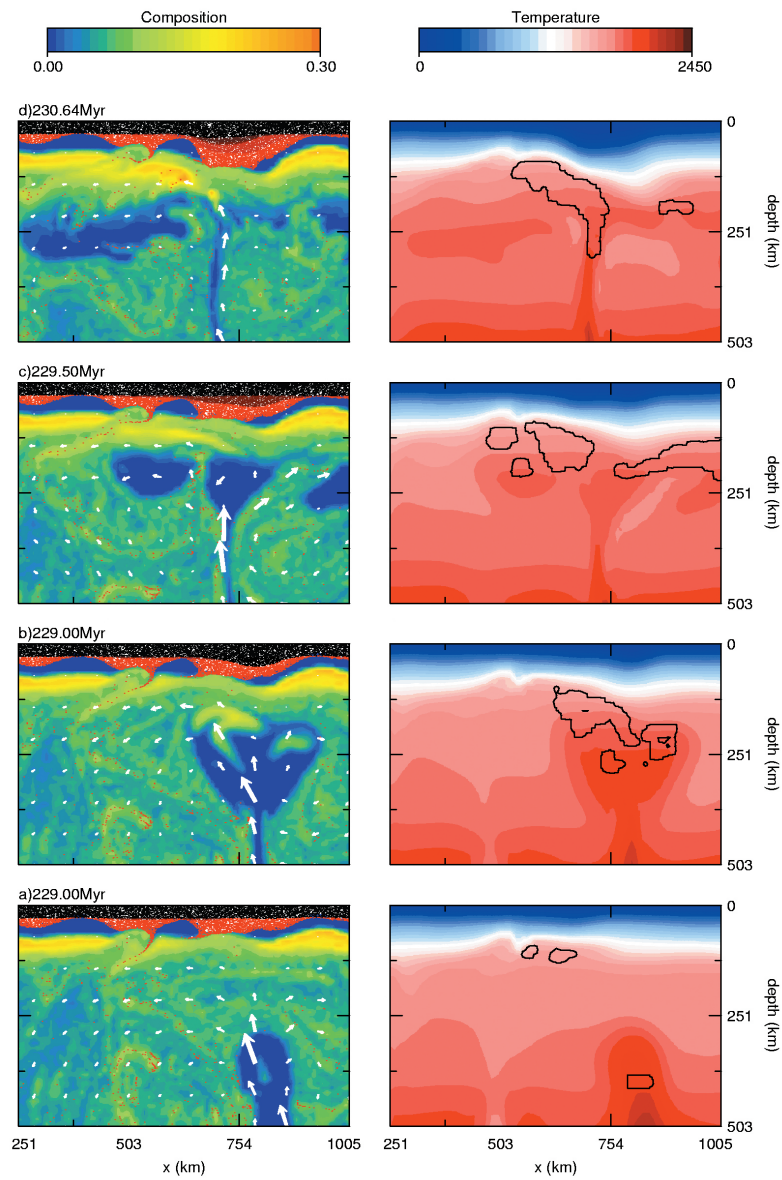


Figure 6.4: Four snapshots of composition and temperature from model Mr show the ascent and decompression melting of a mantle diapir, originating from the lower mantle. For an explanation of the colors, see the caption of Figure 6.3.

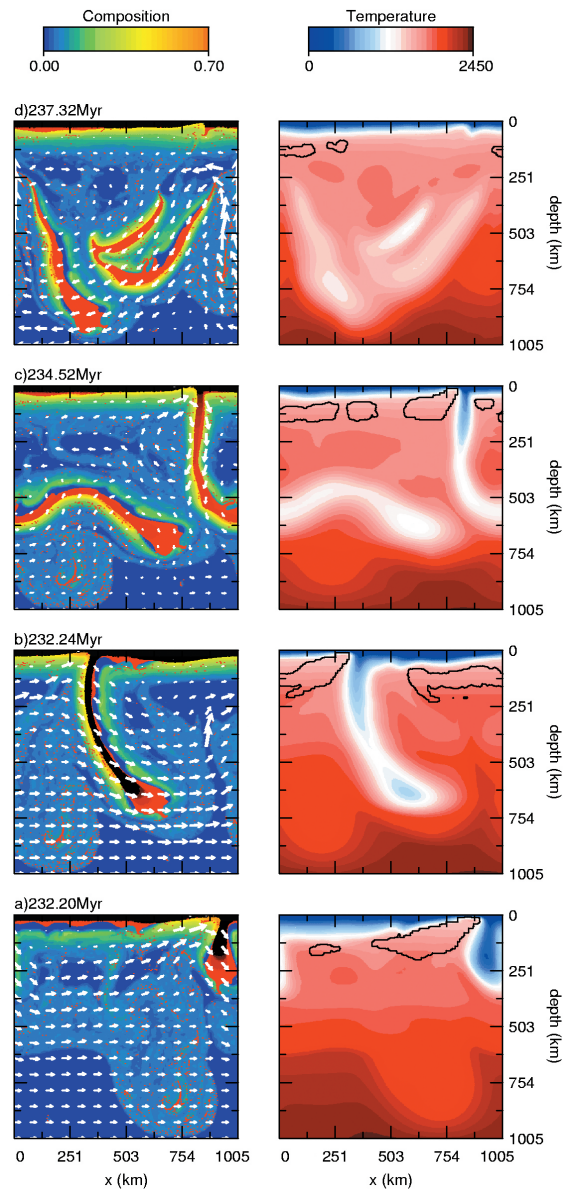


Figure 6.5: Four snapshots of composition and temperature from model Mr show the sinking of the entire crust into the mantle, driven by a large mass of dense eclogite. For an explanation of the colors, see the caption of Figure 6.3.

accumulation of eclogite blobs at the bottom of the upper mantle, some of the depleted material of the upper mantle is dumped into the lower mantle. The lithospheric degree of depletion fluctuates but shows a general decrease because more material is mixed into the upper mantle. After this initial stage, two important events (intrusion of a lower mantle diapir into the upper mantle and subsequent recycling of the thickened crust into the mantle) cause a marked increase in the averaged degree of depletion of the domain. The increase is observable in every reservoir, and practically at the same time (230 Myr). After this, the slow sinking of the crust and associated depleted mantle from the upper into the lower mantle causes an increase in the lower mantle value and a simultaneous decrease in the upper mantle value. Continued exchange of material between the upper and lower mantle reduces the difference over the following hundreds of million years, in line with the effective mixing illustrated in Figure 6.8.

Figure 6.9b shows the development of the approximate volume averaged incompatible trace element concentrations in the lithosphere, upper mantle and lower mantle. The same distinction in two separate phases can be made as in Figure 6.9a. During the first 230 million years, a steady increase in the average incompatible isotope concentration can be observed in the lithosphere. This is due to the accumulation of crust with a high concentration of the incompatible element. Complementary to this trend (but less pronounced because the reservoir is larger), we see a decrease in the average incompatible element concentration of the upper mantle, since the depleted residue that is formed upon partial melting is recycled through the upper mantle. The lower mantle shows a slight decrease in the concentration, which is due to radioactive decay. In the other curves, this is also present but invisible due to the larger effect of differentiation.

The two large scale events around 230 Myr (lower mantle diapir and large scale sinking of the crust into the mantle) have a strong impact on the average incompatible trace element distribution. As the crust forms an important reservoir for this element, its sinking into the lower mantle causes a strong decrease in the average trace element concentration in the lithospheric zone. Two causes can be named. Firstly, the new crust that is formed is much less voluminous than the old crust which has been subducted. And secondly, the new crust was formed from already depleted mantle, so it will have lower average incompatible trace element concentrations. After these events, some entrainment of eclogite tracers from the settled crust at the bottom boundary of the model into the upper mantle somewhat increases the upper mantle average concentration and decreases it in the lower mantle. The effect of radioactive decay is visible in each curve.

6.3.4 Lower mantle size

As has been noted before, the lower mantle in our models is significantly smaller than in the Earth. Including a larger lower mantle at the same resolution, however, is computationally quite expensive. The size of the lower mantle is important for a number of reasons. It is a reservoir for both heat and undepleted peridotite. The models as presented in the previous sections are therefore capable of producing less crust than the Earth and they show a more rapid cooling than expected for the Earth.

Another important aspect is the layering of mantle convection. Christensen and Yuen

(1985) showed that the layering of mantle convection is a function of the Rayleigh number (see Table 6.1 for symbol definitions):

$$Ra = \frac{\rho_0 g \alpha \Delta T h^3}{\eta_0 \kappa} \quad (6.9)$$

In general, high Rayleigh number systems tend to develop a layered convection pattern in the presence of an endothermic phase boundary, whereas low Rayleigh number systems would tend to a whole mantle convection pattern. This suggests that the breakdown of layered convection as takes place e.g. model Mr around 230 Myr (see Figures 6.4 and 6.5) would be delayed in a system with a higher Rayleigh number. In order to test the sensitivity of the results to the depth of the lower mantle part of the model, we have done experiments with an increased domain width (and depth) of 1200 km (model Ms, see Table 6.2), resulting in a lower mantle depth of 530 km. The resulting dynamics of the extended model described above are summarized in the time series of volume averaged temperature and total amount of crust produced in Figure 6.7. Curves for the base model Mr can be used for comparison. As is illustrated by both strong drops in temperature and strong increases in the amount of crust produced, model Ms has a similar resurfacing event as described in section 6.3.2 and shown in Figure 6.5 for model Mr. The model shows a higher melt productivity than the smaller model Mr at a comparable cooling rate. This is a direct result of the reduced surface to volume ratio. Furthermore, the higher volume of fertile peridotite that can act as a source rock for basaltic material allows more crust to be produced. The extended model Ms also shows continued melting (although at a low rate) after the resurfacing event, in contrast to the behavior of model Mr, which shows no more melting after resurfacing.

Although because of the higher Rayleigh number of model Ms, it would be expected that layered convection is maintained for a longer period of time in this models than in model Mr (only 1005 km depth), the extended model shows a somewhat higher crustal production rate and generates a thick unstable crust on a shorter time scale, which causes resurfacing on a shorter time scale as well. Clearly the fact that we are dealing with thermo-chemical convection rather than merely thermal convection frustrates predictions based on the results of Christensen and Yuen (1985) and Steinbach and Yuen (1993) who find stronger layered convection for higher Rayleigh numbers. For the Earth, episodic switching between whole mantle convection and layered mantle convection has been inferred from geochemistry (Stein and Hofmann, 1994) and modeled by Breuer and Spohn (1995). In the extended model Ms, partially layered convection does take place after the resurfacing events, but a complete separation of upper and lower mantle is no longer observed.

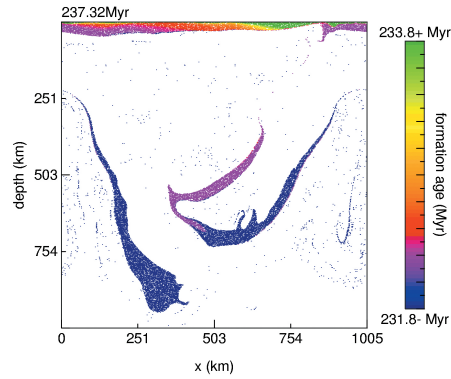


Figure 6.6: The formation age of every basaltic/eclogitic tracer in the domain of model Mr at 237.32 Myr is shown in color. Tracer ages outside the color scale are dark blue (older) or green (younger). The complete domain of 1005x1005 km is shown.

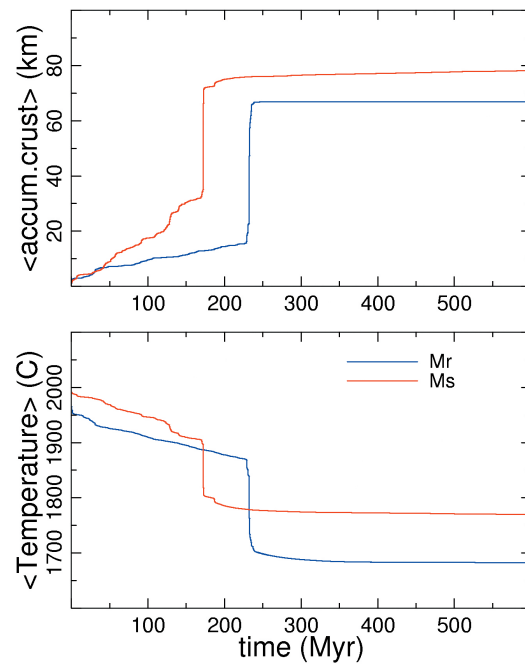


Figure 6.7: Time series of volume averaged temperature (bottom panel) and accumulated amount of created crust represented as an average thickness over the entire domain with (top panel), for models Mr and Ms (larger domain of 1200 km depth).

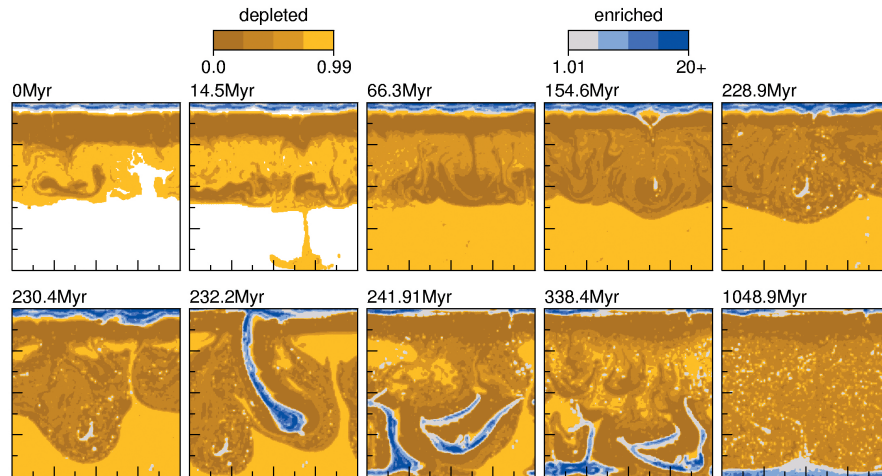


Figure 6.8: Ten snapshots of the trace element concentration field illustrate the chemical differentiation of model Mr. Pristine, undifferentiated material is white. Material that is depleted in trace elements is yellow, and the enriched melt products are blue. The distribution coefficient applied is 10^{-2} .

6.4 Discussion

6.4.1 Large Archean mantle plumes

The strong temperature dependence of the viscosity of the mantle causes the maximum horizontal temperature variations that can be created in the convecting mantle to be a function of mantle temperature (McKenzie and Bickle, 1988). For the present mantle, plume excess temperatures are estimated to be up to 200 to 250 Kelvin (Herzberg and O'Hara, 1998). In a hotter Archean mantle, this would be reduced to about 50 to 150 Kelvin (Nisbet et al., 1993). However, the mantle diapir that enters the upper mantle in model Mr (Figure 6.4) shows excessive melting due to its high excess temperature of about 250 Kelvin. Clearly the argument of reduced maximum excess temperatures for plumes in a hotter mantle of McKenzie and Bickle (1988) and Nisbet et al. (1993) breaks down for plumes originating from a breakthrough between layered convection cells as illustrated here. This demonstrates that in a hotter mantle, which will show a stronger layering of mantle convection (Christensen and Yuen, 1985), plumes with high excess temperatures and massive melting are feasible.

6.4.2 Rapid resurfacing

In section 6.3.2 we have seen that the entire crust may periodically sink into the mantle (see Figure 6.5). In the case of such an event, it is completely replaced by new crust, and a large amount of heat is released from the mantle. The crust sinks because of gravitational instability, caused by the transformation of basalt into eclogite in a crust significantly thickened by the breakthrough of lower mantle material into the upper mantle. An important parameter is the rheology of the sinking crust. In Figure 6.5 it is strong enough to pull down the entire existing (and partly positively buoyant) crust, such that a strong downward force localized at the site of the thickened crust causes resurfacing of the entire model. This type of dynamics resembles models for the dynamics of Venus during its history. Crater counts on the surface of Venus indicate that this planet underwent a global resurfacing event about 500 million years ago (Schaber et al., 1992). Different mechanisms have been proposed to explain the resurfacing event(s). Herrick and Parmentier (1994) suggest on the basis of thermal evolution calculations that the episodic reversal of two layers in the mantle may trigger a period of massive volcanism that completely renews the crust. Solomatov and Moresi (1996) suggest that plate tectonics was active on Venus before 500 Ma, which stopped because the stresses in the lithosphere dropped below the yield strength. A similar argument is used by Fowler and O'Brien (1996) to explain episodic heating of the mantle under a thickening stagnant lid, which experiences increasing buoyancy induced stresses during its cooling up to the point where plastic failure occurs and the lithosphere can subduct into the mantle. Turcotte (1995) compares 'episodic subduction' (p. 16,935) on Venus to the foundering of the solidified crust on a cooling lava lake. Due to the cooling of the crust, it becomes gravitationally unstable and sinks into the lake in parts that are separated by cracks. Our results most resemble the model of Parmentier and Hess (1992), in which the lithosphere episodically becomes negatively buoyant due to cooling, causing it to sink into the mantle. Secondly the basalt to eclogite phase transition in the lower crust causes parts of it to become negatively buoyant and recycle into the mantle. The material sinking into the mantle makes room for new partial melting of mantle peridotite, generating new crustal material and a depleted root, which can start to cool again. The results of Parmentier and Hess (1992) indicate that this process could take place on Venus with a periodicity of 300 to 500 million years. No spatial scale of recycling of lithosphere into the mantle is included in their model. Our results show recycling of eclogite and also depleted peridotite into the mantle on two scales: small-scale delaminations and large-scale sinking of the entire lithosphere into the mantle. However, Parmentier and Hess (1992) assume that eclogite which sinks into the mantle completely mixes with it, also chemically, essentially refertilizing the mantle. The mechanism of mantle refertilization by reaction with eclogite (Yaxley and Green, 1998) is not included in our model. Furthermore, as our model domain includes only a small part of the lower mantle corresponding to the width of the domain, a reduced amount of fertile peridotite and heat is present in our models, which further limits the maximum amount of crust that may be produced.

6.4.3 Thermal evolution of the mantle

Although the limited size of the lower mantle in our models does not allow quantitative statements on the absolute cooling rate of the Earth, the results do show that specifically the resurfacing mechanism as illustrated in Figure 6.5 is a strong cooling agent. The volume averaged temperature curves of Figure 6.7 show temperature decrease values of about 100 to 200°C for a single resurfacing event in each model. We speculate that such a mechanism may have caused rapid cooling in the early history of the Earth over a period of several hundreds of millions of years until the temperature dropped to levels where the mechanisms described in this work are no longer viable.

6.4.4 Geochemical evolution of the mantle

Geochemical studies indicate that the earliest rocks found on Earth were already derived from a depleted mantle (Hamilton et al., 1983; Patchett, 1983; Vervoort et al., 1996; Blichert-Toft et al., 1999). Based on Hf isotope data, this depleted mantle was derived from a uniform chondritic reservoir at least 4.08 billion years before present (Amelin et al., 2000). Furthermore, the compiled isotope data from different Archean terranes suggest that during the Archean the mantle source of greenstone belts became more depleted with time (Condie, 1990; Amelin et al., 2000). Our model results are consistent with this observation. Figure 6.9 shows a steady, though not constant, increase of the averaged extracted melt degree for the upper mantle during the first 230 million years of the model evolution for model Mr. The same trend is illustrated in the incompatible element concentration plots for this model in Figure 6.8, which shows increasingly darker colors (i.e. lower concentrations) in the model upper mantle during the first 230 million years. The small extent of this model lower mantle limits the amount of fertile mantle peridotite that may be transported into the upper mantle. Influx of fresh lower mantle material would lower the average degree of depletion in the upper mantle, as can be observed in Figure 6.9a between 230 and 300 million years.

The range in trace element compositions found in basalts from different geodynamical settings on the present-day Earth indicates that the mantle contains several more or less separate geochemical reservoirs (Hofmann, 1997). Tackley (2000) gives an overview of different models which have been suggested to explain the presence of these reservoirs in the mantle. Furthermore, trace element balance calculations require a 'hidden' reservoir of enriched material apart from the continental crust and the depleted mantle reservoirs to comply with the assumption of a chondritic bulk silicate Earth (e.g. Galer and Goldstein, 1991; McDonough and Sun, 1995). This is also supported by the observation of subchondritic ratios of Nb/La, Nb/Ta, and possibly Ti/Zr in continental crust, depleted mantle and mid-ocean ridge basalt (Rudnick et al., 2000). Rudnick et al. (2000) propose that the missing Nb, Ta and possibly Zr reside in a reservoir of eclogite that underwent partial melting during subduction. They calculate that this reservoir should have a mass of about 0.5 to 6 % of the silicate Earth to compensate for the deficit. The subduction and storage of eclogite in the lower mantle as a mechanism of creating an enriched reservoir in the lower mantle has been investigated in numerical convection models by Christensen

and Hofmann (1994). Our model results show that subduction in the plate tectonics sense is not required to bring large amounts of eclogite into the lower mantle, and keep it there.

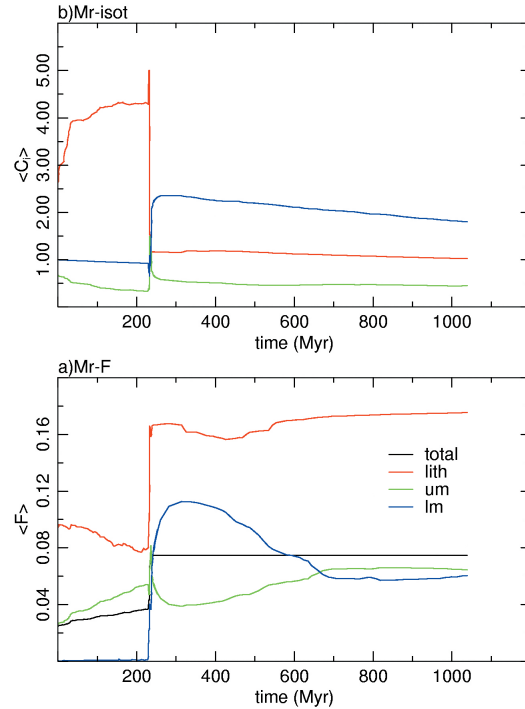


Figure 6.9: The chemical evolution of model Mr is presented in the form of time series for the averaged degree of depletion (a) and the averaged trace element concentration (b). Averaged values for the entire domain are shown in black. A subdivision has been made into the lithosphere (0-150 km depth, red curves), the upper mantle (150-670 km depth, green curves) and the lower mantle (670-1005 km depth, blue curves).

Though the small-scale delamination as described in section 6.3.2 and shown in Figure 6.3 only generates more or less uniformly distributed blobs of eclogite in the entire model mantle, large-scale crustal sinking as shown in Figure 6.5 does generate an enriched reservoir (see Figure 6.8) in the lower mantle which is stable for hundreds of millions of years at least. In recent years geodynamical models have been proposed featuring a dense enriched layer in the bottom third of the mantle (Coltice and Ricard, 1999; Kellogg et al., 1999; Van der Hilst and Káráson, 1999; Albarède and Van der Hilst, 2002), consisting of either primitive or recycled material. We speculate on the basis of our modelling results that such a layer may have been formed during a short time window in the early evolution

of the Earth's mantle by compositional differentiation in pressure release partial melting of mantle peridotite and subsequent large scale sinking of the thick basaltic/eclogitic crust into the lower mantle as an alternative to or precursor of the subduction model proposed by Albarède and Van der Hilst (2002). The resulting reservoir would distinguish from a primitive reservoir by its outgassed nature (low He content, developing a low $^3\text{He}/^4\text{He}$ ratio).

6.5 Conclusions

As argued in the introduction, the geodynamics of the early Earth was probably very different from the recent situation. Our model results, relevant for the hotter conditions in the early Earth, indicate that a number of processes may have been important:

- Small-scale ($x \cdot 10^2 km$) circulations of the shallow upper mantle and the lower crust, with partial melting in the upwelling limb of the convection and delamination and recycling of eclogitic lower crust in the downwelling limb, active over extended periods of time ($x \cdot 10^6 yr$).
- Episodic large-scale resurfacing events, in which a large part of or even the entire crust sinks into the mantle and is replaced by new crust at the surface. These events are quite rapid and take place within a few millions of years.
- Very fast penetration (5 m/yr) of lower mantle diapirs into the upper mantle, bringing hot and fertile mantle material to supersolidus conditions. This process generates large amounts of melt that may locally significantly thicken the crust ($x \cdot 10 km$) and subsequently trigger the aforementioned process of resurfacing.

An important consequence of the latter process is that the penetration of lower mantle diapirs into the upper mantle in a layered convection system allows plume excess temperatures that are significantly higher (about 250 K) than the maximum plume excess temperatures which are predicted from the modified boundary layer theory of McKenzie and Bickle (1988) as applied to the Archean (about 50-150 K) by Nisbet et al. (1993). The episodic resurfacing in particular may have contributed to the formation of a bottom reservoir enriched in incompatible elements, as the 'subducted' crust sinks into the model lower mantle and forms a stable layer at the bottom boundary. We speculate that such a process may be responsible for the complete resurfacing of Venus which is dated at about 500 Ma from crater counts.

Chapter 7

On the formation of continental silicic melts in thermo-chemical mantle convection models: implications for early Earth and Venus

Abstract

Important constituents of Archean cratons, formed in the early and hot history of the Earth, are TTG plutons and greenstone belts. The formation of these granite-greenstone terrains is often ascribed to plate-tectonic processes. Buoyancy considerations, however, do not allow plate tectonics to take place in a significantly hotter Earth. We therefore propose an alternative mechanism for the coeval and proximate production of TTG plutons and greenstone-like crustal successions: When a locally anomalously thick basaltic crust has been produced by continued addition of extrusive or intrusive basalts due to partial melting of the underlying convecting mantle, the transition of a sufficient amount of basalt in the lower crust to eclogite may trigger a resurfacing event, in which a complete crustal section of over 1000 km long sinks into the mantle in less than 2 million years. Pressure release partial melting in the complementary upwelling mantle produces large volumes of basaltic material replacing the original crust. Partial melting at the base of this newly produced crust may generate felsic melts that are added as intrusives and/or extrusives to the generally mafic crustal succession, adding to what resembles a greenstone belt. Partial melting of metabasalt in the sinking crustal section produces a significant volume of TTG melt that is added to the crust directly above the location of ‘subduction’, presumably in

This chapter has been submitted by P. van Thienen, A.P. van den Berg and N.J. Vlaar for publication in *Tectonophysics*.

the form of a pluton. This scenario is self-consistently produced by numerical thermochemical mantle convection models, presented in this paper, including partial melting of mantle peridotite and crustal (meta-)basalt. The metamorphic p, T -conditions under which partial melting of metabasalt takes place in this scenario are consistent with geochemical trace element data for TTG's, which indicate melting under amphibolite rather than eclogite facies. Other geodynamical settings which we have also investigated, including partial melting in small scale delaminations of the lower crust, at the base of an anomalously thick crust and due to the influx of a lower mantle diapir fail to reproduce this behaviour unequivocally and mostly show melting of metabasalt in the eclogite stability field instead. The resurfacing scenario may also have been important in Venus' history, but probably did not produce significant volumes of continental material due to the dryness of this planet.

7.1 Introduction

The finding of detrital zircons up to 4.4 Gyr old, less than 200 million years after the accretion of the Earth, provides evidence that continental crust was already produced at this time (Peck et al., 2001). Growth curves for the continental crust, derived from isotopic analyses of rocks from Archean to present age, also indicate that the formation of continental crust may have started before 4.0 Ga (e.g. Taylor and McLennan, 1985; McCulloch and Bennett, 1994). In the recent Earth, most continental growth is accommodated by the accretion of volcanic arcs, which are formed by partial melting of the mantle wedge above subducting slabs, and intraplate volcanism, associated with hotspots. The material thus produced is on average of basaltic composition, but the continental crust has an andesitic bulk composition (Rudnick, 1995). In Archean cratons, a large fraction of the material consists of Tonalite-Trondhjemite-Granodiorite (TTG) suites, either metamorphosed to amphibolite facies gneiss-migmatites, or as plutons (Goodwin, 1991). Melting experiments indicate that these TTG's may have been formed by partial melting of hydrous metabasalts (eclogites or amphibolites) at pressures between 8 and 32 (optimally 22) kbar (Rapp et al., 1991). The presence of some water is required to lower the melting temperature to plausible values. The required conditions for this process may be found in subduction zone settings, but not exclusively (Rapp et al., 1991). Recent results from Foley et al. (2002, 2003) have shown, on the basis of Nb/Ta and Zr/Sm ratios in TTG's, that for the formation of these rocks, melting must take place in the amphibolite rather than the eclogite stability field. Their experiments show that komatiitic material, which is more mafic than the present basaltic oceanic crust, and which may be expected to be more abundant for higher mantle temperatures (Nisbet, 1982), would transform into pyroxenite instead of eclogite at high pressure, which they infer to produce basaltic melts upon partial melting, and not TTG-like melts.

Eclogitic xenoliths from cratonic regions often show a depleted nature, indicating that melt has been extracted, and it has been suggested that these are remnants of granitoid formation, complementary to these crustal rocks (e.g. Rollinson, 1997; Barth et al., 2001). Furthermore, oxygen isotope studies on coesite inclusions in diamonds from

eclogite xenoliths from the Guyana Shield suggest interaction of the original rock with sea water similar to modern day hydrothermal alteration of oceanic crust at mid-ocean ridges (Schulze et al., 2003). However theoretical considerations and numerical models have shown that maintaining plate tectonics in a hotter Earth is quite difficult (Vlaar and Van den Berg, 1991; Van Hunen, 2001; Van Thienen et al., 2003c, chapter 4). Adakites, formed by partial melting of a young, hot slab in a subduction zone setting, are sometimes considered as a modern day analogue of TTG's (Martin, 1999), and interpreted as supporting early plate tectonics. Smithies (2000) however showed that adakites and TTG's differ in Mg number and SiO₂ contents, indicating that adakitic melts underwent interaction with mantle peridotite whereas TTG melts (especially pre 3.0 Ga) did not. A more suitable setting for producing TTG's than a subduction zone is therefore melting at the base of a thickened crust (Smithies, 2000). The composition of Phanerozoic Na-rich granitoids formed in this way (e.g. Atherton and Petford, 1993; Johnson et al., 1997) more closely matches the range of composition of Archean TTG's (Smithies, 2000). Alternatively, the intrusion and crystallization of mantle melts in the lower crust may provide a heat source for partial melting of the lower crust (Huppert and Sparks, 1988; Petford and Gallagher, 2001). Other mechanisms proposed in the literature use similar settings. Campbell and Hill (1988) suggested that the heat of a hot asthenospheric upwelling interacting with an existing crust may generate felsic melts, thus producing continental material. Theoretical considerations suggest that both the maximum size and the excess temperature of mantle plumes become smaller in a hotter mantle (McKenzie and Bickle, 1988; Nisbet et al., 1993). However, a mantle plume originating from a separately convecting lower mantle entering the upper mantle may have a much greater size and higher excess temperature (Van Thienen et al., 2003b, chapter 6), possibly supplying sufficient heat for partial melting of the lower crust. Zegers and Van Keken (2001) proposed that delamination of an eclogitic lower crust and associated extension of the overlying middle and upper crust may allow warmer mantle material to rise to shallower levels and cause crustal melting to produce continental material. They used a numerical model to demonstrate the feasibility of the mechanism and compared results to geological evidence from the Pilbara craton.

In this work we use numerical thermochemical mantle convection models to investigate different geodynamical settings in which partial melting of (meta-)basalt may take place. This is an extension of earlier work (Van Thienen et al., 2003b, chapter 6), in which the dynamics of the self-consistent growth and recycling of thick Archean oceanic crust was investigated. Four different scenarios in which partial melting of (meta-) basalt may take place are investigated in detail: (1) small scale delamination of the eclogitic lower crust, (2) large scale resurfacing by rapid episodic 'subduction' (though not in a plate tectonic sense), (3) heating of the lower part of a thickening crust by the convecting mantle, and (4) heating of the crust from below by a mantle plume. We compare the melting conditions in our models to those inferred for natural TTG's (Winther, 1996), and apply the geochemical constraints that were found for the metamorphic stability field where TTG generation takes place (Foley et al., 2002, 2003). We also investigate the production rates of continental material that is formed by means of this mechanism using numerical models. Finally, we compare the rock associations produced in our models and their geometry to the granite-greenstone associations that are common in Archean terrains and come up

with a new model for the production of these associations which does not require the operation of plate tectonics.

7.2 Model description

The numerical model used is nearly identical to that of Van Thienen et al. (2003b) and chapter 6. Therefore, the model will be described only briefly and the reader is referred to Van Thienen et al. (2003b) and chapter 6 for more information. A single feature has been added to the model: partial melting of basaltic material. This will be described below in section 7.2.4, after a description of the model equations and solid state phase transitions.

7.2.1 Governing equations

Conservation of energy, mass and momentum under the extended Boussinesq approximation (Steinbach et al., 1989; De Smet et al., 1998) for an infinite Prandtl number medium lead to the energy, continuity and Stokes equations (for symbol definitions see Table 7.1):

$$\rho c_p \left(\frac{\partial T}{\partial t} + u_j \partial_j T \right) - \alpha T \frac{dp}{dt} = \tau_{ij} \partial_j u_i + \partial_j (k \partial_j T) + \rho_0 H + \frac{\Delta S}{c_p} \frac{dF}{dt} T + \sum_k \frac{\gamma_k \delta \rho_k T}{\rho_0^2 c_p} \frac{d\Gamma_k}{dt} \quad (7.1)$$

$$\partial_j u_j = 0 \quad (7.2)$$

$$\partial_j \tau_{ij} = \partial_i \Delta p - \Delta \rho g_i \quad (7.3)$$

symbol	property	definition	value/unit
c_p	heat capacity at constant pressure		1250 Jkg ⁻¹ K ⁻¹
F	degree of depletion		
g	gravitational acceleration		9.8 ms ⁻²
H	radiogenic heat productivity		Wkg ⁻¹
p	pressure		Pa
S	melt productivity function		s ⁻¹
ΔS	entropy change upon full differentiation		300 Jkg ⁻¹ K ⁻¹
t	time		s
T	temperature		°C
T_0	non-dimensional surface temperature		$\frac{273}{\Delta T}$
ΔT	temperature scale		2450 °C
z	depth		m
$z_0(T)$	temperature dependent depth of phase transition		m
α	thermal expansion coefficient		$3 \cdot 10^{-5} \text{ K}^{-1}$
Γ_k	phase function for transition k	$\frac{1}{2} \left(1 + \sin \left(\pi \frac{z - z_0(T)}{\delta z} \right) \right)$	

Table 7.1: Symbols definitions and parameter values.

symbol	property	definition	value/unit
δz	depth range of phase transition		m
κ	thermal diffusivity		$10^{-6} \text{ m}^2 \text{ s}^{-1}$
ρ_0	reference density		3416 kgm^{-3}
$\delta \rho$	density difference upon full depletion	$\frac{\partial \rho}{\partial F}$	-226 kgm^{-3}
$\delta \rho_k$	density increase of phase transition k	$\frac{\partial \rho}{\partial \Gamma_k}$	kgm^{-3}
B_1	diffusion creep prefactor		Pas
B_2	dislocation creep prefactor		$\text{Pa}^n \text{ s}$
C_0	cohesion factor		0 Pa
E_1	diffusion creep activation energy		$270 \cdot 10^3 \text{ Jmol}^{-1}$
E_2	dislocation creep activation energy		$485 \cdot 10^3 \text{ Jmol}^{-1}$
e_{ij}	strain rate tensor	$\partial_j u_i + \partial_i u_j$	s^{-1}
e	second invariant of the strain rate tensor	$[\frac{1}{2} e_{ij} e_{ij}]^{\frac{1}{2}}$	s^{-1}
$f(F)$	composition dependent viscosity prefactor		
n_1	diffusion creep stress exponent		1
n_2	dislocation creep stress exponent		3.25
n_y	yield exponent		10
R	gas constant		$8.341 \text{ Jmol}^{-1} \text{ K}^{-1}$
V_1	diffusion creep activation volume		$6 \cdot 10^{-6} \text{ m}^3 \text{ mol}^{-1}$
V_2	dislocation creep activation volume		$17.5 \cdot 10^{-6} \text{ m}^3 \text{ mol}^{-1}$
$\dot{\epsilon}$	strainrate		s^{-1}
$\dot{\epsilon}_y$	yield strainrate		10^{-15} s^{-1}
η	viscosity		Pas
η_0	reference viscosity		10^{20} Pas
η_y	yield viscosity		Pas
σ_n	normal stress		Pa
τ_{ij}	deviatoric stress tensor	ηe_{ij}	Pa
τ	second invariant of the deviatoric stress tensor	$[\frac{1}{2} \tau_{ij} \tau_{ij}]^{\frac{1}{2}}$	Pa
τ_y	yield stress		Pa

Table 7.1: Symbols definitions and parameter values (continued).

The local and time dependent internal heating term H in the energy equation (7.1) is obtained by multiplying a uniform value of $15 \cdot 10^{-12} \text{ Wkg}^{-1}$ with the concentration of an incompatible trace element. This trace element has an initial concentration of 1, decays with time (half life 2.5 Gyr) and is fractionated upon partial melting (see below) assuming equilibrium melting for each time step and a distribution coefficient of 10^{-2} .

Evolution of the degree of depletion is described by the following equation:

$$\frac{dF}{dt} = S(p, T, F) \quad (7.4)$$

where S is determined by the parameterization of the melting phase diagram under consideration (De Smet et al., 1998).

All motion is driven by density perturbations described by the equation of state:

$$\Delta\rho = \rho_0 \left\{ -\alpha(T - T_{ref}) + \sum_k \Gamma_k \frac{\delta\rho_k}{\rho_0} + \frac{\delta\rho}{\rho_0} F \right\} \quad (7.5)$$

Three deformation mechanisms account for the creep flow deformation of material. The first two, diffusion creep and dislocation creep, are described by an Arrhenius formulation of the corresponding components of the composite viscosity (Karato and Wu, 1993; Van den Berg and Yuen, 1998):

$$\eta_i = f(F) B_i \exp \left[\frac{E_i + PV_i}{RT} \right] \sigma^{1-n_i} \quad (7.6)$$

with $f(F)$ a composition dependent prefactor (for an explanation of the symbols see Table 7.1). Apart from this prefactor, the parameters of expression (7.6) are based on Karato and Wu (1993) assuming a constant and uniform grainsize of 1 mm. The composition dependent prefactor $f(F)$ has a value of 1 for fertile peridotite and basalt (which have the same viscosity parameters in our models). For depleted peridotite (harzburgite) we apply a prefactor value of 10 for a degree of depletion over 0.05, and a linearly increasing value between $F = 0.005$ and $F = 0.05$ from 1 to 10. This is intended to mimic the effect of dehydration during partial melting on the viscosity (Karato, 1986; Hirth and Kohlstedt, 1996; Mei and Kohlstedt, 2000a,b). For eclogite, the prefactor is set to a value of 0.1, to account for the lower flow stress interpreted by Piepenbreier and Stöckhert (2001) from eclogite microstructures.

The third deformation mechanism included, brittle failure, is parameterized by a yield mechanism approximating the effects of fracturing-like behaviour when the shear stress exceeds a certain yield stress τ_y . We use a formulation of Van Hunen et al. (2002):

$$\eta_y = \tau_y \dot{\epsilon}_y^{-1/n_y} \dot{\epsilon}^{(1/n_y)-1} \quad (7.7)$$

The yield stress τ_y , the yield strain rate $\dot{\epsilon}_y$ and the yield exponent n_y are prescribed parameters (see Table 7.1). The yield stress τ_y is determined from Byerlee's law approximating the normal stress with the lithostatic pressure (e.g. Moresi and Solomatov, 1998):

$$\tau_y = C_0 + \mu\rho_0 g_0 z \quad (7.8)$$

We use a low value of 0.03 for the friction coefficient μ , consistent with results of (Moresi and Solomatov, 1998) for the mobilization of the Earth's lithosphere, and assume the cohesion term C_0 to be of minor importance and set it to 0.

The diffusion and dislocation creep viscosities are inversely added to define an effective ductile creep viscosity (Van den Berg et al., 1993) and the minimum of this value and the local yield viscosity is used for the local effective viscosity.

model	process/setting	domain size (km)	modification	Figure
Mdel	small-scale delamination	600x600	-	7.3a
Mres	resurfacing	600x600	-	7.3b,c
Mtcr	thickened crust	1200x1200	l.m. diapirism suppressed	7.3d
Mdia	l.m. diapirism	1200x1200	-	7.3e

Table 7.2: The range of models focussing on different processes and/or settings, with computational domain size and Figure reference visualizing the process or setting. Modifications of the model conditions relative to the original model Ms from Van Thienen et al. (2003b) (see text) are indicated as well.

7.2.2 Computational methods

The model domain of each experiment is square, with a size of 600 or 1200 km (see Table 7.2). It is discretized using: a) finite elements with a boundary nodal point spacing of 6-12 km for the energy and momentum equations, and b) 200 000 to 400 000 particle tracers, advected with the mantle flow, on which the development of depletion, trace element concentration, and metamorphic phase of basaltic material are evaluated. The vertical boundaries are periodic, and the bottom boundary has a free slip condition. On the top boundary, the vertical velocity is prescribed as a function of melt productivity, as will be described below, to allow the production of crust at the surface. The horizontal, tangential stress component is set to zero. The temperature on the top boundary is set to $0^{\circ}C$. On the bottom boundary, a temperature consistent with the initial condition (see section 7.2.7) is prescribed.

7.2.3 Solid state phase transitions

Mantle phase transitions in our model are composition dependent and are accounted for in the energy equation (7.1), and the resulting density effects are included in the equation of state (7.5), which enters the buoyancy term of the momentum equation (7.3). Parameters of the phase transitions are listed in Table 7.3. The transition of basalt into eclogite is treated differently. Basalt is transformed into heavier eclogite upon reaching depths in excess of 30 km in our model. The kinetics of this transition are approximated assuming a constant relaxation time for the transition of 1.25 Myr. The depth of 30 km (0.9 GPa) we use is somewhat less than the depth of about 40 km (1.2 GPa) that Hacker (1996) states as the minimum pressure of basalt to eclogite transformation. However, as we are dealing with melt products in a mantle which is hotter than the present, their composition may be more MgO-rich (more towards komatiitic composition) than present day mid ocean ridge basalt (Nisbet, 1982). Experiments of Green and Ringwood (1967) have shown that the transition may occur at lower pressures and higher temperatures in MgO-rich rocks. Furthermore, lower pressure phase assemblages (above 0.7-0.8 GPa) may also contain garnet (Green and Ringwood, 1967; Ito and Kennedy, 1971; Hacker, 1996), thus raising the bulk density above that of the original basaltic phase assemblage. We do not

transition	material	P_0 (GPa)	T_0 (K)	γ (Pa/K)	δz (km)	$\frac{\delta\rho}{\rho_0}$
400	peridotite	13.4	1756	$3 \cdot 10^6$	50	0.05
400	basalt	12.5	1747	$3 \cdot 10^6$	150	0.10
670	peridotite	22.4	1854	$-2.5 \cdot 10^6$	50	0.05

Table 7.3: Parameters of the phase transitions used in the models. The first column indicates the approximate depth of the transition. P_0 and T_0 are the reference temperature and pressure for the phase transition, defining it in combination with the Clapeyron slope γ . The column marked δz indicates the depth range over which the transition is smeared out in the model and the last column gives the relative density contrast of the phase transition.

consider phase boundary topography due to temperature effects, since we expect this to be dominated by kinetic effects because of the relatively low Clapeyron slope of about 1 MPa/K (Philpotts, 1990).

7.2.4 Partial melting

Partial melting of fertile mantle peridotite may produce a spectrum of melt compositions, ranging from tholeiitic to komatiitic. In general, higher melting pressures and/or greater degrees of melting meaning higher temperatures produce melts that are more MgO-rich, so more to the komatiitic side of the spectrum (Philpotts, 1990). Partial melting of basaltic material may also produce a range of melt compositions, depending on the conditions of melting. This melting behaviour is simplified in our models, where the composition field defines three different basic types of materials: mantle peridotite, basalt and felsic material. These terms are used here to describe larger groups of rocks than their specific geological definitions. *Basaltic* materials are understood here to include all melt products of mantle peridotite, regardless of melting conditions, and the term *felsic* materials is used to indicate all melt products of basaltic material. Mantle peridotite and basalt have an extra component to their composition, which is the *degree of depletion*. Partial melting is modelled as an (irreversible) increase in this degree of depletion F , which is defined here as the mass fraction of melt produced from an initially unmelted material control volume of mantle peridotite or basalt. Since no material is actually removed in our model, the volumes of depleted residual material are somewhat overestimated (De Smet, 1999). The source function S in (7.4) describes the distribution of the rate of partial melting, applying a simple parameterization of the melting phase diagram of mantle peridotite (De Smet et al., 1998). We use third order polynomial parameterizations of the solidus and the liquidus of mantle peridotite, based on Herzberg and Zhang (1996), down to a depth of 400 km (see Figure 7.1), assuming that melt produced below this depth is not segregated. Our isobaric melting curve, which is based on data presented by Jaques and Green (1980), is linear (see De Smet et al., 1998). A similar approach is used for partial melting of basaltic material. Since in our models, all melts that are produced are assumed to migrate

to the surface (see section 7.2.5), we can also assume that the crustal material produced by solidification at the surface becomes hydrated by contact with surface water. This is supported by isotope studies on coesite inclusions in diamonds in eclogite xenoliths from the Guyana Shield (Schulze et al., 2003), which indicate significant interaction with water. We therefore use a hydrous solidus and liquidus in our model experiments, based on data from Green (1982), see Figure 7.1. We use the same linear melting function for the partial melting of basalt as that used for peridotite.

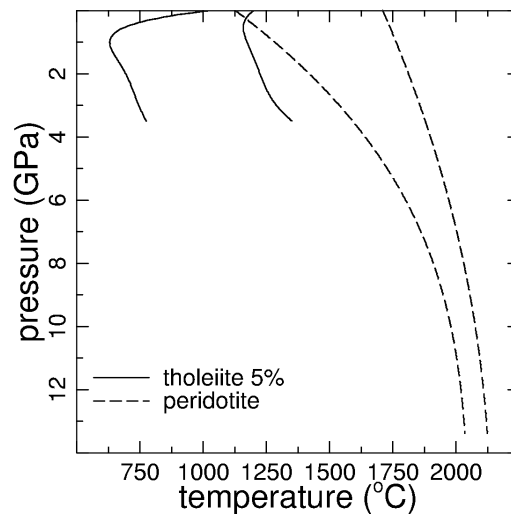


Figure 7.1: Solidus and liquidus parameterizations used in the models for basalt/eclogite (solid curves) and peridotite (dashed curves). The basaltic curves are based on experimental results from a hydrated (5 percent water by weight) tholeiite (Green, 1982). The peridotite curves are based on Herzberg and Zhang (1996).

7.2.5 Crustal growth

An important feature of the model is the self-consistent growth of crust. All melt that is produced in the model domain is assumed to migrate to the surface on time scales much shorter than the characteristic time scales of the model. We therefore let all melt that is produced flow into the model through the top boundary above the region where the melt was formed. When both basaltic and felsic crust is being produced, the inflowing material is a mixture of these two components, defined by different tracer composition values, in relative proportions corresponding to the respective amounts of melt being produced. The trace element concentrations of inflowing basalt and felsics are a function of the fractionation during partial melting of the respective source rocks.

7.2.6 Metamorphic phase stability fields

Trace element ratios (Nb/Ta and Zr/Sm) in TTG's indicate that these rocks have been formed by partial melting of a meta-basalt in the amphibolite rather than the eclogite stability field (Foley et al., 2002, 2003). This is based on the modelling of trace element distribution, which indicates that amphibole must be present in the source rock and rutile, common in Archean eclogite xenoliths (Rudnick et al., 2000), must be absent. It is therefore important to monitor the pressure and temperature conditions under which partial melting takes place in our experiments. Figure 7.2 shows the metamorphic phase diagrams for three different compositions. We have included three different compositions because of the uncertain nature and variability of the dominant rock type in early oceanic crust. Basaltic crust created at a mid-ocean ridge will be thicker for higher temperatures (Vlaar and Van den Berg, 1991), and have a higher MgO content (Nisbet, 1982) than present MORB-like compositions. However, in an alternative geodynamic regime like that which is modelled in this work, production of crust does not take place due to partial melting of focused upwelling mantle in a ridge setting, but by stacking of extrusive units produced at many locations from partial melting of the convecting mantle. Due to the presence of pre-existing crust and a depleted root, partial melting takes place at greater depths, which tends to increase the MgO content (Philpotts, 1990), and to lower degrees of melting, which counteracts this effect. Therefore, the dominant composition of crust produced by partial melting of mantle peridotite is expected to be somewhere in the wide range between a basaltic and a komatiitic composition, and we will include all three phase diagrams of Figure 7.2 in the discussion of the results of the numerical models.

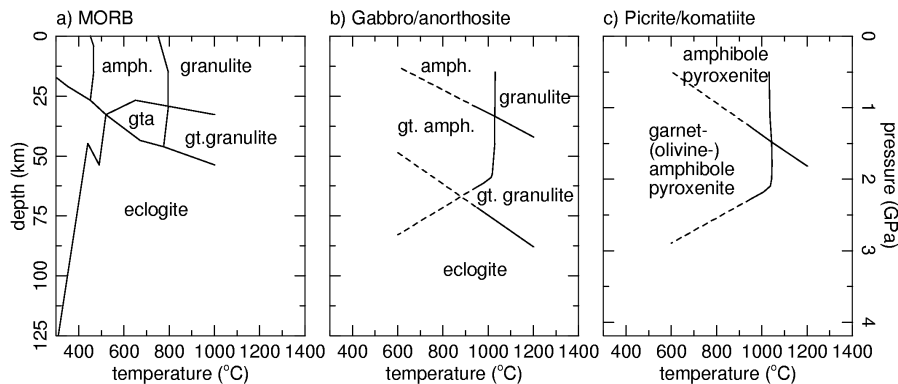


Figure 7.2: Metamorphic phase diagrams for different magmatic rocks, which may be expected in Archean oceanic crust. a) Mid-Ocean Ridge Basalt, from Hacker et al. (2003). *amph.* indicates amphibolite, *gta* is garnet-amphibolite, and *gt. granulite* is garnet granulite. b) Gabbro/anorthosite (Green and Ringwood, 1967; Foley et al., 2003). c) Picrite/Komatiite. Data from experiments on Gorgona komatiite by Foley et al. (2003).

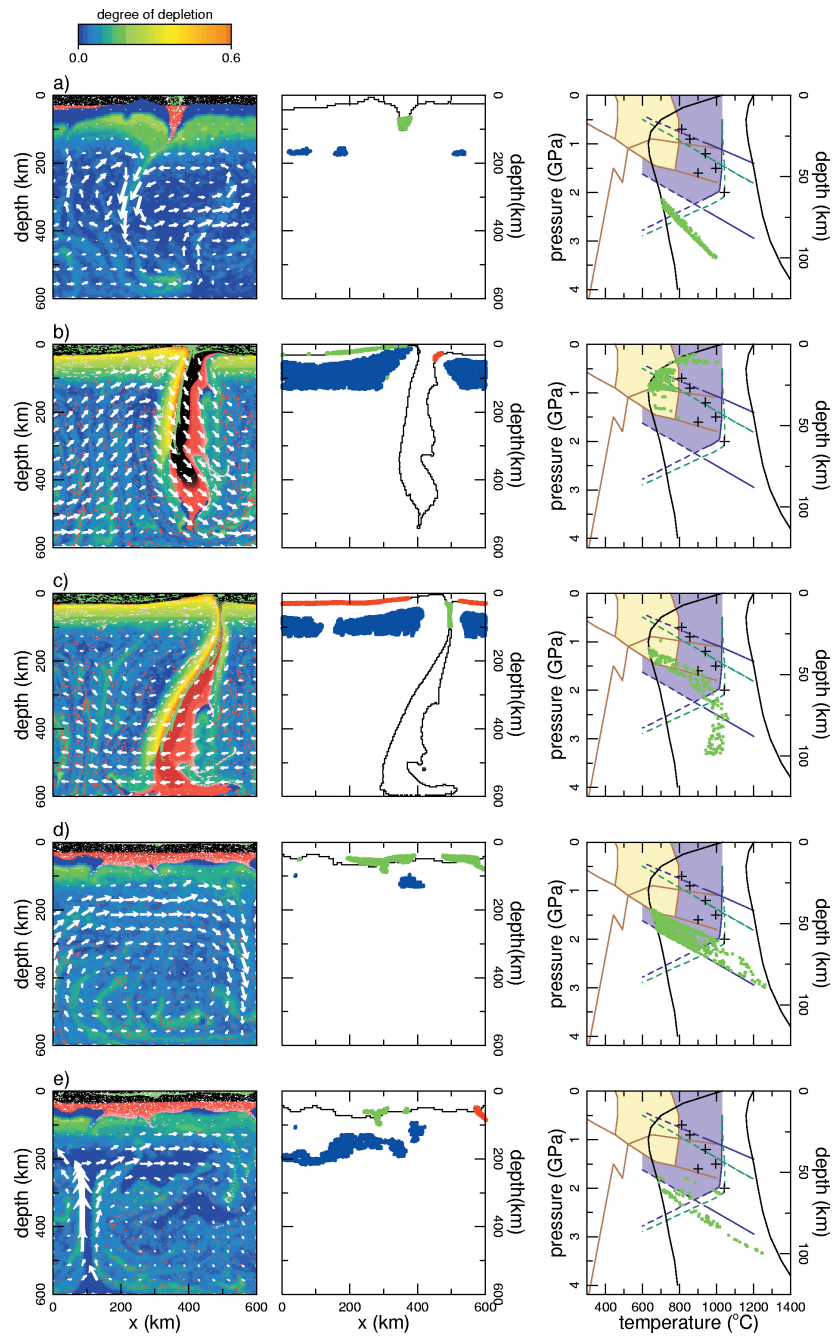


Figure 7.3: (previous page) Partial melting of metabasalt in five different geodynamical settings. The left hand side frames show the composition field, with the colour scale from blue to orange indicating the degree of depletion of peridotite. Black indicates basalt, red is eclogite, and the colour range in between indicates material in the transition stage. Eclogite becomes lighter red as it is more depleted. Greenish crustal material is the product of (meta-) basalt melting. The middle frames show basaltic particle tracers that undergo partial melting in red and green, and melting peridotite in blue. The green tracers are also shown in the right hand side frames, which show the location of partial melting of metabasalt in p,T -space. The phase diagrams represented in Figure 7.2 are included, and the regions that produce Nb/Ta and Zr/Sm ratios consistent with natural TTG's are indicated in yellow (MORB) and purple (gabbro/anorthosite). The inferred melting conditions of some natural TTG's (Winther, 1996) have been included as black crosses, and solidus and liquidus used are indicated by black curves. Note that the frames in the right column have a different depth scale than the other frames. a) Small scale delamination of the lower crust (Mdel). b) Partial melting of a newly produced lower crust associated with a resurfacing event (Mres). c) Partial melting in a 'subducting' crust during a resurfacing event (Mres). d) Partial melting of the base of a thickened crust (Mtr). e) Lower mantle diapirism (Mdia). Frames d) and e) only show 1/4 of the complete computational domain of 1200x1200 km.

Figure 7.2a shows the diagram for a MORB composition (simplified from Hacker et al., 2003). The results of Foley et al. (2002) show that partial melting of metabasalts in the (garnet-) amphibolite stability field produces TTG melts. For a MORB composition, this is at depths less than 50 km at temperatures between approximately 450 and 800°C.

For a gabbroic/anorthositic composition (Figure 7.2b, from a diagram of Foley et al. (2003) based on data from Green and Ringwood (1967)), the amphibolite stability field, and therefore the TTG production field, is larger, extending up to temperatures of about 1000°C and depths of about 75 km (note that the dashed lines are extrapolations of the phase boundaries indicated by solid lines).

No amphibolite is formed for picritic/komatiitic compositions (Figure 7.2c, from Foley et al., 2003), and these rocks do not produce TTG-like melts under any conditions during partial melting, but basaltic liquids instead.

7.2.7 Initial conditions

The initial conditions for the present experiments are derived from model Ms in Van Thienen et al. (2003b) and chapter 6. This original model was started with a cool (sub-solidus) mantle with an extreme heating rate of $250 \cdot 10^{-12} \text{Wkg}^{-1}$, in order to produce a hot and differentiated initial state for our experiments. This extreme internal heating value was reduced to a normal early Earth value of $15 \cdot 10^{-12} \text{Wkg}^{-1}$ after 30 km of basaltic crust had been produced. In the present experiments, we use a snapshot of the entire domain (1200x1200 km) or part of the domain (600x600 km) as a starting condition, see

Table 7.2. Due to the prescribed periodic boundary condition on the vertical boundaries, the latter case results in inconsistencies, since the new boundaries were previously unconnected and therefore did not have the same temperature and velocities. However, these are small and do not significantly influence the solution. In contrast with the present experiments, the original model did not include partial melting of basalt. Therefore, the present experiments show an initial pulse of melting of basaltic material where the temperature is above the basalt solidus. In one experiment (Mctr, see Table 7.2), the generation of a lower mantle diapir is suppressed by increasing the density contrast over the γ -olivine-perovskite phase transition. In every other respect, this model is the same as model Mdia.

7.3 Results

7.3.1 Geodynamical settings

In this work we investigate the partial melting of (meta-)basalt in five different geodynamical settings, associated with different processes that may have been important in the production and recycling of oceanic crust in the early Earth, and which have been described in more detail by Van Thienen et al. (2003b) and in chapter 6. The left hand side and middle frames of Figure 7.3 illustrate all five processes, showing the composition field. In the left hand frames, the colour scale from blue to orange indicates the degree of depletion of peridotite. Basaltic/eclogitic (black/red) and felsic (green) tracers are included. Depleted metabasalt has a lighter red colour. Arrows indicate the instantaneous flow field. The middle frames show the contours of the crust in black, with regions of partial melting of peridotite in blue and partial melting of (meta-) basalt in red and green.

The first process is small scale delamination of the lower crust (Figure 7.3a).

Partial melting in the upwelling limb of a small scale mantle circulation may locally add material to the crust, which becomes thicker. The lower part of the crust may become involved in the circulation. At first this is passive entrainment, but when sufficient basalt has turned into eclogite the involvement becomes active. Partial melting of metabasalt takes place in the tip of the downwelling material, indicated by the green spot in the middle frame.

The second process is large scale resurfacing, shown in Figure 7.3b,c. In this process, a local anomalous thickening of the crust, for example caused by the addition of material by a mantle plume, may become gravitationally unstable when a large part of the (lower) crust has turned into eclogite. This may trigger the entire crust to sink into the mantle on a very short time scale (about 2 million years). New crust is produced by partial melting of upwelling mantle material. Two settings for partial melting of (meta-) basalt can be indicated here. Figure 7.3b shows partial melting, indicated by the green colour in the middle frame, at the base of the freshly produced crust that replaces the material which is sinking into the mantle. The required heat is supplied by upwelling mantle material associated with the resurfacing event. In Figure 7.3c, partial melting takes place in the sinking crustal material itself, indicated by the green colour in the middle frame.

Figure 7.3d shows the third process, which is the partial melting of a locally thickened

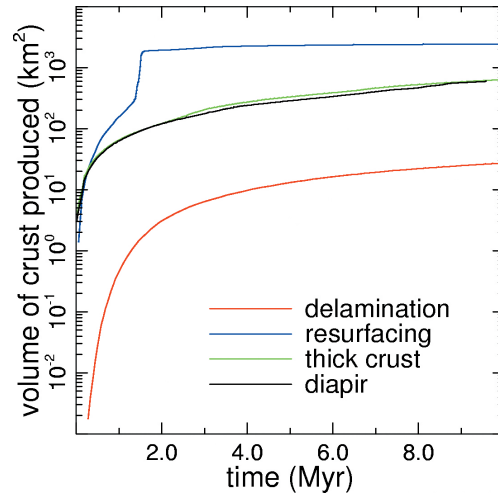


Figure 7.4: 2-D volumes of felsic material produced by partial melting in the different models. Volumes are normalized to a 600 km domain for larger models.

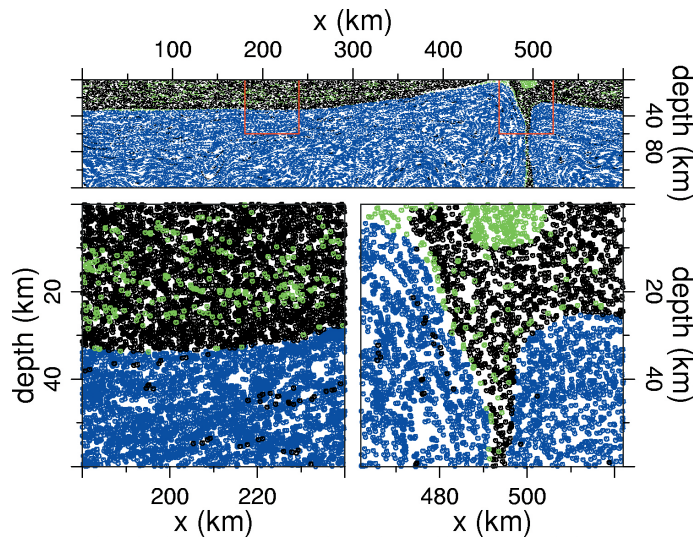


Figure 7.5: Zoom-in on the crust of model Mtr as shown in Figure 7.3c. (Meta-)basaltic tracers are indicated in black, felsic tracers in green, and (both depleted and fertile) peridotitic tracers in blue. Two red squares in the top panel indicate the locations of the zoom-ins of the lower frames.

crust. Due to successive stacking of basaltic extrusives, the crust locally extends to about 80 km depth at temperatures above the hydrous basalt solidus. Penetration of a mantle diapir into the upper mantle as a heat source for melting at the base of the crust is shown in Figure 7.3e.

7.3.2 Conditions of partial melting

The p,T-conditions under which partial melting of metabasalt takes place in the different geodynamical settings with respect to the metamorphic phase boundaries (see Figure 7.2) are indicated in the right hand side frames of Figure 7.3. The p,T-conditions of melting basaltic tracers are indicated in green, and the corresponding locations are indicated in green in the middle frames (melting tracers not indicated in the p,T diagrams are shown in red). These results show that if we assume a MORB-like composition (brownish phase boundaries in Figure 7.3) for the basaltic crust that is partially melting in our experiments, TTG-like melts formed in the amphibole stability field consistent with observations of Nb/Ta and Zr/Sm ratios in natural TTG's can be produced in two of the geodynamical settings, both associated with large-scale resurfacing (see Figure 7.3b,c, where the yellow region indicates the (garnet-) amphibolite stability fields). The melting conditions at the base of the newly produced crust correspond to the shallow conditions inferred for natural TTG's by Winther (1996), indicated by black crosses in the right hand frames. In the sinking crust (Figure 7.3c), conditions correspond to the deepest conditions for natural TTG's inferred by Winther (lowest two crosses in the right hand frame). In the other settings, melting takes place at levels that are too deep for amphibolite stability, well into the eclogite field. For material with a gabbroic/anorthositic composition (purple phase lines), the stability field of (garnet-) amphibolite (purple shaded area, partially overlapping with the yellow MORB region) is extended relative to MORB. The two settings associated with the resurfacing event again produce TTG melts. Partial melting of the lower thickened crust in either the presence (Figure 7.3d) or absence (Figure 7.3e) of a mantle diapir may also produce TTG melts, but the uncertain location of the extrapolated boundary of the amphibole stability field makes this questionable. The small-scale delamination setting does not produce TTG melts in the amphibole stability field consistent with natural TTG's. More mafic material, represented by the greenish phase boundaries in Figure 7.3 for picrite/komatiite, show most melting in the (garnet-) pyroxenite fields, producing basaltic melts.

7.3.3 Production rates of continental material

Figure 7.4 shows the 2-D volume of felsic material produced in the different geodynamical settings listed in Table 7.2 and shown in Figure 7.3. The values for 1200x1200 km models (M_{tr} and M_{dia}) have been normalized to correspond to the 600x600 km domain of the other models. It is clear from this figure that the crustal production rates range over orders magnitude for the different processes. A single small-scale delamination (see Figure 7.3a) produces about 30km² of crust in 10 million years, whereas partial melting of metabasalt associated with a resurfacing event (see Figure 7.3b,c) produces nearly

2000km² in less than 2 million years. This corresponds to equivalent felsic layers spread out over the entire domain width of 50 m and 3.3 km, respectively. Another important point of Figure 7.4 is the near coincidence of the curves of models Mtrc (thickened crust) and Mdia (lower mantle diapirism). This indicates that although much hot lower mantle material is introduced into the upper mantle in model Mdia and not in model Mtrc, it does not pass this heat on directly to the lower crust to allow it to melt. The diapir head spreads out in the upper mantle and does not reach depths less than 100 km (consistent with the maximum depth of 90 km attained by a numerical model diapir in similar thermal and identical rheological conditions in Van Thienen et al., 2003a, and chapter 8), and does not reach shallower levels where crustal material is present.

7.3.4 Distribution of felsic material in the crust

In order to link the results of our numerical experiments to field observations on Archean cratons, we examine the distribution of felsic material in the crust and its association with basaltic material. Figure 7.5 illustrates the distribution of basaltic and felsic material in the crust of model Mtrc (see Figure 7.3c) by showing all individual particle tracer compositions (basaltic: black, felsic: green, peridotitic: blue) in different regions of the domain. Zoom-ins of two settings in which TTG-melts are produced by partial melting of (meta-)basalt, indicated by red squares in the top panel, are presented in the lower frames. The left panel shows a crustal section associated with the partial melting of young lower crust in a resurfacing setting. Although basaltic material dominates the crust, a significant amount of felsic material is interspersed throughout the crust. In our model, this is produced by the successive stacking of basaltic and felsic extrusives, but in a similar setting in the Earth, intrusives are also possible. The lower right panel of Figure 7.5 shows a zoom-in of a crustal section associated with 'subducting' basaltic crust. This image is quite different from the previous, since in the downwelling part only partial melting of metabasalt is taking place, and not of peridotite. This results in the exclusive production of felsic crust without any associated basaltic crust. In our model, a felsic body of about 20 km width and 10 km depth is produced.

7.4 Discussion

The results of our modelling experiments as shown in Figure 7.3 indicate that the production of TTG lavas in the amphibole stability field in a hot Archean mantle is more likely to take place in settings associated with a resurfacing event than in association with a mantle plume or small scale delamination of the lower crust. However, due to the simplifications made in our numerical model, one possibly important agent of heat transfer is not included in our experiments. The emplacement of a basaltic liquid (both the high temperature and the latent heat effect of solidification) may cause significant amounts of partial melting in the lower amphibolitic crust (Huppert and Sparks, 1988; Petford and Gallagher, 2001). Therefore, specifically mantle diapirism may still be important because it may generate large amounts of basaltic melt (see the blue tracers in the middle frame of

Figure 7.3e, indicating peridotite melting), which may in this way cause partial melting in the lower crust. It may also play an additional role in the partial melting of the newly produced crust associated with a resurfacing event in Figure 7.3b. However, because of the smaller length scales of porous 2-phase flow compared to flow of mantle material (Scott and Stevenson, 1984, find magma soliton wave lengths of a few kilometers for plausible estimates of parameter values, which require a spatial resolution of an order of magnitude smaller to be accurately resolved numerically), inclusion of realistic melt segregation through multi-phase flow in upper mantle scale numerical models is a major computational challenge at the moment.

Because the resurfacing events as shown in Figure 7.3b,c are episodic, the production of felsic material in the associated settings is episodic as well. This is consistent with geological evidence, which indicates that the addition of felsic material to cratons was an episodic process, for example in the Pilbara craton (Smith, 2003) and the Kaapvaal craton (Anhaeusser and Walraven, 1999).

On average, Archean cratons consist of 60 percent granitoid gneiss, 30 percent massive granitoid plutons and 10 percent greenstone belts (Goodwin, 1991). These greenstone belts generally consist of successions of major (ultra)mafic and minor felsic supracrustal rocks, and have *preserved* thicknesses of 5-20 km (Condie, 1994). The massive granitoid plutons, on the other hand, are units of tens to over 100 km diameter that consist of granitoids, the early and mid-Archean cases typically belonging to the TTG suite and later granitoids being dominated by potassic granites (Goodwin, 1991). The greenstone association may correspond well to the type of crust produced by partial melting of the lower part of newly produced crust in association with a resurfacing event, as can be seen in the lower left panel of Figure 7.5. The granitoid plutons correspond well to the large volume of felsics that are produced above a sinking crust in a resurfacing setting without any associated basalts, as shown in the lower right panel of Figure 7.5. Zegers et al. (1999) did radiometric dating of felsic intrusives and supracrustal (greenstone belt) rocks from the eastern Pilbara (> 3 Ga), and found two distinct periods of about 50-80 Myr in which both large batholiths and supracrustal rocks were produced. This shows that the coeval production of these two types of rock associations may be consistent with geological observations. Although greenstone belts appear to have been formed in a variety of settings, a number of them show oceanic assemblages (Kimura et al., 1993; Nijman et al., 1998; Kerrich et al., 1999). The setting in which the greenstone-like succession is produced, forming the new crust in a resurfacing event, can also be considered an oceanic environment. The short time scale on which the crust interpreted as greenstone belt in our model is produced contrasts with the fact that the age of individual units within a greenstone belt may show an age range of 300 Myr (Thurston, 1994). Therefore, it may be more realistic to interpret the crustal segment produced in the resurfacing event as a single unit of a greenstone belt, to which new material may be added later by similar or other processes.

On the basis of these results, we propose that resurfacing events may have played an important role in the early formation of Archean cratons. The mechanism coevally forms both greenstone-like successions and massive volumes of felsic melt, which may form large plutons. The TTG's produced have low Nb/Ta and high Zr/Sm ratios as a result of

melting in the amphibolite stability field, consistent with analyses of Archean TTG rocks (Foley et al., 2002). Furthermore, this mechanism does not require the operation of plate tectonics, which is often invoked to explain Archean geology in general (e.g. De Wit, 1998) and greenstone belt formation specifically (see Table 5 of Polat et al., 1998), but against which strong physical arguments have been published for a hotter mantle (Vlaar, 1986; Vlaar and Van den Berg, 1991; Van Thienen et al., 2003c, chapter 4).

Our model results are also relevant for Venus. Crater count studies indicate that a global resurfacing took place on Venus around 500 million years before present (Schaber et al., 1992). Resurfacing may have taken place episodically on Venus (Turcotte, 1995; Fowler and O'Brien, 1996), possible by periodic plate tectonics (Solomatov and Moresi, 1996) or by the resurfacing mechanism that is applied in this work (Van Thienen et al., 2003b, chapter 6). Venus is a dry planet, although it may have been somewhat wetter in its earlier history, possessing a fraction of $x \cdot 10^{-3}$ of the terrestrial oceans (Campbell and Taylor, 1983; Nimmo and McKenzie, 1998). Since the production of granitoids requires water (Campbell and Taylor, 1983), the resurfacing mechanism would not produce granitoids on Venus as it does in our models applied to Earth, in line with the absence of evidence for significant amounts of silicic crust on Venus.

7.5 Conclusions

The model results show partial melting of metabasalt at two distinct settings associated with rapid resurfacing, at the base of newly produced basaltic crust and in the necking part of a 'subducting' old crust, takes place in the amphibolite stability field when assuming a basaltic or gabbroic crustal composition. In the other settings that were investigated, which are small scale delamination of the lower crust, melting at the base of an anomalously thick crust and melting associated with a lower mantle diapir, partial melting of metabasalt generally takes place under uncertain metamorphic conditions or in the eclogite stability field. Since the former type of melting produces TTG melts with Nb/Ta and Zr/Sm ratios consistent with geochemical observations, and the latter does not, we suggest that partial melting of metabasalt associated with resurfacing events may have been an important agent in the production of continental material during the early history of the Earth. Furthermore, the configuration of the rock associations produced in our model resembles Archean granite-greenstone terrains, and we therefore propose that the resurfacing mechanism may have played an important role in the generation of (some of) these granite-greenstone associations found on Archean cratons. The resurfacing mechanism may also have been active on Venus, but due to the dryness of this planet, it probably did not produce large volumes of continental material.

Chapter 8

Interaction between small-scale mantle diapirs and a continental root

Abstract

A possible mechanism for adding material to a continental root is by means of upwellings from the convecting mantle subject to pressure release partial melting.

We present results of numerical modeling of the interaction of melting diapirs with continental roots in an Archean setting characterized by a mantle potential temperature of 1750 °C in a 2-D Cartesian geometry.

In an extension of earlier work (De Smet et al., 2000a) we have investigated the influence of mantle rheology on the behavior of diapirs. We have in particular looked at the difference in behavior of diapirs using a composite rheology combining both grain size sensitive diffusion creep and dislocation creep mechanisms. We have used the grain size, here taken to be uniform, as a control parameter to obtain model cases with varying contribution from the two creep mechanisms. The diapirs in the composite rheology model rise much faster than in a purely Newtonian model. Observed diapiric ascent times from 230 km depth to the top of the ascent path at about 80 km depth are approximately 1 Ma for a Newtonian model (averaged 14 cm/year) compared to about 50 thousand years for a composite rheology model (averaged 3 m/year) with the same parameters for the Newtonian component. This clearly indicates the large impact of the dislocation creep component of the viscous deformation process.

We have also investigated the effect of an increase in the viscosity due to dehydration during partial melting. This increase has a strong influence on the development of rising diapirs. The ascent velocity and lateral spreading of the diapirs at the end of their ascent

This chapter has been published as: Van Thienen, P., A.P. van den Berg, J.H. de Smet, J. van Hunen and M.R. Drury, Interaction between small-scale mantle diapirs and a continental root, *Geochem. Geophys. Geosyst.* 4(2), 8301, doi:10.1029/2002GC000338, 2003

are effectively reduced when a viscosity increase by a factor of 10 is applied, and the effect becomes stronger for larger factors. Average vertical velocities range from 1.4 cm/yr for a factor 10 to 2 mm/yr for a factor 200.

The most striking result of the viscosity increase due to dehydration is the reduction of the ascent velocity, thereby stretching the characteristic time scale of the diapiric intrusion process to a value between 5 and 50 Ma for dehydration viscosity prefactor values of 10 and 200, respectively.

In contrast with the strong difference between the Newtonian and the composite rheology models, small differences are found in the overall dynamics between the composite rheological models, characterized by different values of the uniform grain size. The composite rheological models exhibit a selfregulating behavior where substantial differences between the relative contributions of the two creep components result in very similar effective viscosities, due to a local dominance of dislocation creep at high stresses, and corresponding similar flow dynamics.

Stress levels and P,T-paths in the modeling results are consistent with estimates obtained from Precambrian peridotite bodies which are interpreted to have originated from asthenospheric diapirism.

8.1 Introduction

Numerical modelling experiments have shown that mantle diapirs could be important agents in the growth of continental roots during the Archean and Proterozoic (De Smet et al., 1998). These mantle diapirs are generally on a scale of 50 to 100 km and penetrate an existing root while producing melt, and a complementary depleted low density residue, thus adding depleted material to the continental root. Plumes rising through the mantle are strongly influenced by the type of rheology.

The two important deformation mechanisms in the upper mantle are diffusion creep and dislocation creep (Karato and Wu, 1993). Diffusion creep takes place through diffusion of mass between grain boundaries. The strain rate increases linearly with applied stress, and decreases in a powerlaw fashion with the grain size. Dislocation creep, on the other hand, takes place through the transport of dislocations in the crystal structure. It has a powerlaw relation between applied stress and resulting strain rate (non-linear), and it is insensitive to grain size (Karato and Wu, 1993). The viscosity corresponding to dislocation creep flow decreases with increasing stress, a phenomenon known as shear-thinning. For the present mantle, dislocation creep is generally the dominant mechanism in the asthenosphere, whereas diffusion creep dominates in the lithospheric mantle and in the deeper upper mantle and lower mantle (Karato et al., 1995; Van den Berg and Yuen, 1996). Since olivine is the weakest major phase in mantle peridotite, the rheology of the upper mantle is probably dominated by olivine (Karato and Wu, 1993). Next to the microphysical approach to mantle rheology, the inversion of glacial rebound data also gives information on the viscosity of the mantle. Using this approach, Lambeck et al. (1998) have found the upper mantle viscosity to be about $3 - 4 \cdot 10^{20}$ Pas. The hotter Archean upper mantle, however, may have had a viscosity several orders of magnitude lower than

this figure due to the strong temperature dependence of both diffusion creep and dislocation creep. Furthermore, the temperature dependence of the dislocation creep mechanism as expressed in the activation energy parameter of the rheological flow is higher than for the diffusion creep component. From this one can predict a greater predominance of the dislocation creep component under higher temperature conditions, representative for the early Earth. This has motivated us to extend our previous work on growth mechanisms of continental roots, based on purely diffusion creep models (De Smet et al., 1998; De Smet, 1999; De Smet et al., 1999, 2000c,b), with a detailed investigation of more complete viscous rheology including also the rheological effect of dislocation creep flow and sensitivity for the degree of dehydration induced by partial melting.

Non-linear rheology can greatly enhance the velocity of plumes (Weinberg and Podladchikov, 1994; Larsen et al., 1997; Larsen and Yuen, 1997; Van Keken, 1997) relative to a Newtonian rheology case, and can therefore more effectively transport heat up to shallow lithospheric levels. Another important effect of non-linear rheology is the generation of localized high strain rates, which may result in viscous heating, with a lubricating effect through the temperature dependence of the rheology (Van den Berg and Yuen, 1997; Larsen et al., 1999). Combined, these two effects can cause regions of high temperature at shallow depths, which may induce secondary melting and crustal diapirism (Campbell and Hill, 1988). On the other hand, melting lowers the temperature by means of latent heat consumption, and may also increase the viscosity of the residue directly. This is due to the fact that at low degrees of partial melting, water tends to concentrate in the melt phase, effectively drying the residue. Experiments have shown that water has a weakening effect (e.g. Chopra and Paterson, 1981), and from these observations, Karato (1986) concluded that at low degrees of partial melting, the strength of the residual matrix is increased by melting. This increase of viscosity of the residual depleted peridotite could be as high as a factor of 100 to 180 (Hirth and Kohlstedt, 1996). The importance of this effect for plumes has been ascertained by Ito et al. (1999) and Ito (2001). Karato and Jung (1998) find that this dehydration effect does not only influence the viscosity, but is also connected to the low seismic velocity and high attenuation in the asthenosphere.

Samples of cratonic lithosphere are found as xenoliths in kimberlite intrusions (Nixon and Boyd, 1973) and as larger bodies in some orogenic belts (Brueckner and Medaris, 1998; Van Roermund and Drury, 1998). It is proposed that many of these mantle rocks are emplaced into the lithosphere by diapirs from the convecting sublithospheric mantle (Nicolas, 1986) in a variety of geodynamic environments (Green and Gueguen, 1983; Nicolas et al., 1987; Fabriès et al., 1991). The PT paths derived from some cratonic peridotites from the Norwegian Western Gneiss Region (Van Roermund and Drury, 1998; Drury et al., 2001) imply that these rocks were part of diapirs that intruded cratonic lithosphere of Archean to early Proterozoic age (the cooling age of these rocks is 1.7-1.8 Ga, but the Sm-Nd model age indicates a depletion age of 2.5-3.0 Ga). Drury et al. (2001) have shown that the PT path of these peridotites is consistent with PT paths of diapiric upwellings calculated from the thermo-chemical convection models of De Smet (1999); De Smet et al. (1999).

In this paper, we present results of numerical modelling experiments which were devised to model the interaction of diapirs with the continental root, and we investigate in

particular the sensitivity of the model for the rheological parameterization. We place the models in an Archean setting by prescribing a potential mantle temperature of 1750 °C. We determine the effect of varying the rheological flow law from Newtonian diffusion creep only, into a composite law combining both grainsize sensitive Newtonian diffusion creep and powerlaw (grainsize independent) dislocation creep. Different grain sizes are used to test for varying strengths of the diffusion creep component (dislocation creep is grain size independent). Furthermore, we investigated the effect of dehydration during partial melting. This extends earlier work by De Smet et al. (1998); De Smet (1999); De Smet et al. (1999, 2000c,b) based on purely Newtonian rheology.

The potential temperature of 1750°C which we use is relatively high and may be representative of the earlier half of the Archean. Parametric cooling models for the Earth of Richter (1985) show mantle potential temperatures for the Archean of about 1450 to 1700°C. However, the high MgO contents of Archean komatiites point to higher potential temperatures, up to 1800°C for 2.7 Ga old Belingwe komatiites and even 1900°C for 3.45 Ga old Barberton komatiites (Nisbet et al., 1993). Melting experiments of Walter (1998) show that Archean komatiites can be formed by dry batch melting of pyrolite at pressures of 7 to 10 GPa. Extrapolation along an adiabat of the solidus temperature (using the solidus of Herzberg and Zhang, 1996) at these pressures shows that this corresponds to potential temperatures in the range of 1700 to 1800°C. These temperatures probably represent plume temperatures in a cooler mantle. For the current mantle, estimates for the excess temperature of plumes are up to 200 to 250°C (Herzberg and O'Hara, 1998). In a hotter Earth, the temperature controlled viscosity would be lower and therefore also the maximum horizontal temperature variations would be reduced (McKenzie and Bickle, 1988; Nisbet et al., 1993) to about 50-150°C (Nisbet et al., 1993), which puts our potential temperature of 1750°C within the range indicated by the komatiites of Nisbet et al. (1993). Some authors have suggested that komatiites may be formed by hydrous melting (Stone et al., 1997) at temperatures only about 100 °C higher than present mantle temperatures (Parman et al., 1997). Arndt et al. (1998) however conclude that most komatiites were the product of dry melting. The potential temperature of 1750°C of our models is also consistent with the results of the numerical models of De Smet et al. (2000b) which form the starting point of our investigations.

The analysis of structures and microstructures in mantle rocks may provide estimates of the differential stresses and strain rates during high temperature deformation associated with diapir upwelling in a cratonic lithosphere. We use this information to compare our model results to the peridotites from western Norway mentioned above, which are interpreted as a natural example of a Precambrian asthenosphere diapir (Drury et al., 2001).

In the work of De Smet et al. (op. cit.), small scale diapirs are generated in a self-consistent way in hot upwelling limbs of large scale (1000 km) mantle convection cells. Here we take a different approach and zoom in on a smaller region surrounding a single uprising diapir and follow the detailed evolution during its ascent into and within the chemically distinct mantle root.

8.2 Numerical model setup

8.2.1 Description of the numerical model

We have used a 2-D Cartesian thermo-chemical convection code including partial melting. An extended Boussinesq approach was used assuming infinite Prandtl number, including viscous dissipation, adiabatic compression and latent heat of melting. Partial melting is modelled as an (irreversible) increase in the *degree of depletion* F , which is defined here as the mass fraction of melt which is extracted from an initially unmelted material control volume of mantle material. Since no material is actually removed in our model, volumes of depleted residual material are somewhat overestimated (De Smet, 1999). Because of the relatively short time scale of the models (< 50 Ma), internal heating by the decay of radioactive elements was not included. This model is described by the following non-dimensional equations (De Smet et al., 1998). The energy equation (see Table 8.1 for explanation of the symbols used):

$$\frac{dT}{dt} - Di(T + T_0)w = \nabla^2 T + \frac{Di}{Ra} \Phi - \frac{\Delta S}{c_p} \frac{dF}{dt} (T + T_0) \quad (8.1)$$

The incompressibility condition and the non-dimensional momentum equation:

$$\nabla \cdot \vec{u} = 0 \quad (8.2)$$

$$\nabla[\eta(\nabla\vec{u} + \nabla\vec{u}^T)] - \nabla\Delta p = (RaT + RbF)\hat{z} \quad (8.3)$$

Evolution of the degree of depletion is described by the following equation:

$$\frac{dF}{dt} = S(P, T, F) \quad (8.4)$$

The source function S in (8.4) is used to describe the rate of partial melting, applying a simple parameterization of the melting phase diagram of mantle peridotite in terms of a solidus and liquidus. S is defined by means of expressing the differential dF in terms of pressure and temperature differentials as described in more detail in appendix A of De Smet et al. (1998). We use two different parameterizations of the solidus and the liquidus. The first one has a linear and parallel liquidus and solidus, based on data presented by (Takahashi and Kushiro, 1983, up to 3.5 GPa, so we are extrapolating at higher pressures). The second uses a third order polynomial parameterization, based on data by Herzberg and Zhang (1996). Our isobaric melting curve, which is based on data presented by Jaques and Green (1980), is linear in both cases (Vlaar and Van den Berg, 1991; De Smet et al., 1998).

Two deformation mechanisms are included in the models: diffusion creep (linear) and dislocation creep (non-linear). We test models which use the diffusion creep component exclusively (models N1-N3), as well as models with a composite rheology (models C1-C5), combining the diffusion creep and dislocation creep mechanisms (see Tables 8.2, 8.3 and 8.4 for details). An extra effect also included in some models (models D1-D3) is the effect of dehydration by partial melting. The models will be described in more detail below.

symbol	property	definition	value/unit
c_p	heat capacity at constant pressure		1000/1250 Jkg ⁻¹ K ⁻¹
Di	dissipation number	$\frac{\alpha gh}{c_p}$	0.09408
e_{ij}	strain rate tensor	$\partial_j u_i + \partial_i u_j$	s ⁻¹
e	second invariant of the strain rate tensor	$[\frac{1}{2}e_{ij}e_{ij}]^{\frac{1}{2}}$	s ⁻¹
F	degree of depletion		
g	gravitational acceleration		9.8 ms ⁻¹
h	length scale		400 · 10 ³ m
Ra	thermal Rayleigh number	$\frac{\rho_0 \alpha \Delta T g h^3}{\kappa \eta_0}$	1.24 · 10 ⁶
Rb	compositional Rayleigh number	$\frac{\delta \rho g h^3}{\kappa \eta_0}$	1.42 · 10 ⁶
S	melt productivity function		s ⁻¹
ΔS	entropy change upon full differentiation		300 Jkg ⁻¹ K ⁻¹
t	time		s
T	temperature		°C
T_0	non-dimensional surface temperature		$\frac{273}{\Delta T}$
ΔT	temperature scale		1923 °C
w	vertical velocity		ms ⁻¹
\hat{z}	unit vector in vertical (downward) direction		
α	thermal expansion coefficient		3 · 10 ⁻⁵ K ⁻¹
ϵ_T	relative amplitude of thermal perturbation	$\frac{\delta_T}{T(z)}$	
η	viscosity		Pas
η_0	reference viscosity		10 ²⁰ Pas
κ	thermal diffusivity		10 ⁻⁶ m ² s ⁻¹
ρ_0	reference density		3416 kgm ⁻³
$\delta \rho$	density difference upon full depletion	$\frac{\partial \rho}{\partial F}$	226 kgm ⁻³
τ_{ij}	deviatoric stress tensor	ηe_{ij}	Pa
τ	second invariant of the deviatoric stress tensor	$[\frac{1}{2}\tau_{ij}\tau_{ij}]^{\frac{1}{2}}$	Pa
Φ	viscous dissipation	ηe^2	Jm ⁻³ s ⁻¹

Table 8.1: Symbols of the energy and momentum equations (equations 8.1-8.3), the transport equation (8.4) and the strain equation (8.5).

symbol	property	value / unit
A	strain rate prefactor	s^{-1}
B	effective viscosity prefactor	Pa s or $\text{Pa}^{3.25}\text{s}$
b	length of Burgers vector	$5 \cdot 10^{-10} \text{ m}$
d	grain size	m
E	activation energy	Jmol^{-1}
m	grain size exponent	2.5, 0
n	stress exponent	1.0, 3.25
P	pressure	Pa
R	gas constant	$8.3144 \text{ Jmol}^{-1}\text{K}^{-1}$
T	temperature	K
V	activation volume	$\text{m}^3\text{mol}^{-1}$
μ	shear modulus	$80 \cdot 10^9 \text{ Pa}$
τ	second invariant of deviatoric stress tensor	Pa

Table 8.2: Symbols of the equations describing the rheology (equations 8.7 and 8.8). Values of the viscosity prefactors A and B and grain size and stress exponents m and n are specified in Table 8.3. Two units are specified for the viscosity prefactor, the first being applicable to diffusion creep, and the second to non-linear dislocation creep.

Our composite rheology models combine both the diffusion creep and the dislocation creep mechanisms (see also Van den Berg et al., 1993). Their combined effect is defined through a superposition of the corresponding strain rates:

$$e_{ij} = e_{ij1} + e_{ij2} = \left[\frac{1}{\eta_1} + \frac{1}{\eta_2} \right] \tau_{ij} \quad (8.5)$$

with the subscript 1 indicating diffusion creep and 2 indicating dislocation creep, and the effective viscosity given by

$$\eta = \left[\frac{1}{\eta_1} + \frac{1}{\eta_2} \right]^{-1} \quad (8.6)$$

The corresponding viscosity components η_k are defined by the dimensional Dorn equation:

$$e_k = A_k \left(\frac{\tau}{\mu} \right)^{n_k} \left(\frac{b}{d} \right)^{m_k} \exp \left[-\frac{E_k + PV_k}{RT} \right], \quad k = 1, 2 \quad (8.7)$$

We assume a constant grain size d in (8.7) in the diffusion creep component. This is used as a control parameter to distinguish between model cases with different partitioning between the two creep mechanisms.

JdS					
mechanism	η_{ref} (Pas)	P_{ref} (GPa)	T_{ref} (°C)	E (Jmol ⁻¹)	V (m ³ mol ⁻¹)
diff ($k=1$)	10^{21}	13.39	1750	$250 \cdot 10^3$	$7.5 \cdot 10^{-6}$
KW Composite					
mechanism	A_k (s ⁻¹)	B_k (Pa ^{3.25} s)	n_k, m_k	E_k (Jmol ⁻¹)	V_k (m ³ mol ⁻¹)
diff ($k=1$)	$7 \cdot 10^{15}$	Table 8.4	1.0, 2.5	$270 \cdot 10^3$	$6 \cdot 10^{-6}$
disl ($k=2$)	$2.5 \cdot 10^{20}$	$1.089 \cdot 10^{15}$	3.25, 0	$485 \cdot 10^3$	$17.5 \cdot 10^{-6}$

Table 8.3: Parameters for the different viscosity models which are used. η_{ref} , P_{ref} and T_{ref} are reference viscosity, pressure and temperature, respectively (other symbols are explained in the caption of Table 8.2), and are used following De Smet et al. (1998, 1999, 2000a,b), indicated by JdS. The components of composite rheology are based on data by Karato and Wu (1993), indicated by KW, and are chosen to be intermediate between their 'wet' and 'dry' parameters.

Equation (7) can be transformed into a viscosity expression (see Van den Berg and Yuen, 1998):

$$\eta_k = B_k \exp \left[\frac{E_k + PV_k}{RT} \right] \tau^{1-n_k}, \quad k = 1, 2 \quad (8.8)$$

For values of n unequal to unity, η_k introduces a non-linearity through (8.6) in the momentum equation (8.3) (Van den Berg et al., 1993).

Depending on local values of temperature, pressure and shear stress, one of the two creep mechanisms in (8.5) is dominant. We use the grain size as a control parameter for the transition between these domains. The transition stress τ_t at which both mechanisms are equally important for a specific temperature and pressure can be calculated by equating the viscosity components in (8.5), using (8.8), resulting in:

$$\tau_t^{n-1} = \frac{B_2}{B_1} \exp \left[\frac{(E_2 - E_1) + P(V_2 - V_1)}{RT} \right] \quad (8.9)$$

As shown in Table 8.3, both $\Delta E = E_2 - E_1$ and $\Delta V = V_2 - V_1$ are positive for the parameters we use. Therefore, the temperature and pressure dependence of the parameter τ_t^{n-1} is similar to the P,T dependence of the viscosity components, with a minimum in the asthenosphere (Karato and Wu, 1993). The expression (8.9) indicates that the transition stress decreases for increasing temperature, which implies that for constant pressure non-Newtonian creep becomes more important with increasing temperature. As a consequence of this, the role of dislocation creep in the hotter early Earth must have been greater than today.

The set of equations (8.2), (8.3), (8.4) was solved using finite element methods and a Predictor-Corrector time integration scheme, described in Van den Berg et al. (1993). Picard iteration for the Stokes equation (8.3) was used to deal with the non-linearity arising

from the non-linear rheology. The finite element meshes used contain approximately 10^4 triangular (6 point) elements, with element sizes ranging from about 24 km in areas of low flow velocity to approximately 3 km in high flow velocity areas. The degree of depletion F was modelled (equation 8.4) using a Lagrangian particle tracer method, using $4 \cdot 10^5$ tracers in a random (uniform) distribution. Fourth order Runge-Kutta time integration is used to advect the particle tracers with the mantle flow velocity. The transformation of particle tracer field values (the degree of depletion) to finite element Gauss points uses a Particle in Cell algorithm (Hockney and Eastwood, 1988). We tested two models with the tracer density multiplied by a factor 1.5, which gave no significantly different results, so we are confident that the tracer resolution used ($4 \cdot 10^5$) is sufficient. We also tested our thermochemical code using the widely used benchmark given by (Van Keken et al., 1997, case 1a)

The depletion-dependence of the viscosity (dehydration effect) is modeled as a composition dependent viscosity prefactor $f_\eta(F)$. This uses a piece-wise linear continuous parameterization: $f_\eta = 1$ for $F < 0.005$. For $F > 0.05$ $f_\eta = 10$ (model D1 in Table 8.3), 50 (model D2), or 200 (model D3). In the intermediate interval $0.005 < F < 0.05$ f_η is a linear function of F , continuous at the interval boundaries. The small width of the transition interval from $f_\eta = 1$ to $f_\eta = 10$, 50 or 200 corresponds to the fact that most water is expelled already at low degrees of melting (Karato and Jung, 1998, Figure 3). The choice of the magnitude of this prefactor is based on two observations. The first is experimental results by Hirth and Kohlstedt (1996), indicating a viscosity increase by a factor of 100 to 180 upon dehydration. This gives an upper bound factor of 200. The second observation is evidence for re-hydration found in studies of craton xenoliths (Harte, 1983). Since re-hydration would lower the viscosity again, we have used two, admittedly arbitrary, lower bound values of 10 and 50. The rheological parameters which are used are presented in Tables 8.3 and 8.4, and the labeling of the different model cases is defined in Table 8.4.

For models C1-C5 and D1-D3 (composite rheology cases), we specified the parameters in equation (8.7). We used intermediate values between the wet and dry parameters of Karato and Wu (1993), since they conclude that ‘the rheology of the ... subcontinental upper mantle is between that of dry (water-free) and wet (water-saturated) olivine’, based on the water content of basalts, infrared spectroscopy of mantle minerals, laboratory studies of water solubility in olivine and observations of the electrical conductivity of the suboceanic upper mantle. Each model run has a constant grain size, which is varied between the models from 0.5 to 5 mm. This results in the effective prefactors B_k of equation (8.8), the values of which are specified in Tables 8.3 and 8.4. For models N1-N2 (Newtonian rheology), we specified a reference viscosity η_{ref} at a reference pressure P_{ref} and temperature T_{ref} , and activation energy and volume, following De Smet et al. (2000c), to allow direct comparison of the results.

The density of mantle material is related to the degree of depletion F (Jordan, 1979). In the buoyancy term of the Stokes equation (8.3), we use a linearized parameterization of the composition dependent density (Vlaar and Van den Berg, 1991), and the coefficient $\partial\rho/\partial F$ enters the compositional Rayleigh number Rb , in the momentum equation (8.3) (see also De Smet et al., 1998, 2000b). We assume all melt to be removed instantaneously

to shallower or surface levels, where it can no longer play a role in the development of the diapirs. Because of this assumption, we neglect the buoyancy effect of melt retention, which leads to an underestimate of the buoyancy term (e.g. Scott and Stevenson, 1989; Buck and Su, 1989; Jha et al., 1994). This partly cancels the overestimation of the volume of depleted residue mentioned above.

For most of the models, we use a third order parameterization of the solidus and liquidus in the melting phase diagram of mantle peridotite (Herzberg and Zhang, 1996), which is an improved version of the first order approximation (based on Takahashi and Kushiro, 1983), that is used in models N1 and C5 only. The former is a more accurate description of the solidus and liquidus, especially for melting at depths greater than 100 km.

Since we are working in a 2-D Cartesian geometry, the structures we are modelling can be extended in the third dimension, and we are in fact dealing with a horizontal cylinder rather than a more or less spherical diapir. In an axisymmetric geometry, diapir penetration along the axis of symmetry is easier than in 2-D Cartesian geometry, and subsequent spreading of the diapir head will be more pronounced in 2-D Cartesian geometry than in an axisymmetric geometry. However, we do not expect these differences to dominate the results of our model experiments.

model	rheology model	grain size (mm)	B_1 (Pas)	f_η	T_{pot} ($^{\circ}$ C)	sol.+liq.
N1	JdS	2.8	$8.95 \cdot 10^{11}$	1	1800	TK
N2	KW diff.	1.0	$8.95 \cdot 10^{11}$	1	1750	HZ
C1	KW	0.5	$1.143 \cdot 10^{10}$	1	1750	HZ
C2	KW	1.0	$6.465 \cdot 10^{10}$	1	1750	HZ
C3	KW	5.0	$3.614 \cdot 10^{12}$	1	1750	HZ
C4	KW	50	$1.143 \cdot 10^{15}$	1	1750	HZ
C5	KW	1.0	$6.465 \cdot 10^{10}$	1	1750	TK
D1	KW	1.0	$6.465 \cdot 10^{10}$	10	1750	HZ
D2	KW	1.0	$6.465 \cdot 10^{10}$	50	1750	HZ
D3	KW	1.0	$6.465 \cdot 10^{10}$	200	1750	HZ

Table 8.4: Models and their distinguishing characteristics. The entries under *rheology model* refer to Table 8.3. KW indicates both diffusion and dislocation creep components, unless it is specified otherwise (*diff* for diffusion creep only). JdS indicates a diffusion creep component only. The viscosity prefactor B_k in equation (8.8) is given for the diffusion creep component, as a function of the grainsize. The dislocation creep prefactor B_2 is specified in Table 8.3, as it is insensitive to grainsize. The viscosity depletion factor f_η defines the local relative viscosity increase if the local degree of depletion is larger than a threshold, see text for details. The entries under *sol.+liq.* refer to the parameterization of the solidus and liquidus that was used, which is either linear (TK, based on data by Takahashi and Kushiro, 1983) or third order polynomial (HZ, based on Herzberg and Zhang, 1996).

8.2.2 Model geometry and initial and boundary conditions

We have adopted a 200×400 km spatial domain with a symmetry condition on the vertical boundaries shown in Figure 8.1. Because of the limited aspect ratio of the domain, we have ensured by running tests with aspect ratios up to 6 times higher that possible effects of the right hand side vertical boundary play no significant role in the results of the modelling experiments. We define an initial degree of depletion profile starting with $F=0$ from 400 to 200 km depth and increasing linearly to $F=0.35$ from 200 to 80 km depth, keeping this value up to the surface (see Figure 8.1). This is a reasonable approximation of the continental roots as formed by the long term evolution models of De Smet et al. (1999, 2000b).

As an initial geotherm, we use the minimum value of the following three functions; (1) an adiabat (potential temperature 1750°C), (2) a linear profile from 0°C at the surface to the adiabat at 100 km depth, with a gradient $\partial T/\partial z = 17.9$ K/km, and (3) the solidus of mantle peridotite (see Figure 8.1).

The mantle diapir which is the subject of investigation is initiated here by adding a Gaussian circular shaped thermal perturbation to the local background temperature. We use a perturbation with a radius (defined as the 2σ (2 standard deviations) distance from the maximum) of 48 km at 230 km depth and $x=0$ with an amplitude ϵ_T of 5% of the local background temperature (approximately 95°C), see also Figure 8.1. This is in accordance with thermal anomalies found by De Smet et al. (2000b) in mantle convection models of continental root growth. In their model, a thermal perturbation originating from deeper levels of the mantle crosses the solidus, starts melting and accelerates due to increasing depletion related buoyancy. Since these original models by De Smet et al. (op.cit.) employ a purely Newtonian rheology, the self-consistent generation of these plumes in a composite rheology and thus the choice of our initial condition is an extrapolation.

The results are sensitive to the amplitude and radius of the initial temperature perturbation as will be illustrated in Figures 8.14 and 8.15 below. In case the upper part of the initial perturbation is above the solidus temperature, the local degree of depletion is adjusted accordingly, creating an initial depletion.

All boundaries of the model are impermeable. The top boundary has a no slip condition, the others are free slip. Thermal boundary conditions are 0°C temperature at the top boundary, 1923°C at the bottom (consistent with the potential temperature of 1750°C), and insulating vertical boundaries.

In comparing the different results, it should be kept in mind that in all cases the same initial condition for the starting diapir is used (apart from model N1, which has the same relative perturbation of the temperature field but a higher potential temperature).

8.2.3 Model parameters

Detailed parameters of the different models are specified in Tables 8.3 and 8.4. Further physical parameters are given in Tables 8.1 and 8.2. We note that two different values of the specific heat c_p have been used. The lower value of $1000 \text{ J kg}^{-1} \text{ K}^{-1}$ is used to compare our results directly to previous results from De Smet et al. (1998), model N1

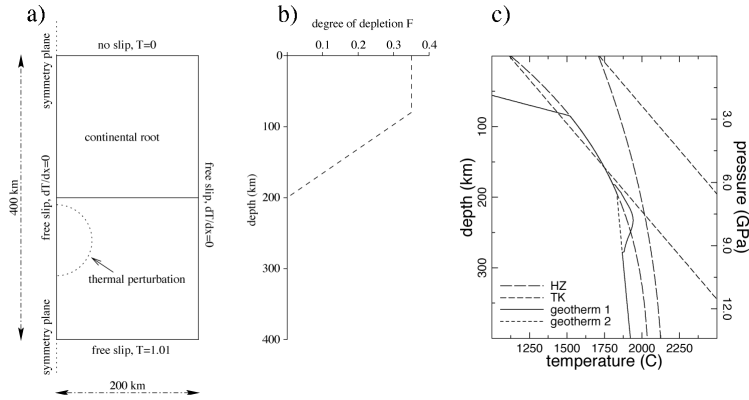


Figure 8.1: (a) Model setup. The rectangular domain is 200×400 km and has free slip boundary conditions except for a no slip to boundary. A symmetry plane is present at $x=0$. Next to the representation of the computational domain, the initial degree of depletion profile is plotted in frame (b). The solidus and liquidus parameterizations used are shown in frame (c) (TK: linear, based on Takahashi and Kushiro, 1983; HZ: third order polynomial, based on Herzberg and Zhang, 1996) with the most commonly used perturbed (geotherm1) and background (geotherm2) initial geotherms, see text for details.

in section 8.3.2. In all other cases we use a constant $c_p = 1250 \text{ J kg}^{-1} \text{ K}^{-1}$, based on data in Fei et al. (1991), resulting in a slightly reduced adiabatic gradient. We also consider two values of the potential temperature characterizing the adiabats used in the initial background temperature in our models. In the comparison case N1 we use a higher value of 1800°C representative for the results of De Smet et al. (1998). In all other models a reduced potential temperature $T_p = 1750^\circ\text{C}$ is used. This lower temperature would cause a lower degree of melting. However, this is countered by the use of the improved third order parameterization of solidus and liquidus (see section 8.2.1), which allows melting at depths greater than 200 km at lower temperatures than the linear parameterization.

8.3 Results of numerical modelling

In this section we present the results of our numerical models. First the results of linear rheology models N1 and N2 will be presented, followed by the composite rheology models C1-C5. For each of these, snapshots of temperature, composition, and viscosity and profiles of the composition and the temperature are shown. The transition between the two viscosity components will be described, illustrated by viscosity ratio plots and deformation maps. Subsequently, the effect of dehydration will be shown in the results of models D1-D3, again presenting snapshots and profiles of temperature and compositions

and snapshots of viscosity. Finally, ascent velocities for the diapirs and, in more detail, P,T paths and stress and strainrate histories for individual tracers will be presented.

8.3.1 General characteristics

In general terms (and ignoring time scales), the development of all diapir models is comparable. This is illustrated in Figures 8.2-8.7 and 8.10-8.12, which show a zoom-in window of part of the computational domain around the rising diapir. Note that the computational domain has been enlarged by adding the region $x < 0$ by symmetric extension around $x = 0$. Snapshots are shown of a rising diapir with time increasing upward labeled in the left hand column. Snapshots of degree of depletion, temperature and viscosity as well as profiles of the degree of depletion and temperature are shown in different columns a through e.

In each case, we see melting taking place by the formation of depleted material visible in frames a1-3. As the diapir rises, the highly depleted material at the top of the diapir head is swept aside, causing a decrease in the magnitude of the depletion peak visible in the composition profiles in frames d1-3 of these figures. The narrow band of low depletion initially surrounding the diapir head is stretched and thinned, reducing its visibility. The temperature snapshots show a decline of the thermal perturbation back to the background temperature field.

8.3.2 Linear rheology results

Results of a case with linear rheology model N1 are presented in Figure 8.2. The degree of depletion snapshots (frames a1-3) show the diapir developing a clear mushroom shape of some 100 km in diameter, quite similar to the diapir examined in De Smet et al. (1998), which developed self-consistently in a convecting upper mantle model. Corresponding temperature snapshots are shown in Figure 8.2b1-3. The figures illustrate the development of the decaying temperature anomaly of the hot diapir. The final snapshot at approximately 50 Ma shows the thermal anomaly has disappeared. The viscosity snapshots (c1-3) show a relatively uniform field in a large part of the domain, with a somewhat lower viscosity down to about 10^{19}Pas inside the diapir resulting from the thermal perturbation. The degree of depletion in the melting diapir reaches a value of about 0.25.

Vertical profiles of the composition (degree of depletion F) and temperature are shown in frames d1-3 and e1-3, respectively. The solid lines corresponding to centerline profiles at $x=0$ reveal the magnitude of the rising perturbation of the composition and temperature constituting the diapir, with respect to the background model which is represented by the dotted curves, corresponding to vertical profiles at $x=200$ km, which is a relatively undisturbed part of the model. The dashed curves in Figure 8.2e1-3 showing the Takahashi and Kushiro type solidus and liquidus used in the model illustrate the changing melting conditions as the diapir rises through the mantle. The results reproduce closely the previous results obtained by (De Smet et al., 1998) for a larger model where diapirs of a similar scale are generated in a self-consistent way in upwelling lines of large scale mantle convection cells.

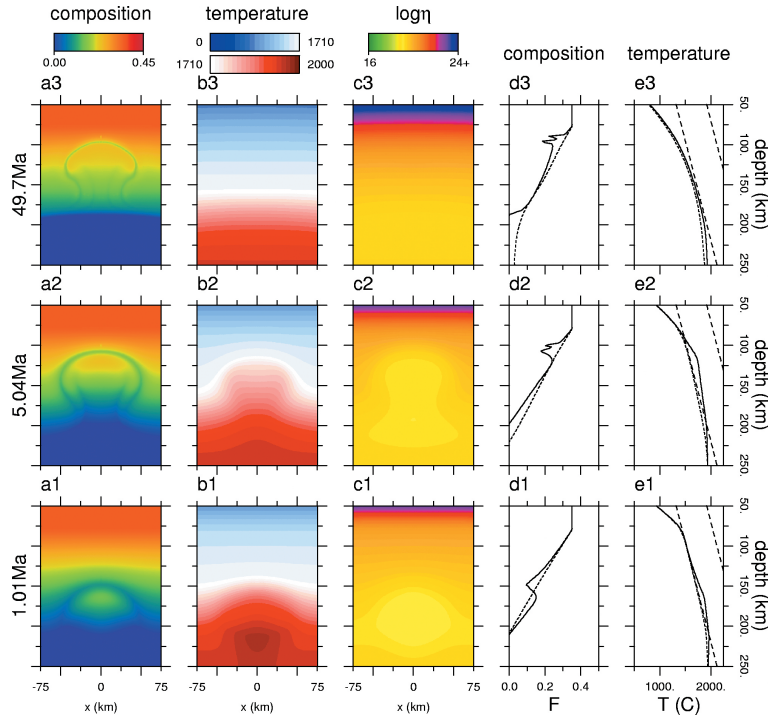


Figure 8.2: Model N1: Newtonian rheology only. Frames a1-3 show snapshots of the composition (or degree of depletion) field at 1.01 Ma, 5.04 Ma and 49.7 Ma after the start of the model run. The dimensions of the model are 400×400 km, but only a part of the domain is shown ($[x, y] = [-75 - 75, 50 - 250]$ km). Snapshots of the temperature field are presented in frames b1-3, and of the viscosity field in c1-3. Frames d1-3 and e1-3 show profiles of the composition and the temperature, respectively. The solid lines are profiles at $x=0$ km, which is the middle of the model, and dashed lines are profiles at $x=200$ km, which are relatively undisturbed. The long-dashed lines of frames e1-3 are the solidus and liquidus.

Figure 8.3 shows the results of model N2 with slightly different rheology parameters (following Karato and Wu, 1993, see Table 8.3, Newtonian component only), and somewhat modified values for the potential temperature (1750°C) and c_p ($1250 \text{ J kg}^{-1} \text{ K}^{-1}$, see Table 8.4). The modified rheology parameters result in a lower viscosity than in model N1, with a minimum value of about $2.8 \cdot 10^{18} \text{ Pa s}$ (frames c1-3), resulting in faster diapir ascent and much stronger deformation of the diapir head (see frames a1-3). The head rises to about 85 km depth in less than 5 million years, and is split in two by colder root material. In spite of the reduced initial temperature compared to model N1 as shown in frames e1-3, a higher degree of depletion is attained with a maximum of 0.38 due to the

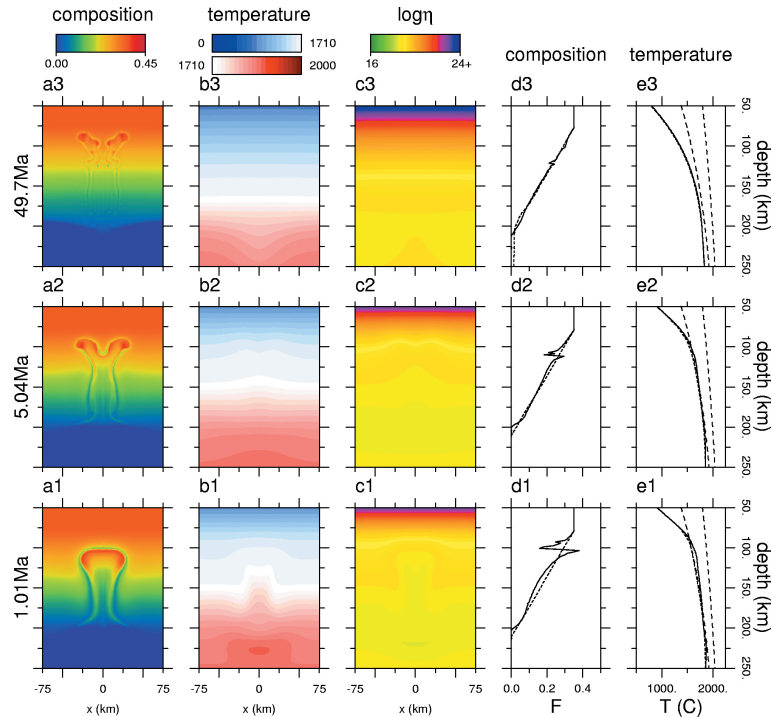


Figure 8.3: Model N2: Newtonian rheology. Only a part of the domain is shown ($[x, y] = [-75 - 75, 50 - 250]$ km). Frames a1-4 show the composition field and frames b1-3 show the temperature field at 1.01 Ma, 5.04 Ma and 49.7 Ma after the start of the model run. Snapshots of the viscosity field are presented in frames c1-3. Profiles of composition and temperature are presented in frames d1-3 and e1-3, respectively. For an explanation of line types, see caption of Figure 8.2.

faster ascent.

8.3.3 Composite rheology results: grain size variation

Models C1, C2, C3 and C4 have a composite rheology (see Tables 8.3 and 8.4) with a grain size parameter of 0.5 mm, 1.0 mm, 5.0 and 50 mm respectively. Results of these models are presented in Figures 8.4, 8.5, 8.6 and 8.7, respectively. Note that snapshot times are different from those in Figure 8.2. The development of the degree of depletion field is also shown in an animation (animation 1). Frames a1-3 show the development of the degree of depletion field, which reaches a value of about 0.38 in the diapir head. Initially the diapir shows very rapid ascent (1500 m/yr), but strongly decelerates, drop-

ping below 1 cm/yr after 150 ka. These four models show only slightly different ascent velocities (slower for larger grain size), which will be discussed in section 8.3.7. The viscosity field (frames c1-3) shows large local variations because of the strain rate dependence, showing a minimum of comparable magnitude ($6.7 \cdot 10^{16} \text{ Pas}$ to $8.5 \cdot 10^{16} \text{ Pas}$ for models C1 to C4) in each case. A horseshoe shaped zone characterized by high strain rate and (through the strainrate dependence of dislocation creep) low viscosity forms around the diapir facilitating the rise of the diapir with a much higher velocity compared to the Newtonian model. While minimum viscosities are quite similar for the different cases C1 to C4, the mantle and root material surrounding the diapir shows much higher viscosities for larger grain sizes, since the strain rate in these regions is much smaller than in the narrow low viscosity region directly bordering the diapiric head. The fact that characteristic time scales in these four models are quite similar despite the large variation in grain size and consequently the relative importance of the deformation mechanisms shows a selfregulating mechanism to be operative, producing similar viscosity minima and corresponding velocities and ascent times. Even for the smallest grain size, stresses locally become sufficiently large to become greater than the transition stress and the dislocation creep mechanism becomes dominant. As stresses drop during the ascent, they get close to the transition stress and the diffusion creep mechanism starts to play a more important role.

Here we have to keep in mind that the models are based on a constant grainsize and taking into account grainsize variation may change this conclusion (Kameyama et al., 1997). However, experimental results of De Bresser et al. (1998, 2001) indicate that significant weakening by grain size reduction can only take place if the grain size reduction is 'caused by a process other than dynamic recrystallization'. De Bresser et al. (2001) do find that the effect of temperature on recrystallized grain size 'cannot be neglected a priori.' In the upper mantle the grainsize is expected to be controlled either by dynamic recrystallization (Karato et al., 1980; Karato and Wu, 1993) or by secondary phase content (Drury and Fitz Gerald, 1998, , their fig 11.7f). For dynamic recrystallization the grainsize will depend strongly on the stress (smaller grains at higher stress) with a weaker dependence on temperature (smaller grains at higher temperature) and water content (larger grains at higher water content) (Karato et al., 1980; Ross et al., 1980; Van der Wal et al., 1993; De Bresser et al., 1998, 2001; Jung and Karato, 2001). At low stress and high temperature the olivine grainsize will be controlled by secondary phase size and content (Drury and Fitz Gerald, 1998). In this case the grainsize will depend strongly on the degree of depletion, which determines the second phase content. This is a subject of continuing research.

Model C1 (composite rheology after Karato and Wu (1993), see Tables 8.3 and 8.4) was calculated also using the linear parameterization of solidus and liquidus based on Takahashi and Kushiro (1983) (which was also used in model N1) instead of the third order polynomial parameterization based on Herzberg and Zhang (1996) (also used in models N2 and C1-4, see also section 8.2.1 and Figure 8.1), which gives us model C5. Because of the linear parameterization, which has considerably higher solidus and liquidus temperatures at greater depths ($> 100 \text{ km}$), the thermal perturbation which should have developed into a diapir does not penetrate the root at all, and produces very little

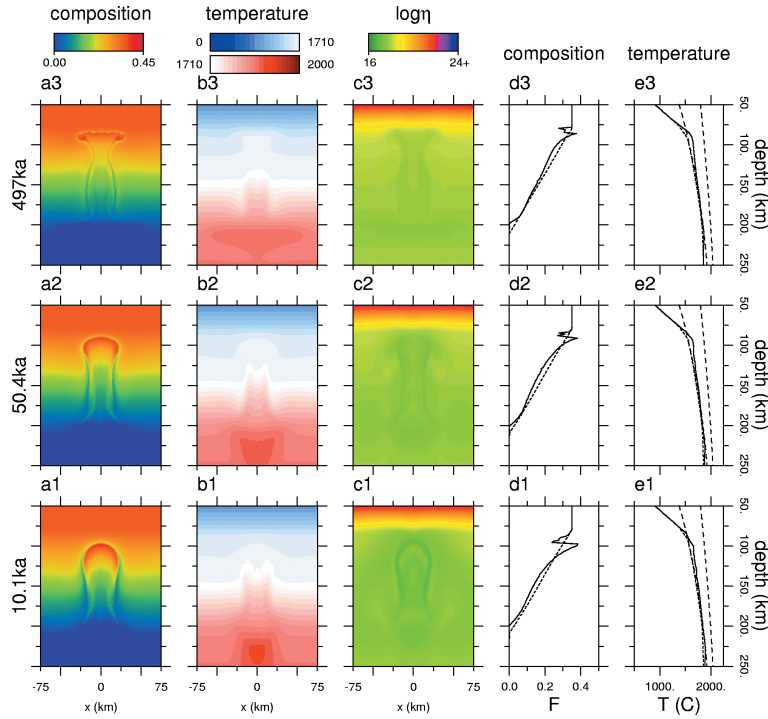


Figure 8.4: Model C1: Composite rheology. Only a part of the domain is shown ($[x, y] = [-75 - 75, 50 - 250]$ km). Frames a1-3 show the composition field and frames b1-3 show the temperature field at 10.1 ka, 50.4 ka and 497 ka after the start of the model run. Snapshots of the viscosity field are presented in frames c1-3. Profiles of composition and temperature are presented in frames d1-3 and e1-3, respectively. For an explanation of line types, see caption of Figure 8.2.

melt. This result underlines the key role of compositional differentiation. The generation of depleted peridotite causes compositional buoyancy which further drives the upward movement of the diapir. In this way it provides a self-accelerating mechanism which allows mantle diapirs to penetrate an existing continental root.

8.3.4 Viscosity component ratios

The relative importance of the two deformation mechanisms which are included in the composite rheology is illustrated by Figure 8.8, showing the logarithmic ratio of dislocation creep viscosity over diffusion creep viscosity (both defined in equation (8.8)) for the entire domain (dashed rectangle shows the zoom-in part shown in Figures 8.4-8.7) for models C1, C2, C3 and C4, respectively. Note that the mechanism which has the lowest

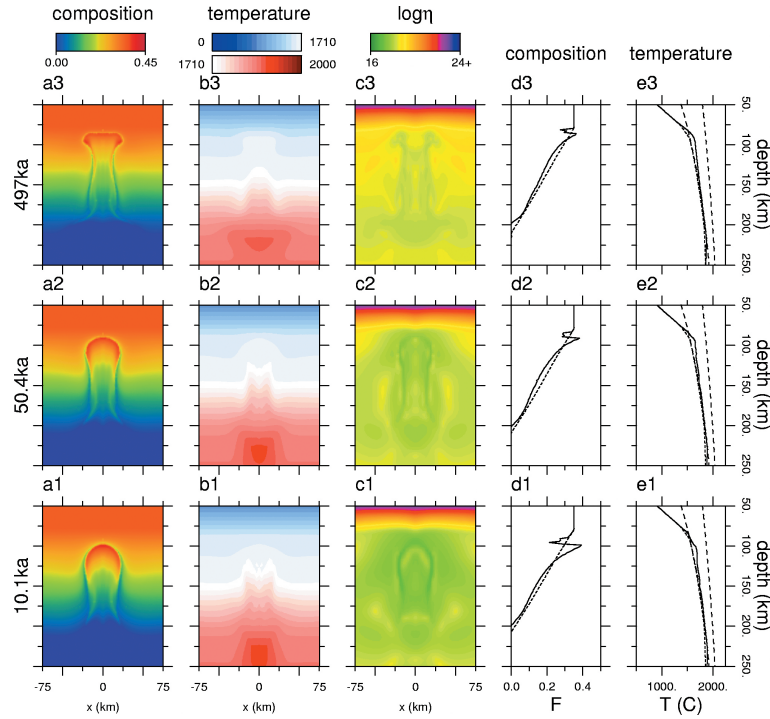


Figure 8.5: Model C2: Composite rheology. Only a part of the domain is shown ($[x, y] = [-75 - 75, 50 - 250]$ km). Frames a1-3 show the composition field and frames b1-3 show the temperature field at 10.1 ka, 50.4 ka, 497 ka after the start of the model run. Snapshots of the viscosity field are presented in frames c1-3. Profiles of composition and temperature are presented in frames d1-3 and e1-3, respectively. For an explanation of line types, see caption of Figure 8.2.

effective viscosity for the local conditions dominates the local deformation. Minima of the viscosity ratio η_2/η_1 are visible in the diapir and its surroundings. These are produced by the high stresses and strain rates at these locations which cause a reduction of the non-linear dislocation creep viscosity component, resulting in a decrease of the effective viscosity (equation (8.6)). The increase of this ratio with time for each model illustrates the decrease of strainrates during the diapir ascent, which causes strainrate dependent dislocation creep viscosities to increase. Another feature of this figure is the greater dominance of dislocation creep for larger grain sizes, which is the result of the grain size dependence of the diffusion creep component (higher viscosity for larger grains). We note here that the grain size dependence of our rheological models characterized by constant grainsize represents a simplified version of the stress, temperature, water content and secondary phase dependent grainsize in nature (Karato et al., 1980; Van der Wal et al., 1993; De

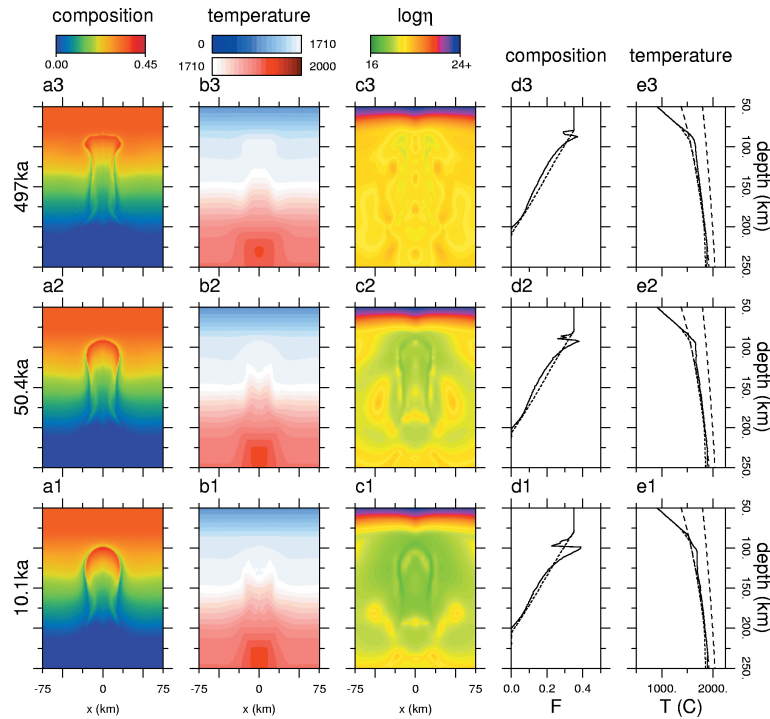


Figure 8.6: Model C3: Composite rheology. Only a part of the domain is shown ($[x, y] = [-75 - 75, 50 - 250]$ km). Frames a1-3 show the composition field and frames b1-3 show the temperature field at 10.1 ka, 50.4 ka and 497 ka after the start of the model run. Snapshots of the viscosity field are presented in frames c1-3. Profiles of composition and temperature are presented in frames d1-3 and e1-3, respectively. For an explanation of line types, see caption of Figure 8.2.

Bresser et al., 2001; Drury and Fitz Gerald, 1998; Jung and Karato, 2001). A constant grainsize model may indeed be a good approximation for the undepleted sub-lithospheric mantle (Drury and Fitz Gerald, 1998), although, in the lithosphere grainsize variation with depth would occur related to variations in the degree of depletion. Kameyama et al. (1997) and Braun et al. (1999) have investigated 1-D models including dynamic grainsize evolution exhibiting strong localization, however, the rheological effect of dynamic recrystallization remains uncertain and controversial (Rutter and Brodie, 1988; De Bresser et al., 1998, 2001). Including dynamic grainsize evolution in 2-D models is a subject for further research both in terms of the modeling and the micro-physical aspects.

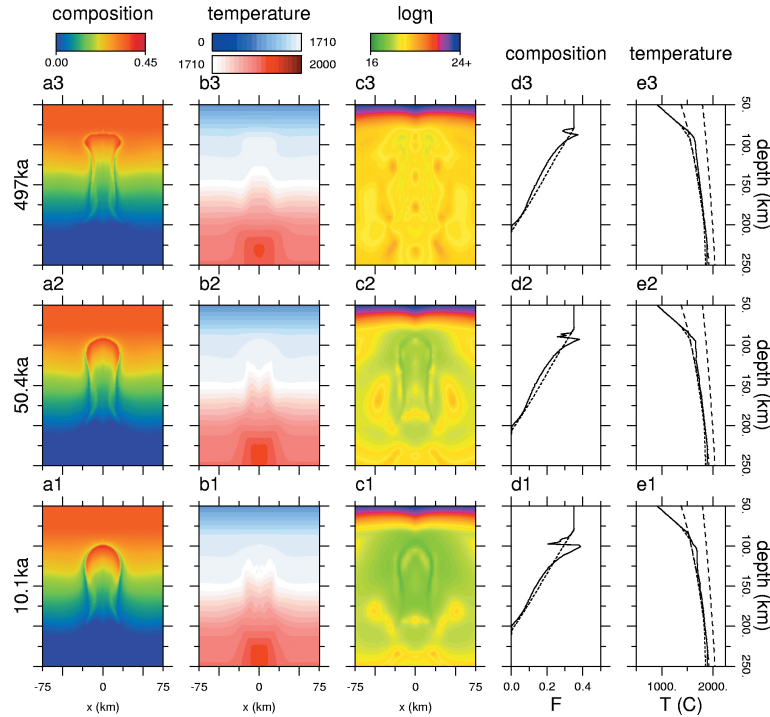


Figure 8.7: Model C4: Composite rheology. Only a part of the domain is shown ($[x, y] = [-75 - 75, 50 - 250]$ km). Frames a1-3 show the composition field and frames b1-3 show the temperature field at 10.1 ka, 50.4 ka, 497 ka after the start of the model run. Snapshots of the viscosity field are presented in frames c1-3. Profiles of composition and temperature are presented in frames d1-3 and e1-3, respectively. For an explanation of line types, see caption of Figure 8.2.

8.3.5 Deformation maps

In Figure 8.9, the logarithmic transition stress τ_t defined in equation (8.9) is contoured as a function of temperature and pressure (depth), for four different values of the grain size corresponding to models C1-4. Geotherms at $x = 0$ (through the diapir) and $x = 200\text{ km}$ (undisturbed) are included as well. At stresses higher than τ_t , dislocation creep is dominant, at lower stress diffusion creep prevails. The variation of the grain size directly controls the diffusion component of the viscosity, resulting in different magnitudes of the transition stress for equal P,T-conditions. As the figure clearly shows, a larger grain size decreases the transition stress τ_t from about 1 MPa in the region of the diapir, as illustrated by the geotherms included in the figure, for a grain size of 0.5 mm to less than 10^4 Pa for a grain size of 50 mm. These features relate to the viscosity ratios which are presented

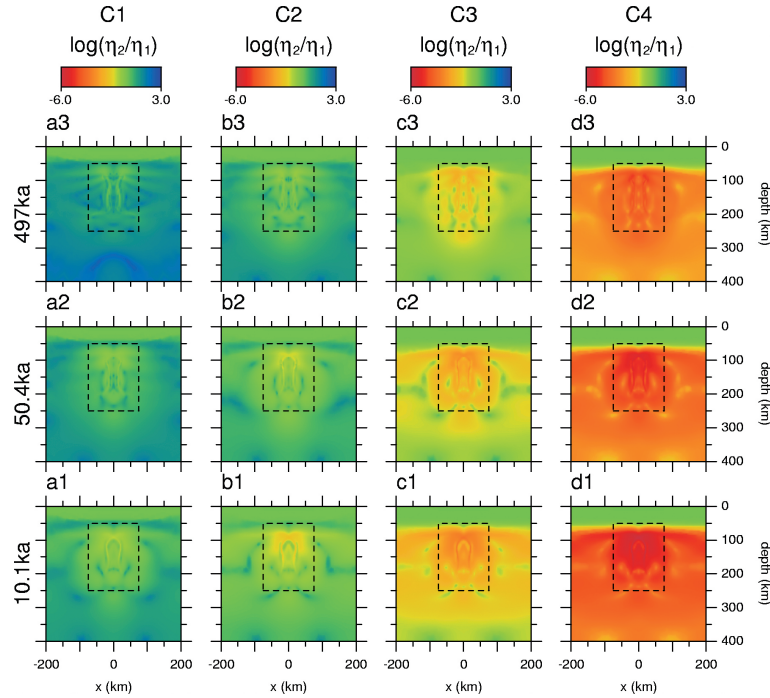


Figure 8.8: Models C1, C2, C3, C4: Composite rheology. The dashed square indicates the region which is shown in Figures 8.4-8.6. The logarithmic ratio of non-Newtonian to Newtonian component viscosity of the composite rheology at 101 ka, 50.4 ka and 497 ka is presented in frames a1-3 for model C1, frames b1-3 for model C2, frames c1-3 for model C3 and frames d1-3 for model C4.

in Figure 8.8. For model C1 with a 0.5 mm grain size, stresses in the diapiric region are approximately of the same magnitude as the transition stress, causing the viscosity ratio of the two creep components to be roughly 1. For increasingly larger grain sizes in models C2-4, the transition stress drops more and more below the actual stress levels observed in the diapirs, and the viscosity ratio becomes lower, down to about 10^{-6} for model C4 with grain size of 50 mm.

8.3.6 Dehydration and viscosity

The effect of dehydration due to partial melting on the rheology, is investigated in models D1-3. The dehydration prefactor in the viscosity applied in these models is used irrespective of the dominant creep mechanism. This is justified by experimental results (Karato, 1986; Mei and Kohlstedt, 2000a,b), indicating similar increases in creep velocity due to hydration for both diffusion creep and dislocation creep.

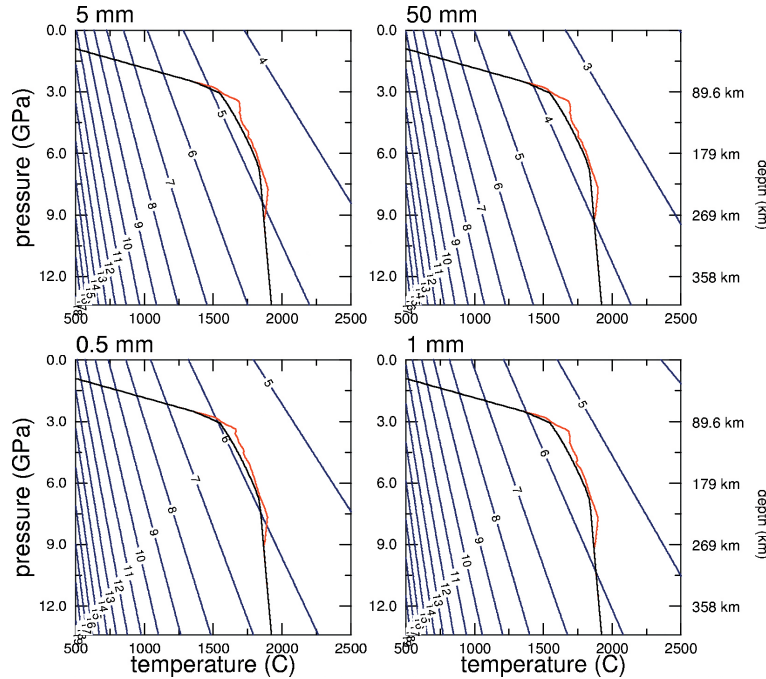


Figure 8.9: Models C1, C2, C3, C4: Composite rheology. Deformation maps are shown for the composite rheology models used (0.5 mm, 1.0 mm, 5.0 mm and 50 mm grainsize) and geotherms at $x=0$ (diapir center, red lines) and $x=200$ km (undisturbed background, black lines) at $t=10.1$ ka. Contours show the (logarithmic) stress τ_t at which dislocation creep viscosity is equal to diffusion creep viscosity. At a higher stress than τ_t , dislocation creep is the dominant deformation mechanism.

In model D1, the viscosity is multiplied by a factor 10 when the degree of depletion becomes higher than a threshold value, as described in the model section (8.2.1). The results of this viscosity prefactor are illustrated in Figure 8.10. Frames c1-3 show the viscosity field, in which the effect is clearly recognizable in the viscosity contrast around 200 km depth which coincides with the bottom of the (chemical) root. The development of the diapir is illustrated in frames a1-3, which show the degree of depletion. The diapir develops a mushroom shape during its ascent to about 90 km depth, where the head flattens. The diapir reaches a minimum depth in about 10 Ma. The maximum degree of depletion attained is 0.39, as shown in frames d1-3.

The dehydration prefactor in the viscosity model is increased to 50 in model D2, of which results are presented in Figure 8.11, and in an animation file (animation 2). Again the effect of the viscosity prefactor is clearly visible in the viscosity snapshots (frames c1-3). The diapir now rises more slowly (compared to model D1). It develops a similar

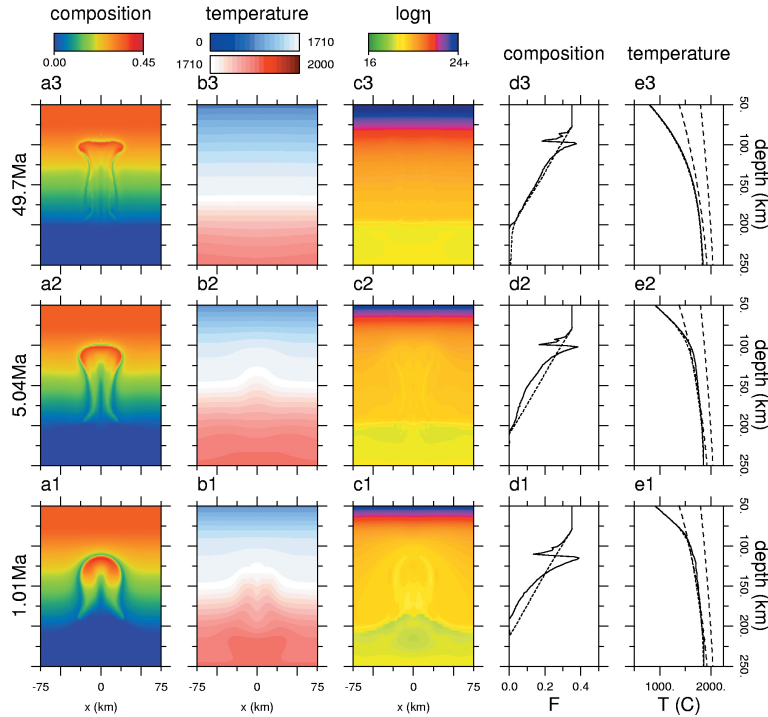


Figure 8.10: Model D1: Composite rheology, $f_{\eta}=10$. Only a part of the domain is shown ($[x, y] = [-75 - 75, 50 - 250]$ km). Frames a1-3 show the composition field and frames b1-3 show the temperature field at 1.01 Ma, 5.04 Ma and 49.7 Ma after the start of the model run. Snapshots of the viscosity field are presented in frames c1-3. Profiles of composition and temperature are presented in frames d1-3 and e1-3, respectively. For an explanation of line types, see caption of Figure 8.2.

mushroom shape, though it takes more time. The diapir head rises to about 100 km depth, which is reached in about 25 Ma. The maximum degree of depletion $F_{max} = 0.39$ is similar to that of model D1.

Figure 8.12 shows results of model D3, which has a dehydration prefactor of 200 in the viscosity equation, slightly higher than the upper limit of 180 given by Hirth and Kohlstedt (1996). This results in a strong viscosity contrast at the base of the lithospheric root at 200 km depth (see frames c1-3), where now also the shape of the melting diapir can be recognized in the viscosity fields, and a very slow penetration of the diapir into the root. The diapir head flattens during its ascent and has reached a depth of about 125 km at 49.7 Ma (frame a3), where the ascent velocity is less than 1 mm/yr and still dropping.

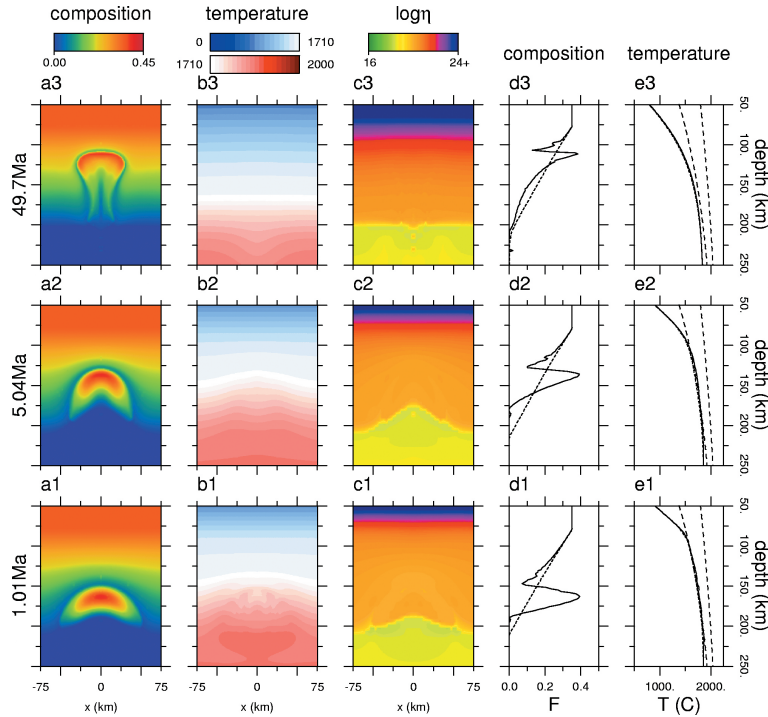


Figure 8.11: Model D2: Composite rheology, $f_{\eta}=50$. Only a part of the domain is shown ($[x, y] = [-75 - 75, 50 - 250]$ km). Frames a1-3 show the composition field and frames b1-3 show the temperature field at 1.01 Ma, 5.04 Ma and 49.7 Ma after the start of the model run. Snapshots of the viscosity field are presented in frames c1-3. Profiles of composition and temperature are presented in frames d1-3 and e1-3, respectively. For an explanation of line types, see caption of Figure 8.2.

8.3.7 Ascent velocities

Time series of the vertical velocity were calculated for a number of monitor tracer particles to determine the ascent velocity of the diapiric head. Representative results are presented in Figure 8.13. Two stages can be discerned for each model. During the initial stage, the diapir rises at a more or less constant velocity. At some point the diapir starts to slow down as it encounters stiffer resistance.

Model N1 (frame a) shows an ascent velocity which is several centimeters per year for about the first 10 million years, with a maximum of just over 10 cm/yr in the initial phase. Model N2, which has a somewhat weaker rheology, shows rapid ascent in the order of meters per year in the initial phase, but the velocity drops below 1 m/yr around 180 ka.

The composite rheology models C1, C2 and C3 show similar shapes of the velocity

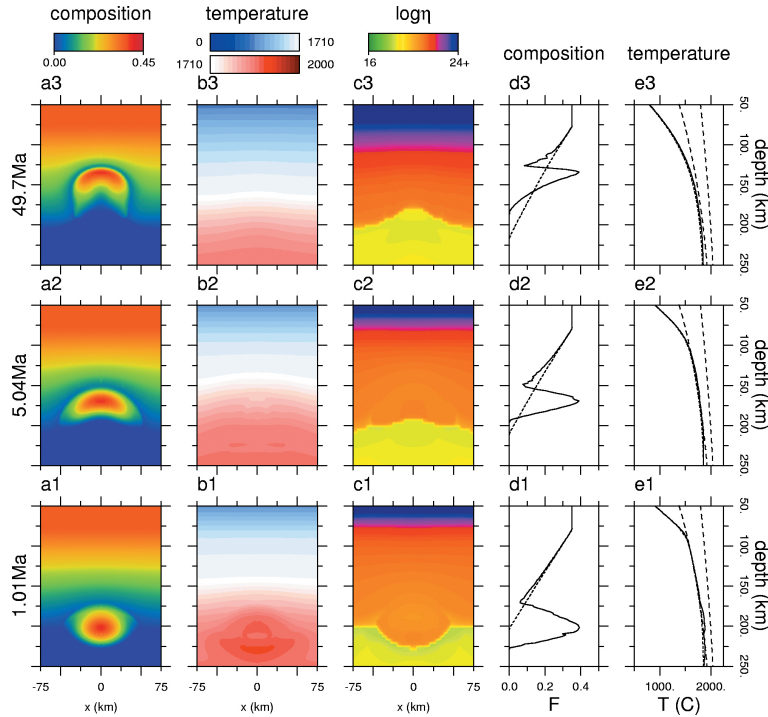


Figure 8.12: Model D3: Composite rheology, $f_{\eta}=200$. Only a part of the domain is shown ($[x, y] = [-75 - 75, 50 - 250]$ km). Frames a1-3 show the composition field and frames b1-3 show the temperature field at 1.01 Ma, 5.04 Ma and 49.7 Ma after the start of the model run. Snapshots of the viscosity field are presented in frames c1-3. Profiles of composition and temperature are presented in frames d1-3 and e1-3, respectively. For an explanation of line types, see caption of Figure 8.2.

evolution (Figure 8.13b), however with much higher velocities compared to model cases N1 and N2, with a high maximum value in the initial stage of nearly 1500 m/yr and values of several 100 m/yr during the first 500 years of the run. The velocity drops to about 100 m/yr at 1 ka and 1 cm/yr at 150 ka. Note that three almost identical curves are shown in Figure 8.13b, illustrating the self-regulating effect of the composite rheology, resulting in very similar ascent velocities for very different overall viscosities.

The maximum vertical velocity for the dehydration models D1, D2 and D3 is 16 m/yr, 50 cm/yr and 8 cm/yr, respectively, attained in the early stages of diapir ascent (Figure 8.13c). The influence of the dehydration prefactor in the viscosity equation is evident from the lower ascent velocities compared to the composite rheology models. Compared to the composite rheology model C1, initial ascent velocities are 2 to 4 orders of magnitude lower. Velocities drop off to approximately 1 cm/yr at 1.2 Ma, 1.6 Ma and

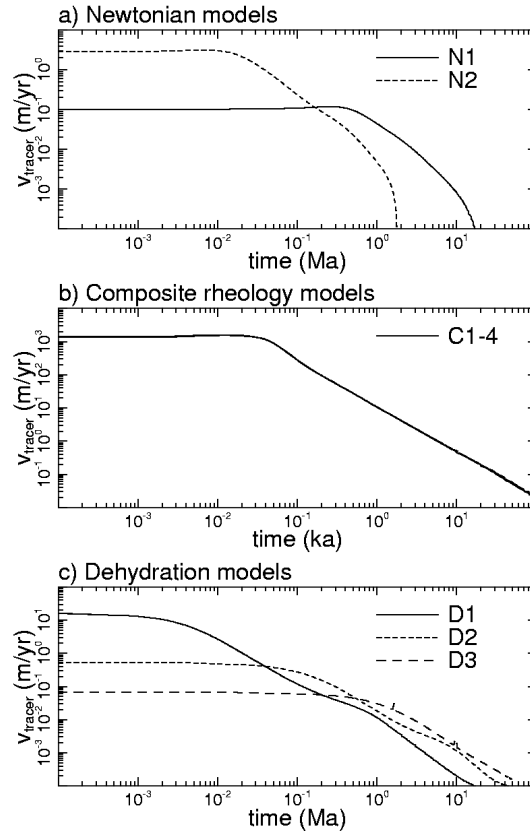


Figure 8.13: Time series of the vertical velocity of selected monitor tracers. Note the different time and velocity scales used in a, b and c.

2.7 Ma, respectively, and continue to drop to negligible levels.

We have tested the sensitivity of the model to the amplitude of the thermal perturbation which initiates the diapirs. Figure 8.14 shows three series of 3 snapshots of the degree of depletion field of a composite rheology model with grain size 1 mm and with three different perturbation amplitudes ϵ_T of 3%, 4% and 5%, respectively, of the background temperature, which is approximately 1850°C . The frames show the results to be quite sensitive to the amplitude of the initial perturbation.

The maximum root mean square velocity V_{rms} (see Van den Berg et al., 1993) values observed have been plotted as a function of the relative amplitude ϵ_T of the thermal perturbation in Figure 8.15. The maximum V_{rms} which was observed during a model run (generally during the initial phase of diapir ascent, illustrated in Figure 8.13) has been included in frame (a), for three different model cases (composite 1mm(model case C2),

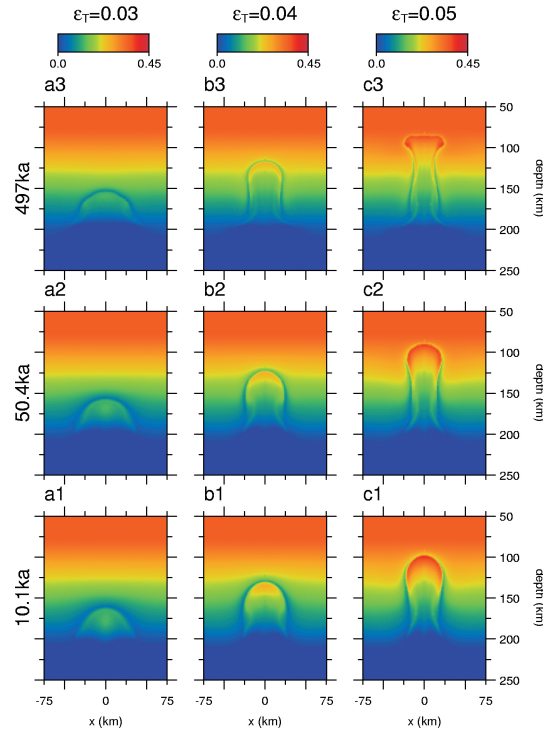


Figure 8.14: Diapir development for different values $\epsilon_T = \frac{\delta T}{T(z)}$ of the amplitude of the thermal perturbation which initiates the diapir. Values are fractions of the background temperature, which is about 1850°C at the location of the initial perturbation. The other model parameters are the same as in case C2 (represented in the third column, see also Figure 8.5). The colour contours indicate the degree of depletion F .

dehydration 1mm with $f_\eta = 50$ (model case D2), and Newtonian 1mm (model case N2)). The curves in Figure 8.15a are shaped as the bottom end of a sigmoidal curve (although the shape is less pronounced in the Newtonian case) revealing a transition between two different regimes. The lower amplitude part with a small slope represents cases where the diapir does not fully penetrate the continental root. The upper part with a larger slope corresponds to cases where the initial perturbation is greater than the critical value resulting in penetrating diapirs. Clearly, the transition between these regimes shifts to higher amplitudes ϵ_T considering successively stronger rheologies from composite C2, to Newtonian N2 to hydration dependent composite D2.

Figure 8.15b shows the relation between the 2σ (2 standard deviations) radius of the thermal perturbation at a constant perturbation amplitude ϵ_T of 5% of the background temperature. The linear relation in log-log space is quite clear.

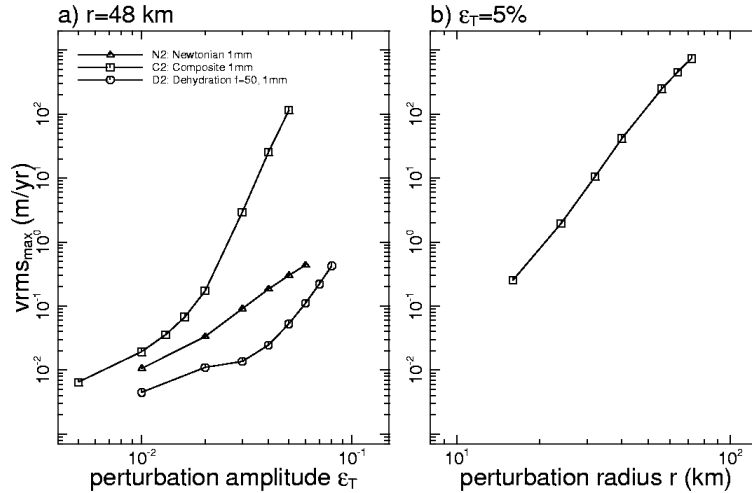


Figure 8.15: Variation of diapir ascent (measured as the maximum root mean square velocity of the domain) as a function of: a) the perturbation amplitude $\epsilon_T = \frac{\delta T}{T(z)}$ at a constant 2σ (2 standard deviations) radius of 48 km; b) the radius of the initial perturbation (2σ) at a constant ϵ_T of 5%.

8.3.8 P,T paths

P,T-paths of selected monitor tracers have been plotted in Figure 8.16, where separate tracers are indicated by different colours. Tracers were selected on the basis of penetration to shallow depths and to show the variation of different paths to shallower levels. A P,T-path inferred from cratonic peridotites (Drury et al., 2001) has been included as a solid black line. Only one composite model is shown (C2), as the paths for the same tracers are quite similar in the other composite models. Although the time scales of the diapiric processes are vastly different for the different models, the resulting P,T-paths are roughly the same for the cases shown, and similar to the inferred cratonic peridotite path by Drury et al. (op.cit.) and model results by De Smet et al. (2000b) and Drury et al. (2001). Such a similarity between paths derived from numerical models for diapirism and paths inferred for natural cratonic peridotites was also noted by Drury et al. (2001). Some models show more cooling to lower temperatures (N2, D1) than other models (C2) but this is mainly caused by the running time of the different models, ranging from 497 ka for the composite models to 49.7 Ma for the Newtonian and dehydration models. The short length of the cooling leg (almost horizontal line) of the paths in models D2 and D3 is caused by the low ascent velocity of these models, such that conductive cooling becomes important only at a late stage.

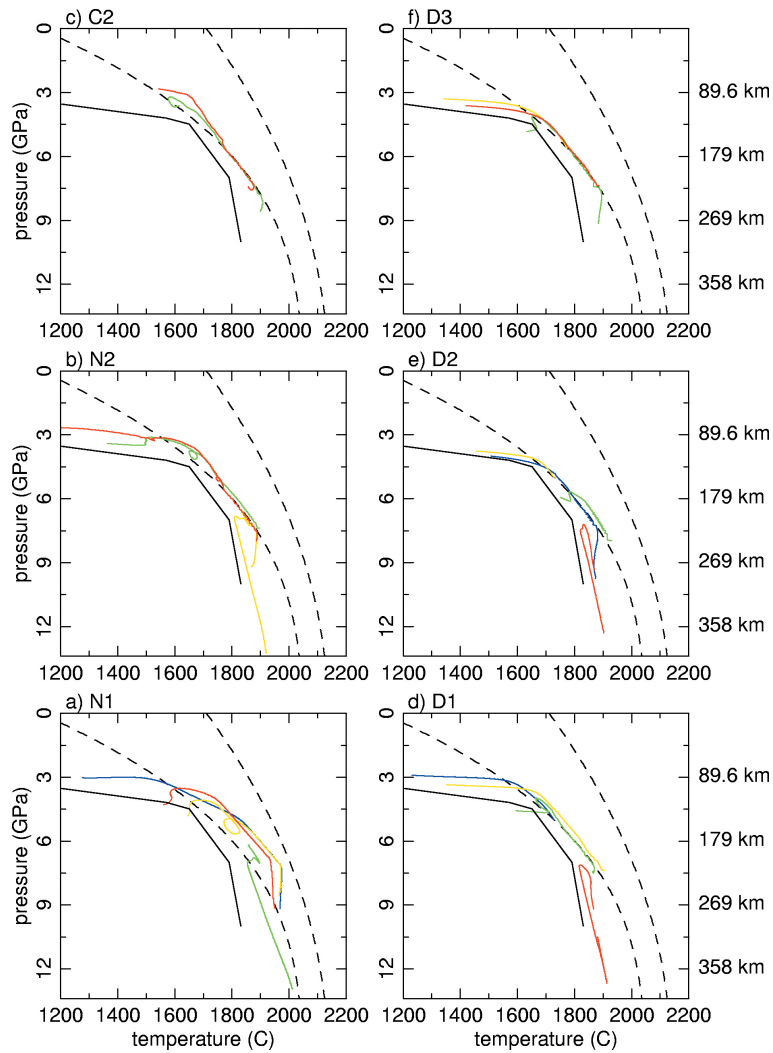


Figure 8.16: Pressure-Temperature-paths for selected monitor tracers, each indicated by a different colour. The solidus and liquidus (third order parameterization) are indicated by dashed lines. Also included (in a black solid line) are inferred P,T paths from eclogites of the Western Gneiss Region, Norway (Drury et al., 2001). a) Model N1, running time is 49.7 Ma, b) model N2, running time is 49.7 Ma, c) model C2 (models C1, C3 and C4 are similar), running time 497 ka, d) model D1, running time 49.7 Ma, e) model D2, running time 49.7 Ma, f) model D3, running time 49.7 Ma.

8.3.9 Stress and strainrate histories

Grain size characteristics of rock samples can render estimates of the stress and strainrate history of these rocks, and may therefore be a link between our numerical modelling results and the real Earth. We have used monitor tracer particles to log the second invariant of the local strainrate and stress tensors in time. The modelling results reveal that the maximum strainrates and stresses observed depend quite strongly on the viscosity model. Only monitor particles are presented which experienced partial melting, and which were part of the diapir. Maximum strain rate and stress values which were observed are presented in Table 8.5, and the stress and strainrate versus depth for selected tracer particles are plotted in Figure 8.17. The maximum stresses observed which are listed in Table 8.5 vary by less than one order of magnitude. The maximum strainrates, however, vary over nearly five orders of magnitude. The Newtonian models N1 and N2 have maximum strainrates of $7.53 \cdot 10^{-14} s^{-1}$ and $1.62 \cdot 10^{-12} s^{-1}$, respectively. This difference is caused by the smaller grain size and therefore lower viscosity of the latter model. The four composite rheology models C1-4 show very similar maximum strainrate values, much higher (3-5 orders of magnitude) than those observed for the Newtonian models, just over $1 \cdot 10^{-9} s^{-1}$. Here, the effect of the non-linear component of the rheology becomes apparent. As can be expected, the dehydration models show lower strain rates because of their higher viscosities, ranging from $1.75 \cdot 10^{-11} s^{-1}$ to $3.16 \cdot 10^{-13} s^{-1}$ for models D1 to D3.

model	max strainrate (s^{-1})	max stress (Pa)
N1	$7.53 \cdot 10^{-14}$	$1.21 \cdot 10^6$
N2	$1.62 \cdot 10^{-12}$	$4.90 \cdot 10^6$
C1	$1.28 \cdot 10^{-9}$	$3.68 \cdot 10^6$
C2	$1.25 \cdot 10^{-9}$	$3.66 \cdot 10^6$
C3	$1.25 \cdot 10^{-9}$	$3.66 \cdot 10^6$
C4	$1.25 \cdot 10^{-9}$	$3.66 \cdot 10^6$
D1	$1.75 \cdot 10^{-11}$	$5.43 \cdot 10^6$
D2	$5.93 \cdot 10^{-13}$	$7.27 \cdot 10^6$
D3	$3.16 \cdot 10^{-13}$	$7.97 \cdot 10^6$

Table 8.5: Maximum observed values for the second invariant of the strainrate tensor and the second invariant of the stress tensor, respectively. Only monitor tracers which have undergone partial melting during the model run have been considered.

8.4 Discussion and conclusions

Comparison of the results of models N1 and N2 versus models C1-4 show that the addition of a non-linear creep component to the Newtonian diffusion creep component of the rheology model strongly increases the ascent velocity and thus reduces the characteristic emplacement time scale for a diapir considerably to less than a conservative hundred thou-

sand years. The results of model C5 (relative to model C1) show that a third order parameterization of solidus and liquidus, based on Herzberg and Zhang (1996) (used in models N2, C1-4 and D1-3), strongly favors diapir development relative to a linear parameterization. The latter third order parameterization allows for melting at lower temperatures for depths greater than about 200 km than the former linear, thus facilitating melting at these depths. Depletion-induced compositional buoyancy further drives the upward movement of the diapir, thus providing a self-accelerating mechanism for diapir intrusion into and within a continental root. This illustrates the importance of compositional differentiation in the evolution of mantle diapirs.

The results of all models show locally sharp variations in the degree of depletion, most readily observable in the degree of depletion profiles (frames d1-3) of the model result Figures 8.2-8.7 and 8.10-8.12. Numerical models have indicated that these sharp compositional variations in the lithosphere resulting from mantle diapirism of the kind investigated here may act as seismic P-wave reflectors De Smet et al. (1999). Possibly, the sheetlike structures of flattened diapir heads, as predicted by some of our models for a composite rheology, will be detectable in the uppermost mantle by seismic methods as have been applied in recent mantle reflection seismic studies (e.g. Pavlenkova and Yegorkin, 1983; Ellis and Bostock, 1996; Pavlenkova et al., 1996).

Another aspect related to direct observables is the seismic anisotropy which may be created by the deformation processes included in our models (see e.g. Tommasi et al., 1999). Silver et al. (2001) find evidence for preservation of Archean mantle deformation in small or vertically incoherent seismic anisotropy in their region of study (Kaapvaal and Zimbabwe cratons).

The results of the modelling experiments show that a relatively large variations in grain size (two orders of magnitude, which translates to five orders of magnitude in the diffusion creep viscosity prefactor through the grainsize exponent $m = 2.5$) have a limited effect on the dynamics of the diapirs modeled in this work. Although the dominant creep mechanism clearly shifts from diffusion creep to dislocation creep as a result of increasing the grainsize parameter, the overall dynamics of the different cases are roughly similar. Detailed analysis of snapshots of the viscosity field reveals a localized zone of high stress and strain rate and low viscosity surrounding the diapiric head. Roughly the same viscosity minima are found in this localized deformation zone for the different composite rheology cases, indicating that a self-regulating mechanism is operative, controlling the ascent.

Concerning the effect of dehydration on the rheology, we have found that this has a strong effect on diapir dynamics. Although two of the three depletion viscosity factors are smaller than those reported by Hirth and Kohlstedt (1996, factor 100-180), it is quite apparent from the results of models D1, D2 and D3 (Figures 8.10, 8.11 and 8.12) that even the effect of a relatively small dehydration factor (as low as 10) is considerable. This smaller factor may be justified by assuming that the material becomes (partially) rehydrated by mobile volatile phases originating from other areas of partial melting, since studies of craton xenoliths show evidence for re-hydration (Harte, 1983).

The fact that peridotites have been emplaced in the Archean at depths of up to 100 km (Drury et al., 2001), and that this depth is not reached by the diapir model with maximum

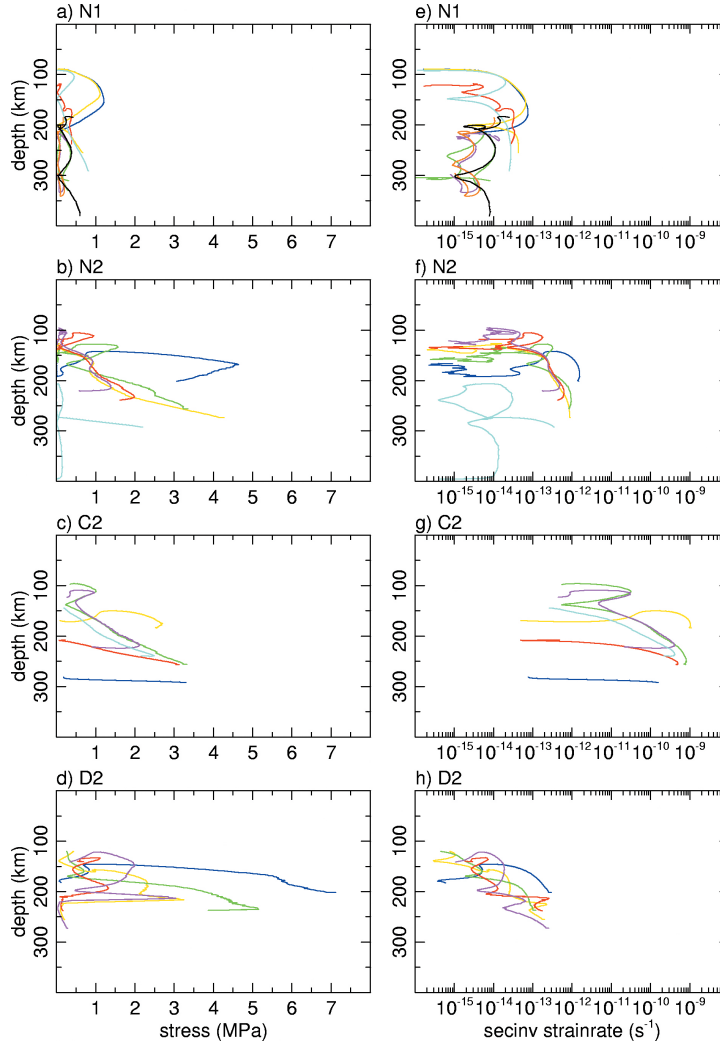


Figure 8.17: Paths for selected tracers of model(s) N1, N2, C2 and D2 in stress-depth space and strainrate-depth space, respectively. Frames a-d show the stress as a function of depth for these models, and frames e-h show the second invariant of the strain rate as a function of depth for selected monitor particle tracers.

dehydration prefactor $f_{\eta} = 200$ (model D3, Figure 8.12) suggests that during the Archean the rheology of the cratonic lithosphere was not completely dry. The model case C2 is used as a reference (Figure 8.5) in the investigation of the effect of the viscosity factor f_{η} .

The shape of the diapir head, the vertical velocity of the diapir and the level to which the diapir penetrates are all strongly influenced by this dehydration factor. With increasing viscosity factor, the shape tends to be more mushroom-like, the ascent velocity of the diapir decreases and the penetrating power is diminished as well.

The different experiments which we have conducted have yielded diapirs showing ascent velocities of several centimeters per year for purely Newtonian model N1 and dehydration model D3 (factor 200) up to several hundred meters per year for the composite rheology models C1, C2, C3 and C4. Although these high end values seem extreme, other workers have reported high velocities in non-Newtonian mantle models. Larsen et al. (1997) and Larsen and Yuen (1997) report ascent velocities for non-Newtonian diapirs over 10 m/yr. Weinberg and Podladchikov (1994) showed that a diapir may rise with velocities of 10-100 m/yr into the middle or upper crust if the wall rock exhibits power law behaviour, and Solomatov and Moresi (2000) find velocities of several meters per year for cold plumes formed in a stagnant lid regime convection model. The very high ascent velocities in our models are also facilitated by weakening of the surrounding rock by a large strain rate and a power law rheology (the dislocation creep component), as can be observed in frames c1-3 of Figures 8.4-8.7.

A comparison of stress and strainrate histories obtained in this study with geological observations might help to constrain models of mantle diapirism in view of the large uncertainty in the model parameters applied. Structures and microstructures in these mantle rocks provide some independent control on the conditions of deformation during diapir upwelling in cratonic lithosphere. The differential stress during high temperature deformation can be estimated from the dynamic recrystallized grain size. If the temperature during deformation is known then strainrates can be estimated from the stress and temperature estimates.

The stress and strainrate histories within the model diapirs show relatively high initial strainrates (up to 10^{-10} to $10^{-9}s^{-1}$ for model C2, see Figure 8.17 and Table 8.5) and stress levels (2-7 MPa). The dynamic recrystallized grainsize produced during the initial diapir intrusion should be around 1 to 15 mm. As upwelling continues stress and strainrate decrease overall, although many tracers experience a strainrate and stress pulse at shallow depths with stress levels up to 1 MPa. The last stages of deformation at shallow depth occur with decreasing stress and strainrate at stress levels less than 1 to 0.5 MPa. The decaying strainrates can be related to the cooling of the diapir as it accretes into the lithosphere. If the dynamic recrystallized grain size remained "in equilibrium" with the stress in the final stages of deformation then a grainsize between 1.5- 10 cm would be expected. This estimate of the dynamically recrystallized grainsize is based on an experimental calibration for olivine with low water content over a temperature range of 1100 – 1650°C (Karato et al., 1980; Van der Wal et al., 1993). As the diapir cools down the stress and strainrate decrease to very low values such that the material will become "annealed". In this situation the grainsize will be modified by static recrystallization with the grainsize depending on the amount of residual strain in the grains, the time of annealing and the temperature during annealing.

In the cratonic peridotites from Norway and kimberlite xenoliths the average grain-sizes are in the range of 0.5 to 10 mm (Avé Lallemant et al., 1980; Van Roermund et al.,

2001). The microstructures of the Norwegian peridotites are consistent with significant static recrystallization as strain free grains (1-4 mm) have replaced much larger deformed grains (1-10 cm diameter). Similar trends are found in kimberlite xenoliths and in the spinel peridotites from the North Pyrenean fault zone (Fabriès et al., 1991). The large grain sizes found as relict grains in the cratonic peridotites are consistent with the grain-size to be expected from the numerical models. The large grain sizes (1-30 cm) found as relict grains in the cratonic peridotites are consistent with the dynamic recrystallized grainsize predicted (1.5-10 cm) from the stress levels in the numerical models for the last stage of deformation. The static recrystallized microstructure of cratonic peridotites is also consistent with the thermo-mechanical history of diapirs in the numerical models. In the Norwegian peridotites, however, the recrystallized grainsize is smaller than the initial grainsize which suggests a more complex history with a second deformation and recrystallization cycle, possibly related to later subduction and exhumation, superimposed on the coarse microstructure produced by diapiric intrusion.

Rough estimates of the strainrates during the high temperature history of the Norwegian cratonic peridotites can be made from stress and temperature estimates combined with experimental flow laws. For a stress of 0.5 MPa and a temperature range of 1350-1600°C estimated from early mineral assemblages (Van Roermund and Drury, 1998; Drury et al., 2001) strainrates in the range of $7 \cdot 10^{-15}$ to $1.4 \cdot 10^{-12} s^{-1}$ are indicated for dry olivine and $1.4 \cdot 10^{-12}$ to $2.0 \cdot 10^{-10} s^{-1}$ for wet olivine (Chopra and Paterson, 1984). This broad range of strainrates is compatible with strainrates obtained from the numerical models (Figure 8.17) during the last stages of diapir intrusion into the lithosphere.

Note that local strain rates in the diapir can be very high and much higher than strainrates expected from typical plate tectonic rates. Some spectacularly sheared xenoliths are found in kimberlites (Nixon and Boyd, 1973; Boullier and Nicolas, 1973) and estimates of deformation conditions imply very high stress and strain rates (Goezte, 1978; Mercier, 1979). Kimberlite magmatism may be associated with diapirs in the modern mantle (Green and Gueguen, 1983; Haggerty, 1994). These diapirs would be quite different from those modelled in this study, if only because the potential temperature of the mantle is of the order of 300°C lower, which strongly increases viscosities. However, we note that the very high strain rates and stress levels estimated for the sheared xenoliths could be consistent with deformation during diapiric intrusion, although this would need to be tested with models which include wet melting in a modern mantle.

Chapter 9

Summary and Conclusions

9.1 Summary

The contents of this thesis revolve around the question of what type of geodynamics was active in the Early Earth and other terrestrial planets. The geology of the Archean (4.0-2.5 billion years before present) is quite different from recent geology, and therefore it is likely that different processes were responsible for its formation than the present-day plate tectonics. Several lines of evidence indicate internal temperatures for the early Earth significantly higher than the present. The physical consequences expected of a higher mantle temperature add arguments to the inference of a different geodynamical regime for the early Earth. Both Venus and Mars are comparable to the Earth regarding composition, and Venus also has a similar size, whereas Mars has about half the diameter of the Earth. In spite of the similarities, the surfaces of both planets look quite different from that of the Earth. For example, no evidence of recent plate tectonics is found on either planet.

In this thesis, the conditions under which plate tectonics and alternative geodynamic regimes may operate were investigated for the terrestrial planets using numerical models. For the Earth, more detailed studies of the different types of dynamics were used to compare the results of the processes that were modelled with remnants of Archean material which are still present on the surface of the Earth.

After presenting the numerical models used in this thesis, and describing the numerical methods used in getting model solutions, a number of studies were presented in which problems pertaining to the theme of the thesis are investigated.

Chapter 4 deals with conditions that allow plate tectonics to operate on the different terrestrial planets.

Plate tectonics is largely controlled by the buoyancy distribution in oceanic lithosphere, which correlates well with the lithospheric age. Buoyancy also depends on compositional layering resulting from pressure release partial melting under mid-ocean ridges, and this process is sensitive to pressure and temperature conditions that vary between

the terrestrial planets and also during the secular cooling histories of the planets. In the modelling experiments, a range of values for the gravitational acceleration (representing different terrestrial planets), potential temperatures (representing different times in the history of the planets) and surface temperatures were applied in order to investigate under which conditions plate tectonics is a viable mechanism for the cooling of the terrestrial planets. Included in the models are the effects of mantle temperature on the composition and density of melt products and the thickness of the lithosphere. The results show that the onset time of negative buoyancy for oceanic lithosphere is reasonable (less than a few hundred million years) below a potential temperature of about 1500°C for the Earth and about 1450°C for Venus. In the reduced gravity field of Mars, a much thicker stratification is produced and the model indicates that plate tectonics could only operate on reasonable time scales at a potential mantle temperature below about $1300 - 1400^{\circ}\text{C}$.

In the following chapter (5), the cooling characteristics of plate tectonics and an alternative mechanism which is flood volcanism are quantified using parametric models.

Geophysical arguments based on buoyancy considerations against plate tectonics in a hotter Earth require an alternative means of cooling the planet from its original hot state to the present situation. Such an alternative could be extensive flood volcanism in a more stagnant-lid like setting. Starting from the notion that all heat output of the Earth is through its surface, we have constructed two parametric models to evaluate the cooling characteristics of these two mechanisms: plate tectonics and basalt extrusion / flood volcanism. Our model results show that for a steadily (exponentially) cooling Earth, plate tectonics is capable of removing all the required heat at a rate comparable to or even lower than its current rate of operation, contrary to earlier speculations. The extrusion mechanism may have been an important cooling agent in the early Earth, but requires global eruption rates two orders of magnitude greater than those of Phanerozoic flood basalt provinces. This may not be a problem, since geological observations indicate that flood volcanism was both stronger and more ubiquitous in the early Earth. Because of its reduced size, Mars is capable of cooling conductively through its lithosphere at significant rates, and as a result has possibly never required an additional cooling mechanism. Venus, on the other hand, has required the operation of an additional cooling agent for probably every cooling phase of its possibly episodic history, needing rates of activity comparable to those of the Earth.

After the conditions under which plate tectonics may operate and the cooling characteristics of both plate tectonics and flood volcanism have been studied, the flood volcanism regime is studied in more detail in chapter 6, focusing on the dynamics and geochemical effects.

Numerical thermochemical convection models including partial melting and a simple mechanism for melt segregation and oceanic crust production were used to investigate an alternative suite of dynamics that may have been in operation in the early Earth. The modelling results show three processes that may have played an important role in the production and recycling of oceanic crust: (1) Small scale ($x \cdot 100$ km) convection involving the lower crust and shallow upper mantle with partial melting and thus crustal production in the upwelling limb and delamination of the eclogitic lower crust in the downwelling limb. (2) Large scale resurfacing events in which (nearly) the complete crust sinks into

the (eventually lower) mantle, thereby forming a stable reservoir enriched in incompatible elements in the deep mantle. New crust is simultaneously formed at the surface from segregating melt. (3) Intrusion of lower mantle diapirs with a high excess temperature (about 250 K) into the upper mantle, causing massive melting and crustal growth. This allows for plumes in the Archean upper mantle with a much higher excess temperature than previously expected from theoretical considerations.

Chapter 7 looks at the formation of continental material in the geodynamical setting of the previous chapter.

Important constituents of Archean cratons, formed in the early and hot history of the Earth, are TTG plutons and greenstone belts. The formation of these granite-greenstone terrains is often ascribed to plate-tectonic processes. Buoyancy considerations, however, do not allow plate tectonics to take place in a significantly hotter Earth. Therefore, an alternative mechanism for the coeval and proximate production of TTG plutons and greenstone-like crustal successions is proposed: When a locally anomalously thick basaltic crust has been produced by continued addition of extrusive or intrusive basalts due to partial melting of the underlying convecting mantle, the transition of a sufficient amount of basalt in the lower crust to eclogite may trigger a resurfacing event, in which a complete crustal section of over 1000 km long sinks into the mantle in less than 2 million years. Pressure release partial melting in the complementary upwelling mantle produces large volumes of basaltic material replacing the original crust. Partial melting at the base of this newly produced crust may generate felsic melts that are added as intrusives and/or extrusives to the generally mafic crustal succession, adding to what resembles a greenstone belt. Partial melting of metabasalt in the sinking crustal section produces a significant volume of TTG melt that is added to the crust directly above the location of 'subduction', presumably in the form of a pluton. This scenario is self-consistently produced by numerical thermo-chemical mantle convection models including partial melting of mantle peridotite and crustal (meta-)basalt, which were presented in this chapter. The p, T -conditions under which partial melting of metabasalt takes place in this scenario are consistent with geochemical trace element data for TTG's, which indicate melting under amphibolite rather than eclogite facies. Other geodynamical settings which have also been investigated, including partial melting in small scale delaminations of the lower crust, at the base of an anomalously thick crust and due to the influx of a lower mantle diapir fail to reproduce this behaviour unequivocally and mostly show melting of metabasalt in the eclogite stability field instead. The resurfacing scenario may also have been important in Venus' history, but probably did not produce significant volumes of continental material due to the dryness of this planet.

The stability against recycling of Archean cratons is often ascribed to the presence of a low density root beneath these continental fragments. In chapter 8, the importance of different deformation processes in the formation of such a root were investigated.

A possible mechanism for adding material to a continental root is by means of upwellings from the convecting mantle subject to pressure release partial melting.

Results of numerical modelling of the interaction of melting diapirs with continental roots in an Archean setting characterized by a mantle potential temperature of 1750 °C in a 2-D Cartesian geometry are presented.

In an extension of earlier work (De Smet et al., 2000a) the influence of mantle rheology on the behaviour of diapirs has been investigated, in particular looking at the difference in behaviour of diapirs using a composite rheology combining both grain size sensitive diffusion creep and dislocation creep mechanisms. The grain size, here taken to be uniform, was used as a control parameter to obtain model cases with varying contribution from the two creep mechanisms. The diapirs in the composite rheology model rise much faster than in a purely Newtonian model. Observed diapiric ascent times from 230 km depth to the top of the ascent path at about 80 km depth are approximately 1 Ma for a Newtonian model (averaged 14 cm/year) compared to about 50 thousand years for a composite rheology model (averaged 3 m/year) with the same parameters for the Newtonian component. This clearly indicates the large impact of the dislocation creep component of the viscous deformation process.

The effect of an increase in the viscosity due to dehydration during partial melting was also investigated. This increase has a strong influence on the development of rising diapirs. The ascent velocity and lateral spreading of the diapirs at the end of their ascent are effectively reduced when a viscosity increase by a factor of 10 is applied, and the effect becomes stronger for larger factors. Average vertical velocities range from 1.4 cm/yr for a factor 10 to 2 mm/yr for a factor 200.

The most striking result of the viscosity increase due to dehydration is the reduction of the ascent velocity, thereby stretching the characteristic time scale of the diapiric intrusion process to a value between 5 and 50 Ma for dehydration viscosity prefactor values of 10 and 200, respectively.

In contrast with the strong difference between the Newtonian and the composite rheology models, small differences are found in the overall dynamics between the composite rheological models, characterized by different values of the uniform grain size. The composite rheological models exhibit a selfregulating behaviour where substantial differences between the relative contributions of the two creep components result in very similar effective viscosities, due to a local dominance of dislocation creep at high stresses, and corresponding similar flow dynamics.

Stress levels and P,T-paths in the modelling results are consistent with estimates obtained from Precambrian peridotite bodies that are interpreted to have originated from asthenospheric diapirism.

9.2 Conclusions

From the various results obtained for the Earth, Venus and Mars in this thesis, tentative planetary histories may be constructed.

9.2.1 Earth

The initial stage immediately after accretion and core differentiation was probably characterized by a magma ocean (Murthy, 1992b; Abe, 1993a, 1997). After solidification of the magma ocean, the mantle was still very hot, too hot to allow plate tectonics on the

basis of lithosphere buoyancy considerations (see chapter 4). However, some effective cooling mechanism was required (chapter 5), and the combination of extensive flood volcanism and periodic resurfacing probably played an important role in the dynamics, and also in cooling of the planet. Additionally, the resurfacing events generated significant volumes of felsic material that formed proto-continents (see chapter 7). When the mantle temperature dropped to about 1500°C , oceanic lithosphere became negatively buoyant on time scale of some hundreds of million years or less, and active plate tectonics became possible (chapter 4). It is speculated that a more or less gradual transition from resurfacing dominated dynamics to plate tectonics took place around this mantle temperature, possibly during the late Archean. The advent of plate tectonics also provided an additional mechanism of continental growth through arc accretion. Continued operation of plate tectonics and resulting cooling of the mantle has brought it to its present state.

9.2.2 Venus

Though comparable in size and composition to the Earth, Venus did not undergo the same evolution. Periodic resurfacing has been suggested for Venus (Turcotte, 1995; Fowler and O'Brien, 1996), possibly by periodically operating plate tectonics (Solomatov and Moresi, 1996) or by the resurfacing mechanism presented in chapter 6. Currently, Venus is a dry planet, which would hinder plate tectonics specifically by increasing the fault strength (Nimmo and McKenzie, 1998). During its earlier history, the planet may have been less dry (Campbell and Taylor, 1983; Nimmo and McKenzie, 1998), but the mantle temperature was probably too high to allow plate tectonics (see chapter 4). It is therefore speculated that after an initial magma ocean regime during the earliest history, Venus stayed in a dynamic regime of periodic resurfacing through the process described in chapter 6 up to the present day.

9.2.3 Mars

The small size of Mars compared to Earth and Venus makes its surface to volume ratio ($\sim R^2/R^3$) much larger, making conductive cooling through the lithosphere of the planet much more efficient (see chapter 5). Observations and geophysical considerations indicate that if any large scale tectonic regime was active on Mars, it was probably during its early history (Zuber, 2001), although mantle convection models including pressure release partial melting show the rapid production of a thick thick buoyant outer shell under low gravity conditions, which would hinder plate tectonics (Schott et al., 2001). However, due to its reduced gravity compared to Earth, the operational window of potential temperatures for plate tectonics is limited to low mantle temperatures below $1300 - 1400^{\circ}\text{C}$ (chapter 5). The hotter mantle temperature expected for the early Martian history thus hinders plate tectonics. It is possible that the resurfacing mechanism of chapter 6 was active during the planet's early history. But after a potential period of this resurfacing regime, Mars probably rapidly went into the stagnant lid mode, continuing conduction-dominated cooling up to the present day.

Bibliography

- Abbott, D. H. and Isley, A. E. (2002). The intensity, occurrence and duration of superplume events and eras over geological time. *Journal of Geodynamics*, 34:265–307.
- Abe, Y. (1993a). Physical state of the very early Earth. *Lithos*, 30:223–235.
- Abe, Y. (1993b). Thermal Evolution and Chemical Differentiation of the Terrestrial Magma Ocean. In Takahashi, E., Jeanloz, R., and Rubie, D., editors, *Evolution of the Earth and Planets, Geophysical Monograph 74*, pages 41–54. AGU.
- Abe, Y. (1997). Thermal and chemical evolution of the terrestrial magma ocean. *Phys. Earth Planet. Inter.*, 100:27–39.
- Acuña, M. H., Connery, J. E. P., Ness, N. F., Lin, R. P., Mitchell, D., Carlson, C. W., McFadden, J., Anderson, K. A., Rème, H., Mazelle, C., Vignes, D., Wazilewsky, P., and Cloutier, P. (1999). Global Distribution of Crustal Magnetization Discovered by the Mars Global Surveyor MAG/ER Experiment. *Science*, 284(5415):790–793.
- Albarède, F. and Van der Hilst, R. D. (2002). Zoned Mantle Convection. *Philos. T. Roy. Soc. A*, 360(1800):2569–2592.
- Allègre, C. J., Manhès, G., and Göpel, C. (1995). The age of the Earth. *Geochimica et Cosmochimica Acta*, 59(8):1445–1456.
- Amelin, Y., Lee, D.-C., and Halliday, A. N. (2000). Early-middle Archean crustal evolution deduced from Lu-Hf and U-Pb isotopic studies of single zircon grains. *Geochimica et Cosmochimica Acta*, 64(24):4205–4225.
- Anderson, O. L. (2002). The power balance at the core-mantle boundary. *Phys. Earth Planet. Inter.*, 131:1–17.
- Anhaeusser, C. R. and Walraven, F. (1999). Episodic granitoid emplacement in the western Kaapvaal Craton: evidence from the Archean Kraaipan granite-greenstone terrane, South Africa. *Journal of African Earth Sciences*, 28(2):289–309.
- Arndt, N. (1983). Role of a thin, komatiite-rich oceanic crust in the Archean plate-tectonic process. *Geology*, 11:372–375.
- Arndt, N. (1999). Why was flood volcanism on submerged continental platforms so common in the Precambrian? *Precambrian Res.*, 97:155–164.
- Arndt, N., Ginibre, C., Chauvel, C., Albarède, F., Cheadle, M., C., H., Jenner, G., and Lahay, Y. (1998). Were komatiites wet? *Geology*, 26(8):739–742.
- Arndt, N. and Nesbitt, R. W. (1982). Geochemistry of Munro Township basalts. In Arndt, N. and Nisbet, E., editors, *Komatiites*, pages 209–330, London. George Allen & Unwin.
- Atherton, M. P. and Petford, N. (1993). Generation of sodium-rich magmas from newly underplated basaltic crust. *Nature*, 362:144–146.
- Avé Lallemant, H. G., Carter, N. L., Mercier, J.-C. C., and Ross, J. V. (1980). Rheology of the uppermost mantle: inferences from peridotite xenoliths. *Tectonophysics*, 70:1–27.
- Baker, V. R. (2001). Water and the martian landscape. *Nature*, 412:228–236.
- Ballard, S. and Pollack, H. N. (1987). Diversion of heat by Archean cratons: a model for southern Africa. *Earth Plan. Sci. Let.*, 85:253–264.
- Ballard, S. and Pollack, H. N. (1988). Modern and ancient geotherms beneath southern Africa. *Earth Plan. Sci. Let.*, 88:132–142.
- Barth, M. G., Rudnick, R. L., Horn, I., McDonough, W. F., Spicuzza, M. J., Valley, J. W., and Haggerty, S. E. (2001). Geochemistry of xenolithic eclogites from West Africa, Part I: A link between low MgO eclogites and Archean crust formation. *Geochimica et Cosmochimica Acta*, 65(9):1499–1527.

- Beattie, P. (1993). The generation of uranium series disequilibria by partial melting of spinel peridotite: constraints from partitioning studies. *Earth Plan. Sci. Let.*, 117:379–391.
- Bercovici, D., Ricard, Y., and Schubert, G. (2001). A two-phase model for compaction and damage. I. General Theory. *J. Geophys. Res.*, 106(B5):8887–8906.
- Bickle, M. J. (1978). Heat loss from the Earth: A constraint on Archaean tectonics from the relation between geothermal gradients and the rate of plate production. *Earth Plan. Sci. Let.*, 40:301–315.
- Bickle, M. J. (1986). Implications of melting for stabilisation of the lithosphere and heat loss in the Archaean. *Earth Plan. Sci. Let.*, 80:314–324.
- Blichert-Toft, J., Albarède, F., Rosing, M., Frei, R., and Bridgwater, D. (1999). The Nd and Hf isotopic evolution of the mantle through the Archean. Results from the Isua supracrustals, West Greenland, and from the Birimian terranes of West Africa. *Geochimica et Cosmochimica Acta*, 63(22):3901–3914.
- Boullier, A.-M. and Nicolas, A. (1973). Texture and fabric of peridotite nodules from kimberlite at mothae, thaba putsoa and kimberley. In *Lesotho Kimberlites*, pages 57–66. Lesotho National Development Corporation.
- Braun, J., Chery, J., Poliakov, A., Mainprice, D., Vauchez, A., Tommasi, A., and Daignerles, M. (1999). A simple parameterization of strain localization in the ductile regime due to grain size reduction: A case study for olivine. *J. Geophys. Res.*, 181(B11):25,167–25,181.
- Breuer, D. and Spohn, T. (1995). Possible flush instability in mantle convection at the Archaean-Proterozoic transition. *Nature*, 378:608–610.
- Brueckner, H. K. and Medaris, L. G. (1998). A tale of two orogens: The contrasting T-P-t history and geochemical evolution of mantle in high and ultra-high pressure metamorphic terranes of the Norwegian Caledonides and the Czech Variscides. *Schweiz. Mineral. Petrogr. Mitt.*, 78:293–307.
- Buck, W. R. and Su, W. (1989). Focused mantle upwelling below mid-ocean ridges due to feedback between viscosity and melting. *Geophys. Res. Let.*, 16(7):641–644.
- Buffett, B. A. (2003). The thermal state of the Earth's core. *Science*, 299(5613):1675–1676.
- Campbell, I. H. and Hill, R. I. (1988). A two-stage model for the formation of the granite-greenstone terrains of the Kalgoorlie-Norseman area, Western Australia. *Earth Plan. Sci. Let.*, 90:11–25.
- Campbell, I. H. and Taylor, S. R. (1983). No water, no granites - no oceans, no continents. *Geophys. Res. Let.*, 10(11):1061–1064.
- Carslaw, H. S. and Jaeger, J. C. (1959). *Conduction of heat in solids*. Clarendon Press, Oxford.
- Chopra, P. and Paterson, M. S. (1984). The role of water in the deformation of dunite. *J. Geophys. Res.*, 106:7861–7876.
- Chopra, P. N. and Paterson, M. S. (1981). The experimental deformation of dunite. *Tectonophysics*, 78:453–473.
- Christensen, U. R. (1985). Thermal evolution models for the earth. *J. Geophys. Res.*, 90(B4):2995–3007.
- Christensen, U. R. (1988). Is subducted lithosphere trapped at the 670-km discontinuity? *Nature*, 336:462–463.
- Christensen, U. R. and Hofmann, A. W. (1994). Segregation of subducted oceanic crust in the convecting mantle. *J. Geophys. Res.*, 99(B10):19867–19884.
- Christensen, U. R. and Yuen, D. A. (1985). Layered convection induced by phase transitions. *J. Geophys. Res.*, 99:10291–10300.
- Coltice, N. and Ricard, Y. (1999). Geochemical observations and one layer mantle convection. *Earth Plan. Sci. Let.*, 174:125–137.
- Condie, K. (1981). *Archean Greenstone Belts. Developments in Precambrian Geology 3*. Elsevier, Amsterdam.
- Condie, K. C. (1990). Geochemical characteristics of Precambrian basaltic greenstones. In Hall, R. P. and Hughes, D. J., editors, *Early Precambrian basic magmatism*, pages 40–55, Glasgow. Blackie.
- Condie, K. C. (1994). Greenstones through

- time. In Condie, K. C., editor, *Archean crustal evolution*, pages 85–120, Amsterdam, The Netherlands. Elsevier.
- Connerney, J. E. P., Acuña, M. H., Wasilewski, P. J., Ness, N. F., Rème, H., Mazelle, C., Vignes, D., Lin, R. P., Mitchell, D. L., and Cloutier, P. A. (1999). Magnetic Lineation in the Ancient Crust of Mars. *Science*, 284:794–798.
- Conrad, C. P. and Hager, B. H. (2001). Mantle convection with strong subduction zones. *Geophys. J. Int.*, 144:271–288.
- Crough, S. T. (1975). Thermal model of oceanic lithosphere. *Nature*, 256:388–390.
- Cuvelier, C., Segal, A., and Van Steenhoven, A. A. (1986). *Finite element methods and Navier-Stokes equations*. D. Reidel Publishing Company, Dordrecht, The Netherlands.
- Davies, G. F. (1979). Thickness and thermal history of continental crust and root zones. *Earth Plan. Sci. Let.*, 44:231–238.
- Davies, G. F. (1980). The Histories of Convective Earth Models and Constraints on Radiogenic Heat Production in the Earth. *J. Geophys. Res.*, 85(B5):2517–2530.
- Davies, G. F. (1992). On the emergence of plate tectonics. *Geology*, 20:963–966.
- De Bresser, J. H. P., Peach, C. J., Reijjs, J. P. J., and Spiers, C. J. (1998). On dynamic recrystallization during solid state flow: Effects of stress and temperature. *Geophys. Res. Let.*, 25:3457–3460.
- De Bresser, J. H. P., ter Heege, J. H., and Spiers, C. J. (2001). Grain size reduction by dynamic recrystallization: can it result in major rheological weakening? *Int. J. Earth Sciences*, 90(1):28–45.
- De Smet, J. H. (1999). *Evolution of the continental upper mantle: numerical modelling of thermo-chemical convection including partial melting*. PhD thesis, Utrecht University, The Netherlands.
- De Smet, J. H., Van den Berg, A. P., and Vlaar, N. J. (1998). Stability and growth of continental shields in mantle convection models including recurrent melt production. *Tectonophysics*, 296:15–29.
- De Smet, J. H., Van den Berg, A. P., and Vlaar, N. J. (1999). The evolution of continental roots in numerical thermo-chemical mantle convection models including differentiation by partial melting. *Lithos*, 48:153–170.
- De Smet, J. H., Van den Berg, A. P., and Vlaar, N. J. (2000a). Early formation and long-term stability of continents resulting from decompression melting in a convecting mantle. *Tectonophysics*, 322:19–33.
- De Smet, J. H., Van den Berg, A. P., and Vlaar, N. J. (2000b). Early formation and long-term stability of continents resulting from decompression melting in a convecting mantle. *Tectonophysics*, 322:19–33.
- De Smet, J. H., Van den Berg, A. P., Vlaar, N. J., and Yuen, D. A. (2000c). A characteristics-based method for solving the transport equation and its application to the process of mantle differentiation and continental root growth. *Geophys. J. Int.*, 140:651–659.
- De Wit, M. J. (1998). On Archean granites, greenstones, cratons and tectonics: does the evidence demand a verdict? *Precambrian Res.*, 91:181–226.
- Dohm, J. D. and Tanaka, K. L. (1999). Geology of the Thaumasia region, Mars: plateau development, valley origins, and magmatic evolution. *Planetary and Space Science*, 47:411–431.
- Doin, M. P. and Fleitout, L. (1996). Thermal evolution of the oceanic lithosphere: an alternative view. *Earth Plan. Sci. Let.*, 142:121–136.
- Drury, M. R. and Fitz Gerald, J. D. (1998). Mantle rheology: insights from laboratory studies of deformation and phase transition. In Jackson, I., editor, *The Earth's mantle: composition, structure and evolution*, pages 503–559. Cambridge University Press.
- Drury, M. R., van Roermund, H. L. M., Carswell, D. A., de Smet, J. H., van den Berg, A. P., and Vlaar, N. J. (2001). Emplacement of deep upper mantle rocks into cratonic lithosphere by convection and diapiric upwelling. *Journal of Petrology*, 42:131–140.
- Dumoulin, C., Doin, M.-P., and Fleitout, L.

- (2001). Numerical simulation of the cooling of an oceanic lithosphere above a convective mantle. *Earth Plan. Sci. Let.*, 125:45–64.
- Ellis, R. M. and Hajnal, Z. and Bostock, M. G. (1996). Seismic studies on the trans-hudson orogen of western Canada. *Tectonophysics*, 262:35–50.
- Fabriès, J., Lorand, J. P., Bodinier, J. L., and Dupuy, C. (1991). Evolution of the upper mantle beneath the Pyrenees: Evidence from orogenic spinel lherzolite massifs. *Journal of Petrology*, 32:55–76.
- Fei, Y., Moa, H., and Mysen, B. O. (1991). Experimental determination of element partitioning and calculation of phase relations in the MgO-FeO-SiO₂ system at high pressure and high temperature. *J. Geophys. Res.*, 96:2157–2169.
- Fischer, K. M. and Van der Hilst, R. D. (1999). A seismic look under the continents. *Science*, 285:1365–1366.
- Foley, S. F., Buhre, S., and Jacob, D. E. (2003). Evolution of the Archaean crust by delamination and shallow subduction. *Nature*, 421:249–252.
- Foley, S. F., Tiepolo, M., and Vannucci, R. (2002). Growth of early continental crust controlled by melting of amphibolite in subduction zones. *Nature*, 417:837–840.
- Folkner, W. M., Yoder, C. F., Yuan, D. N., Standish, E. M., and Preston, R. A. (1997). Interior structure and seasonal mass redistribution of Mars from radio tracking of Mars Pathfinder. *Science*, 278:1749–1751.
- Forte, A. M. and Perry, H. K. C. (2000). Geodynamic evidence for a chemically depleted continental tectosphere. *Science*, 290:1940–1944.
- Fowler, A. C. and O'Brien, S. B. G. (1996). A mechanism for episodic subduction on Venus. *J. Geophys. Res.*, 101(E2):4755–4763.
- Galer, S. and Goldstein, S. (1991). Early mantle differentiation and its thermal consequences. *Geochimica et Cosmochimica Acta*, 55:227–239.
- Goetze, C. (1978). Sheared lherzolites from the point of view of rock mechanics. *Geology*, 3:172–173.
- Goodwin, A. M. (1991). *Precambrian Geology*. Academic Press Limited, London.
- Grand, S. P. (1994). Mantle shear structure beneath the Americas and surrounding oceans. *J. Geophys. Res.*, 99(B6):11,591–11,612.
- Green, D. H., Nicholls, I. A., Viljoen, M., and Viljoen, R. (1975). Experimental demonstration of the existence of peridotitic liquids in earliest Archean magmatism. *Geology*, 3:11–14.
- Green, D. H. and Ringwood, A. E. (1967). An experimental investigation of the gabbro to eclogite transformation and its petrological applications. *Geochimica et Cosmochimica Acta*, 31:767–833.
- Green, H. T. (1982). Anatexis of mafic crust and high pressure crystallization of andesite. In Thorpe, R. S., editor, *Andesites*. John Wiley and Sons.
- Green, H. W. and Gueguen, Y. (1983). Deformation of peridotite in the mantle and extraction by kimberlite: A case history documented by fluid and solid precipitates in olivine. *Tectonophysics*, 92:71–92.
- Hacker, B. R. (1996). Eclogite formation and the rheology, buoyancy, seismicity and H₂O content of oceanic crust. In *Subduction: Top to Bottom*, pages 337–346. AGU Monogr.
- Hacker, B. R., Abers, G. A., and Peacock, S. M. (2003). Subduction factory I. Theoretical mineralogy, densities, seismic wave speeds, and H₂O contents. *J. Geophys. Res.*, 107.
- Haggerty, S. E. (1994). Superkimberlites: A geodynamic diamond window to the Earth's core. *Earth Plan. Sci. Let.*, 122:57–69.
- Halliday, A. N. and Lee, D.-C. (1999). Tungsten isotopes and the early development of the Earth and Moon. *Geochimica et Cosmochimica Acta*, 63(23/24):4157–4279.
- Hamilton, P. J., O'Nions, R. K., Bridgwater, D., and Nutman, A. (1983). Sm-Nd studies of Archaean metasediments and metavolcanics from West Greenland and their implications for the Earth's early history. *Earth Plan. Sci. Let.*, 62:263–272.

- Hamilton, W. B. (1998). Archean magmatism and deformation were not products of plate tectonics. *Precambrian Res.*, 91:143–179.
- Hargraves, R. B. (1986). Faster spreading or greater ridge length in the Archean? *Geology*, 14:750–752.
- Harte, B. (1983). Mantle peridotites and processes: The kimberlite sample. In Hawkesworth, C. J. and Norry, M. J., editors, *Continental basalts and mantle xenoliths*, Cambridge, Mass. Birkhäuser Boston.
- Hartmann, W. K., Malin, M., McEwen, A., Carr, M., Soderblom, L., Thomas, P., Danielson, E., James, P., and Veverka, J. (1999). Evidence for recent volcanism on Mars from crater counts. *Nature*, 397:586–589.
- Hartmann, W. K. and Neukum, G. (2001). Cratering chronology and the evolution of Mars. *Space Science Reviews*, 96:165–194.
- Helmstaedt, H. H. and Scott, D. J. (1992). The Proterozoic ophiolite problem. In Condie, K. C., editor, *Proterozoic crustal evolution*, pages 55–95, Amsterdam, The Netherlands. Elsevier.
- Henderson, P. (1982). *Inorganic geochemistry*. Pergamon.
- Herrick, D. L. and Parmentier, E. L. (1994). Episodic large-scale overturn of two-layer mantles in terrestrial planets. *J. Geophys. Res.*, 99(E1):2053–2062.
- Herzberg, C. and O'Hara, M. J. (1998). Phase equilibrium constraints on the origin of basalts, picrites and komatiites. *Earth-Science Reviews*, 44(1-2):39–79.
- Herzberg, C. and Zhang, J. (1996). Melting experiments on anhydrous peridotite KLB-1: Compositions of magmas in the upper mantle and the transition zone. *J. Geophys. Res.*, 101:8271–8295.
- Hirose, K., Fei, Y., Ma, Y., and Mao, H.-K. (1999). The fate of subducted basaltic crust in the earth's lower mantle. *Nature*, 397:53–56.
- Hirth, G. and Kohlstedt, D. L. (1996). Water in the oceanic upper mantle: implications for rheology, melt extraction and the evolution of the lithosphere. *Earth Plan. Sci. Let.*, 144:93–108.
- Hockney, R. W. and Eastwood, J. W. (1988). *Computer simulations using particles*. IOP Publishing Ltd, Bristol.
- Hofmann, A. W. (1997). Mantle geochemistry: the message from oceanic volcanism. *Nature*, 385:219–229.
- Hofmeister, A. (1999). Mantle values of thermal conductivity and the geotherm from phonon lifetimes. *Science*, 283:1699–1706.
- Honda, S. and Iwase, Y. (1996). Comparison of the dynamic and parameterized models of mantle convection including core cooling. *Earth Plan. Sci. Let.*, 139:133–145.
- Horedt, G. P. (1980). Gravitational heating of planets. *Phys. Earth Planet. Inter.*, 21:22–30.
- Huppert, H. E. and Sparks, S. J. (1988). The generation of granitic magmas by intrusion of basalt into continental crust. *Journal of Petrology*, 29(3):599–624.
- Irifune, T. and Ringwood, A. E. (1993). Phase transformations in subducted oceanic crust and buoyancy relations at depths of 600–800 km in the mantle. *Earth Plan. Sci. Let.*, 117:101–110.
- Ito, G. (2001). Reykjanes 'V'-shaped ridges originating from a pulsing and dehydrating mantle plume. *Nature*, 411:681–684.
- Ito, G., Shen, Y., Hirth, G., and J., W. C. (1999). Mantle flow, melting, and dehydration of the Iceland mantle plume. *Earth Plan. Sci. Let.*, 165:81–96.
- Ito, K. and Kennedy, G. C. (1971). An experimental study of the basalt-garnet granulite-eclogite transition. In Heacock, J. G., editor, *The structure and physical properties of the Earth's crust*, pages 303–314, Washington D. C. American Geophysical Union.
- Jakosky, B. M. and Phillips, R. J. (2001). Mars' volatile and climate history. *Nature*, 412:237–244.
- Jaques, A. L. and Green, D. H. (1980). Anhydrous Melting of Peridotite at 0–15 Kb Pressure and the Genesis of Tholeiitic Basalts. *Contrib. Mineral. Petrol.*, 73:287–310.
- Jha, K., Parmentier, E. M., and Morgan, J. P. (1994). The role of mantle-depletion and

- melt-retention buoyancy in spreading-center segmentation. *Earth Plan. Sci. Let.*, 125:221–234.
- Jin, Z.-M., Zhang, J., Green II, H. W., and Jin, S. (2001). Eclogite rheology: Implications for subducted lithosphere. *Geology*, 29(8):667–670.
- Johnson, K., Barnes, C. G., and Miller, C. A. (1997). Petrology, geochemistry, and genesis of high-Al tonalite and trondjemites of the Cornucopia Stock, Blue Mountains, northeastern Oregon. *Journal of Petrology*, 38(11):1585–1611.
- Jordan, T. H. (1979). Mineralogies, densities, and seismic velocities of garnet lherzolites and their geophysical implications. In *The Mantle Sample: Inclusions in Kimberlites and Other Volcanics*, pages 1–14. American Geophysical Union.
- Jung, H. and Karato, S.-I. (2001). Effects of water on dynamically recrystallized grain-size of olivine. *J. Struct. Geol.*, 23:1337–1344.
- Juteau, T. and Maury, R. (1999). *The Oceanic Crust, from Accretion to Mantle Recycling*. Springer-Praxis.
- Kameyama, M., Fujimoto, H., and Ogawa, M. (1996). A thermo-chemical regime in the upper mantle in the early earth inferred from a numerical model of magma-migration in a convecting upper mantle. *Phys. Earth Planet. Inter.*, 94:187–215.
- Kameyama, M., Yuen, D. A., and Fujimoto, H. (1997). The interaction of viscous heating with grain-size dependent rheology in the deformation of localized slip zones. *Geophys. Res. Let.*, 20:2523–2526.
- Karato, S. (1986). Does partial melting reduce the creep strength of the upper mantle? *Nature*, 319:309–310.
- Karato, S.-i. and Jung, H. (1998). Water, partial melting and the origin of the seismic low velocity and high attenuation zone in the upper mantle. *Earth Plan. Sci. Let.*, 157:193–207.
- Karato, S.-i., Toriumi, M., and Fujii, T. (1980). Dynamic recrystallization of olivine single crystals during high-temperature creep. *Geophys. Res. Let.*, 7:649–652.
- Karato, S.-i., Wang, Z., Lui, M., and Fujino, K. (1995). Plastic deformation of garnets: systematics and implications for the rheology of the mantle transition zone. *Earth Plan. Sci. Let.*, 130:13–30.
- Karato, S.-i. and Wu, P. (1993). Rheology of the upper mantle: a synthesis. *Science*, 260:771–778.
- Kellogg, L., Hager, B. H., and Van der Hilst, R. D. (1999). Compositional Stratification in the Deep Mantle. *Science*, 283:1881–1884.
- Kerr, A. C., Marriner, G. F., Arndt, N. T., Tarney, J., Nivia, A., Saunders, A. D., and Duncan, R. A. (1996). The petrogenesis of Gorgona komatiites, picrites and basalts: new field, petrographic and geochemical constraints. *Lithos*, 37:245–260.
- Kerrick, R., Polat, A., Wyman, D., and Hollings, P. (1999). Trace element systematics of Mg-, to Fe-tholeiitic basalt suites of the Superior Province: implications for Archean mantle reservoirs and greenstone belt genesis. *Lithos*, 46:163–187.
- Kimura, G., Ludden, J. N., Desrochers, J.-P., and Hori, R. (1993). A model of ocean-crust accretion for the Superior province, Canada. *Lithos*, 30:337–355.
- Kubo, T., Ohtani, E., Kondo, T., Takumi, K., Toma, M., Hosoya, T., Sano, A., Kikegawa, T., and Nagase, T. (2002). Metastable garnet in oceanic crust at the top of the lower mantle. *Nature*, 420:803–806.
- Kusky, T. M. (1998). Tectonic setting and terrane accretion of the Archean Zimbabwe craton. *Geology*, 26(2):163–166.
- Kusky, T. M., Li, J.-H., and Tucker, R. D. (2001). The Archean Dongwanzi ophiolite complex, North China craton: 2.505-Billion-year-old oceanic crust and mantle. *Science*, 292:1142–1145.
- Labrosse, S. (2002). Hotspots, mantle plumes and core heat loss. *Earth Plan. Sci. Let.*, 199:147–156.
- Labrosse, S., Poirier, J.-P., and Le Mouél, J.-L. (1997). On cooling of the earth's core. *Phys. Earth Planet. Inter.*, 99:1–17.
- Lambeck, K., Smither, C., and Johnston, P.

- (1998). Sea-level change, glacial rebound and mantle viscosity for northern Europe. *Geophys. J. Int.*, 134:102–144.
- Larsen, T. B. and Yuen, D. A. (1997). Ultrafast upwelling bursting through the upper mantle. *Earth Plan. Sci. Let.*, 146:393–399.
- Larsen, T. B., Yuen, D. A., Smedsmo, J. L., and Malevsky, A. V. (1997). Generation of fast timescale phenomena in thermo-mechanical processes. *Phys. Earth Planet. Inter.*, 102:213–222.
- Larsen, T. B., Yuen, D. A., and Storey, M. (1999). Ultrafast mantle plumes and implications for flood basalt volcanism in the northern Atlantic region. *Tectonophysics*, 311:31–43.
- Lockner, D. A. (1995). Rock Failure. In Ahrens, T. J., editor, *Rock Physics and Phase Relations. A Handbook of Physical Constants*, pages 127–147. American Geophysical Union.
- Ludden, J. H. and Gelinas, L. (1982). Trace element characteristics of komatiites and komatiitic basalts from the Abitibi metavolcanic belt of Quebec. In Arndt, N. T. and Nisbet, E. G., editors, *Komatiites*, pages 331–346, London. George Allen & Unwin.
- Mackwell, S. J., Zimmerman, M. E., and Kohlstedt, D. L. (1998). High-temperature deformation of dry diabase with application to tectonics on Venus. *J. Geophys. Res.*, 103(B1):975–984.
- Martin, H. (1999). Adakitic magmas: modern analogues of Archaean granitoids. *Lithos*, 46:411–429.
- McCulloch, M. T. and Bennett, V. C. (1994). Progressive growth of the Earth's continental crust and depleted mantle: Geochemical constraints. *Geochimica et Cosmochimica Acta*, 58(21):4717–4738.
- McDonough, W. F. and Sun, S.-s. (1995). The composition of the Earth. *Chemical Geology*, 120:223–253.
- McFarlane, E. A., Drake, M. J., and Rubie, D. C. (1994). Element partitioning between Mg-perovskite, magnesiowüstite, and silicate melt at conditions of the Earth's mantle. *Geochimica et Cosmochimica Acta*, 58(23):5161–5172.
- McKenzie, D. (1977). The initiation of trenches: a finite amplitude instability. In Talwani, M. and Pitman, W. C. I., editors, *Island Arcs, Deep Sea Trenches and Back-Arc Basins*, pages 57–61, Washington. American Geophysical Union.
- McKenzie, D. P. (1967). Some remarks on heat flow and gravity anomalies. *J. Geophys. Res.*, 72(24):6261–6273.
- McKenzie, D. P. (1984). The generation and compaction of partially molten rock. *Journal of Petrology*, 25:713–765.
- McKenzie, D. P., Barnett, D. N., and Yuan, D.-N. (2002). The relationship between martian gravity and topography. *Earth Plan. Sci. Let.*, 195:1–16.
- McKenzie, D. P. and Bickle, M. J. (1988). The Volume and Composition of Melt Generated by Extension of the Lithosphere. *Journal of Petrology*, 29:625–679.
- McNutt, M. K. (1984). Lithospheric flexure and thermal anomalies. *J. Geophys. Res.*, 89(B13):11,180–11,194.
- Mei, S. and Kohlstedt, D. L. (2000a). Influence of water on plastic deformation of olivine aggregates 1: Diffusion creep regime. *J. Geophys. Res.*, 105:21457–21469.
- Mei, S. and Kohlstedt, D. L. (2000b). Influence of water on plastic deformation of olivine aggregates 2: Dislocation creep regime. *J. Geophys. Res.*, 105:21471–21481.
- Mercier, J.-C. C. (1979). Peridotite xenoliths and the dynamics of kimberlite intrusions. In Boyd, F. R. and Meyer, H. O., editors, *The Mantle sample: Inclusions in Kimberlites and other Volcanics*, Washington. American Geophysical Union.
- Monnereau, M. and Dubuffet, F. (2002). Is Io's mantle really molten? *Icarus*, 158:450–459.
- Moresi, L. and Solomatov, V. (1998). Mantle convection with a brittle lithosphere: thoughts on the global tectonic styles of the Earth and Venus. *Geophys. J. Int.*, 133:669–682.
- Murthy, V. R. (1992a). Geochemical evidence

- for an initially molten Earth. *Phys. Earth Planet. Inter.*, 71:46–51.
- Murthy, V. R. (1992b). Geochemical evidence for an initially molten Earth. *Phys. Earth Planet. Inter.*, 71:46–51.
- Nicolas, A. (1986). Structure and petrology of peridotites: Clues to their geodynamic environment. *Rev. of Geophysics*, 24:875–895.
- Nicolas, A., Lucazeau, F., and Bayer, R. (1987). Peridotite xenoliths in Massif Central basalts, France: Textural and geophysical evidence for asthenospheric diapirism. In Nixon, P. H., editor, *Mantle xenoliths*, pages 563–574, New York. Wiley-Intersci.
- Nielsen, S. G., Baker, J. A., and Krogstad, E. J. (2002). Petrogenesis of an early Archaean (3.4 Ga) norite dyke, Isua, West Greenland: evidence for early Archaean crustal recycling? *Precambrian Res.*, 118:133–148.
- Nijman, W., De Bruijne, C. H., and Valkering, M. E. (1998). Growth fault control of Early Archaean cherts, barite mounds and chert-barite veins, North Pole Dome, Eastern Pilbara, Western Australia. *Precambrian Res.*, 88:25–52.
- Nimmo, F. (2002). Why does Venus lack a magnetic field? *Geology*, 30(11):987–990.
- Nimmo, F. and McKenzie, D. (1996). Modelling plume-related uplift, gravity and melting on Venus. *Earth Plan. Sci. Let.*, 145:109–123.
- Nimmo, F. and McKenzie, D. (1998). Volcanism and tectonics on Venus. *Ann. Rev. Earth Planet. Sci.*, 26:23–51.
- Nimmo, F. and Stevenson, D. J. (2000). Influence of early plate tectonics on the thermal evolution and magnetic field of Mars. *J. Geophys. Res.*, 105(E5):11,969–11,979.
- Nisbet, E. G. (1982). The tectonic setting and petrogenesis of komatiites. In Arndt, N. T. and Nisbet, E. G., editors, *Komatiites*, pages 501–520, London. George Allen & Unwin.
- Nisbet, E. G., Cheadle, M. J., Arndt, N. T., and Bickle, M. J. (1993). Constraining the potential temperature of the Archaean mantle: A review of the evidence from komatiites. *Lithos*, 30:291–307.
- Nisbet, E. G. and Fowler, C. M. R. (1983). Model for Archean plate tectonics. *Geology*, 11:376–379.
- Nishihara, Y. and Takahashi, E. (2001). Phase relation and physical properties of an Al-depleted komatiite to 23 GPa. *Earth Plan. Sci. Let.*, 190:65–77.
- Nixon, P. H. and Boyd, F. R. (1973). Petrogenesis of the granular and sheared ultrabasic nodule suite in kimberlites. In Nixon, P. H., editor, *Lesotho Kimberlites*, pages 48–56, Meseru, Lesotho. Lesotho Natl. Dev. Corp.
- Ogawa, M. (1988). Numerical Experiments on Coupled Magmatism-Mantle Convection System: Implications for Mantle Evolution and Archean Continental Crusts. *J. Geophys. Res.*, 93(B12):15,119–15,134.
- Ogawa, M. (1997). A bifurcation in the coupled magmatism-mantle convection system and its implications for the evolution of the earth's upper mantle. *Phys. Earth Planet. Inter.*, 102:259–276.
- Ogawa, M. (2000). Coupled magmatism-mantle convection system with variable viscosity. *Tectonophysics*, 322:1–18.
- Oxburgh, E. R. and Parmentier, E. M. (1977). Compositional and density stratification in oceanic lithosphere - causes and consequences. *J. Geol. Soc. Lond.*, 133:343–355.
- Parman, S. W., Dann, J. C., Grove, T. L., and De Wit, M. J. (1997). Emplacement conditions of komatiite magmas from the 3.49 Ga Komati formation, Barberton Greenstone Belt, South Africa. *Earth Plan. Sci. Let.*, 150:303–323.
- Parmentier, E. M. and Hess, P. C. (1992). Chemical differentiation of a convecting planetary interior: Consequences for a one plate planet such as Venus. *Geophys. Res. Let.*, 19(20):2015–2018.
- Parsons, B. and McKenzie, D. (1978). Mantle convection and the thermal structure of plates. *J. Geophys. Res.*, 83(B9):4485–4496.
- Parsons, B. and Sclater, J. G. (1977). An analysis of the variation of ocean floor bathymetry and heat flow with age. *J. Geophys. Res.*, 82(B5):803–827.
- Patchett, P. J. (1983). Importance of the

- Lu-Hf isotopic system in studies of planetary chronology and chemical evolution. *Geochimica et Cosmochimica Acta*, 47:81–91.
- Pavlenkova, N. I., Pavlenkova, G. A., and Solodilov, L. N. (1996). High velocities in the uppermost mantle of the siberian craton. *Tectonophysics*, 262:51–65.
- Pavlenkova, N. I. and Yegorkin, A. V. (1983). Upper mantle heterogeneity in the northern part of eurasia. *Phys. Earth Planet. Inter.*, 33:180–193.
- Peck, W. J., Valley, J. W., Wilde, S. M., and Graham, C. M. (2001). Oxygen isotope ratios and rare earth elements in 3.3 to 4.4 Ga zircons: Ion microprobe evidence for high ^{18}O continental crust and oceans in the Early Archean. *Geochimica et Cosmochimica Acta*, 65(22):4215–4229.
- Petford, N. and Gallagher, K. (2001). Partial melting of mafic (amphibolitic) lower crust by periodic influx of basaltic magma. *Earth Plan. Sci. Let.*, 193:483–499.
- Philpotts, A. R. (1990). *Principles of igneous and metamorphic petrology*. Prentice Hall, New Jersey.
- Piepenbreier, D. and Stöckhert, B. (2001). Plastic flow of omphacite in eclogites at temperatures below 500°C - implications for interplate coupling in subduction zones. *Int. J. Earth Sciences*, 90:197–210.
- Polat, A., Kerrich, R., and Wyman, D. A. (1998). The late Archean Schreiber-Hemlo and White River-Dayohessarah greenstone belts, Superior Province; collages of oceanic plateaus, oceanic arcs, and subduction-accretion complexes. *Tectonophysics*, 289(4):295–326.
- Pollack, H. N., Hurter, S. J., and Johnson, J. R. (1993). Heat flow from the Earth's interior: analysis of the global data set. *Rev. of Geophysics*, 31(3):267–280.
- Presnall, D. C., Weng, Y.-H., Milholland, C. S., and Walter, M. J. (1998). Liquidus phase relations in the system MgO-MgSiO_3 at pressures up to 25 GPa - constraints on crystallization of a molten Hadean mantle. *Phys. Earth Planet. Inter.*, 107:83–95.
- Puchtel, I. S., Hofmann, A. W., Mezger, K., Jochum, K. P., Shchipansky, A. A., and Samsonov, A. V. (1998). Oceanic plateau model for continental crustal growth in the archaean: A case study from the Kostomuksha greenstone belt, NW Baltic Shield. *Earth Plan. Sci. Let.*, 155:57–74.
- Rapp, R. P., Watson, B. E., and Miller, C. F. (1991). Partial melting of amphibolite/eclogite and the origin of Archean trondhjemites and tonalites. *Precambrian Res.*, 51:1–25.
- Reese, C. C., Solomatoc, V. S., and Moresi, L.-N. (1998). Heat transport efficiency for stagnant lid convection with dislocation viscosity: Application to Mars and Venus. *J. Geophys. Res.*, 103(E6):13,643–13,657.
- Ricard, Y., Bercovici, D., and Schubert, G. (2001). A two-phase model for compaction and damage. 2. Application to compaction, deformation, and the role of interfacial tension. *J. Geophys. Res.*, 106(B5):8907–8924.
- Richards, M. A., Duncan, R. A., and Courtillot, V. E. (1989). Flood Basalts and Hot-Spot Tracks: Plume Heads and Tails. *Science*, 246:103–107.
- Richter, F. M. (1985). Models for the Archean thermal regime. *Earth Plan. Sci. Let.*, 73:350–360.
- Richter, F. M. (1988). A Major Change in the Thermal State of the Earth at the Archean-Proterozoic Boundary: Consequences for the Nature and Preservation of Continental Lithosphere. *Journal of Petrology, Special Lithosphere Issue*, pages 39–52.
- Ringwood, A. E. and Irifune, T. (1988). Nature of the 650-km seismic discontinuity; implications for mantle dynamics and differentiation. *Nature*, 331(6152):131–136.
- Rollinson, H. (1997). Eclogite xenoliths in west African kimberlites as residues from Archean granitoid crust formation. *Nature*, 389:173–176.
- Ross, J. V., Ave Lallemand, H. G., and Carter, N. L. (1980). Stress dependence of recrystallized-grain and subgrain size in olivine. *Tectonophysics*, 70:39–61.

- Rudnick, R. L. (1995). Making continental crust. *Nature*, 378:571–578.
- Rudnick, R. L., Barth, M., Horn, I., and McDonough, W. F. (2000). Rutile-bearing refractory eclogites: missing link between continents and depleted mantle. *Science*, 287:278–281.
- Ruff, L. and Anderson, D. L. (1980). Core formation, evolution and convection: a geophysical model. *Phys. Earth Planet. Inter.*, 21:181–201.
- Rutter, E. H. and Brodie, K. (1988). The role of tectonic grain size reduction in the rheological stratification of the lithosphere. *Geologische Rundschau*, 77(1):295–308.
- Sanloup, C., Jambon, A., and Gillet, P. (1999). A simple chondritic model of Mars. *Phys. Earth Planet. Inter.*, 112:43–54.
- Saxena, S. (1996). Earth mineralogical mode: Gibbs free energy minimization computation in the system MgO – FeO – SiO₂. *Geochimica et Cosmochimica Acta*, 60:2379–2395.
- Schaber, G. G., Strom, R. G., Moore, H. J., Soderblom, L. A., Kirk, R. L., Chadwick, D. J., Dawson, D. D., Gaddis, L. R., Boyce, J. M., and Russel, J. (1992). Geology and distribution of impact craters on Venus: what are they telling us? *J. Geophys. Res.*, 97(E8):13,257–13,301.
- Schmeling, H., Monz, R., and Rubie, D. C. (1999). The influence of olivine metastability on the dynamics of subduction. *Earth Plan. Sci. Let.*, 165:55–66.
- Schott, B., Van den Berg, A. P., and Yuen, D. A. (2001). Focussed Time-Dependent Martian Volcanism From Chemical Differentiation Coupled With Variable Thermal Conductivity. *Geophys. Res. Let.*, 28(22):4271–4274.
- Schott, B., Van den Berg, A. P., and Yuen, D. A. (2002). Slow secular cooling and long lived volcanism on Mars explained. *Lunar and Planetary Science Conference 33*. <http://www.lpi.usra.edu/meetings/lpsc2002>.
- Schubert, G. and Spohn, T. (1990). Thermal history of Mars and the sulfur content of its core. *J. Geophys. Res.*, 95(B9):14,095–14,104.
- Schulze, D. J., Harte, B., Valley, J. W., Brenan, J. M., and Channer, D. M. (2003). Extreme crustal oxygen isotope signatures preserved in coesite in diamond. *Nature*, 423:68–70.
- Sclater, J. G., Jaupart, C., and Galson, D. (1980). The Heat Flow Through Oceanic and Continental Crust and the Heat Loss of the Earth. *Reviews of Geophysics and Space Physics*, 18(1):269–311.
- Scott, D. R. and Stevenson, D. J. (1984). Magma solitons. *Geophys. Res. Let.*, 11(11):1161–1164.
- Scott, D. R. and Stevenson, D. J. (1989). A self-consistent model of melting, magma migration and buoyancy-driven circulation beneath mid-ocean ridges. *J. Geophys. Res.*, 94:2973–2988.
- Segal, A. (1993). Finite element methods for advection-diffusion equations. In Vreugdenhil, C. B. and Koren, B., editors, *Numerical methods for advection-diffusion problems. Notes on Numerical Fluid Mechanics, volume 45*, pages 195–214, Braunschweig, Germany. Vieweg.
- Segal, A. and Praagman, N. P. (2002). The sepran package. Technical report, <http://dutita0.twi.tudelft.nl/NW/sepran.html>.
- Segal, A. and Vuik, C. (2000). *Computational Fluid Dynamics II, course manual*. J.M. Burgerscentrum, Research School for Fluid Mechanics, Delft, The Netherlands.
- Sharpe, H. N. and Peltier, W. R. (1978). Parameterized mantle convection and the Earth's thermal history. *Geophys. Res. Let.*, 5(9):737–740.
- Silver, P. G., Gao, S. S., Liu, K. H., and the Kaapvaal Seismic Group (2001). Mantle deformation beneath southern africa. *Geophys. Res. Let.*, 28(13):2493–2496.
- Sleep, N. H. (1990). Hotspots and Mantle Plumes: Some Phenomenology. *J. Geophys. Res.*, 95(B5):6715–6736.
- Sleep, N. H. (1994). Martian plate tectonics. *J. Geophys. Res.*, 99(E3):5639–5655.
- Sleep, N. H. (2000). Evolution of the mode of convection within terrestrial planets. *J. Geo-*

- phys. Res.*, 105(E7):17563–17578.
- Sleep, N. H. (2002). Local lithospheric relief associated with fracture zones and ponded plume material. *Geochem. Geophys. Geosyst.*, 3(12).
- Sleep, N. H. and Windley, B. F. (1982). Archean plate tectonics: constrains and inferences. *Journal of Geology*, 90:363–379.
- Smith, H. S., Erlank, A. J., and Duncan, A. R. (1980). Geochemistry of some ultramafic komatiite lava flows from the Barberton Mountain Land, South Africa. *Precambrian Res.*, 11:399, 415.
- Smith, J. B. (2003). The episodic development of intermediate to silicic volcano-plutonic suites in the Archean West Pilbara, Australia. *Chemical Geology*, 194:275–295.
- Smithies, R. H. (2000). The Archean tonalite-trondhjemite-granodiorite (TTG) series is not an analogue of Cenozoic adakite. *Earth Plan. Sci. Lett.*, 182:115–125.
- Smrekar, S. E. and Parmentier, E. M. (1996). The interaction of mantle plumes with surface thermal and chemical boundary layers: Applications to hotspots on Venus. *J. Geophys. Res.*, 101(B3):5397–5410.
- Solomatov, V. S. and Moresi, L.-N. (1996). Stagnant lid convection on Venus. *J. Geophys. Res.*, 101(E2):4737–4753.
- Solomatov, V. S. and Moresi, L.-N. (2000). Scaling of time-dependent stagnant lid convection: application to small-scale convection on earth and other terrestrial planets. *J. Geophys. Res.*, 105(B9):1,795–21,817.
- Solomatov, V. S. and Zharkov, V. N. (1990). The thermal regime of Venus. *Icarus*, 84:280–295.
- Solomon, S. C. and Head, J. W. (1990). Heterogeneities in the thickness of the elastic lithosphere of Mars: constraints on heat flow and internal dynamics. *J. Geophys. Res.*, 95(B7):11,073–11,083.
- Spiegelman, M. (1993a). Flow in deformable porous media. part 1. simple analysis. *J. Fluid Mech.*, 247:17–38.
- Spiegelman, M. (1993b). Flow in deformable porous media. part 2. Numerical analysis: The relationship between shock waves and solitary waves. *J. Fluid Mech.*, 247:39–63.
- Spohn, T., Acuña, M. H., Breuer, D., Golombek, M., Greeley, R., Halliday, A., Hauber, E., Jaumann, R., and Sohl, F. (2001). Geophysical constraints on the evolution of Mars. *Space Science Reviews*, 96:231–262.
- Spohn, T. and Schubert, G. (1982). Modes of mantle convection and the removal of heat from the earth's interior. *J. Geophys. Res.*, 87(B6):4682–4696.
- Stacey, F. D. (1992). *Physics of the Earth*. Brookfield Press, Australia, third edition.
- Stein, C. A. (1995). Heat flow of the Earth. In *Global Earth Physics. A handbook of physical constants*, pages 144–158. AGU.
- Stein, C. A. and Stein, S. (1992). A model for the global variation in oceanic depth and heat flow with lithospheric age. *Nature*, 359:123–129.
- Stein, M. and Hofmann, A. W. (1994). Mantle plumes and episodic crustal growth. *Nature*, 372:63–68.
- Steinbach, V., Hansen, U., and Ebel, A. (1989). Compressible convection in the Earth's mantle - a comparison of different approaches. *Geophys. Res. Lett.*, 16(7):633–636.
- Steinbach, V. and Yuen, D. A. (1993). Instabilities from phase-transitions and the timescales of mantle thermal evolution. *Geophys. Res. Lett.*, 20(12):1119–1122.
- Stevenson, D. J. (2003). Styles of mantle convection and their influence on planetary evolution. *C. R. Geoscience*, 335:99–111.
- Stevenson, D. J., Spohn, T., and Schubert, G. (1983). Magnetism and thermal evolution of the terrestrial planets. *Icarus*, 54:466–489.
- Stixrude, L. and Cohen, R. E. (1993). Stability of orthorhombic MgSiO₃ perovskite in the earth's lower mantle. *Nature*, 364(6438):613–636.
- Stone, W. E., Deloule, E., Larson, M. S., and Leshner, C. M. (1997). Evidence for hydrous high-MgO melts in the Precambrian. *Geology*, 25(2):143–146.
- Tackley, P. J. (2000). Mantle Convection and Plate Tectonics: Toward an Integrated

- Physical and Chemical Theory. *Science*, 288:2002–2007.
- Takahashi, E. and Kushiro, I. (1983). Melting of dry peridotite at high pressures and basalt magma genesis. *American Mineralogist*, 68:859–879.
- Taylor, S. R. and McLennan, S. M. (1985). *The Continental Crust: its Composition and Evolution*. Blackwell Scientific Publications.
- Thurston, P. C. (1994). Archean volcanic patterns. In Condie, K. C., editor, *Archean crustal evolution*, pages 45–84, Amsterdam, The Netherlands. Elsevier.
- Tommasi, A., Tikoff, B., and Vauchez, A. (1999). Upper mantle tectonics: three-dimensional deformation, olivine crystallographic fabrics and seismic properties. *Earth Plan. Sci. Let.*, 168:173–186.
- Trampert, J. and Woodhouse, J. H. (1996). High resolution global phase velocity distributions. *Geophys. Res. Let.*, 23(1):21–24.
- Turcotte, D. L. (1980). On the thermal evolution of the earth. *Earth Plan. Sci. Let.*, 48:53–58.
- Turcotte, D. L. (1993). An Episodic Hypothesis for Venusian Tectonics. *J. Geophys. Res.*, 98(E9):17,061–17,068.
- Turcotte, D. L. (1995). How does Venus lose heat? *J. Geophys. Res.*, 100(E8):16931–16940.
- Turcotte, D. L., Morein, G., Roberts, D., and Malamud, B. D. (1999). Catastrophic resurfacing and episodic subduction on Venus. *Icarus*, 139:49–54.
- Turcotte, D. L. and Oxburgh, E. R. (1967). Finite amplitude convective cells and continental drift. *J. Fluid Mech.*, 28:29–42.
- Turcotte, D. L. and Schubert, G. (2002). *Geodynamics, Applications of continuum physics to geological problems*. John Wiley & Sons, 2nd edition.
- Vacquier, V. (1998). A theory of the origin of the Earth's internal heat. *Tectonophysics*, 291:1–7.
- Van den Berg, A. P., Rainey, E. S. G., and Yuen, D. A. (2003). The influences of variable thermal conductivity, variable viscosity and core-mantle coupling on thermal evolution.
- Van den Berg, A. P., Van Keken, P. E., and Yuen, D. A. (1993). The effects of a composite non-Newtonian and Newtonian rheology on mantle convection. *Geophys. J. Int.*, 115:62–78.
- Van den Berg, A. P. and Yuen, D. A. (1996). Is the lower-mantle rheology Newtonian today? *Geophys. Res. Let.*, 23(16):2033–2036.
- Van den Berg, A. P. and Yuen, D. A. (1997). The role of shear heating in lubricating mantle flow. *Earth Plan. Sci. Let.*, 151:33–42.
- Van den Berg, A. P. and Yuen, D. A. (1998). Modelling planetary dynamics by using the temperature at the core-mantle boundary as a control variable: effects of rheological layering on mantle heat transport. *Phys. Earth Planet. Inter.*, 108:219–234.
- Van den Berg, A. P. and Yuen, D. A. (2002). Delayed cooling of the earth's mantle due to variable thermal conductivity and the formation of a low conductivity zone. *Earth Plan. Sci. Let.*, 199:403–413.
- Van der Hilst, R. D. and Káráson, H. (1999). Compositional Heterogeneity in the Bottom 1000 km of the Earth's Mantle: Toward a Hybrid Convection Model. *Science*, 283:1885–1888.
- Van der Wal, D., Chopra, P., Drury, M., and Fitz Gerald, J. (1993). Relationships between dynamically recrystallized grain size and deformation conditions in experimentally deformed olivine rocks. *Geophys. Res. Let.*, 14:1479–1482.
- Van Hunen, J. (2001). *Shallow and buoyant lithosphere subduction: causes and implications from thermo-chemical numerical modelling*. PhD thesis, Utrecht University, The Netherlands.
- Van Hunen, J., Van den Berg, A. P., and Vlaar, N. J. (2002). On the role of subducting oceanic plateaus in the development of shallow flat subduction. *Tectonophysics*, 352:317–333.
- Van Hunen, J., Van den Berg, A. P., and Vlaar, N. J. (2003). Various mechanisms to induce present-day shallow flat subduction and implications for the younger earth: a numerical parameter study. submitted to *Phys. Earth*

- Planet. Inter.
- Van Keken, P. E. (1997). Evolution of starting mantle plumes: a comparison between numerical and laboratory experiments. *Earth Plan. Sci. Let.*, 148:1–11.
- Van Keken, P. E., King, S. D., Schmeling, H., Christensen, U. R., Neumeister, D., and Doin, M.-P. (1997). A comparison of methods for the modeling of thermochemical convection. *J. Geophys. Res.*, 102:22477–22495.
- Van Roermund, H. L. M. and Drury, M. R. (1998). Ultra-high pressure (P>6 GPa) garnet peridotites in western Norway: Exhumation of mantle rocks from more than 185 km. *Terra Nova*, 10:195–301.
- Van Roermund, H. L. M., Drury, M. R., Barnhoorn, A., and de Ronde, A. (2001). Relict majoritic garnet microstructures from ultra-deep orogenic peridotites in western Norway. *Journal of Petrology*, 42:117–130.
- Van Thienen, P., Van den Berg, A. P., De Smet, J. H., Van Hunen, J., and Drury, M. R. (2003a). Interaction between small-scale mantle diapirs and a continental root. *Geochem. Geophys. Geosyst.*, 4:10.1029/2002GC000338.
- Van Thienen, P., Van den Berg, A. P., and Vlaar, N. J. (2003b). Production and recycling of oceanic crust in the early earth. submitted to *Tectonophysics*.
- Van Thienen, P., Vlaar, N. J., and Van den Berg, A. P. (2003c). Plate tectonics on the terrestrial planets. submitted to *Physics of the Earth and Planetary Interiors*.
- Vervoort, J. D., Patchett, P. J., Gehrels, G. E., and Nutman, A. P. (1996). Constraints on early Earth differentiation from hafnium and neodymium isotopes. *Nature*, 379:624–627.
- Vlaar, N. J. (1985). Precambrian geodynamical constraints. In Tobi, A. C. and Touret, J. L. R., editors, *The deep proterozoic crust in the North Atlantic provinces*, pages 3–20. Reidel.
- Vlaar, N. J. (1986). Archaean global dynamics. *Geologie en Mijnbouw*, 65:91–101.
- Vlaar, N. J. and Van den Berg, A. P. (1991). Continental evolution and archeo-sea-levels. In Sabadini, R., Lambeck, K., and Boschi, E., editors, *Glacial Isostasy, Sea-Level and Mantle Rheology*, Dordrecht, Netherlands. Kluwer.
- Vlaar, N. J., Van Keken, P. E., and Van den Berg, A. P. (1994). Cooling of the Earth in the Archaean: Consequences of pressure-release melting in a hotter mantle. *Earth Plan. Sci. Let.*, 121:1–18.
- Vreugdenhil, C. B. (1993). Introduction. In Vreugdenhil, C. B. and Koren, B., editors, *Numerical methods for advection-diffusion problems. Notes on Numerical Fluid Mechanics, volume 45*, Braunschweig, Germany. Vieweg.
- Walter, M. J. (1998). Melting of Garnet Peridotite and the Origin of Komatiite and Depleted Lithosphere. *Journal of Petrology*, 39(1):29–60.
- Walzer, U. and Hendel, R. (1997). Time-dependent thermal convection, mantle differentiation and continental-crust growth. *Geophys. J. Int.*, 130:303–325.
- Walzer, U. and Hendel, R. (1999). A new convection-fractionation model for the evolution of the principal geochemical reservoirs of the earth's mantle. *Phys. Earth Planet. Inter.*, 112:211–256.
- Weinberg, R. F. and Podladchikov, Y. (1994). Diapiric ascent of magmas through power law crust and mantle. *J. Geophys. Res.*, 99(B5):9543–9559.
- White, R. S. and McKenzie, D. (1995). Mantle plumes and flood basalts. *J. Geophys. Res.*, 100(B9):17543–17585.
- Wilde, S. A., Valley, J. D., Peck, W. H., and Graham, C. M. (2001). Evidence from detrital zircons for the existence of continental crust and oceans on the Earth 4.4 Gyr ago. *Nature*, 409:175–178.
- Winther, K. T. (1996). An experimentally based model for the origin of tonalitic and trondhjemitic melts. *Chemical Geology*, 127:43–59.
- Yaxley, G. M. and Green, D. H. (1998). Reactions between eclogite and peridotite: mantle refertilization by subduction of oceanic crust.

- Schweiz. Mineral. Petrogr. Mitt.*, 78:243–255.
- Yoder, C. F., Konoplic, A. S., Yuan, D. N., Standish, E. M., and Folkner, W. M. (2003). Fluid core size of Mars from detection of the solar tide. *Science*, 300:299–303.
- Yukutake, T. (2000). The inner core and the surface heat flow as clues to estimating the initial temperature of the earth's core. *Phys. Earth Planet. Inter.*, 121:103–137.
- Zegers, T. E. and Van Keken, P. E. (2001). Middle archean continent formation by crustal delamination. *Geology*, 29:1083–1086.
- Zegers, T. E., Wijbrans, J. R., and White, S. H. (1999). $^{40}\text{Ar}/^{39}\text{Ar}$ age constraints on tectonothermal events in the Shaw ware of the eastern Pilbara granite-greenstone terrain (W Australia): 700 Ma of Archean tectonic evolution. *Tectonophysics*, 311:45–81.
- Zhai, M., Zhao, G., and Zhang, Q. (2002). Is Dongwanzi Complex an Archean Ophiolite? *Science*, 295(5557):923.
- Zhang, C. Z. and Zhang, K. (1995). On the internal structure and magnetic fields of Venus. *Earth, Moon and Planets*, 69:237–247.
- Zuber, M. T. (2001). The crust and mantle of Mars. *Nature*, 412:220–227.

Appendix A

Error magnitude in the conservation of energy in the approximate melt segregation scheme

A.1 Conservation of energy

The approximate melt segregation used in the thermochemical convection models of chapters 6 and 7 has an impact on the conservation of energy, because although 'segregated' melt is added to the system at the top boundary, compaction in the region where the melt is removed is neglected in the numerical model. Here the magnitude of this effect is calculated for a simplified situation to estimate the effect in the convection models. This is done by computing the thermal energy content of an undifferentiated column (case 1, see figure A.1) and comparing it to two differentiated cases (i.e. with a basaltic crust and complementary depleted zone). In the first differentiated case (case 2a, see figure A.1), melt segregation is accompanied by compaction of the melting region. This is the 'true' reference case, in which conservation of both mass and energy are observed. The second differentiated case (case 2b, see figure A.1) is comparable to the result of the approximate melt segregation in scheme in the thermochemical convection models (see section 2.7). Compaction in the melting zone is neglected here, but in spite of this, the produced melt is forced into the top of the model. This results in a certain artificial compaction of the modelled material. This artificial compaction is assumed to be accommodated by the entire domain in a uniform fashion, consistent with test results. The approximations made in the calculations below are:

- the densities of basaltic crust and mantle material are the same;

- the density of mantle material does not change upon depletion;
- the density of any material is independent of temperature and pressure.

The latter two approximations are in line with the (extended) Boussinesq approximation used in the numerical simulations. The result of these assumptions is that partial melting and melt segregation can be regarded as simple transport of material from the melting region to the surface *with conservation of volume*, which simplifies the calculations.

A.2 Thermal energy content

In a 1-D situation the thermal energy content of a domain $[0, z_m]$ is given by:

$$Q = \int_0^{z_m} \rho c_p T dz \quad (\text{A.1})$$

This can be applied to the different cases shown in Figure A.1. The temperature drop ΔT associated with the consumption of latent heat due to partial melting is found from the following expression, which is valid under the conditions listed above:

$$T dS = c_p dT \quad (\text{A.2})$$

$$\Delta T = T_m \cdot \left(1 - e^{-\frac{F \Delta S}{c_p}}\right) \quad (\text{A.3})$$

case 1

$$\begin{aligned} Q_1 &= \left(\frac{1}{2} \cdot z_{tr} + (z_m - z_{tr})\right) \rho_m c_{pm} T_m \\ &= \left(z_m - \frac{1}{2} \cdot z_{tr}\right) \rho_m c_{pm} T_m \end{aligned} \quad (\text{A.4})$$

case 2a

$$\begin{aligned} Q_{2a} &= \frac{1}{2} z_{tr} \rho_m c_{pm} T_m + \{z_m - z_{tr} - z_b - (z_{mz} - z_b)\} \rho_m c_{pm} T_m \\ &\quad + (z_{mz} - z_b) \rho_m c_{pm} (T_m - \Delta T) \\ &= \frac{1}{2} z_{tr} \rho_m c_{pm} T_m + (z_m - z_{tr} - z_{mz}) \rho_m c_{pm} T_m \\ &\quad + (z_{mz} - z_b) \rho_m c_{pm} (T_m - \Delta T) \end{aligned} \quad (\text{A.5})$$

case 2b

$$Q_{2b} = \frac{1}{2} \frac{z_m}{z_m + z_b} z_{tr} \rho_m c_{pm} T_m$$

symbol	parameter	value
ρ_m	density	3416kgm ⁻³
c_{pm}	specific heat	1250Jkg ⁻¹ K ⁻¹
T_m	mantle temperature	1500 K
F	degree of depletion	
ΔS	entropy of melting	300Jkg ⁻¹ K ⁻¹

Table A.1: Symbol definitions and parameter values.

$$\begin{aligned}
& + \left(z_m - \frac{z_m}{z_m + z_b} z_b - \frac{z_m}{z_m + z_b} z_{tr} - \frac{z_m}{z_m + z_b} z_{mz} \right) \rho_m c_{pm} T_m \\
& + \frac{z_m}{z_m + z_b} z_{mz} \rho_m c_{pm} (T_m - \Delta T) \\
& = \frac{1}{2} \frac{z_m}{z_m + z_b} z_{tr} \rho_m c_{pm} T_m + \left(z_m - \frac{z_m}{z_m + z_b} z_b - \frac{z_m}{z_m + z_b} z_{tr} \right) \cdot \\
& \rho_m c_{pm} T_m - \frac{z_m}{z_m + z_b} z_{mz} \rho_m c_{pm} \Delta T
\end{aligned} \tag{A.6}$$

A.3 Error magnitude

Using the parameter values listed in Table A.1, we have calculated the difference between heat loss upon differentiation between the scenario including consistent compaction (case 1 \rightarrow case 2a) and the approximate scenario (case 1 \rightarrow case 2b), the latter of which is representative of the implementation in the thermochemical convection models of chapters 6 and 7. The results, for three different values of the uniform degree of depletion in the melting zone, are listed in Table A.2. The amount of heat removed from the system by partial melting and cooling of the segregated melt is underestimated by about 10 percent in the approximate melt segregation scheme.

F	ΔQ_{2a}	ΔQ_{2b}	$\frac{\Delta Q_{2b} - \Delta Q_{2a}}{\Delta Q_{2a}}$
(-)	($\cdot 10^{13}$ J)	($\cdot 10^{13}$ J)	(-)
0.1	3.886	3.518	-0.105
0.2	7.606	6.932	-0.097
0.3	11.17	10.24	-0.090

Table A.2: Resulting thermal energy content drops upon differentiation between cases 1 and 2a (ΔQ_{2a}) and 1 and 2b (ΔQ_{2b}), for three different degrees of depletion F (uniform value within the melting zone). The resulting relative errors in the last column show that the approximate scenario of case 2b, comparable to the implementation in the thermochemical convection models of chapters 6 and 7, result in an underestimation of the removal of heat from the system of about 10 percent. Values for the dimensional parameters are: $z_m = 400$ km, $z_{tr} = 100$ km, $z_{mz} = 50$ km (although the relative results are independent of this value).

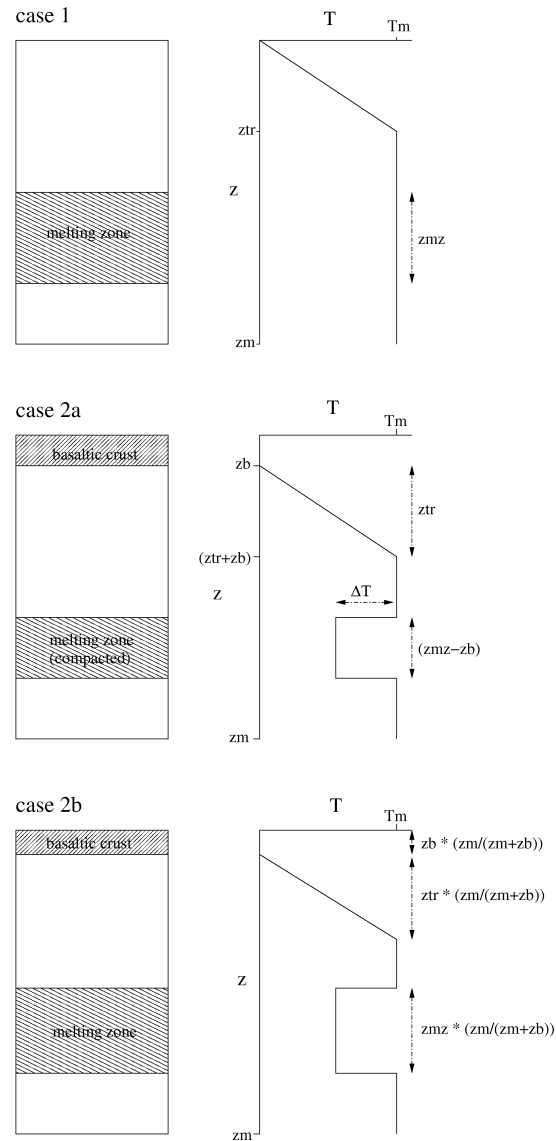


Figure A.1: The geometry (1-D) and geotherms are shown for the three different cases. The first case is before melting. Case 2a is an exact solution after melting. The melting zone compacts as the melt is removed. Case 2b is the approximate solution corresponding to the implementation of the melt segregation process in the numerical models of chapters 6 and 7. No compaction of the melting zone takes place and the compaction required because basaltic material is forced into the domain is accommodated by the entire domain, resulting in prefactors $(z_m / (z_m + z_b))$ in the layer thicknesses.

Appendix B

Discretization and benchmarking of the energy equation

In this appendix, the discretization of the energy equation will be presented, following De Smet (1999), and benchmark results concerning the latent heat terms in the energy equation will be shown.

B.1 The energy equation

The non-dimensional energy equation (2.4), presented in chapter 2, has the following form:

$$\begin{aligned} \frac{\partial T'}{\partial t'} + u'_j \partial_j T' - Di(T' + T'_0)w' = \partial_j \partial_j T' + \frac{Di}{Ra} \Phi' - \frac{\Delta S}{c_p} \frac{dF}{dt'} (T' + T'_0) + \\ \sum_k \gamma'_k \frac{Rc_k}{Ra} Di(T' + T'_0) \frac{d\Gamma_k}{dt'} + RH' \end{aligned} \quad (\text{B.1})$$

The explicit time derivatives of the degree of depletion F and the phase function Γ_k are rewritten to implicit forms. For the time derivative of F , this is done using an expansion of the dimensional differential dF/dt (De Smet, 1999):

$$\frac{dF}{dt} = \frac{\partial F}{\partial p} \frac{dp}{dt} + \frac{\partial F}{\partial T} \frac{dT}{dt} = A(p, T) \frac{dp}{dt} + B(p, T) \frac{dT}{dt} \quad (\text{B.2})$$

The functions A and B are computed from the parameterized phase diagram. Non-dimensionalization of this expression results in:

$$\frac{dF}{dt'} = \frac{\rho_0 g h^3}{\eta_0 \kappa} A' w' + B' \frac{dT'}{dt'} \quad (\text{B.3})$$

with w' the non-dimensional vertical velocity component.

In the same manner, the term $d\Gamma_k/dt$ scaling the heat effect of solid state phase transitions is treated (De Smet, 1999):

$$\frac{d\Gamma_k}{dt} = \frac{d\Gamma_k}{d\pi_k} \left(\frac{d\pi_k}{dp} \frac{dp}{dt} + \frac{d\pi_k}{dT} \frac{dT}{dt} \right) \quad (\text{B.4})$$

in which π_k is the reduced pressure for phase transition k , relative to the reference pressure $P_{ref,k}$ and Clapeyron slope γ_k :

$$\pi_k = p - P_{ref,k} - \gamma_k T \quad (\text{B.5})$$

The non-dimensional time derivative of the phase function Γ_k can now be written as:

$$\frac{d\Gamma_k}{dt'} = \frac{d\Gamma_k}{d\pi'_k} \left(\frac{\rho_0 g h^3}{\eta_0 \kappa} w' - \gamma'_k \frac{dT'}{dt'} \right) \quad (\text{B.6})$$

in which $\frac{d\Gamma_k}{d\pi'_k}$ follows from the definition of the harmonic parameterized phase function Γ , see Table 2.1.

The non-dimensional energy equation now becomes

$$\begin{aligned} & \left[1 + \frac{\Delta S}{c_p} B'(T' + T'_0) - \sum_k \gamma'_k \frac{d\Gamma_k}{d\pi'_k} \frac{Rc_k}{Ra} Di(T' + T'_0) \right] \cdot \left(\frac{\partial T'}{\partial t'} + u'_j \partial_j T' \right) - \\ & \left[\left(1 - \frac{\Delta S}{\alpha c_p \Delta T} \frac{Ra}{Di} A' + \sum_k \gamma'_k \frac{d\Gamma_k}{d\pi'_k} \frac{Rc_k}{Ra} \right) Di T' w' \right] = \\ & \partial_j \partial_j T' + \left[\frac{Di}{Ra} \Phi' + RH' + \left(-\frac{\Delta S}{\Delta T} \frac{Ra}{\alpha c_p} A' + \sum_k \gamma'_k \frac{d\Gamma_k}{d\pi'_k} \frac{Rc_k}{Ra} \right) Di T'_0 w' \right] \end{aligned} \quad (\text{B.7})$$

which is simplified by assigning symbols to the bracketed terms:

$$K \left(\frac{\partial T}{\partial t} + u_j \partial_j T \right) + LT = \partial_j \partial_j T + P \quad (\text{B.8})$$

B.2 Discretization

The energy equation in the formulation of expression (B.8) is discretized using the standard Galerkin Approach (SGA), following Segal and Vuik (2000). First equation (B.8) is multiplied by a time independent test function ϕ and integrated over the domain:

$$\int_V K \frac{\partial T}{\partial t} \phi dV + \int_V \left(-\partial_j \partial_j T + u_j \partial_j T + LT \right) \phi dV = \int_V P \phi dV \quad (\text{B.9})$$

The Gauss theorem is applied, resulting in

$$\int_V K \frac{\partial T}{\partial t} \phi dV + \int_V \left(\partial_j T \partial_j \phi + u_j \partial_j T \phi + LT \phi \right) dV - \int_{\partial V} \phi \partial_j T n_j dA = \int_V P \phi dV \quad (\text{B.10})$$

The boundary of the domain is split into two parts, one, ∂V_1 , having an essential boundary condition $T|_{\partial V_1} = g_1$ and one, ∂V_2 , having a natural boundary condition $\partial_j T n_j = g_2$. The weak formulation of the problem is found:

$$\int_V K \frac{\partial T}{\partial t} \phi dV + \int_V \left((\partial_j T \partial_j \phi) + u_j \partial_j T \phi + LT \phi \right) dV = \int_V P \phi dV + \int_{\partial V_2} g_2 \phi dA \quad (\text{B.11})$$

This formulation is applied to a finite element mesh, spanning the computational domain, on which the solution is approximated by a summation of time independent basis functions N :

$$T_h(\vec{x}, t) = \sum_{j=1}^n T_j(t) N_j(\vec{x}) + T_0(\vec{x}, t) \quad (\text{B.12})$$

The essential boundary condition on boundary ∂V_1 is included in the computation by demanding $N_j(\vec{x})$ and $T_0(\vec{x}, t)$ to satisfy this condition. The test functions ϕ are replaced by the basis functions N . This results in the Galerkin formulation of the problem. In matrix notation, this is

$$M\dot{\vec{T}} + A\vec{T} = \vec{R} \quad (\text{B.13})$$

The matrix elements are defined by

$$M_{ij} = \int_V K N_i N_j dV \quad (\text{B.14})$$

$$A_{ij} = \int_V \left(\nabla N_j \cdot \nabla N_i + (\vec{u} \cdot \nabla N_j) N_i + L N_i N_j \right) dV \quad (\text{B.15})$$

$$R_i = \int_V P N_i dV - \int_V \left(\nabla T_0 \cdot \nabla N_i + (\vec{u} \cdot \nabla T_0) N_i + L T_0 N_i \right) dV + \int_{\partial V_2} g_2 N_i dA \quad (\text{B.16})$$

B.3 Benchmarks of latent heat consumption

Separate experiments for the benchmarking of the latent heat consumption of partial melting and solid state phase transitions have been conducted. The former is benchmarked in the following experiment. In a narrow vertical tube, fertile material is forced to rise with a temperature sufficiently high to attain full melting. Between the linear and parallel solidus and liquidus, the rising material melts and this results in a lowering of the temperature. When the material rises fast enough, thermal diffusion cannot keep up with this heat consumption, and the resulting geotherm will be mainly determined by the latent heat consumption.

An analytical solution for this experiment has been obtained when assuming diffusion to be negligible and ignoring the effects of adiabatic compression, viscous dissipation and radiogenic heating. The temperature profile between solidus and liquidus then follows:

$$\frac{dT}{dz} = -\frac{\Delta S}{c_p} \frac{dF}{dz} T \quad (\text{B.17})$$

in which T is the absolute temperature (K), z the vertical coordinate (m), which is positive upwards and zero at the crossing of the geotherm with the solidus, ΔS the entropy change upon full melting ($\text{Jkg}^{-1}\text{K}^{-1}$), c_p the heat capacity ($\text{Jkg}^{-1}\text{K}^{-1}$), and F the degree of depletion, which is a function of the supersolidus temperature only. For a linear and parallel solidus and liquidus, this results in the following expression for the temperature between solidus and liquidus as a function of depth:

$$\frac{1}{\beta\gamma} \ln T + \frac{1}{\beta} T = z + c \quad (\text{B.18})$$

with $\beta = -\frac{dT_{\text{solidus}}}{dz}$, $\gamma = \frac{\Delta S}{c_p \Delta T_{st}}$ and c a constant.

A temperature profile can be obtained numerically from this expression by successive substitution. Both the temperature profile obtained from the benchmark described above and the analytical solution for parameter values listed in Table B.1 are presented in Figure B.1, showing a good agreement.

Benchmarking the latent heat effects due to solid state phase transitions is done in a similar way, by considering a 1-D vertical flow through a phase transition, disregarding all other heat effects (conduction, adiabatic compression, viscous dissipation, radiogenic heating). The temperature jump associated with the phase transition is given by:

$$\Delta T_{\text{analyt}} = T_0 \left[\exp\left(-\frac{\Delta S}{c_p}\right) - 1 \right] \quad (\text{B.19})$$

Numerically obtained and analytical results for parameter values listed in Table B.1 are compared in Table B.2 for a positive and a negative value of the Clapeyron slope, showing a relatively high accuracy of the numerical solution.

Melting		
symbol	parameter	value
ΔS	entropy change	$300\text{Jkg}^{-1}\text{K}^{-1}$
c_p	specific heat	$1250\text{Jkg}^{-1}\text{K}^{-1}$
ΔT_{sl}	solidus-liquidus temperature difference	600 K
$\frac{dT_{sol}}{dp} = \frac{dT_{liq}}{dp}$	solidus and liquidus gradient	120KPa^{-1}
ρ_0	density	3416kgm^{-3}
g_0	acceleration of gravity	9.81ms^{-2}
T_{scale}	temperature scale	2700 K
z_{scale}	depth scale	$800 \cdot 10^3 \text{ m}$
Solid state phase transitions		
symbol	parameter	value
T_0	temperature scale	1273 K
ΔS	entropy change	87.82Jkg^{-1}
c_p	specific heat	$1250\text{Jkg}^{-1}\text{K}^{-1}$

Table B.1: Parameters and their values of the benchmark cases for melting and solidus state phase transition latent heat effects, respectively.

$\gamma(\text{PaK}^{-1})$	$\Delta T_{analyt}(\text{K})$	$\Delta T_{obs}(\text{K})$	$\ \Delta T_{analyt} - \Delta T_{obs}\ /\ \Delta T_{analyt}\ $
$-3 \cdot 10^6$	-18.52205	-18.51578	$3.4 \cdot 10^{-4}$
$3 \cdot 10^6$	19.8697	19.8793	$4.8 \cdot 10^{-4}$

Table B.2: Benchmark results of the temperature jump at a solid state phase transition ΔT_{obs} compared to the analytical results ΔT_{analyt} for a positive and a negative Clapeyron slope γ .

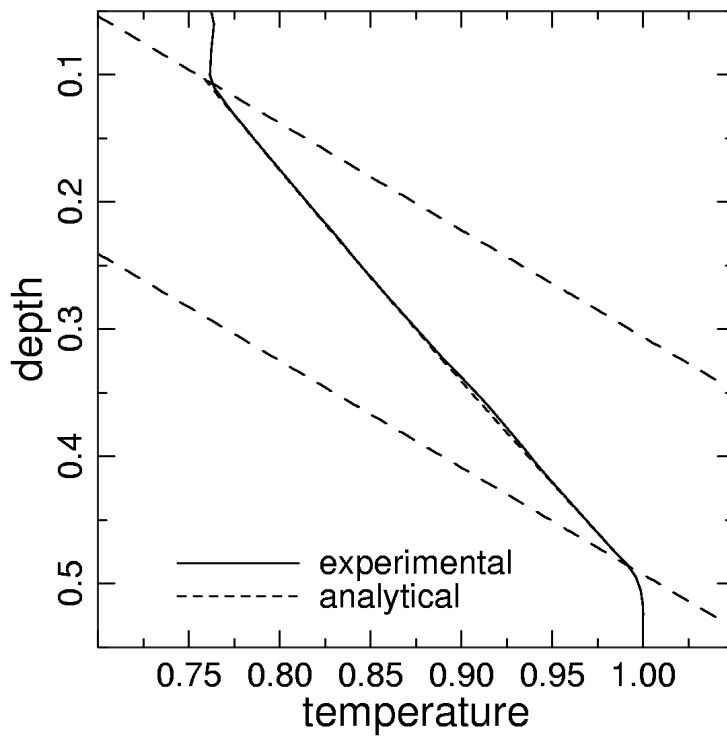


Figure B.1: Numerical (solid) and analytical (dotted) solution of the geotherm between solidus and liquidus (dashed).

Samenvatting en conclusies (Summary and conclusions in Dutch)

Samenvatting

Dit proefschrift draait om de vraag welk type geodynamica actief was in de vroege Aarde en andere terrestrische planeten, met name Mars en Venus. De geologie van het Archaïcum (4.0-2.5 miljard jaar geleden) verschilt aanzienlijk van de recente geologie, en daarom is het waarschijnlijk dat andere processen verantwoordelijk waren voor de vorming hiervan dan de hedendaagse plaattektoniek. Deze wordt gekenmerkt door ten opzichte van elkaar bewegende platen die uiteen drijven (mid-oceanische ruggen), botsen (bijvoorbeeld de Himalaya) of de mantel in duiken in subductiezones (bijvoorbeeld aan de westkust van Zuid Amerika). Er zijn diverse aanwijzingen dat de interne temperatuur van de jonge Aarde beduidend hoger was dan de huidige. De fysische gevolgen die te verwachten zijn voor een hogere manteltemperatuur ondersteunen de conclusie dat een ander geodynamisch regime in de vroege Aarde actief moet zijn geweest.

Zowel Venus als Mars is vergelijkbaar met de Aarde wat betreft samenstelling, en Venus heeft ook een vergelijkbare grootte, terwijl Mars een diameter van ongeveer de helft van die van de Aarde heeft. Ondanks de overeenkomsten zien de oppervlakken van beide planeten er beduidend anders uit dan dat van de Aarde. Zo zijn er bijvoorbeeld op geen van beide planeten aanwijzingen voor recente plaattektoniek gevonden.

In dit proefschrift worden de omstandigheden waaronder plaattektoniek en alternatieve geodynamische regimes kunnen opereren onderzocht voor de terrestrische planeten. Hiervoor wordt gebruik gemaakt van computermodellen. Voor de Aarde worden tevens meer gedetailleerde studies van de verschillende typen dynamica gebruikt om de resultaten van de gemodelleerde processen te vergelijken met overblijfselen van materiaal uit het Archaïcum die tegenwoordig nog op bepaalde plaatsen aan het aardoppervlak te vinden zijn (zie Figuur 1.1).

Na een bespreking van de numerieke modellen die in dit proefschrift worden gebruikt, en een beschrijving van de numerieke methoden die gebruikt zijn voor het verkrijgen van modeloplossingen, wordt een aantal studies gepresenteerd waarin de problemen die verband houden met het centrale thema van het proefschrift worden onderzocht.

Hoofdstuk 4 behandelt de omstandigheden waaronder plaattektoniek kan opereren op de verschillende terrestrische planeten.

Een belangrijke factor voor de werking van plaattektoniek is de verdeling van drijfvermogen (ten opzicht van de onderliggende mantel) in oceanische lithosfeer, hetgeen gerelateerd is aan de ouderdom van de lithosfeer. Het drijfvermogen hangt ook af van

compositionele gelaagdheid die het gevolg is van decompressiesmelten van mantelgesteente onder mid-oceanische ruggen. Het verloop van dit proces is afhankelijk van de temperatuur- en drukcondities die variëren tussen de terrestrische planeten en ook gedurende de afkoelingsgeschiedenissen van de planeten. In de modelexperimenten is een reeks van waarden voor de zwaartekrachtsversnelling (representatief voor verschillende terrestrische planeten), potentiële manteltemperatuur (representatief voor verschillende tijdstippen in de geschiedenis van de planeten) en oppervlaktetemperatuur toegepast om de condities waaronder plaattektoniek mogelijk is als mechanisme voor de afkoeling van de terrestrische planeten te onderzoeken. De effecten van manteltemperatuur op de samenstelling en dichtheid van smeltprodukten en op de lithosfeerdikte zijn meegenomen in de modelberekeningen. De resultaten tonen aan dat de tijd die nodig is voor oceanische lithosfeer om negatief drijfvermogen te ontwikkelen (ten opzichte van de onderliggende mantel) redelijk (minder dan enkele honderden miljoenen jaren) is voor een potentiële temperatuur onder de $\sim 1500^{\circ}\text{C}$ voor de Aarde. Voor Venus is dit ongeveer 1450°C (ter vergelijking: de huidige potentiële temperatuur van de Aarde is ongeveer 1350°C). In het geringere zwaartekrachtsveld van Mars wordt een veel dikkere gelaagdheid geproduceerd en het model geeft aan dat plaattektoniek alleen actief kan zijn op redelijke tijdschalen bij potentiële manteltemperaturen onder $1300 - 1400^{\circ}\text{C}$.

In het volgende hoofdstuk (5) worden afkoelingskarakteristieken van plaattektoniek en een alternatief mechanisme, i.e. grootschalig uitvloeiingsvulkanisme, gekwantificeerd. Hiervoor wordt gebruik gemaakt van parametrische modellen.

Geofysische argumenten tegen plaattektoniek in een hete Aarde, gebaseerd op beschouwing van het drijfvermogen van oceanische lithosfeer, vereisen een alternatief middel om de planeet af te koelen van zijn vroege hete staat naar de huidige situatie. Grootschalig uitvloeiingsvulkanisme zou zo'n alternatief kunnen zijn in een situatie die meer lijkt op het *stagnant lid* regime waarin Mars en Venus zich tegenwoordig bevinden. Uitgaande van het idee dat de volledige warmte-afgifte van de Aarde door haar oppervlak moet komen zijn parametrische modellen opgezet om de afkoelingskarakteristieken van deze twee mechanismen, plaattektoniek en grootschalig uitvloeiingsvulkanisme, te evalueren. De modelresultaten laten zien dat, in het geval van een gelijkmatig (exponentieel) afkoelende Aarde, plaattektoniek in staat is om alle benodigde warmte af te voeren op een tempo dat vergelijkbaar of zelfs kleiner dan het huidige tempo. Dit is in strijd met eerdere speculaties. Het uitvloeiingsmechanisme is mogelijk een belangrijk afkoelingsmechanisme geweest in de vroege Aarde. Dit mechanisme vereist echter uitvloeiingssnelheden die tot twee orden van grootte groter zijn dan die van recente (van de laatste paar honderd miljoen jaar) grootschalige uitvloeiingsprovincies om een belangrijke bijdrage te kunnen leveren aan de afkoeling van de Aarde. Dit hoeft echter geen probleem te zijn, aangezien geologische waarnemingen aangeven dat uitvloeiingsvulkanisme grootschaliger was en bovendien vaker voorkwam in de vroege Aarde. Vanwege zijn geringere afmetingen is Mars in staat om via warmtegeleiding door de lithosfeer heen met een aanzienlijke snelheid af te koelen. Dientengevolge heeft het waarschijnlijk nooit een extra afkoelingsmechanisme nodig gehad. Venus daarentegen heeft waarschijnlijk gedurende iedere fase van haar mogelijk episodische geschiedenis een extra afkoelingsmechanisme nodig gehad, met een tempo vergelijkbaar met Aardse snelheden.

Nu de omstandigheden waaronder plaattektoniek kan opereren en de afkoelingskarakteristieken van zowel plaattektoniek als grootschalig uitvloeiingsvulkanisme bestudeerd zijn, wordt het uitvloeiingsmechanisme in meer detail onderzocht in hoofdstuk 6, met de nadruk op de dynamica en geochemische effecten.

Numerieke thermochemische convectiemodellen met inbegrip van partieel smelten en een simpel mechanisme voor de segregatie van smelt en produktie van oceaankorst worden gebruikt om een alternatieve reeks van dynamische processen die mogelijk actief zijn geweest in de vroege aarde te bestuderen. De modelresultaten tonen drie processen die mogelijk een belangrijke rol hebben gespeeld in de produktie van oceanische korst en haar terugkeer de mantel in: (1) Kleinschalige ($x \cdot 100$ km) convectie van de onderkorst en ondiepe bovenmantel, met partieel smelten en dientengevolge korstproduktie in de opwaartse stroming, en delaminatie van eclogitische onderkorst in de neerwaartse stroming. (2) Grootschalige *oppervlaktevernieuwing* waarin (bijna) de volledige korst de (uiteindelijk onder-) mantel in zinkt. Dit zorgt voor het ontstaan van een stabiel reservoir aangerijkt in incompatibele elementen in de diepe mantel. Nieuwe korst wordt gelijktijdig gevormd aan het oppervlak. (3) De intrusie van diapieren (vergelijkbaar met opstijgende blobs in een lavalamp op een wat grotere schaal) met een hoge temperatuur (ongeveer 250 K warmer dan de omringende mantel) uit de ondermantel, hetgeen smelten van mantelgesteente en korstvorming op grote schaal veroorzaakt. Dit mechanisme produceert diapieren in de Archaische bovenmantel die veel warmer zijn dan totnogtoe verwacht vanuit theoretische overwegingen.

Hoofdstuk 7 behandelt de vorming van continentaal materiaal in de geodynamische context van het vorige hoofdstuk.

Archaische cratons, gevormd in de vroege en hete geschiedenis van de Aarde, bestaan voor een belangrijk deel uit TTG-intrusieven (Tontaliet-Trondhjemet-Granodioriet) en groensteengordels. De vorming van deze graniet-groensteengebieden wordt vaak toegeschreven aan plaattektonische processen, die echter waarschijnlijk niet zijn opgetreden tijdens de vroege geschiedenis van de Aarde. Daarom wordt er hier een alternatief mechanisme voorgesteld voor de gelijktijdige en naburige produktie van TTG-intrusieven en groensteen-achtige korstsegmenten: Als een lokaal anomaal dikke basaltische korst wordt geproduceerd door achtereenvolgende opeenstapeling van extrusieve of intrusieve basalten door partieel smelten van de onderliggende convecterende mantel kan de overgang van een voldoende grote hoeveelheid basalt in de onderkorst naar eclogiet een oppervlaktevernieuwingsepisode veroorzaken. Hierbij zinkt een korstsectie van meer dan 1000 km lang in minder dan 2 miljoen jaar de mantel in. Decompressiesmelten in de complementair omhoog stromende mantel genereert een grote hoeveelheid basaltisch materiaal, die de oorspronkelijke (eveneens basaltische) korst vervangt. Partieel smelten aan de basis van deze nieuw gevormde korst kan felsische smelten opleveren die als intrusiva en/of extrusiva aan de overwegend mafische korst worden toegevoegd. Dit resulteert in een korstsequentie die lijkt op een groensteengordel. Partieel smelten van metabasalt in de zinkende korstsectie produceert een aanzienlijk volume TTG-smelt dat direct boven de plaats van 'subductie' aan de korst wordt toegevoegd, mogelijk in intrusieve vorm (batholiet). Dit scenario wordt op zelf-consistente wijze geproduceerd door numerieke thermochemische mantelconvectiemodellen met inbegrip van partieel smelten van mantel- en

korstmateriaal. De temperatuur- en drukcondities waaronder partieel smelten van metabasalten plaatsvindt in dit scenario zijn consistent met geochemische sporenelementgegevens voor TTG's. Deze resultaten geven aan dat smelten plaatsvindt onder amfibolietcondities, en niet onder eclogiet-condities (hogere druk/grotere diepte). Andere geodynamische settings die ook zijn onderzocht, namelijk partieel smelten in kleinschalige delaminaties van de onderkorst, aan de basis van een anomaal dikke korst en door de instroom van een diapier uit de ondermantel, vertonen veelal smelten in het eclogiet stabiliteitsveld en reproduceren dit gedrag dus niet. Het oppervlaktevernieuwingsscenario is mogelijk ook belangrijk geweest in de geschiedenis van Venus, maar waarschijnlijk heeft het hier geen grote volumina continentaal materiaal geproduceerd vanwege het droge karakter van de planeet.

De stabiliteit van Archaïsche cratons wordt vaak toegeschreven aan de aanwezigheid van een wortel met een lage dichtheid onder deze continentale fragmenten. In hoofdstuk 8 wordt het belang van verschillende deformatieprocessen in de vorming van een dergelijke wortel onderzocht.

Een mogelijk mechanisme voor het toevoegen van materiaal aan een continentale wortel is met behulp van opwaartse stromingen vanuit de convecterende mantel waarin decompressiesmelten optreedt. Dit hoofdstuk toont resultaten van numerieke modellen van de interactie tussen smeltende diapieren en continentale wortels onder Archaïsche omstandigheden. In een uitbreiding van eerder werk (De Smet et al., 2000a) wordt de invloed van mantelrheologie op het gedrag van diapieren onderzocht, met nadruk op het verschil in gedrag van diapieren met een composiete rheologie, waarin zowel het korrelgroottegevoelige diffusiekruip-mechanisme als het dislocatiekruip-mechanisme zijn meegenomen. De korrelgrootte, hier uniform verondersteld, wordt gebruikt als een regelparameter om modelgevallen te verkrijgen met een variabele bijdrage van de twee kruipmechanismen. De diapieren in het composiete rheologiemodel stijgen veel sneller dan in een puur Newtoniaans model (alleen diffusiekruip). Waargenomen stijgtijden voor de diapieren van 230 km diepte tot de top van het pad op ongeveer 80 km diepte zijn ongeveer 1 miljoen jaar voor een Newtoniaans model (gemiddeld 14 cm/jaar), terwijl een composiet rheologiemodel er slechts 50 duizend jaar over doet (gemiddeld 3 m/jaar) met dezelfde parameters voor de Newtoniaanse component. Dit illustreert de grote invloed van de dislocatiekruipcomponent op het visceuze deformatieproces.

Het effect van een toename van de viscositeit (strokerigheid) ten gevolge van dehydratie (waterverlies) gedurende partieel smelten werd ook onderzocht. Deze toename heeft een sterke invloed op de ontwikkeling van stijgende diapieren. De stijgsnelheid en laterale uitspreiding van de diapieren aan de top van hun stijgpaden worden effectief verminderd als een viscositeitstoename met een factor 10 wordt toegepast, en het effect wordt sterker voor grotere factoren. Gemiddelde verticale snelheden variëren van 1.4 cm/jaar voor een factor 10 tot 2 mm/jaar voor een factor 200. Hierdoor worden karakteristieke tijdschalen van diapierintrusie opgerekt tot een waarde tussen 5 en 50 miljoen jaar voor dehydratie viscositeitsprefactorwaarden van respectievelijk 10 en 200.

In tegenstelling tot het grote verschil tussen Newtoniaanse en composiete rheologiemodellen worden slechts kleine verschillen gevonden in de algehele dynamica tussen de composiete rheologiemodellen onderling, gekarakteriseerd door verschillende waarden

voor de uniforme korrelgrootte.

De compositie rheologiemodellen tonen een zelfregulerend gedrag, waarbij substantiële verschillen tussen de relatieve bijdragen van de twee deformatiemechanismen resulteren in vergelijkbare effectieve viscositeiten, en corresponderende stromingsdynamica, als gevolg van de lokaal overheersende werking van dislocatiekruip bij hoge spanningen.

Spanningsniveau's en druk- en temperatuurpaden in de modelresultaten zijn consistent met schattingen voor Precambrische peridotietlichamen, die waarschijnlijk voortgekomen zijn uit diapirisme zoals in dit hoofdstuk gemodelleerd.

Conclusies

Uitgaande van de diverse resultaten verkregen voor de Aarde, Venus en Mars in dit proefschrift kunnen grove planetaire geschiedenissen worden geconstrueerd.

Aarde

Het initiële stadium direct na accretie en differentiatie van de kern werd waarschijnlijk gekarakteriseerd door een magma-oceaan (Murthy, 1992b; Abe, 1993a, 1997). Na het stollen van de magma-oceaan was de mantel nog erg heet, te heet om plaattektoniek toe te staan op basis van het drijfvermogen van oceanische lithosfeer (zie hoofdstuk 4). Desalniettemin was er een effectief afkoelingsmechanisme noodzakelijk (hoofdstuk 5), en een combinatie van grootschalig uitvloeiingsvulkanisme en periodieke oppervlaktevernieuwing speelde waarschijnlijk een belangrijke rol in de dynamica, en ook in de afkoeling van de planeet. Daarbij produceerden de oppervlaktevernieuwingen aanzienlijke hoeveelheden felsisch materiaal, dat proto-continenten vormde (zie hoofdstuk 7). Toen de manteltemperatuur tot ongeveer 1500°C daalde verkreeg oceanische lithosfeer een negatief drijfvermogen op een tijdschaal van enkele honderden miljoenen jaren of minder en werd actieve plaattektoniek mogelijk (hoofdstuk 4). Er kan worden gespeculeerd dat een min of meer gelijkmatige overgang van overheersend oppervlaktevernieuwingen naar plaattektoniek plaatsvond rond deze manteltemperatuur, mogelijk gedurende het laat-Archæicum. De komst van plaattektoniek voorzag bovendien in een additioneel mechanisme voor continentgroei via de accretie van vulkanische eilandbogen. Voortgaande activiteit van plaattektoniek en de resulterende afkoeling van de mantel brachten de Aarde in haar huidige toestand.

Venus

Hoewel Venus vergelijkbaar is met de Aarde wat betreft omvang en samenstelling, onderging Venus niet dezelfde ontwikkeling. Periodieke vernieuwing van de korst van Venus is gesuggereerd (Turcotte, 1995; Fowler and O'Brien, 1996), mogelijk door periodieke activiteit van plaattektoniek (Solomatov and Moresi, 1996) of door het oppervlaktevernieuwingsmechanisme dat in hoofdstuk 6 is gepresenteerd. Tegenwoordig is Venus een droge planeet, hetgeen plaattektoniek zou tegenwerken, met name door een toename in

de breuksterkte (Nimmo and McKenzie, 1998). Tijdens haar vroege geschiedenis was de planeet mogelijk minder droog (Campbell and Taylor, 1983; Nimmo and McKenzie, 1998), maar de manteltemperatuur was waarschijnlijk te hoog om plaattektoniek mogelijk te maken (zie hoofdstuk 4). Hieruit volgt de speculatie dat Venus na een initieel magma-oceaan regime gedurende de vroegste geschiedenis in een dynamisch regime van periodieke oppervlaktevernieuwing, beschreven in hoofdstuk 6, is blijven hangen tot op de dag van vandaag.

Mars

Als gevolg van de geringe grootte van Mars in vergelijking met de Aarde en Venus is zijn verhouding tussen oppervlak en volume ($\sim R^2/R^3$) veel groter, hetgeen conductieve afkoeling door de lithosfeer veel efficiënter maakt (zie hoofdstuk 5). Waarnemingen en geofysische overwegingen geven aan dat als er al een grootschalig tektonisch regime actief is geweest op Mars, dit tijdens de vroege geschiedenis moet zijn geweest (Zuber, 2001), hoewel mantelconvectiemodellen met decompressiesmelten onder geringe zwaartekrachtscondities laten zien dat een dikke, lichte schil in de bovenmantel wordt gevormd die plaattektoniek tegenwerkt (Schott et al., 2001). Echter, vanwege zijn zwakke zwaartekrachtveld in vergelijking met de Aarde zijn de omstandigheden waaronder plaattektoniek actief kan zijn beperkt to potentiële manteltemperaturen beneden $1300 - 1400^\circ C$ (hoofdstuk 5). De hogere manteltemperatuur die wordt verwacht voor de vroege geschiedenis van Mars werkt plaattektoniek dus tegen. Het is mogelijk dat het oppervlaktevernieuingsmechanisme van hoofdstuk 6 actief is geweest tijdens de vroege geschiedenis van de planeet. Maar na een mogelijke periode van dit regime ging Mars waarschijnlijk snel over naar het *stagnant lid* regime, waarin afkoeling overheersend door geleiding tot in het heden doorgaat.

Dankwoord (Acknowledgments)

Allereerst ben ik professor N.J. Vlaar veel dank verschuldigd voor zijn wetenschappelijke bijdragen tijdens discussies en presentaties van mij voortkomend uit zijn grote kennis van en gevoel voor het wetenschapsgebied van de geofysica, met name wat betreft de diepe en jonge Aarde. Zijn werk en publicaties op dit gebied hebben bovendien aan de basis gestaan voor dit project. Ik vind het erg spijtig dat zijn gezondheidstoestand dit jaar te wensen over heeft gelaten, en dat hij dientengevolge het laatste (en drukste) halve jaar van mijn project geen bijdragen meer heeft kunnen leveren en dat hij om dezelfde redenen niet meer eerste promotor heeft kunnen zijn.

Professor Rob van der Hilst wil ik graag bedanken voor zijn bereidheid om in te springen als eerste promotor, en om de input die hij gedurende de laatste maanden nog heeft gegeven op het project, ondanks het feit dat hij pas op het laatste moment erbij betrokken raakte en hij gedurende die periode ook erg druk was met een aantal andere zaken buiten de normale werkzaamheden als hoogleraar.

Verder wil ik mijn co-promotor en dagelijks begeleider Arie van den Berg bedanken voor zijn inzet gedurende de viereneenhalf jaar die ik met mijn promotieproject bezig ben geweest. De vele discussies die wij hebben gehad over diverse geofysische onderwerpen hebben een belangrijke bijdrage geleverd aan mijn ontwikkeling als wetenschapper. Zijn brede blik op diverse zaken en positieve instelling brachten steevast nieuwe wegen en mogelijkheden op momenten dat ik dacht vast te zitten, en zijn correcties op mijn pennevruchten (of eigenlijk toetsenbordvruchten) hebben mij duidelijk beter leren schrijven.

Jeroen de Smet (gedurende de eerste maanden van mijn project) en Jeroen van Hunen (in de daarop volgende twee jaar) hebben mij wegwijs gemaakt in de gebruikte codes en libraries, waarvoor ik hun erkentelijk ben. Bovendien is Jeroen van Hunen een jaar lang een gezellig kamergenoot geweest.

Gedurende vrijwel mijn hele promotieperiode heeft Annemarie Bos twee kamers naast de mijne gezeten, eerst op de oostgang en daarna op de zuidgang. Haar wil ik bedanken voor de gezelligheid en goede gesprekken over wetenschap en allerlei andere zaken tijdens de vele lunch- en theepauzes die we samen of in een grotere groep doorgebracht hebben.

De rol van kamergenoot werd na het vertrek van Jeroen van Hunen overgenomen door Thomas Geenen, die, op momenten dat niet als zo vaak een van ons beiden thuis werkte, bijdroeg aan een zeer prettige sfeer.

Anderen die met name de lunchpauzes veraangenaamd hebben zijn Caroline Beghein, Jojanneke van den Berg, Ildiko Csikós, Rob Govers, Paul Meijer, Hanneke Paulssen, Bertram Schott, Wim Spakman, Sri Sumarti, Jeannot Trampert, Antonio Villaseñor, Robbert van Vossen, Arie van Wettum, en anderen.

The weekly sessions of the *Old Rocks Literature Club* (and also discussions with members outside these sessions) have greatly added to my knowledge and understanding of the geology and geochemistry of the Archean, and I would like to thank the following persons for this: Tanja Zegers, Matthias Barth, Sjoukje de Vries, Jason Herrin, Geert Strik

and Kike Beintema.

The petrological input of Martyn Drury in one of the chapters is gratefully acknowledged. Michel Jacobs heeft enige bijdragen geleverd op thermodynamisch gebied, waarvoor dank.

Computermodellen draaien niet zonder computers, en de computers van Aardwetenschappen draaien niet zonder Theo van Zessen en Joop Hoofd. Beiden wil ik graag hartelijk bedanken voor de technische ondersteuning die zij talloze keren hebben verleend, van het branden van een dvd'tje tot het oplossen van hard- en softwareproblemen, en bovendien voor de vele interessante gesprekken op computergebied.

De medewerkers van de bibliotheek Aardwetenschappen (en later Geowetenschappen) ben ik erkentelijk voor veel hulp bij het vinden vele boeken en tijdschriften en voor het laten overkomen van vele hiervan vanuit andere bibliotheken.

I'd like to express my gratitude to the members of my dissertation committee, prof. dr. B.H.W.S. de Jong, prof. dr. Y. Ricard, prof. dr. H.A. van der Vorst, prof. dr. M.J.R. Wortel, and prof. dr. D.A. Yuen, for their thorough reading of the manuscript and constructive criticism which helped improve the work.

Voor het gebruik van supercomputerfaciliteiten bij dit onderzoek is subsidie verleend door de Stichting Nationale Computer Faciliteiten (NCF), met financiële steun van de Nederlandse Organisatie voor Wetenschappelijk Onderzoek (NWO). Tevens is er gebruik gemaakt van computerfaciliteiten gefinancierd door ISES (Netherlands Research Centre for Integrated Solid Earth Science).

Ook buiten het wetenschappelijke wereldje hebben diverse personen indirect een bijdrage geleverd aan mijn promotiewerk. Mijn ouders wil ik graag bedanken voor hun steun en aanmoediging tijdens mijn studie, en verdere stimulans tijdens het promotieproject. Voor de broodnodige ontspanning gaat mijn dank uit naar o.a. Maarten van Thienen, Erik Koffijberg, Miriam Fossen, Edgar de Reus, Nathalie van Klaveren, Juriaan Slee, Stefan Berghuis, en de familie Visser.

En natuurlijk gaat mijn dank uit naar Karin Visser, die gedurende de afgelopen bijna 3 jaar mij als geliefde en het laatste jaar bovendien als fijne en gezellige collega heeft bijgestaan met veel liefde, steun en zo nu en dan wijze raad.

Curriculum vitae

De auteur werd geboren op 10 oktober 1975 in Rotterdam. Van 1988 tot 1994 doorliep hij het VWO op de Christelijke Scholengemeenschap Blaise Pascal te Spijkenisse. In 1994 begon hij met de studie geologie in Utrecht, en na het behalen van de propedeuse in 1995 begon hij met de doctoraalstudie geochemie. Deze studie werd afgerond in 1998 (judicium: *cum laude*) met een onderzoeksproject over de petrologie en geochemie van een Indonesische vulkaan en numerieke modellen van uitbarstingen van deze vulkaan. Op 1 april 1999 begon hij aan zijn promotieproject.

